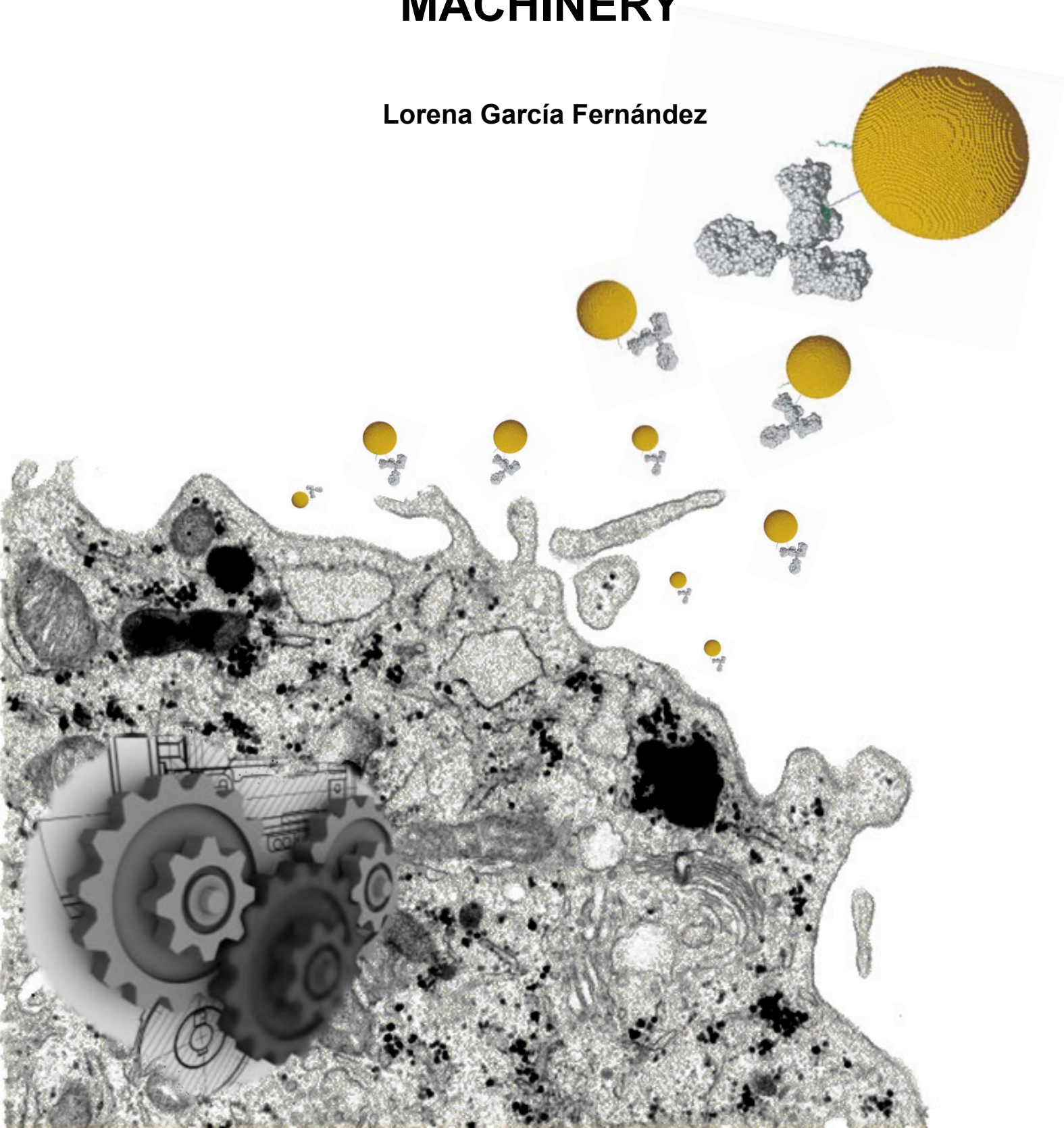


INTRODUCING GOLD NANOPARTICLE BIOCONJUGATES WITHIN THE BIOLOGICAL MACHINERY

Lorena García Fernández



PhD Thesis

INTRODUCING GOLD NANOPARTICLE BIOCONJUGATES WITHIN THE BIOLOGICAL MACHINERY

Memòria presentada per:

Lorena García Fernández

Per optar al grau de

Doctor per la Universitat Autònoma de Barcelona

Programa de Doctorat en Bioquímica, Biologia Molecular
i Biomedicina

Tesi realitzada sota la direcció del Prof. Víctor Franco Puentes,
Inorganic Nanoparticles Group, Institut Català de Nanotecnologia,
i amb la tutoria de la Dra. Ester Boix Borràs,
Departament de Bioquímica i Biologia Molecular, Universitat Autònoma de
Barcelona.

Cerdanyola del Vallès, Març 2013

*Mi más sincero agradecimiento a mi familia,
amigos, compañeros de poyata y director de tesis,
a todos aquellos de los que he aprendido, cuyo
apoyo ha sido esencial en el transcurso de esta
tesis.*



Chema Madoz

“Where Nature finishes producing its own species, man begins, using natural things and with the help of this nature, to create an infinity of species”

Leonardo da Vinci, XV-XVI

TABLE OF CONTENTS

Abstract	i
INTRODUCTION	
Chapter 1. General introduction: rational design of gold nanoparticle bioconjugates for exploring the nano-bio interface.	1
1.1. Au NP synthesis: controlling size, shape and surface chemistry.	3
1.2. State of the art in the functionalization of Au NPs with biomolecules.	8
1.3. The “gold standard”: Au NPs as model systems for investigating the nano-bio interface.	13
1.4. Parameters of influence at the nano-bio interface.	16
1.5. References.	26
PART I. INTRODUCTION TO CATIONIC GOLD NANOPARTICLES.	37
Chapter 2. Synthesis of cationic gold nanoparticles by competitive reducers.	41
2.1. Introduction to the synthetic routes for preparing cationic Au NPs.	42
2.2. Results and discussion.	46
2.2.1. Independent control of nucleation and growth using different reducers at substoichiometric concentrations.	46
2.2.2. Independent control of nucleation and growth using different reducers <i>via</i> seeded growth.	50
2.3. Conclusions.	52
2.4. References.	53
Chapter 3. Synthesis of cationic gold nanoparticles by organic-aqueous phase transfer.	57
3.1. Introduction.	58
3.1.1. Synthesis of Au NPs in organic solvents.	58

3.1.2. Phase transfer methods.	61
3.2. Results and discussion.	64
3.2.1. Preparation and characterization of Au NPs in the organic phase.	64
3.2.2. Phase transfer with a cationic alkanethiolate ligand.	66
3.3. Conclusions.	69
3.4. References.	70
Chapter 4. Bioconjugation of cationic peptides to gold nanoparticles for cell penetration.	75
4.1. Introduction. Role of cationic charge in Au NPs internalization by cells.	76
4.1.1. Origins of cationic cellular uptake.	76
4.1.2. Physicochemical properties of cationic NPs in the extracellular media.	80
4.1.3. Mechanism of cation-mediated internalization of Au NPs.	82
4.2. Results and discussion.	86
4.2.1. Design of the peptidic biomolecules for functionalization.	86
4.2.2. Synthesis and physicochemical characterization of peptide-Au NP bioconjugates.	88
4.2.3. Stability and physicochemical properties of peptide-Au NP bioconjugates in physiological conditions.	91
4.2.4. <i>In vitro</i> toxicity, cellular uptake and intracellular fate of cationic peptide-Au NP bioconjugates.	95
4.3. Conclusions.	101
4.4. References.	102
PART II. INTRODUCTION TO THE CONTROLLED BIOCONJUGATION OF ANTIBODIES ON GOLD NANOPARTICLES.	109
Chapter 5. Controlled display of antibodies on Au NPs: biomolecular orientation and ratio of bioconjugation.	113
5.1. Introduction.	114

5.1.1. Antibody functions and isotypes.	114
5.1.2. Polyclonal and monoclonal antibodies.	117
5.1.3. Immunoglobulin G (IgG) structure.	118
5.1.4. Antibody-NP bioconjugation strategies.	120
5.1.5. Synthesis of different sized citrate-capped Au NPs.	123
5.2. Results and discussion.	128
5.2.1. Controlled formation of antibody-Au NP bioconjugates by a site-directed chemistry.	128
5.2.2. Theoretical calculations of the loading of antibodies on Au NPs.	139
5.2.3. Rational design and formation antibody-Au NP superstructures.	141
5.3. Conclusions.	145
5.4. References.	146
Chapter 6. Targeting the Epidermal Growth Factor Receptor by rationally designed Cetuximab antibody-Au NP bioconjugates.	153
6.1. Background and overview. Targeted Therapy of the Epidermal Growth Factor Receptor (EGFR) by Cetuximab monoclonal antibodies.	154
6.1.1. EGFR structure and function.	155
6.1.2. Binding of Cetuximab monoclonal antibody to EGFR.	159
6.2. Cellular receptor-mediated interactions with Au NP bioconjugates.	162
6.3. Results and discussion.	165
6.3.1. Synthesis of Cetuximab- 1 -Au NP bioconjugates by controlling the orientation and number of antibodies onto Au NPs.	166
6.3.2. Binding of Cetuximab- 1 -Au NP bioconjugates to EGFR.	171
6.3.3. Blockade of EGF ligand binding to EGFR.	174
6.3.4. Uptake and intracellular fate of Cetuximab- 1 -Au NP bioconjugates.	176
6.3.5. EGFR down-regulation.	181

6.3.6. Inhibition of ligand-induced EGFR tyrosine kinase activation and signalling downstream.	184
6.3.7. Cell viability studies.	189
6.4. Conclusions.	190
6.5. References.	191
7. General conclusions.	197
8. Future perspectives.	199
List of abbreviations.	201
Annex I. Materials and methods.	205
Experimental from Chapter 2.	205
Experimental from Chapter 3.	206
Experimental from Chapter 4.	208
Experimental from Chapter 5.	210
Experimental from Chapter 6.	213
References	219
Annex II. Manuscripts.	221

Abstract

The rapid development in nanotechnology during the past decades offers wide prospects in using micro- and nano-scale materials in different areas of industry, technology and medicine. However, their safe and efficient use and implementation in such areas require much greater control over their physicochemical properties and their related molecular interactions in living systems. Current knowledge in the scientific community agrees that a considerable gap exists in our understanding of such “nano-bio” interface. As a step forward in this direction, this Thesis work aimed to provide insights into the formation of rationally designed gold nanoparticle (Au NP) bioconjugate architectures to modulate and understand cellular interactions and processes.

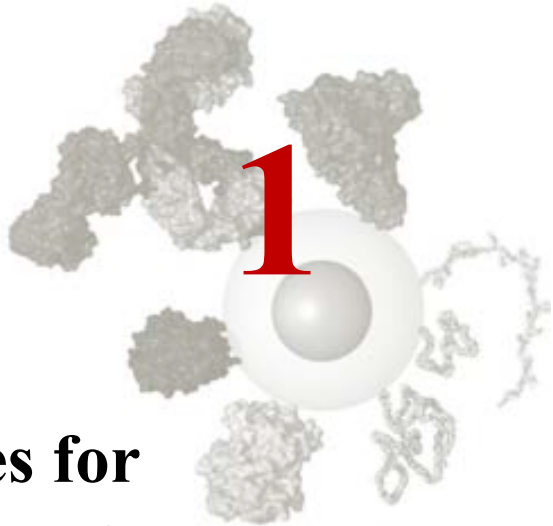
In such a context, **Chapter 1** gives a brief overview of the trend evolution in Au NPs synthesis and biofunctionalization towards strictly controlled architectures, and includes the main advantages and important advances of using Au NP bioconjugates at the nano-bio interface.

In the first part of this Thesis, **Chapter 2** describes the synthesis of positively charged Au NPs by using simultaneously a weak and a strong reducer. We show that both reducers act sequentially in a one-pot synthesis to yield monodisperse cationic Au NPs with sizes comprised between 10.3 and 19.7 nm. A two-step seeding growth method is also described in which preformed Au NPs are grown larger (up to ~28 nm in size) by addition of fresh precursor solution and the weak reducer. **Chapter 3** faces the rising demand of cationic Au NPs of different sizes and ligands by developing an organic-aqueous phase transfer methodology. This method is employed to synthesize cationic Au NPs of 4.6, 8.9 and 13.4 nm in diameter using a positively charged alkanethiolate ligand. The important benefits resulting from the combination of organic and aqueous synthetic methods are described. Finally, **Chapter 4** furthers the practical applications of the phase-transfer methodology (Chapter 3) to produce ~ 13-nm-in-size cationic and anionic peptide-Au NP bioconjugates. The physicochemical properties of these bioconjugates in cell culture media as well as their uptake and toxicity on human fibroblast cells are discussed.

In the second part of this Thesis, **Chapter 5** describes the rational design of antibody-Au NP bioconjugates through a site-directed chemistry, which allows controlling the ratio and orientation of bioconjugation. The formation of well-defined bioconjugates makes possible the creation of novel NP-based assemblies using antibody-antigen cross-links. **Chapter 6** expands upon this initial work (Chapter 5) by exploring the interaction of a biologically relevant antibody (Cetuximab) with Au NPs. Cetuximab-Au NP bioconjugates of controlled configuration and multivalency are used to examine their interaction with the cell surface receptor EGFR (epidermal growth factor receptor), a receptor tyrosine kinase overexpressed in a large number of cancers.

General Introduction:

Rational Design of Gold Nanoparticle Bioconjugates for Exploring the Nano-Bio Interface



Rapid growth of nanotechnology is opening up novel avenues for a myriad of applications that were unthinkable some decades ago, ranging from chemical sensing and imaging¹⁻⁴ to cancer treatment and targeted drug delivery,⁴⁻⁹ to name a few. Many of these innovative applications take advantage of the possibility to associate biologically relevant molecules at the interface of nanoparticles (NPs) to create new hybrid nanomaterials (hereafter called NP bioconjugates). These NP bioconjugates provide the obvious potential advantages of intimately mixing the attractive properties of both **-the physicochemical signatures of the NPs and the programmability of biomolecules-** in single entities that incorporate not only the sum of these properties but they also provide synergistic effects. Thus, as the interest in such NP bioconjugates and related applications continues to grow, there are arising concerns about their interactions with living systems: the nano-bio interface. Recent findings demonstrate that, besides their potential deliberate function, these nanomaterials can lead to unanticipated or detrimental effects on living cells and organisms.^{10,11} In this scenario, the ability to prepare NP bioconjugates in a precise manner is critical to understand how small variations in their architecture impact their interaction with cells.^{12,13} This, taken in conjunction with the increasing demand of scientists for an improved quality of nanomaterials, make essential to investigate both, the controlled formation of NP bioconjugates and the wealth of scenarios that these may have at the nano-bio interface.

The synthesis of gold nanoparticles (Au NPs) has been in the spotlight since Faraday¹⁴ discovered in 1857 the mechanism of formation of pure gold colloids. This synthesis has been the keystone of a large amount of chemical routes to obtain Au NPs with controlled size, shape and surface chemistry. Today, scientists have a wide catalog of Au NPs available, which can be used as excellent model systems to investigate the nano-bio interface; that is, when Au NPs come into contact with biological components, such as biomolecules, cells, etc.

Since the 1970s, Au NPs have been used in combination with antibodies (Abs) or other proteins to visualize specific cellular compartments, proteins and receptors (Figure 1.1-A).¹⁵ Another well-known application of Au NPs is their use as probes of biomarkers in the pregnancy test (e.g. First Response®, marketed in the 1990's) (Figure 1.1-B). This test is based on the specific recognition of human chorionic gonadotropin (hCG), an hormone produced during pregnancy, by Au NPs conjugated with an anti-hCG Ab. When a drop of urine is added to the test strip, this Au NP bioconjugate binds to hCG, and the complex (hCG-Au NP bioconjugate) move chromatographically along the membrane. Then, an anti-hCG Ab immobilized on the membrane capture these complexes, and concentrates them appearing as a red line. Nowadays, advanced NP bioconjugate chemistries allow scientists to tailor NPs for much higher sophisticated purposes, such as orchestrating chemical reactions inside cells^{16,17} and manipulating the cells response.^{18,19} The successful development of these challenging tasks relies on intelligent surface structure design and the ability to synthesize NP bioconjugates with the desired architecture, which is also paramount in obtaining a well-defined and reproducible behavior. The fundamental problem is that the design principles of synthetic NP bioconjugates for specific cellular interactions are today far from being properly understood.

This Thesis aims to contribute to this emerging field, in which the organic and synthetic worlds merge into a new science concerned with the safe and efficient use of nanomaterials for biological applications. For a more comprehensive view, and addressing it to multidisciplinary readers, this introductory Chapter provides a practical overview of the design and synthesis of Au NP bioconjugates to study NP-cell interactions. First, synthetic efforts to the controlled formation of Au NPs (e.g. with

controlled size, shape and surface chemistry) and their rational functionalization with biomolecules (e.g. with controlled orientation and bioconjugation chemistry) are described. And second, the controlled formation of complex Au NP bioconjugates (e.g. with proteins and additional components) is a critical and yet poorly studied issue that, in turn, dictates the molecular interactions between NPs and cells. Therefore, the main physicochemical parameters shaping NP-cell interactions as well as various precedents in the literature showing evidence of the importance of the NP design at the nano-bio interface are thoroughly discussed.

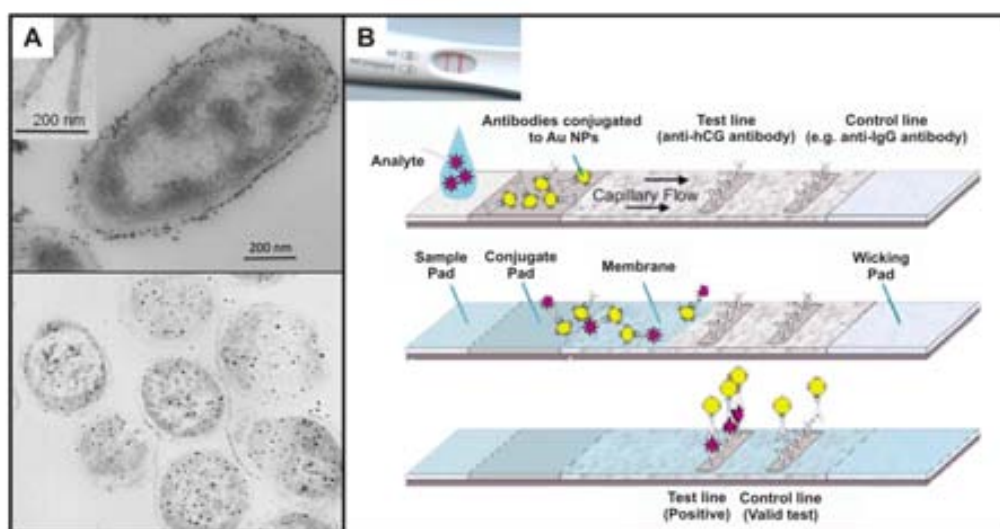


Figure 1.1. Illustrative examples of the first uses of Ab-Au NP bioconjugates as probes in biological systems. A) Representative transmission electron microscopy images from Au NPs conjugated to Abs for labelling cellular features (images extracted from ref. 20 and 21). B) Image depicting the mechanism of lateral flow assay in which is based the pregnancy test (image extracted from Cytodiagnosics, Inc).

1.1. Au NP synthesis: controlling size, shape and surface chemistry.

Gold is a valuable precious metal that has been used for therapeutic and decorative purposes since ancient times. Colloidal gold was first used in China for medicinal potions. In the 16th century, the alchemist Paracelsus claimed to have created a potion called *Aurum Potabile* (from the Latin: potable gold). However, the mechanisms of formation and therapeutic action of this “drinkable” gold were not well understood. It was not until 1857 that Faraday¹⁴ described the first synthesis of a pure gold colloid. In 1951, Turkevich *et al.*²² performed the first structural studies of Au NPs by electron microscopy, and further work developed by Frens²³ showed the possibility to tune the

size of spherical Au NPs from ~ 16 to ~ 150 nm (although larger sizes were obtained at the cost of monodispersity). These studies became the cornerstone of a large amount of posterior colloidal synthetic methods developed for obtaining Au NPs with defined size, shape and surface chemistry.

Nowadays, the term gold colloid is applied for Au NPs in a dispersion medium typically ranging from 1 to 200 nm in size. Very small Au NPs (< 3 nm) that are composed by a few to some hundred atoms are often called clusters. The synthesis of Au NPs is generally performed by reduction of a solvated gold salt in the presence of surface capping ligands, which prevent aggregation of the formed NPs by electrostatic and/or physical repulsion.* By varying the ratio of gold ion:reducing agent or the ratio of gold ion:stabilizer, the NP size can be adjusted, obtaining larger (and less monodisperse) sizes from larger ratios.

One of the first examples of Au clusters (1.4 ± 0.4 nm-in-size) synthesis was reported by Schmid *et al.*²⁴ in 1981, in which they examined their stabilization with a phosphine linkage in benzene. Later in 1994, Brust *et al.*²⁵ introduced the synthesis of Au clusters and NPs (1.5 to 5.2 nm in size) stabilized by thiols (Figure 1.2-A), which became very popular due to its interesting molecule-like properties (e.g. isolation and redispersion in various organic solvents and facile conjugation). This synthesis is based on a two-phase methodology, in which gold chloride is first transferred to the organic phase by a quaternary ammonium salt, and then reduced in the organic phase in the presence of stabilizing dodecanethiol molecules (for more details see Chapter 3, Section 3.1.1). Leff *et al.*²⁶ introduced a variation from this method, consisting on the use of amine-functionalized ligands to stabilize the Au NPs, thus obtaining larger Au NP sizes (from 2.5 to 7 nm) due to the weaker covalent bonds between amines and Au surfaces. Other variations include different amine-containing ligand molecules^{27,28} and different solvent systems (Figure 1.2-B).²⁹

* For a more detailed discussion on NPs colloidal stability, the reader is referred to some excellent reviews: a) Casals, E.; Vázquez-Campos, S.; Bastús, N. G.; Puentes, V. *Distribution and Potential Toxicity of Engineered Inorganic Nanoparticles and Carbon Nanostructures in Biological Systems*. TrAC Trends in Anal. Chem., **2008**, 27, 672-683; b) Casals, E.; Gonzalez, E.; Puentes, V. F. *Reactivity of Inorganic Nanoparticles in Biological Environments: Insights into Nanotoxicity Mechanisms*. J. Phys. D: Appl. Phys., **2012**, 45, 443001; and the book chapter: Ohshima, H. *DLVO Theory of Colloid Stability*. Biophys. Chem. Biointerfaces, **2010**, John Wiley & Sons, Inc., 420-430.

Amongst the aqueous synthetic methods, Au NPs are typically produced by the reduction of gold salts in citrate, either in the presence of a strong reducing agent (e.g. borohydride)³⁰ or using citrate as both the reducer and the stabilizer (*i.e.* Turkevich-Frens method) (Figure 1.2-C, top left).^{22,23} The Au NPs are stabilized by citrate ions bound to their surface, resulting in negatively charged Au NPs that repel each other by electrostatic repulsion. Reduction with borohydride is performed at room temperature, and normally yields Au NPs of small sizes (~ 3.5-5.0 nm) and fairly good monodispersity. The citrate-reduction route is normally performed at 100°C and yields Au NPs with an average diameter from 5 to 150 nm by simply varying the reaction conditions (sodium citrate to gold salt ratio,²³ solution pH,³¹ and solvent).³² However, the quality of the Au NPs (size and size distribution) is compromised for NP sizes larger than ~ 40 nm, also obtaining irregular shapes, such as quasi-spheres, ellipsoids, and triangles.³³ Larger Au NP sizes with precisely controlled size and shape can be obtained by seeding growth methods (Figure 1.2-C). These syntheses are based on the temporal separation of the nucleation and growth processes. Typically, small Au NPs (named seeds) are first produced, which are then used as nucleation centers for further reduction of gold salt, resulting in a homogeneous growth. Recently, a citrate-reduction seeding-mediated method has been developed by our group,³⁴ which yields citrate-capped Au NPs with good monodispersity up to 200 nm. Further information on citrate-reduction and seeding-growth methods is given in Chapter 5, Section 5.1.5.

Alternatively, the aqueous reduction of Au salts can be performed with other reducing agents (e.g. ascorbic acid,^{33,35} H₂O₂)³⁶ and in the presence of a variety of ligands stabilizing the NPs, mainly thiolates (e.g. mercaptosuccinic acid,³⁷ thiolated derivatives of polyethylene glycol (PEG),³⁸ tiopronin (N-2-mercaptopropionyl-glycine),³⁹ coenzyme A (CoA)³⁹ and glutathione)⁴⁰ or amines (e.g. bis(2-(4-aminophenoxy)ethyl)ether⁴¹ and oleyl amine),⁴² among others. The ligand of choice determines the NP growth and the surface properties of the NPs. For greater detail and more examples of Au NP synthesis, the reader is referred to some excellent reviews.^{43,44}

Besides spherical Au NPs, there is a growing interest in creating different Au NP shapes. Some examples include rods,⁴⁵ cubes,⁴⁶ prisms,⁴⁷ branched particles,⁴⁸ hollow shells,⁴⁹ and cages⁵⁰ (Figure 1.2-E-N). A typical strategy involves the use of ligands that allow the preferred anisotropic growth along certain crystal axes, e.g. by stronger

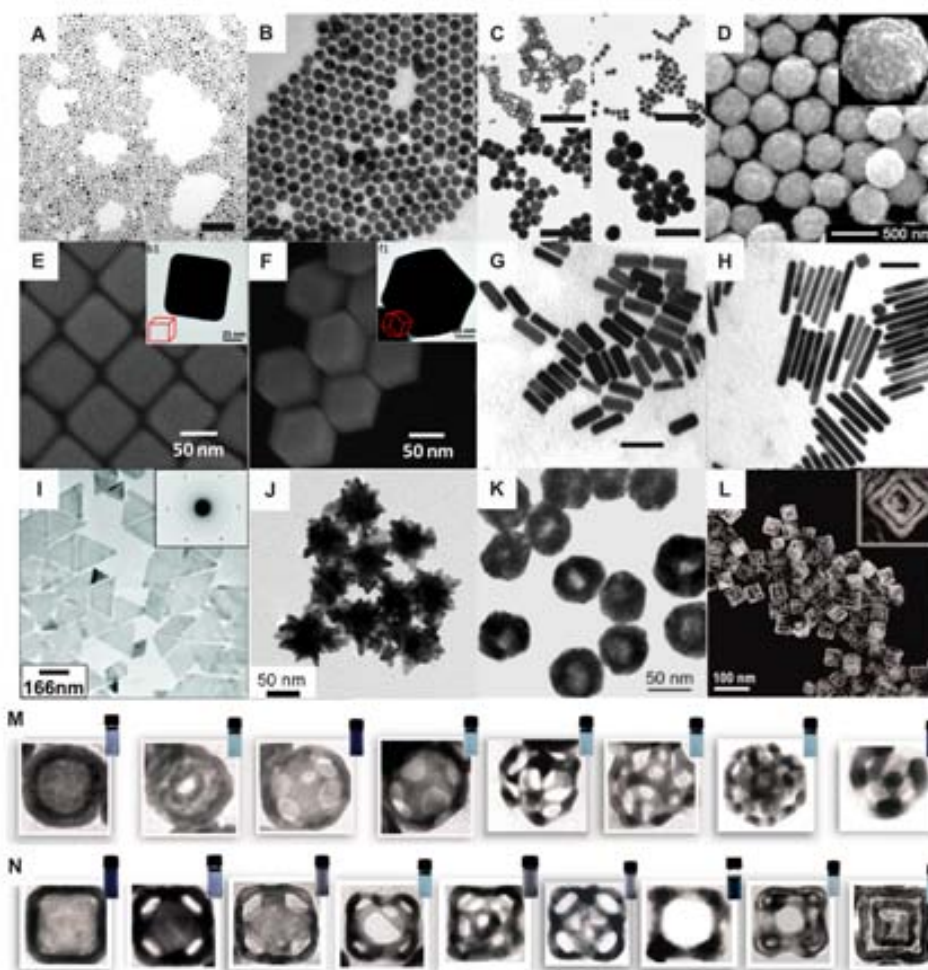


Figure 1.2. Exemplary Au NPs of various sizes and shapes obtained by different synthetic approaches. A-D) Small and large nanospheres; E) cubes; F) rhombic dodecahedra; G, H) rods with lower and higher aspect ratio; I) prisms; J) star-shaped branched particles; K, M) hollow shells; L, N) hollow cages. NPs in A (4.6 ± 1.1 nm-in-size), B (14.1 ± 1.7 nm-in-size) and C (7.4 ± 1.5 , 14.6 ± 1.6 , 24.0 ± 3.8 and 35.9 ± 6.0 nm-in-size) were synthesized in this Thesis by following the reduction methods from Brust *et al.*,²⁵ Hiramatsu *et al.*,²⁹ Turkevich *et al.*²² and the seeding growth method from Bastús *et al.*,³⁴ respectively. Scale bars are 50 nm (A), 40 nm (B) and 100 nm (C). Images from D to N were extracted from references 35 and 45-50. NPs in D were produced by aqueous reduction with ascorbic acid, NPs in E-J were produced by seeding growth methods, and NPs in K-N were produced by galvanic replacement. Note that only NPs in A-C and L-N were produced by our group.

binding of the ligand to certain crystal facets. A recent outstanding method developed by González *et al.*⁵⁰ describes the formation of multiple-shaped NPs by the sequential action of galvanic replacement and Kirkendall effect. By this strategy, they elegantly converted Ag spheres and cubes into a wide variety of polymetallic hollow shells and nanoboxes (Figure 1.2-L-N). This kind of structures are appealing in many areas of science and technology, due to their enhanced properties in catalysis,⁵¹ plasmonics,⁴⁸ bioencapsulation⁵² and drug delivery,⁵³ amongst others. The interest in controlling NP shape continues today, as reflected in a number of reviews.⁵⁴⁻⁵⁶

The inorganic core of the Au NP can be coated by the desired organic ligands, immediately after reduction, as briefly explained before, or by ligand-exchange.^{57,58} For example, the citrate-coating is easily replaced by other ligands such as thiol- or amine-containing ligands, which have higher binding affinities for Au surfaces (~ 50 Kcal/mol and ~ 6 Kcal/mol, respectively).^{43,59} However, in the case of NPs stabilized with thiolated ligands, the ligand-exchange is not as straightforward; it will depend on the mole ratio of incoming *versus* coating ligands, their relative steric bulk and their chain lengths (see also Chapter 3, Section 3.1.1).⁶⁰ Alternatively, functional groups present on the NP surface can be converted to other functional groups; e.g. by bifunctional or crosslinker molecules such as 1-ethyl-3-(3-dimethylaminopropyl)carbodiimide/N-hydroxysuccinimide (EDC/NHS),⁶¹ or polymer coatings, such as polyelectrolytes.⁶²

NP-ligand interactions can be conveniently monitored photometrically. Normally, the formation of stable NP conjugates is characterized by an increase and/or red shift of the plasmon absorption band in the visible spectrum. On the contrary, some ligands may cause aggregation of the NPs by interacting with ions or species in solution, which can be identified by a decrease and/or broad red shift of the plasmon absorption band. An illustrative example is shown in Figure 1.3-A,⁶³ in which the conjugation of a COOH-terminated peptidic biomolecule (CIPGNVG-PEG-COOH) onto citrate-capped Au NPs reached a stable formation of Au NP bioconjugates, indicated by an increase in

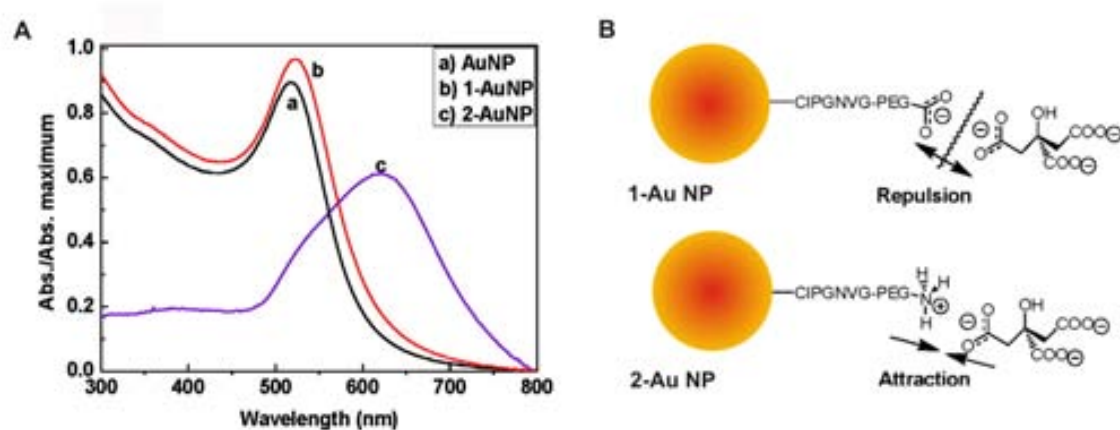


Figure 1.3. UV-Vis study of NP-ligand interactions. A) UV-Vis spectrum of 8 nm-in-size Au NPs (a) and related changes after conjugation of the peptidic biomolecules CIPGNVG-PEG-COOH and CIPGNVG-PEG-NH₂, indicating stability (b) and aggregation (c) of the peptide-Au NP bioconjugates, respectively. B) Representative model for electrostatic repulsion vs attraction between peptide-AuNP bioconjugates and citrate ions. Figure adapted from reference 63.

absorbance and a red-shift in their surface plasmon resonance (SPR) band. Oppositely, its analog NH₂-terminated peptide induced aggregation of the Au NPs, clearly indicated by a decrease of the absorbance and wavelength broadening, and accompanied by a color change of the solution from red to purple. This effect was attributed to the electrostatic interactions between the citrate ions and the bioconjugates (Figure 1.3-B).

Importantly, the surface capping ligands define the properties of the NPs in a solvent (e.g. hydrophilicity/hydrophobicity, surface charge, ligand arrangement, chemical reactivity, etc.), and they are responsible for their stabilization against aggregation. Particularly in biological environments, it must be taken into consideration that the choice of a particular ligand may provide the desired NP properties and stability in complex solvents, e.g. cell culture medium containing high-protein concentration and high ionic strength. Towards this end, thiolates are generally preferred since they can remain stably adsorbed onto the NP for a long time,⁶⁴ probably due to the strength of the Au-S bond and the high packing density of the ligands.⁴³ Oppositely, if a labile anchoring is required (e.g. to release a drug), amine or carboxylate anchoring groups may be used.⁶⁵ NPs are also generally covered with thiolated PEG (SH-PEG) to increase their hydrophilicity³⁸ and reduce their nonspecific binding to serum proteins,⁶⁶ amongst other advantages. Otherwise, if the intended application requires NP-protein/cell binding, ligands that provide negative or positive charge to the NPs are generally used.⁶⁷ A more detailed explanation can be found in Section 1.4. Besides, a number of strategies to modify the surface chemistry of NPs, so as to control their specific interaction with biological surfaces or entities, are discussed elsewhere.¹¹⁻¹³

1.2. State of the art in the functionalization of Au NPs with biomolecules.

Nature offers a rich variety of organic molecules of different composition, size and complexity that provide structure and function to biological processes and organisms. Examples include small molecules like lipids, vitamins, peptides, and sugars, and larger ones including proteins, enzymes, DNA and RNA. The similarity in size of inorganic NPs with these natural biological ligands (Figure 1.4-A)⁶⁸ allows investigating their interactions and creating promising Au NP bioconjugates in a controlled fashion. In

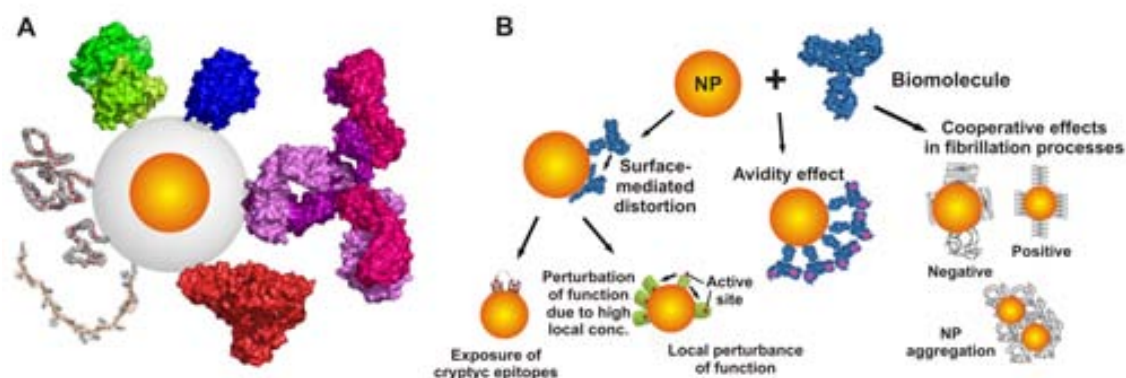


Figure 1.4. A) Relative size of NPs and biomolecules, drawn to scale. Schematic representation of a 5 nm-core Au NP, 10 nm shell diameter, with PEG molecules of 2000 g/mol and 5000 g/mol (on the left, light grey), streptavidin (green), transferrin (blue), antibody (IgG, purple), albumin (red), single-stranded DNA (20mer, cartoon and space-filling). Image extracted from reference 68. B) Effects of interaction of a biomolecule with a ~ 5-15 nm Au NP: altered protein conformation leading to exposure of cryptic epitopes and perturbation of functions (left), avidity effects arising from close spatial repetition of the same protein (center) and reduced formation of fibrils, e.g. in the presence of small Au NPs, due to the enhanced stability of proteins (right). Image extracted from reference 69.

principle, Au NP bioconjugates bring together the unique properties of both components: the functionality and specificity of biomolecules, and the physicochemical properties of the Au NPs (e.g. magnetic response or light absorption and scattering). However, the combination of both, Au NPs and biomolecules, does not only result in a sum of properties but they also have synergistic or cooperative effects (Figure 1.4-B). For instance, Au NPs may provide increased stability to the proteins and additional multivalent capacity to the surface-bound biomolecules. As well, proteins may change their conformation upon adsorption on the Au NPs, leading to a perturbation of their function. Other cooperative effects are reviewed elsewhere.⁶⁹

Despite the interest in applications using Au NP bioconjugates continues to grow almost unabated, today's technology is limited by the design and quality of such bioconjugates. Thus, if we want to go beyond tagging and detecting biomarkers (e.g. hCG in urine), from a "yes" or "no" answer to more detailed and complex responses, further efforts towards this direction need to be done. This is reflected by the limited number of existing chemical methods for the coupling and functionalization of biological components to various types of NPs. Amongst them, however, an evolution from the initial unspecific electrostatic binding to more complex current bioconjugation

chemistries can be observed. Today, the strategies used so far generally fall into four classes: i) adsorption (electrostatic, hydrophobic and Van der Waals interactions), ii) chemisorption (e.g. through thiol groups), iii) covalent coupling, and iii) non-covalent, affinity-based receptor-ligand systems.

The simplest method to couple biomolecules to Au NPs lies in weak interactions between the NPs and the biological ligand of interest (Figure 1.5-A). For instance, the addition of a protein to a citrate-capped Au NPs solution will result in spontaneous adsorption of this protein on the surface of the Au NP due to electrostatic, hydrophobic, and Van der Waals interactions. In addition, the NPs surface properties (e.g. surface charge) and thus their interactions with biomolecules, can be tuned by different means, including ligand functionalization,⁷⁰ hydrophilic polymer coating⁷¹ and surface enrichment with metal ions.⁷² An illustrative example is the functionalization of Au NPs with NH₂-terminal ligands, thus interacting electrostatically with the negatively charged phosphate groups of the DNA backbone.⁷⁰ This method provides a facile conjugation but lacks of chemical specificity, which is a handicap in the formation of well-defined Au NP bioconjugates.

Another common strategy is the direct attachment of biomolecules to NPs through chemisorption, mainly due to strong Au-S interactions (Figure 1.5-B). Similar to the functionalization of NPs with synthetic organic ligands (see Section 1.1), biomolecules can be coupled to Au NPs during reduction (e.g. the amino acid sequence of a peptide may play a role in controlling the size and shape of NPs)⁷³ or by posterior ligand-exchange.⁷⁴⁻⁷⁶ The former method is less popular since many biomolecules can undergo denaturation under a strong reductive environment, and in general the polydispersity of the NPs obtained is quite high. The success of the second method lies on the facile replacement of the citrate coating of Au NPs by amino acid residues present in the surface of proteins, e.g. through their amine and carboxylic groups.⁷⁴ In this regard, we note that thiol groups provide structure to the proteins and are rarely accessible. If such residues are not available, sulfhydryl groups can be incorporated by chemical and molecular approaches, e.g. via reduction of protein disulfide bonds with reducing agents such as dithiothreitol (DTT) or Cleland's reagent,⁶¹ (although at the cost of structure integrity) or via modification of its primary amines with heterobifunctional linkers, such

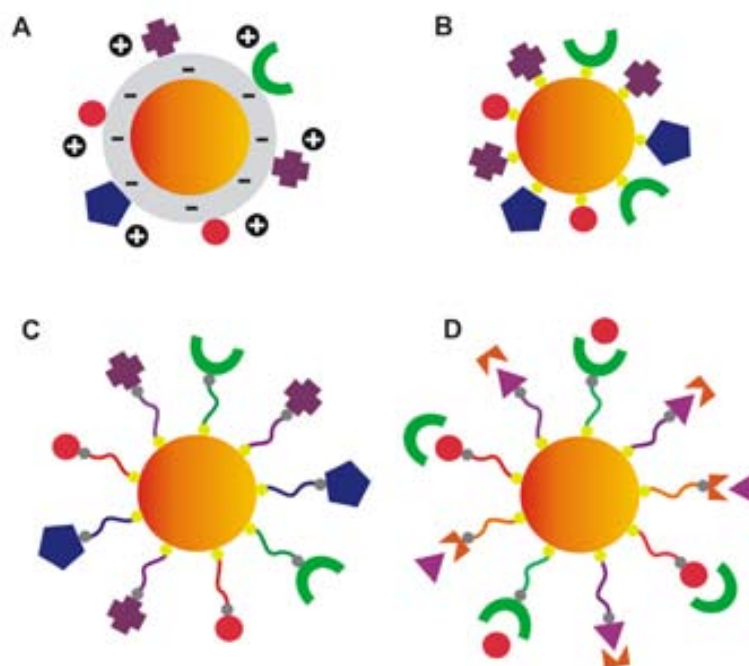


Figure 1.5. General synthetic routes used for the coupling of biomolecules onto Au NPs. A) Adsorption (electrostatic, hydrophobic and Wan de Waals interactions); B) chemisorption (e.g. through thiol groups); C) covalent linkage (e.g. through bifunctional linkers), and D) non-covalent, affinity-based receptor-ligand systems. Small spheres indicate functional groups from the linker interacting with the NP surface (yellow) and the biomolecule (grey). The other geometrical figures represent small molecules like lipids, vitamins, peptides, and sugars, and larger ones including proteins, enzymes, DNA and RNA.

as 2-iminothiolane (Traut's reagent).⁶¹ It must be taken into account that upon adsorption on the NPs, the biomolecule may undergo a partial loss of conformation.^{74,77} Chemical denaturation has also been claimed,⁷⁸ although care must be taken since the conditions required for the chemistry of reactive groups or colloidal stability of the NPs are often not compatible structure integrity of biomolecules. In addition, the protein reactive sites can be partially occluded by the NP surface, thus diminishing its specific activity.

A large variety of bifunctional linkers can be employed for a covalent coupling between biomolecules and Au NPs (Figure 1.5-C). These linkers possess two different functionalities, one of which is responsible of interacting with the surface of Au NPs (e.g. via Au-S covalent-like interaction), whereas the other terminus readily interacts with a variety of functional groups existing on the biomolecules (e.g. amine, carboxylate, succinimide or iodoacetyl functional groups). Perhaps the most common example is the use of thiolated ligands with terminal carboxylic groups, which bind on

one terminus to the Au NPs through strong Au-S interactions and on the other terminus with amine-containing biomolecules, e.g. peptides⁷⁹ or antibodies,^{80,81} by following standard EDC/NHS coupling chemistry. Besides, other linkers providing higher reaction efficiency and specificity have been used. For example, Matoussi and co-workers⁸² synthesized a linker made of a thioctic acid (TA)-appended PEG end-functionalized with a maleimide (Mal) group (TA-PEG-Mal). Au NPs functionalized with TA-PEG-Mal were reacted with the terminal cysteine on a peptide sequence. In other strategies, additional functional groups are also incorporated to the biomolecules. Brust and co-workers⁸³ functionalized Au NPs with a SH-PEG linker terminated in an azide group, which were then reacted to an acetylene-functionalized lipase using click chemistry. Abs were also modified with trans-cyclooctene or maleimide groups, thus interacting with tetrazine or furan groups incorporated on the NPs by cycloaddition⁸⁴ and Diels-Alder⁸⁵ chemistries, respectively. Importantly, the use of such approaches presents an improved selectivity and stoichiometric control over the formation of Au NP bioconjugates.⁸⁶

A different approach takes advantage of non-covalent, specific receptor-ligand binding for the coupling of biomolecules onto Au NPs (Figure 1.5-D). Examples of this strategy make use of avidin/streptavidin-biotin and nitrilotriacetic acid (NTA)-polyhistidine interactions. Biotin, a small molecule, is well-known to bind proteins such as avidin and streptavidin with a very strong affinity ($K_a = 10^{15} \text{ M}^{-1}$),⁸⁷ which results into a very fast and extremely stable bond formation. Practical methods exploiting this interaction immobilize first avidin or biotin onto NPs, through electrostatic interactions,^{88,89} chemisorption,⁹⁰ or covalent binding (e.g. activation via EDC/NHS).⁹¹ These NPs are then added to their corresponding binding ligand or protein, coupled to an agent of interest (e.g. DNA⁹² or Abs).⁸⁸ Based on this system, Goldman *et al.*⁸⁸ demonstrated the coupling of Abs through the use of an avidin bridge adsorbed to the CdSe-ZnS nanocrystal surface. A similar approach was applied by Wang *et al.*,⁹² who used avidin-coated iron oxide NPs to attach a biotinylated single-stranded DNA for further hybridization with a DNA probe. Also a large variety of biomolecules readily modified with biotin, avidin or derivatives (e.g. DNA, oligomers, peptides, and Abs) are commercially available, which enable their coupling to avidin/streptavidin- or biotin-functionalized Au NPs.

The binding of hexahistidine (His6) sequence tags to transition metal chelates of NTA provides also a powerful approach to the formation of Au NP bioconjugates. The Ni-NTA-6His binding, for example, has a higher affinity ($K_a = 10^{13} \text{ M}^{-1}$) than most antibodies binding ($K_a = 10^6$ to 10^9 M^{-1}).⁹³ This binding chemistry involves the formation of a hexagonal complex between the tetradentate ligand NTA and divalent metal ions like Ni^{2+} . Since NTA occupies four of the six coordination sites of Ni^{2+} , the two remaining sites are accessible to other Lewis bases, e.g. the histidines of tagged proteins. This system has been widely used for affinity purification of proteins that have been expressed with this polyhistidine tag (e.g. by nickel affinity columns).^{94,95} In addition, Hainfeld *et al.*⁹⁶ pioneered the formation of Ni-NTA-Au clusters (1.8 nm-in-size) to specifically target the His6 region of tagged proteins for electron microscopy. Similar approaches have used Au NPs and CdSe/ZnS quantum dots modified with NTA-containing ligands that have been reacted with bivalent ions for the specific binding to proteins with polyhistidine residues.^{97,98} It remains to be noted that the NTA-polyhistidine approach offers the important advantage that the attached proteins remain fully functional and can be oriented via their C-terminal or N-terminal His6 tag.

1.3. The “gold standard”: Au NPs as model systems for investigating the nano-bio interface.

Because of their chemical stability, optical properties and high electron density, Au NPs have been used as probes and reference materials since the late 1970s. Au NPs have been largely used in electron microscopy for high-magnification calibration and to visualize cellular compartments, proteins and receptors by their combination with Abs (the so-called *immunogold*).⁹⁹ In addition, Au NPs have demonstrated to be excellent probes in biological imaging,^{100,101} such as in plasmon based techniques, photoacoustic imaging, differential interference contrast (DIC) microscopy, fluorescence microscopy, photothermal optical coherence tomography (PT-PCT) and X-ray and Raman scattering.

Therefore, it is not surprising their current extensive use as model systems to study the nano-bio interface. **The nano-bio interface comprises the dynamic physicochemical interactions, kinetics and thermodynamic exchanges between nanomaterial surfaces and the surfaces of biological components** (e.g. proteins,

membranes, phospholipids, endocytic vesicles, organelles, DNA and biological fluids). To explore the parameters shaping these interactions, Au NPs are excellent standards because of its many advantages over other inorganic materials: i) the bulk material is chemically inert and its therapeutic use date back to ancient times; ii) the development of a wide variety of synthetic methods to produce Au NPs allows a better control over their size, shape, and surface chemistry (see Section 1.1); iii) Au is not naturally found in biological systems, therefore its concentration can be measured at very low detection levels (part-per-billion level or lower) by inductively coupled plasma mass spectrometry (ICP-MS) (Figure 1.6-A); and iv) the unique physicochemical properties of Au NPs (especially optical properties) can be used for different measurement modes of NP-cell interactions.

A direct technique to study NP-cell interactions is transmission electron microscopy (TEM), which takes advantage of the high atomic weight of Au to localize it within thin sections of cells or tissue (Figure 1.6-B). In addition, as a result of the characteristic localized surface plasmon resonance (LSPR) of Au NPs (*i.e.* the collective oscillation of the conductive electrons owing to the resonant excitation by incident photons), they exhibit strong elastic light scattering and light absorption properties¹⁰² (extinction coefficients of $\sim 10^9 \text{ M}^{-1} \text{ cm}^{-1}$) that can be exploited in imaging and chemical sensing. For example, dark-field optical microscopy can be used to infer the Au NP positions in fixed or live cells (Figure 1.6-C). As well, the cellular fate of Au NPs can be tracked by confocal microscopy due to their strong light scattering (Figure 1.6-D). Although this technique is normally used to track fluorescently labeled molecules, Au NPs can be visualized by reflected light. The LSPR effect can also be used to detect selective binding interactions of Au NPs on the cell membrane based on colorimetric changes (Figure 1.6-E).¹⁰³ For example, the SPR absorption band from Ab-Au NP bioconjugates was found to sharpen and red shift upon binding to cancerous cells. Au NPs are also effective quenchers of fluorescence, and they provide elastically scattered light intensities that are orders of magnitude larger than the fluorescence emission of dyes.^{104,105} This property has been exploited, for example, to detect intracellular place-exchange reactions at the NP-biomolecule interface by glutathione, the main thiol component of the cell, by posterior release of the fluorophore.¹⁰⁶

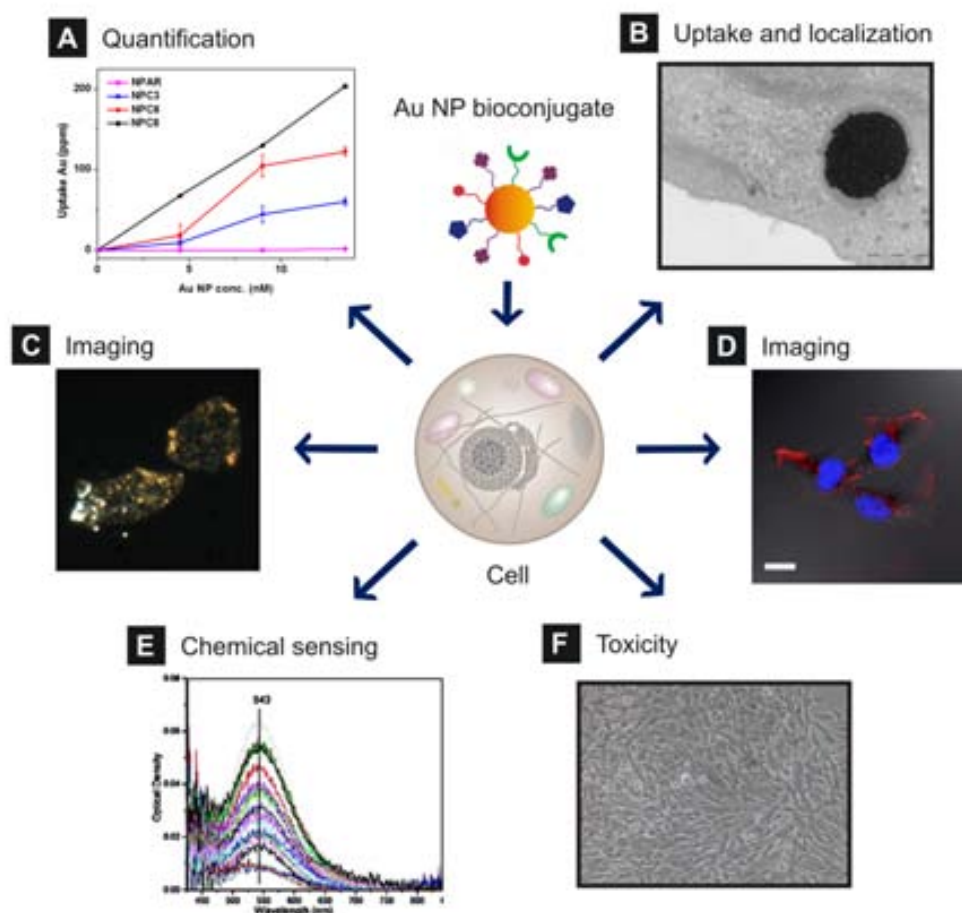


Figure 1.6. Measurement modes for Au NP-cell interactions. A) Cellular uptake quantification of different Ab-Au NP bioconjugates using ICP-MS. B) Representative TEM image showing uptake of Ab-Au NP bioconjugates and their accumulation in endocytic vesicles in cancerous epithelial cells (A431). C) Optical microscope image in dark-field mode of Ab-Au NP bioconjugates attached and internalized in cancerous epithelial cells (A431). D) Confocal microscope image of cationic peptide-Au NP bioconjugates attached and internalized in dermal fibroblast cells (1BR3G); Au NPs are visualized by reflected light. E) Shift in SPR absorption bands from Ab-Au NP bioconjugates upon binding to cancerous epithelial cells (HOC 313 clone 8 and HSC 3). F) Optical image of dermal fibroblast cells (1BR3G) with Trypan Blue staining showing mostly live cells (dead coloured blue) upon exposure to cationic peptide-Au NP bioconjugates. Note that these images correspond to experimental results from this Thesis, except image E (ref. 103).

It should be also noted that Au NPs have been employed as model systems to evaluate the toxicity of nanomaterials. Since their core is chemically inert, apparent toxicity may arise from other NP properties different than its core composition, including size, shape, surface chemistry and colloidal stability.¹¹ Note that other species in the Au NP solution can also be responsible for toxicity, such as the surfactants used for their stabilization.¹⁰⁷ Thus, Au NPs can be used to explore and identify the

parameters at the nano-bio interface that may be responsible for the apparent toxicity, and at the same time, develop strategies that can alleviate the toxic response. As to assess for toxicity, commonly used colorimetric assays are 3-(4,5-dimethylthiazol-2-yl)-2,5-diphenyltetrazolium bromide (MTT) and 3-(4,5-dimethylthiazol-2-yl)-5-(3-carboxymethoxyphenyl)-2-(4-sulfophenyl)-2H-tetrazolium (MTS). Such type of assays are based on the measurement of the activity of cellular enzymes (*i.e.* NAD(P)H-dependent cellular oxidoreductase enzymes) that reduce the tetrazolium dye to its insoluble, coloured formazan derivatives. The number of viable cells (cell proliferation) can be assessed from the absorbance of this coloured solution, which can be quantified by measuring at a certain wavelength (usually between 500 and 600 nm) by a spectrophotometer. Herein, special care must be taken since Au NPs strongly absorb light and previous NP washes might be required. Alternatively, other methodologies to screen for cytotoxicity use vital stainings (e.g. Trypan Blue assay), which are negatively charged chromophores that interact with the membrane of damaged cells and selectively colour them, thus being easily distinguished under an optical microscope and counted manually with a hemocytometer (*i.e.* without the optical interference of Au NPs) (Figure 1.6-F).

1.4. Parameters of influence at the nano-bio interface.

When a nanomaterial comes into contact with a biological component, e.g. with the cell membrane, there are three main factors influencing their interaction (Figure 1.7):¹⁰⁸ i) the NP core and surface properties, which define the solid-liquid interface; ii) the suspending medium, in which the surface properties of NPs can be modified; and iii) the dynamic interaction of the solid-liquid interface in the cell membrane.

First, one of the most relevant factors affecting these interactions are the chemical composition, size and shape of the core, surface functionalization, porosity and surface crystallinity, heterogeneity, roughness, and hydrophobicity or hydrophilicity. In addition, the characteristics of the suspending medium, such as ionic strength, pH, temperature and the presence of organic molecules (e.g. proteins) or detergents, affect the physicochemical properties of NPs, e.g. surface charge, NP aggregation, state of

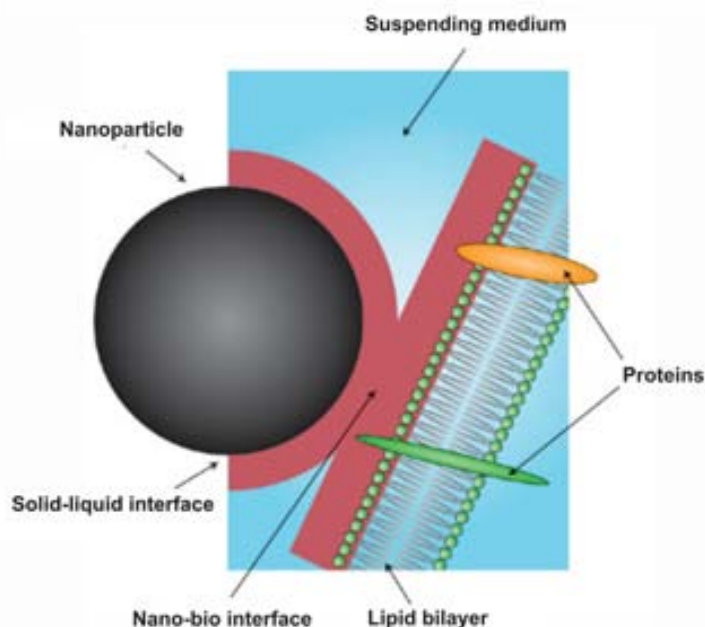


Figure 1.7. Schematic representation of the interface between a NP and a lipid bilayer. The main components influencing their interaction are the material properties (NP core and surface), the suspending medium which can modify the NP properties (e.g. by interaction with proteins in cell culture medium), and the dynamic interactions between the solid-liquid interface and the lipid bilayer (e.g. receptor-ligand binding interactions). Figure extracted from ref. 108.

dispersion, stability/biodegradability, dissolution characteristics, hydration and valence of the surface layer. Therefore, every transient environment that the NPs may undergo (such as their incubation in biological medium, changes in the medium by secreted cell products, etc.) can modify their properties, and thus, their dynamic interactions with cells. Finally, these dynamic interactions will be dictated by the nature of the NP or its surface-bound ligands; for example through receptor-ligand binding, contact with hydrophobic or charged regions, conformational changes in biomolecules or oxidant injury. The type of interactions between the NPs and the cell surface will strongly influence membrane wrapping and NP uptake. The internalized NPs will be exposed to a new interface, in which the state or integrity of the NPs, as well as the nature of their interactions with intracellular compartments, needs further exploration.

Several authors have demonstrated experimentally and by dynamic simulations the importance of the Au NP bioconjugates design at the nano-bio interface. Thus far, **NPs properties such as size, shape and surface state have been identified as important factors in cellular uptake** (Figure 1.8). For instance, Chitrani *et al.*¹⁰⁹ performed a

systematic uptake study of Au NPs of different sizes (from 14 to 100 nm) and shapes (spheres and rods with different aspect ratios). They observed that Au NPs of ~ 50 nm-in-diameter exhibited an optimum size for uptake rather than smaller or larger NP sizes (Figure 1.8-A). In addition, shape-dependent internalization was also demonstrated, with lower aspect ratio rod-shaped Au NPs having the greatest uptake (Figure 1.8-B). This was explained by the lower contact area with the cell membrane receptors, which decreases the membrane wrapping time. Other studies from Aoyama *et al.*¹¹⁰ and Osaki *et al.*¹¹¹ showed a size-dependent uptake of artificial “glycoviruses” (*i.e.* glycocluster NPs), where a similar size regime (~ 50 nm) was found to have the maximum uptake. From these studies, a NP size effect in cellular uptake was clearly determined, although the nature and surface state of the NPs was very different, and thus might not be comparative.

These experimental results were supported by different theoretical models. According to Gao’ and Zhang’ models,^{112,113} NPs of ~ 50 nm have the optimal diameter for endocytosis. They argued that at higher size regime (> 50 nm) the endocytic rate of NPs is limited by the diffusion of receptors towards the NP. In contrast, in a smaller size regime (< 20 nm), the NPs form clusters with a radius of sufficient size that eventually satisfy the thermodynamic requirement for endocytosis.

Note that although these later studies were based on bare Au NPs, all models agree that the mechanism of Au NPs internalization is receptor-mediated endocytosis (RME) since there was no internalization at 4°C. Chitrani *et al.*¹⁰⁹ attributed this effect to the non-specific adsorption of serum proteins onto the Au NPs (e.g. albumin, α - and β -globulin proteins), allowing the entrance of NPs into the cells via multiple receptors that bind such proteins. In other studies from Jiang *et al.*,¹¹⁴ this effect was examined by using Herceptin (Her) Ab-Au NP bioconjugates which bind specifically to ErbB2 receptors on the cell membrane. Interestingly, they found that, amongst Au NP bioconjugates within a size range from 2 to 100 nm, 40-50 nm Au NPs showed the greatest effect in ErbB2 receptor internalization, membrane ErbB2 expression, downstream protein expression and apoptotic activity. In this regard, we note that colloidal stability has a tremendous effect on dosing in *in vitro* assays. Overall, NP size

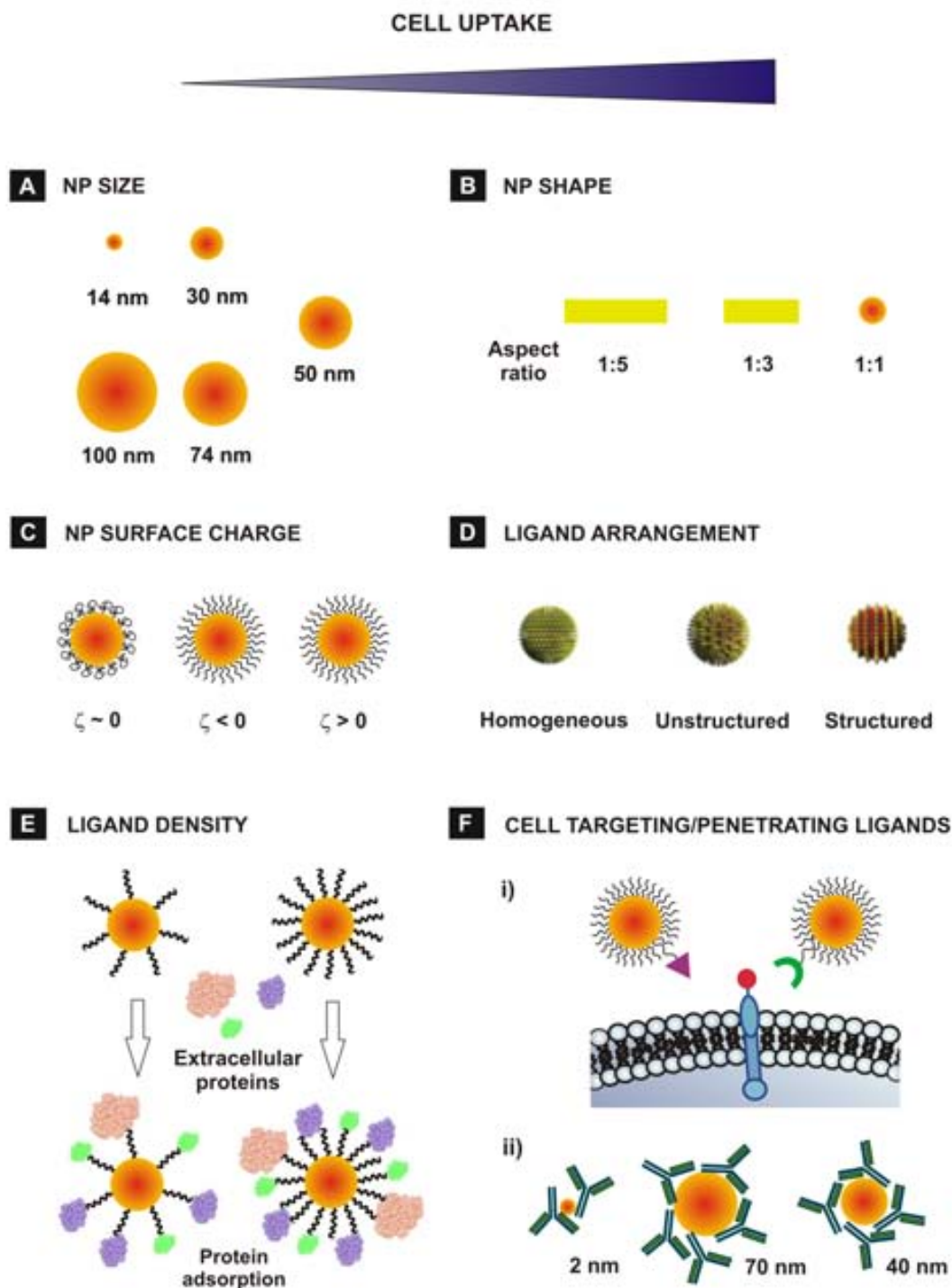


Figure 1.8. Illustrative examples of the main parameters influencing Au NP-cell interactions. A) NP size; B) shape; C) surface charge; D) ligand arrangement; E) ligand density; F) use of targeting/penetrating ligands (F), e.g. i) CPPs or ii) Abs. These parameters have been demonstrated experimentally to affect the cellular uptake of Au NPs/Au NP bioconjugates and determine other cellular functions.

is a determinant factor in molecular processes that are essential for regulating cell functions.

Another parameter influencing NP-cell interactions is the NPs surface chemistry; that is, the functional groups on their surface and their relative arrangement. This surface chemistry dependence has been explored by studying: i) the nature of the functional groups (e.g. surface charge); ii) the ligand arrangement; and iii) the functionalization with natural biological ligands (e.g. oligonucleotides, cell penetrating peptides (CPPs) and proteins, amongst others).

The Au NPs surface charge plays a decisive role in their interaction with cells. It is generally agreed that Au NPs bearing positively charged groups are enormously attracted by cells and, conversely, negative or neutral functional groups reduce or completely avoid NP-cell interactions (Figure 1.8-C). This effect has been attributed to the high affinity of proteins present in the extracellular environment for cationic surfaces (see Chapter 4, Section 4.1.2).

In a case study from Cho *et al.*,⁶⁷ the surface charge from citrate-capped Au NPs (17.7 ± 1.6 nm-in-diameter) was tuned from negative (ζ -potential = -10 mV) to neutral (ζ -potential = -4 mV) and positive (ζ -potential = +20 mV) by functionalizing them with poly(vinyl alcohol) (PVA) and poly(allyamine hydrochloride) (PAA), respectively. They used an effective etching solution (I₂/KI) to selectively dissolve the membrane-bound Au, so that they could differentiate between the adsorbed Au NPs onto the cell surface and the internalized Au NPs.⁶⁷ In their studies, the amount of both the adsorbed and internalized Au NPs was highly dependent on the type of surface charge, despite the different chemical group of the moiety bearing that charge, obtaining the highest values for the positively charged Au NPs. On the contrary, negatively charged NPs reached a low level of adsorption and uptake, and neutral charged NPs seemed to be “unseen” by the cell.

In another study from Villanueva *et al.*,¹¹⁵ a similar behavior was observed with iron oxide NPs (~10 nm-in diameter) functionalized with differently charged carbohydrates (*i.e.* dextran (D), aminodextran (AD), heparin (H) and dimercaptosuccinic acid (DMSA)). No intracellular uptake was detected in HeLa (cervical cancer) cells incubated with neutral charged hydrophilic NPs (D), whereas negative NPs (H, DMSA) showed different uptake and toxicity depending on the nature

of the coating. Cationic NPs (AD) entered the cells much more efficiently and did not show significant cytotoxicity after 24 hours of treatment. Again, comparative results were done between different objects: NPs bearing moieties of different chemical nature, and with different size and polydispersity. Surprisingly, TEM images of the cationic NPs were not shown. Overall, these studies have mainly attributed the enhanced uptake of cationic NPs to the electrostatic nature of the NP binding with the cell membrane. Since the cell membrane has net negative charge, it is more likely to interact with the positively charged NPs (e.g. by their negatively charged groups such as sialic acid). However, it has been observed that the cell surface charge is not homogeneously distributed,¹¹⁶ having also cationic residues where the negatively charged NPs could be bound. In addition, there are two very important factors that should be also considered: the stability of cationic NPs in the cell culture media and their interactions with proteins containing that media. These parameters may dictate the identity of the NPs (e.g. size and surface presentation to the cell), and thus the biological outcome and interpretation results (see also Chapter 4, Section 4.1.2).

Neutral charged hydrophilic Au NPs have been further proved to avoid interactions with biomolecules and the cell membrane,^{117,118} so that they can be used as excellent systems to prevent nonspecific adsorption of proteins or unwanted NP-cell interactions. Typically, neutral ligands used to avoid such interactions are PEG and polyvinylpyrrolidone (PVP). For instance, the amount and conformation of PEG ligand has shown to play a determinant role in cellular uptake, with a higher PEG density showing less protein binding and cell interaction.^{66,119}

The high potential of the positive charge to enhance the NPs intracellular transportation has been exploited for DNA transfection and gene delivery.⁷ For example, Rotello and co-workers^{120,121} have examined the capacity of small (~ 2 nm-in-size) cationic Au NPs of a variety of functional groups (e.g. alkaneamines and amino acids) to efficiently deliver DNA and plasmid DNA. Nevertheless, serious concerns have arisen about the toxicity of these small cationic Au NPs.^{11,122,123} Their toxicity has been mostly attributed to their mechanism of internalization through pore-membrane formation (Figure 1.9),^{123,124} which breaks the delicate balance between intracellular and extracellular ions, proteins and other macromolecules that are required to protect the integrity and normal function of a cell. In this regard, Rotello and co-workers showed

that the nature of the cationic groups on the NPs could strongly affect cellular internalization and toxicity. In their studies, Au NPs of 2 nm in diameter featuring quaternary ammonium functionalities were shown to be highly penetrating and potentially toxic,¹²² whereas the same sized Au NPs functionalized with cationic amino acids exhibited different levels of uptake, and all of them were highly biocompatible.¹²¹ Given the potential benefits of these systems for transfection and gene delivery, further exploration of the parameters required to optimize their uptake with no concomitant toxicity would be a worthwhile goal.

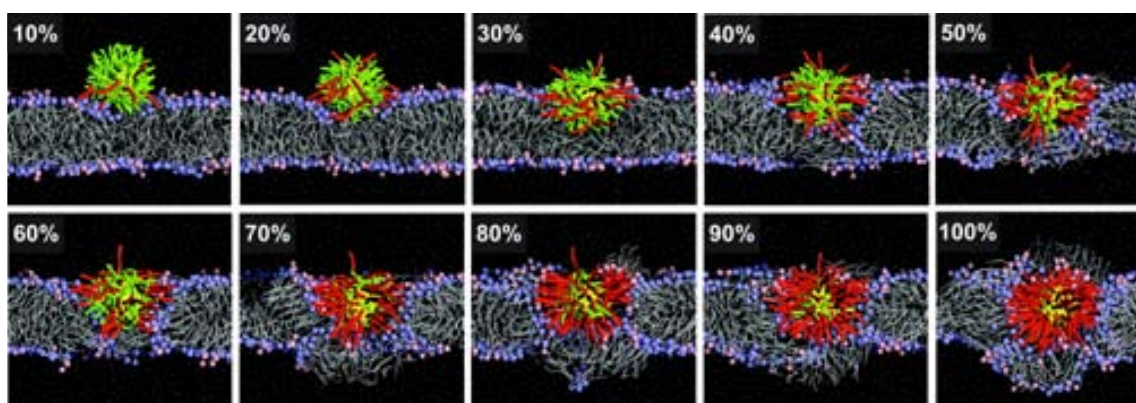


Figure 1.9. Illustration showing the interaction between a small (~ 2.2 nm-in-size) cationic AuNP and the negative lipid bilayer (model of a typical mammalian cell membrane). Disruption on the bilayer is caused by the strong attractions between the terminals of Au NPs' cationic ligands (ammonium) and the phosphate groups of DPPC (dipalmitoylphosphatidylcholine) and DPPG (dipalmitoylphosphatidylglycerol) of the membrane. The level of penetration and disruption goes higher as the Au NPs' surface charge increases. Figure extracted from ref. 123.

The structural organization of chemical groups on the NP surface is a less studied parameter that has also been proved to be crucial on Au NP-cell interactions (Figure 1.8-D). In a pioneering work from Stellacci and co-workers,¹²⁵⁻¹²⁷ they found that Au NPs coated with binary mixtures of hydrophobic and hydrophilic organic molecules spontaneously formed ribbon-like domains of alternating composition. By simply varying the composition of the organic ligand mixture, they created water-soluble NPs with precisely controlled ordered and disordered amphiphilic ligand shells. Thus, by taking advantage of such control in the spatial distribution of surface-chemical groups, they examined this effect in the cell-membrane penetration capacities of a series of Au NPs with nearly identical physical characteristics except for the composition and structure of the ligand shell.¹²⁸ As a first observation, the “striped” Au NPs (with

ordered ligand shell) were resistant to non-specific protein adsorption, whereas the “non-stripped” NPs underwent protein adsorption, as indicated in DLS measurements by an increase in size. More importantly, striped nanoparticles were capable of directly passing through the plasma membrane of the cells and reach the cytosol, whereas non-stripped Au NPs did not penetrate the cell membrane but were internalized *via* endocytosis. The behavior of striped Au NPs was similar to CPPs and differed from that observed for cationic Au NPs, since they passed through cell membranes without causing overt membrane poration and with minimal cytotoxicity. This effect was attributed to the “rigid” arrangement of the amphiphilic domains on the NPs, allowing non-disruptive fusion of the NP with cell membranes (a more fluid mixed layer) and subsequent penetration through the bilayer.

Finally, **another important factor determining the fate of NP-cell interactions is the functionalization of Au NPs with natural biological ligands, such as oligonucleotides, cell penetrating peptides (CPPs) and proteins** (Figure 1.8-E,F). These ligands are normally bound to the Au NPs for applications such as cellular transfection, gene delivery, protein delivery, and targeting,^{5,12,129} amongst others, by taking advantage of their biological activity. In such applications, however, besides the inherent properties of these biological ligands, controlling the NP bioconjugate physicochemical parameters (e.g. stability, binding constant, resistance to nuclease degradation, protein epitope exposure, biomolecule orientation, etc.) plays a crucial role in regulating NP-cell interactions. For example, the binding of oligonucleotides to Au NPs (13 ± 1 nm) was reported to act as both a cellular transfection and genetic regulation entity.^{130,131} A surprising finding was that despite the negative charge displaying the densely packed monolayer of DNA, these bioconjugates showed a highly efficient uptake (> 99%). This effect was attributed to the interactions of these Au NPs with positively charged proteins in the extracellular environment, although a negative ζ -potential was displayed after protein adsorption on the NPs. By varying the amount of oligonucleotides loaded onto the NPs, they could control the number of adsorbed proteins, and thus, modulate the cellular interactions of the Au NP bioconjugates (Figure 1.8-E). In this regard, it has been recently reported that the form and composition of the NP “protein corona” in culture medium (*i.e.* proteins adsorbed onto the NPs surface) is characteristic from a particular Au NP size and functionality, together with other factors such as incubation time, protein-to-NP ratio and type of

media.^{74,132} Therefore, the protein corona constitutes a major element of the biological identity of the NPs.

A second class of interesting biological ligands that have been linked to Au NPs includes natural CPPs. CPPs are short polycationic or amphiphilic peptides that are well-known to translocate the cell membrane without disruption. Thus, they are effective transporters of NPs into the cells. Some examples of CPPs that have been conjugated to Au NPs for cell internalization include Tat^{133,134} and amphipathic proline-rich peptides.^{135,136} For instance, Brust and co-workers¹³³ reported the cellular uptake of Tat-Au NP bioconjugates into HeLa cells. Their experiments revealed a cytosolic delivery of these bioconjugates, apparently by either passing through the cell membrane or via endosomal escape. In addition, nuclear targeting was reached by a combination of Tat (2%), nuclear localization sequence (NLS, 2%) and Pntn (2%) peptides on the surface of the NPs. In further work,¹³⁴ they demonstrated that Au NPs modified with Tat (5%) were effective promoters of nuclear targeting, and showed much higher uptake than their analogues with Pntn and NLS peptides. In other studies from Bastús *et al.*¹³⁵ and Pujals *et al.*,¹³⁶ they incorporated an amphipathic proline-rich peptide, the so-called sweet arrow peptide (SAP, C(VRLPPP)₃), onto Au NPs to investigate their internalization in HeLa tumoral cells and the pro-inflammatory response of macrophages towards these conjugates. In the first case,¹³⁵ they confirmed the effective cellular uptake of such bioconjugates. In further related work,¹³⁶ they examined the macrophage response to a variety of peptides linked to Au NPs: (C(VRLPPP)₃ (SAP), CLPFFD-NH₂ ((AGIP), CLPDDF-NH₂ (ISO1) and CDLPFF-NH₂ (ISO2). Interestingly, they found that the type of macrophage response was strongly dependent on the degree of packing of the peptide coating, besides the differences in size, charge and composition between the peptides. Note that here the effect of the order of ligands on the Au NPs was predominant over other peptide features, indicating the importance of the bioconjugate design on its cellular interaction. Several other peptide motifs, such as Arg-Lys-His¹³⁷ and Arg-Gly-Asp (RGD),¹³⁸ and arginine-rich peptides,¹³⁹ have also been coupled onto Au NPs for cell penetration.

A third class of biologically relevant ligands that have been used to equip Au NPs with uptake mechanisms include proteins, such as transferrin, albumin and Abs,

amongst others. These proteins are normally internalized via the process of receptor-mediated endocytosis, and they have been extensively investigated as potential ligands to enable drug targeting and delivery of therapeutic agents.¹⁴⁰ Their chemical coupling to Au NPs impart additional recognition capacities to those NPs towards particular receptors on the cell membrane, thus entering the cells via a receptor-mediated endocytic process. For example, Chitrani *et al.*¹⁴¹ examined the uptake of transferrin-coated Au NPs in STO (mouse embryonic fibroblasts), HeLa and SNB19 (human glioblastoma) cells. They demonstrated that these Au NP bioconjugates were efficiently taken up by the cell via a receptor-mediated clathrin-dependent endocytosis pathway. Similarly, albumin has at least four types of surface receptors¹⁴² that can bind to and induce endocytosis. Indeed, it is a common belief that albumin can act as an endocytic ligand for NPs that develop an adsorbed protein corona in serum (mostly composed by albumin),⁷⁴ such as the case of citrate-coated Au NPs (from 14 and 100 nm-in-size)¹¹⁰ and cationic polystyrene NPs (200 nm-in-size).¹⁴³ Contrary to this, Rotello and co-workers¹⁴⁴ demonstrated very recently that an increased binding of BSA onto Au NPs dramatically decreased the NP uptake. By using a series of cationic Au NPs (~2 nm-in-size) with different degrees of hydrophobicity, they could modulate the protein adsorption onto the NP surface. They identified albumin as one of the major components forming the NP-protein complex, together with immunoglobulin G (IgG) and transferrin (Tf). However, only albumin was responsible for the reduced NP uptake. They attributed this effect to the tighter binding of albumin on the more hydrophobic Au NPs, effectively inhibiting direct interactions between the cells and the Au NPs. In this regard, note that besides the number and packing of the BSA molecules adsorbed, their orientation and/or denaturation state can be very different amongst different NP functionalities, thus altering the albumin-mediated endocytic pathways. It should be also mentioned that the stability of such NPs in serum-supplemented medium is an important parameter that was not elucidated and might influence the interpretation results: the reduced NP uptake could be due to the enhanced stabilization of cationic Au NPs with albumin, whereas the non-supplemented medium might cause aggregation of the NPs, thus having a higher effective diameter and an increased uptake.

Other examples of NP receptor-mediated endocytosis include their binding to Abs (see more detailed information on Chapter 6, Section 6.2). In a study from Chan and co-workers,¹¹⁴ the coupling of differently-sized Au NPs (from 2 to 100 nm) to Herceptin

Abs allowed to selectively control specific interactions between the Au NP bioconjugates and the membrane receptor ErbB2. The binding capacity of Her-Au NPs was controlled by the NP size, as larger NPs have a higher protein-to-NP ratio. However, these authors found that 40 to 50 nm Au NPs entered the cells more efficiently than smaller or larger Au NPs (Figure 1.8-F). In addition, they demonstrated that in this size range, the Au NPs had the greatest effect in membrane receptor internalization, down-regulation, signalling downstream and apoptotic activity. This effect was attributed to the maximum capacity of these NPs to interact with cell receptors. In this regard, we note that NPs stability and concentration and protein distribution were very different between different NP sizes. In other study, Battacharya *et al.*¹⁴⁵ demonstrated that Cetuximab Ab-Au NP bioconjugates (5 nm-in-diameter) had a distinct patterning and dynamics of epidermal growth factor receptor (EGFR) internalization than the non-conjugated Cetuximab Abs. A possible mechanism of such alteration of endocytic pathways upon bioconjugation to Au NPs is their increase in avidity, thus maximizing their interaction with EGF receptors. Taken together, all these results show that an accurate design of the Au NP bioconjugates is fundamental to understand their role in mediating cellular processes at the molecular level.

1.5. References.

1. Alivisatos, P. *The use of nanocrystals in biological detection*. Nat. Biotech., **2004**, 22, 47-52.
2. Drechsler, U.; Erdogan, B.; Rotello, V. M. *Nanoparticles: Scaffolds for Molecular Recognition*. Chem. Eur. J., **2004**, 10, 5570-5579.
3. Rosi, N. L.; Mirkin, C. A. *Nanostructures in Biodiagnostics*. Chem. Rev., **2005**, 105, 1547-1562.
4. De, M.; Ghosh, P. S.; Rotello, V. M. *Applications of Nanoparticles in Biology*. Adv. Mater., **2008**, 20, 4225-4241.
5. Peer, D.; Karp, J. M.; Hong, S.; Farokhzad, O. C.; Margalit, R.; Langer, R. *Nanocarriers as an emerging platform for cancer therapy*. Nat. Nano, **2007**, 2, 751-760.
6. Sperling, R. A.; Rivera-Gil, P.; Zhang, F.; Zanella, M.; Parak, W. J. *Biological applications of gold nanoparticles*. Chem. Soc. Rev., **2008**, 37, 1896-1908.
7. Ghosh, P.; Han, G.; De, M.; Kim, C. K.; Rotello, V. M. *Gold Nanoparticles in Delivery Applications*. Adv. Drug Deliv. Rev., **2008**, 60, 1307-1315.

8. Farokhzad, O. C.; Langer, R. *Impact of Nanotechnology on Drug Delivery*. ACS Nano, **2009**, 3, 16-20.
9. Dreaden, E. C.; Alkilany, A. M.; Huang, X.; Murphy, C. J.; El-Sayed, M. A. *The Golden Age: Gold Nanoparticles for Biomedicine*. Chem. Soc. Rev., **2012**, 41, 2740-2779.
10. Shemetov, A. A.; Nabiev, I.; Sukhanova, A. *Molecular Interaction of Proteins and Peptides with Nanoparticles*. ACS Nano, **2012**, 6, 4585-4602.
11. Rivera-Gil, P.; Jimenez De Aberasturi, D.; Wulf, V.; Pelaz, B.; Del Pino, P.; Zhao, Y.; De La Fuente, J. M.; Ruiz De Larramendi, I.; Rojo, T.; Liang, X.-J.; Parak, W. J. *The Challenge to Relate the Physicochemical Properties of Colloidal Nanoparticles to their Cytotoxicity*. Acc. Chem. Res., **2013**, 46, 743-749.
12. Verma, A.; Stellacci, F. *Effect of Surface Properties on Nanoparticle-Cell Interactions*. Small, **2010**, 6, 12-21.
13. Albanese, A.; Tang, P. S.; Chan, W. C. W. *The Effect of Nanoparticle Size, Shape, and Surface Chemistry on Biological Systems*. Annu. Rev. Biomed. Eng., **2012**, 14, 1-16.
14. Faraday, M. *Experimental Relations of Gold (and Other Metals) to Light*. Philos. Trans. R. Soc. London, **1857**, 147, 145-181.
15. Faulk, W. P.; Taylor, G. M. *An Immunocolloid Method for the Electron Microscope*. Immunochem., **1971**, 8, 1081-1083.
16. Kreft, O.; Javier, A. M.; Sukhorukov, G. B.; Parak, W. J. *Polymer Microcapsules as Mobile Local pH-Sensors*. J. Mater. Chem., **2007**, 17, 4471-4476.
17. Kim, C.; Agasti, S. S.; Zhu, Z.; Isaacs, L.; Rotello, V. M. *Recognition-Mediated Activation of Therapeutic Gold Nanoparticles Inside Living Cells*. Nat. Chem., **2010**, 2, 962-966.
18. Jiang, W.; KimBetty, Y. S.; Rutka, J. T.; Chan Warren, C. W. *Nanoparticle-Mediated Cellular Response is Size-Dependent*. Nat. Nano, **2008**, 3, 145-150.
19. Huang, Y.-F.; Liu, H.; Xiong, X.; Chen, Y.; Tan, W. *Nanoparticle-Mediated IgE-Receptor Aggregation and Signaling in RBL Mast Cells*. J. Am. Chem. Soc., **2009**, 131, 17328-17334.
20. Shetty, A.; Chen, S.; Tocheva, E. I.; Jensen, G. J.; Hickey, W. J. *Nanopods: A New Bacterial Structure and Mechanism for Deployment of Outer Membrane Vesicles*. Plos One, **2011**, 6, e20725.
21. Kaur, R.; Dikshit, K. L.; Raje, M. *Optimization of Immunogold Labeling TEM: An ELISA-based Method for Evaluation of Blocking Agents for Quantitative Detection of Antigen*. J. Histochem. Cytochem., **2002**, 50, 863-873.
22. Turkevich, J.; Stevenson, P. C.; Hillier, J. *A Study of the Nucleation and Growth Processes in the Synthesis of Colloidal Gold*. Discuss. Farad. Soc., **1951**, 11, 55-75.
23. Frens, G. *Controlled Nucleation For Regulation of Particle Size in Monodisperse Gold Suspensions*. Nat. Phys. Sci., **1973**, 241, 20-22.

24. Schmid, G.; Pfeil, R.; Boese, R.; Bandermann, F.; Meyer, S.; Calis, G. H. M.; van der Velden, J. W. A. *Au₅₅[P(C₆H₅)₃]₁₂Cl₆ — ein Goldcluster Ungewöhnlicher Größe*. Chem. Ber., **1981**, 114, 3634-3642.
25. Brust, M.; Walker, M.; Bethell, D.; Schiffrin, D. J.; Whyman, R. *Synthesis of Thiol-Derivatised Gold Nanoparticles in a Two-Phase Liquid-Liquid System*. J. Chem. Soc., Chem. Commun., **1994**, 801-802.
26. Leff, D. V.; Ohara, P. C.; Heath, J. R.; Gelbart, W. M. *Thermodynamic Control of Gold Nanocrystal Size: Experiment and Theory*. J. Phys. Chem., **1995**, 99, 7036-7041.
27. Kumar, A.; Mandal, S.; Pasricha, R.; Mandale, A. B.; Sastry, M. *Investigation into the Interaction between Surface-Bound Alkylamines and Gold Nanoparticles*. Langmuir, **2003**, 19, 6277-6282.
28. Jana, N. R.; Peng X. *Single-Phase and Gram-Scale Routes toward Nearly Monodisperse Au and Other Noble Metal Nanocrystals*. J. Am. Chem. Soc., **2003**, 125, 14280-14281.
29. Hiramatsu, H.; Osterloh, F. E. *A Simple Large-Scale Synthesis of Nearly Monodisperse Gold and Silver Nanoparticles with Adjustable Sizes and with Exchangeable Surfactants*. Chem. Mat. **2004**, 16, 2509-2511.
30. Jana, N. R.; Gearheart, L.; Murphy, C. J. *Seeding Growth for Size Control of 5–40 nm Diameter Gold Nanoparticles*. Langmuir, **2001**, 17, 6782-6786.
31. Ji, X.; Song, X.; Li, J.; Bai, Y.; Yang, W.; Peng, X. *Size Control of Gold Nanocrystals in Citrate Reduction: The Third Role of Citrate*. J. Am. Chem. Soc., **2007**, 129, 13939-13948.
32. Ojea-Jiménez, I.; Romero, F. M.; Bastús, N. G.; Puentes, V. *Small Gold Nanoparticles Synthesized with Sodium Citrate and Heavy Water: Insights into the Reaction Mechanism*. J. Phys. Chem. C, **2010**, 114, 1800-1804.
33. Kimling, J.; Maier, M.; Okenve, B.; Kotaidis, V.; Ballot, H.; Plech, A. *Turkevich Method for Gold Nanoparticle Synthesis Revisited*. J. Phys. Chem. B, **2006**, 110, 15700-15707.
34. Bastús, N. G.; Comenge, J.; Puentes, V. *Kinetically Controlled Seeded Growth Synthesis of Citrate-Stabilized Gold Nanoparticles of up to 200 nm: Size Focusing versus Ostwald Ripening*. Langmuir, **2011**, 27, 11098-11105.
35. Wang, H.; Halas, N. J. *Mesoscopic Au “Meatball” Particles*. Adv. Mater., **2008**, 20, 820-825.
36. Liu, X.; Xu, H.; Xia, H.; Wang, D. *Rapid Seeded Growth of Monodisperse, Quasi-Spherical, Citrate-Stabilized Gold Nanoparticles via H₂O₂ Reduction*. Langmuir, **2012**, 28, 13720-13726.
37. Chen, S.; Kimura, K. *Synthesis and Characterization of Carboxylate-Modified Gold Nanoparticle Powders Dispersible in Water*. Langmuir, **1999**, 15, 1075-1082.
38. Kanaras, A. G.; Kamounah, F. S.; Schaumburg, K.; Kiely, C. J.; Brust, M. *Thioalkylated tetraethylene glycol: a new ligand for water soluble monolayer protected gold clusters*. Chem. Commun., **2002**, 2294-2295.
39. Templeton, A. C.; Chen, S.; Gross, S. M.; Murray, R. W. *Water-Soluble, Isolable Gold Clusters Protected by Tiopronin and Coenzyme A Monolayers*. Langmuir, **1998**, 15, 66-76.

40. Schaaff, T. G.; Knight, G.; Shafigullin, M. N.; Borkman, R. F.; Whetten, R. L. *Isolation and Selected Properties of a 10.4 kDa Gold:Glutathione Cluster Compound*. J. Phys. Chem. B, **1998**, 102, 10643-10646.
41. Selvakannan, P. R.; Kumar, P. S.; More, A. S.; Shingte, R. D.; Wadgaonkar, P. P.; Sastry, M. *One Pot, Spontaneous and Simultaneous Synthesis of Gold Nanoparticles in Aqueous and Nonpolar Organic Solvents Using a Diamine-Containing Oxyethylene Linkage*. Langmuir, **2003**, 20, 295-298.
42. Aslam, M.; Fu, L.; Su, M.; Vijayamohanan, K.; Dravid, V. P. *Novel One-Step Synthesis of Amine-Stabilized Aqueous Colloidal Gold Nanoparticles*. J. Mater. Chem., **2004**, 14, 1795-1797.
43. Love, J. C.; Estroff, L. A.; Kriebel, J. K.; Nuzzo, R. G.; Whitesides, G. M. *Self-Assembled Monolayers of Thiolates on Metals as a Form of Nanotechnology*. Chem. Rev., **2005**, 105, 1103-1170.
44. Daniel, M.-C.; Astruc, D. *Gold Nanoparticles: Assembly, Supramolecular Chemistry, Quantum-Size-Related Properties, and Applications toward Biology, Catalysis, and Nanotechnology*. Chem. Rev., **2003**, 104, 293-346.
45. Nikoobakht, B.; El-Sayed, M. A. *Preparation and Growth Mechanism of Gold Nanorods (NRs) Using Seed-Mediated Growth Method*. Chem. Mater., **2003**, 15, 1957-1962.
46. Wu, H.-L.; Kuo, C.-H.; Huang, M. H. *Seed-Mediated Synthesis of Gold Nanocrystals with Systematic Shape Evolution from Cubic to Trisoctahedral and Rhombic Dodecahedral Structures*. Langmuir, **2010**, 26, 12307-12313.
47. Millstone, J. E.; Park, S.; Shuford, K. L.; Qin, L.; Schatz, G. C.; Mirkin, C. A. *Observation of a Quadrupole Plasmon Mode for a Colloidal Solution of Gold Nanoprisms*. J. Am. Chem. Soc., **2005**, 127, 5312-5313.
48. Barbosa, S.; Agrawal, A.; Rodríguez-Lorenzo, L.; Pastoriza-Santos, I.; R. A. Álvarez-Puebla; Kornowski, A.; Weller, H.; Liz-Marzán, L. M. *Tuning Size and Sensing Properties in Colloidal Gold Nanostars*. Langmuir, **2010**, 26, 14943-14950.
49. Liang, H.-P.; Wan, L.-J.; Bai, C.-L.; Jiang, L. *Gold Hollow Nanospheres: Tunable Surface Plasmon Resonance Controlled by Interior-Cavity Sizes*. J. Phys. Chem. B, **2005**, 109, 7795-7800.
50. González, E.; Arbiol, J.; Puentes, V. F. *Carving at the Nanoscale: Sequential Galvanic Exchange and Kirkendall Growth at Room Temperature*. Science, **2011**, 334, 1377-1380.
51. Kim, S.-W.; Kim, M.; Lee, W. Y.; Hyeon, T. *Fabrication of Hollow Palladium Spheres and Their Successful Application to the Recyclable Heterogeneous Catalyst for Suzuki Coupling Reactions*. J. Am. Chem. Soc., **2002**, 124, 7642-7643.
52. Hyuk Im, S.; Jeong, U.; Xia, Y. *Polymer Hollow Particles with Controllable Holes in their Surfaces*. Nat. Mater., **2005**, 4, 671-675.
53. Yavuz, M. S.; Cheng, Y.; Chen, J.; Cobley, C. M.; Zhang, Q.; Rycenga, M.; Xie, J.; Kim, C.; Song, K. H.; Schwartz, A. G.; Wang, L. V.; Xia, Y. *Gold Nanocages Covered by Smart Polymers for Controlled Release with Near-Infrared Light*. Nat. Mater., **2009**, 8, 935-939.

54. Burda, C.; Chen, X.; Narayanan, R.; El-Sayed, M. A. *Chemistry and Properties of Nanocrystals of Different Shapes*. Chem. Rev., **2005**, 105, 1025-1102.
55. Skrabalak, S. E.; Chen, J.; Sun, Y.; Lu, X.; Au, L.; Cobley, C. M.; Xia, Y. *Gold Nanocages: Synthesis, Properties, and Applications*. Acc. Chem. Res., **2008**, 41, 1587-1595.
56. Tao, A. R.; Habas, S.; Yang, P. *Shape Control of Colloidal Metal Nanocrystals*. Small, **2008**, 4, 310-325.
57. Ingram, R. S.; Hostetler, M. J.; Murray, R. W. *Poly-hetero- ω -functionalized Alkanethiolate-Stabilized Gold Cluster Compounds*. J. Am. Chem. Soc., **1997**, 119, 9175-9178.
58. Templeton, A. C.; Wuelfing, W. P.; Murray, R. W. *Monolayer-Protected Cluster Molecules*. Acc. Chem. Res., **1999**, 33, 27-36.
59. Di Felice, R.; Selloni, A. *Adsorption Modes of Cysteine on Au(111): Thiolate, Amino-Thiolate, Disulfide*. J. Chem. Phys., **2004**, 120, 4906-4914.
60. Hostetler, M. J.; Templeton, A. C.; Murray, R. W. *Dynamics of Place-Exchange Reactions on Monolayer-Protected Gold Cluster Molecules*. Langmuir, **1999**, 15, 3782-3789.
61. Hermanson, G. T. *Bioconjugate Techniques*, 2nd ed., Academic Press, San Diego, **2008**.
62. Mayya, K. S.; Schoeler, B.; Caruso, F. *Preparation and Organization of Nanoscale Polyelectrolyte-Coated Gold Nanoparticles*. Adv. Funct. Mater., **2003**, 13, 183-188.
63. Ojea-Jiménez, I.; Puentes, V. *Instability of Cationic Gold Nanoparticle Bioconjugates: The Role of Citrate Ions*. J. Am. Chem. Soc., **2009**, 131, 13320-13327.
64. Flynn, N. T.; Tran, T. N. T.; Cima, M. J.; Langer, R. *Long-Term Stability of Self-Assembled Monolayers in Biological Media*. Langmuir, **2003**, 19, 10909-10915.
65. Cheng, Y.; Samia, A. C.; Li, J.; Kenney, M. E.; Resnick, A.; Burda, C. *Delivery and Efficacy of a Cancer Drug as a Function of the Bond to the Gold Nanoparticle Surface*. Langmuir, **2009**, 26, 2248-2255.
66. Walkey, C. D.; Olsen, J. B.; Guo, H.; Emili, A.; Chan, W. C. W. *Nanoparticle Size and Surface Chemistry Determine Serum Protein Adsorption and Macrophage Uptake*. J. Am. Chem. Soc., **2011**, 134, 2139-2147.
67. Cho, E. C.; Xie, J.; Wurm, P. A.; Xia, Y. *Understanding the Role of Surface Charges in Cellular Adsorption versus Internalization by Selectively Removing Gold Nanoparticles on the Cell Surface with a I2/KI Etchant*. Nano Lett., **2009**, 9, 1080-1084.
68. Sperling, R. A. *Surface Modification and Functionalization of Colloidal Nanoparticles*. Thesis Dissertation from Philipps-Universität, Marburg, 2008.
69. Shemetov, A. A.; Nabiev, I.; Sukhanova, A. *Molecular Interaction of Proteins and Peptides with Nanoparticles*. ACS Nano, **2012**, 6, 4585-4602.

70. McIntosh, C. M.; Esposito, E. A.; Boal, A. K.; Simard, J. M.; Martin, C. T.; Rotello, V. M. *Inhibition of DNA Transcription using Cationic Mixed Monolayer Protected Gold Clusters*. *J. Am. Chem. Soc.*, **2001**, 123, 7626-7629.
71. Bhumkar, D. R.; Joshi, H. M.; Sastry, M.; Pokharkar, V. B. *Chitosan Reduced Gold Nanoparticles as Novel Carriers for Transmucosal Delivery of Insulin*. *Pharm. Res.*, **2007**, 24, 1415-1426.
72. Mahtab, R.; Harden, H. H.; Murphy, C. J. *Temperature- and Salt-Dependent Binding of Long DNA to Protein-Sized Quantum Dots: Thermodynamics of "Inorganic Protein"-DNA Interactions*. *J. Am. Chem. Soc.*, **2000**, 122, 14-17.
73. Slocik, J. M.; Stone, M. O.; Naik, R. R. *Synthesis of Gold Nanoparticles Using Multifunctional Peptides*. *Small* **2005**, 1, 1048-1052.
74. Casals, E.; Pfaller, T.; Duschl, A.; Oostingh, G. J.; Puntès, V. *Time Evolution of the Nanoparticle Protein Corona*. *ACS Nano*, **2010**, 4, 3623-3632.
75. Loweth, C. J.; Caldwell, W. B.; Peng, X.; Alivisatos, A. P.; Schultz, P. G. *DNA-Based Assembly of Gold Nanocrystals*. *Angew. Chem. Int. Ed.*, **1999**, 38, 1808-1812.
76. Krpetić, Ž.; Saleemi, S.; Prior, I. A.; Sée, V.; Qureshi, R.; Brust, M. *Negotiation of Intracellular Membrane Barriers by TAT-Modified Gold Nanoparticles*. *ACS Nano* **2011**, 5, 5195-5201.
77. Hong, R.; Fischer, N. O.; Verma, A.; Goodman, C. M.; Emeric, T.; Rotello, V. M. *Control of Protein Structure and Function through Surface Recognition by Tailored Nanoparticle Scaffolds*. *J. Am. Chem. Soc.*, **2004**, 126, 739-743.
78. Zhang, D.; Neumann, O.; Wang, H.; Yuwono, V. M.; Barhoumi, A.; Perham, M.; Hartgerink, J. D.; Wittung-Stafshede, P.; Halas, N. J. *Gold Nanoparticles Can Induce the Formation of Protein-based Aggregates at Physiological pH*. *Nano Lett.*, **2009**, 9, 666-671.
79. Bartczak, D.; Sanchez-Elsner, T.; Louafi, F.; Millar, T. M.; Kanaras, A. G. *Receptor-Mediated Interactions between Colloidal Gold Nanoparticles and Human Umbilical Vein Endothelial Cells*. *Small*, **2011**, 7, 388-394.
80. Eck, W.; Craig, G.; Sigdel, A.; Ritter, G.; Old, L. J.; Tang, L.; Brennan, M. F.; Allen, P. J.; Mason, M. D. *PEGylated Gold Nanoparticles Conjugated to Monoclonal F19 Antibodies as Targeted Labeling Agents for Human Pancreatic Carcinoma Tissue*. *ACS Nano*, **2008**, 2, 2263-2272.
81. Di Pasqua, A. J.; Mishler, R. E.; Ship, Y. L.; Dabrowiak, J. C.; Asefa, T. *Preparation of Antibody-Conjugated Gold Nanoparticles*. *Mater. Lett.*, **2009**, 63, 1876-1879.
82. Oh, E.; Susumu, K.; Blanco-Canosa, J. B.; Medintz, I. L.; Dawson, P. E.; Mattoussi, H. *Preparation of Stable Maleimide-Functionalized Au Nanoparticles and Their Use in Counting Surface Ligands*. *Small*, **2010**, 6, 1273-1278.
83. Brennan, J. L.; Hatzakis, N. S.; Tshikhudo, T. R.; Razumas, V.; Patkar, S.; Vind, J.; Svendsen, A.; Nolte, R. J. M.; Rowan, A. E.; Brust, M. *Bionanoconjugation via Click Chemistry: The Creation of Functional Hybrids of Lipases and Gold Nanoparticles*. *Bioconj. Chem.*, **2006**, 17, 1373-1375.
84. Haun, J. B.; Devaraj, N. K.; Hilderbrand, S. A.; Lee, H.; Weissleder, R. *Bioorthogonal Chemistry Amplifies Nanoparticle Binding and Enhances the Sensitivity of Cell Detection*. *Nat. Nano*, **2010**, 5, 660-665.

85. Shi, M.; Wosnick, J. H.; Ho, K.; Keating, A.; Shoichet, M. S. *Immuno-Polymeric Nanoparticles by Diels–Alder Chemistry*. *Angew. Chem. Int. Ed.*, **2007**, 119, 6238-6243.
86. Algar, W. R.; Prasuhn, D. E.; Stewart, M. H.; Jennings, T. L.; Blanco-Canosa, J. B.; Dawson, P. E.; Medintz, I. L. *The Controlled Display of Biomolecules on Nanoparticles: A Challenge Suited to Bioorthogonal Chemistry*. *Bioconj. Chem.*, **2011**, 22, 825-858.
87. Green, N. M. *Avidin*. *Advances in Protein Chemistry*. Anfinsen, J. T. E. C.B. and Frederic, M. R., Academic Press, **1975**, 29, 85-133.
88. Goldman, E. R.; Balighian, E. D.; Mattoussi, H.; Kuno, M. K.; Mauro, J. M.; Tran, P. T.; Anderson, G. P. *Avidin: A Natural Bridge for Quantum Dot-Antibody Conjugates*. *J. Am. Chem. Soc.*, **2002**, 124, 6378-6382.
89. Lin, Z.; Su, X.; Wan, Y.; Zhang, H.; Mu, Y.; Yang, B.; Jin, Q. *Labeled avidin bound to water-soluble nanocrystals by electrostatic interactions*. *Russ. Chem. Bull.*, **2004**, 53, 2690-2694.
90. Caswell, K. K.; Wilson, J. N.; Bunz, U. H. F.; Murphy, C. J. *Preferential End-to-End Assembly of Gold Nanorods by Biotin–Streptavidin Connectors*. *J. Am. Chem. Soc.*, **2003**, 125, 13914-13915.
91. Aslan, K.; Luhrs, C. C.; Pérez-Luna, V. H.. *Controlled and Reversible Aggregation of Biotinylated Gold Nanoparticles with Streptavidin*. *J. Phys. Chem. B*, **2004**, 108, 15631-15639.
92. Wang, T.-H.; Lee, W.-C. *Immobilization of proteins on magnetic nanoparticles*. *Biotechnol. Bioprocess Eng.*, **2003**, 8, 263-267.
93. Schmitt, J.; Hess, H.; Stunnenberg, H. *Affinity Purification of Histidine-Tagged Proteins*. *Mol. Biol. Rep.*, **1993**, 18, 223-230.
94. Hochuli, E. *Large-scale chromatography of recombinant proteins*. *J. Chromatogr. A*, **1988**, 444, 293-302.
95. Porath, J.; Carlsson, J. A. N.; Olsson, I.; Belfrage, G. *Metal Chelate Affinity Chromatography, a New Approach to Protein Fractionation*. *Nature*, **1975**, 258, 598-599.
96. Hainfeld, J. F.; Liu, W.; Halsey, C. M. R.; Freimuth, P.; Powell, R. D. *Ni–NTA–Gold Clusters Target His-Tagged Proteins*. *J. Struct. Biol.*, **1999**, 127, 185-198.
97. Kim, J.; Park, H.-Y.; Kim, J.; Ryu, J.; Kwon, D. Y.; Grailhe, R.; Song, R. *Ni-Nitrilotriacetic Acid-Modified Quantum Dots as a Site-Specific Labeling Agent of Histidine-Tagged Proteins in Live Cells*. *Chem. Commun.*, **2008**, 1910-1912.
98. Briñas, R. P.; Hu, M.; Qian, L.; Lyman, E. S.; Hainfeld, J. F. *Gold Nanoparticle Size Controlled by Polymeric Au(I) Thiolate Precursor Size*. *J. Am. Chem. Soc.*, **2007**, 130, 975-982.
99. Faulk, W. P.; Taylor, G. M. *An Immunocolloid Method for the Electron Microscope*. *Immunochem.*, **1971**, 8, 1081-1083.
100. Aaron, J.; Travis, K.; Harrison, N.; Sokolov, K. *Dynamic Imaging of Molecular Assemblies in Live Cells Based on Nanoparticle Plasmon Resonance Coupling*. *Nano Lett.*, **2009**, 9, 3612-3618.

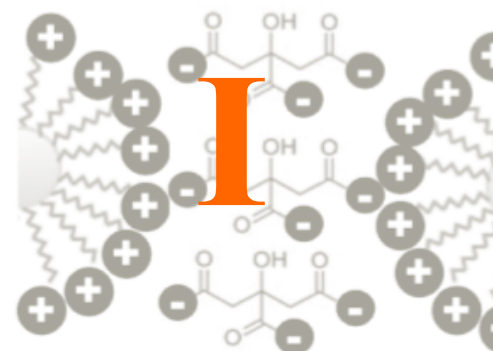
101. Boisselier, E.; Astruc, D. *Gold Nanoparticles in Nanomedicine: Preparations, Imaging, Diagnostics, Therapies and Toxicity*. Chem. Soc. Rev., **2009**, 38, 1759-1782.
102. Alkilany, A.; Murphy, C. *Toxicity and Cellular Uptake of Gold Nanoparticles: What we Have Learned so Far?* J. Nanopart. Res., **2010**, 12, 2313-2333.
103. El-Sayed, I. H.; Huang, X.; El-Sayed, M. A. *Surface Plasmon Resonance Scattering and Absorption of anti-EGFR Antibody Conjugated Gold Nanoparticles in Cancer Diagnostics: Applications in Oral Cancer*. Nano Lett., **2005**, 5, 829-834.
104. Jain, P. K.; Huang, X.; El-Sayed, I. H.; El-Sayed, M. A. *Noble Metals on the Nanoscale: Optical and Photothermal Properties and Some Applications in Imaging, Sensing, Biology, and Medicine*. Acc. Chem. Res., **2008**, 41, 1578-1586.
105. Murphy, C. J.; Gole, A. M.; Stone, J. W.; Sisco, P. N.; Alkilany, A. M.; Goldsmith, E. C.; Baxter, S. C. *Gold Nanoparticles in Biology: Beyond Toxicity to Cellular Imaging*. Acc. Chem. Res., **2008**, 41, 1721-1730.
106. (a) Hong, R.; Han, G.; Fernández, J. M.; Kim, B.-J.; Forbes, N. S.; Rotello, V. M. *Glutathione-Mediated Delivery and Release Using Monolayer Protected Nanoparticle Carriers*. J. Am. Chem. Soc., **2006**, 128, 1078-1079. (b) Han, G.; Chari, N. S.; Verma, A.; Hong, R.; Martin, C. T.; Rotello, V. M. *Controlled Recovery of the Transcription of Nanoparticle-Bound DNA by Intracellular Concentrations of Glutathione*. Bioconj. Chem., **2005**, 16, 1356-1359.
107. Alkilany, A. M.; Nagaria, P. K.; Hexel, C. R.; Shaw, T. J.; Murphy, C. J.; Wyatt, M. D. *Cellular Uptake and Cytotoxicity of Gold Nanorods: Molecular Origin of Cytotoxicity and Surface Effects*. Small, **2009**, 5, 701-708.
108. Nel, A. E.; Madler, L.; Velegol, D.; Xia, T.; Hoek, E. M. V.; Somasundaran, P.; Klaessig, F.; Castranov, V.; Thompson, M. *Understanding Biophysicochemical Interactions at the Nano-Bio Interface*. Nat. Mater., **2009**, 8, 543-557.
109. Chithrani, B. D.; Ghazani, A. A.; Chan, W. C. W. *Determining the Size and Shape Dependence of Gold Nanoparticle Uptake into Mammalian Cells*. Nano Lett., **2006**, 6, 662-668.
110. Aoyama, Y.; Kanamori, T.; Nakai, T.; Sasaki, T.; Horiuchi, S.; Sando, S.; Niidome, T. *Artificial Viruses and Their Application to Gene Delivery. Size-Controlled Gene Coating with Glycocluster Nanoparticles*. J. Am. Chem. Soc., **2003**, 125, 3455-3457.
111. Osaki, F.; Kanamori, T.; Sando, S.; Sera, T.; Aoyama, Y. *A Quantum Dot Conjugated Sugar Ball and Its Cellular Uptake. On the Size Effects of Endocytosis in the Subviral Region*. J. Am. Chem. Soc., **2004**, 126, 6520-6521.
112. Gao, H.; Shi, W.; Freund, L. B. *Mechanics of Receptor-Mediated Endocytosis*. Proc. Natl. Acad. Sci. U. S. A., **2005**, 102, 9469-9474.
113. Zhang, S.; Li, J.; Lykotrafitis, G.; Bao, G.; Suresh, S. *Size-Dependent Endocytosis of Nanoparticles*. Adv. Mater., **2009**, 21, 419-424.
114. Jiang, W.; KimBetty, Y. S.; Rutka, J. T.; Warren, C. W. C. *Nanoparticle-Mediated Cellular Response is Size-Dependent*. Nat. Nano, **2008**, 3, 145-150.

115. Villanueva, A.; Cañete, M.; Roca, A. G.; Calero, M.; Veintemillas-Verdaguer, S.; Serna, C. J.; Morales, M. P.; Miranda, R. *The Influence of Surface Functionalization on the Enhanced Internalization of Magnetic Nanoparticles in Cancer Cells*. *Nanotechnol.*, **2009**, *20*, 115103.
116. Ghitescu, L.; Fixman, A. *Surface Charge Distribution on the Endothelial Cell of Liver Sinusoids*. *J. Cell Biol.*, **1984**, *99*, 639-647.
117. Zheng, M.; Davidson, F.; Huang, X. *Ethylene Glycol Monolayer Protected Nanoparticles for Eliminating Nonspecific Binding with Biological Molecules*. *J. Am. Chem. Soc.*, **2003**, *125*, 7790-7791.
118. Nativo, P.; Prior, I. A.; Brust, M. *Uptake and Intracellular Fate of Surface-Modified Gold Nanoparticles*. *ACS Nano*, **2008**, *2*, 1639-1644.
119. Hu, Y.; Xie, J.; Tong, Y. W.; Wang, C.-H. *Effect of PEG Conformation and Particle Size on the Cellular Uptake Efficiency of Nanoparticles with the HepG2 Cells*. *J. Control. Rel.*, **2007**, *118*, 7-17.
120. Sandhu, K. K.; McIntosh, C. M.; Simard, J. M.; Smith, S. W.; Rotello, V. M. *Gold Nanoparticle-Mediated Transfection of Mammalian Cells*. *Bioconj. Chem.*, **2002**, *13*, 3-6.
121. Ghosh, P. S.; Kim, C.-K.; Han, G.; Forbes, N. S.; Rotello, V. M. *Efficient Gene Delivery Vectors by Tuning the Surface Charge Density of Amino Acid-Functionalized Gold Nanoparticles*. *ACS Nano*, **2008**, *2*, 2213-2218.
122. Goodman, C. M.; Mc Cusker, C. D.; Yilmaz, T.; Rotello, V. M. *Toxicity of Gold Nanoparticles Functionalized with Cationic and Anionic Side Chains*. *Bioconj. Chem.*, **2004**, *15*, 897-900.
123. Lin, J.; Zhang, H.; Chen, Z.; Zheng, Y. *Penetration of Lipid Membranes by Gold Nanoparticles: Insights into Cellular Uptake, Cytotoxicity, and Their Relationship*. *ACS Nano*, **2010**, *4*, 5421-5429.
124. Leroueil, P. R.; Berry, S. A.; Duthie, K.; Han, G.; Rotello, V.M.; McNerny, D. Q.; Baker, J. R.; Orr, B. G.; BanaszakHoll, M. M. *Wide Varieties of Cationic Nanoparticles Induce Defects in Supported Lipid Bilayers*. *Nano Lett.* **2008**, *8*, 420-424.
125. Jackson, A. M.; Myerson, J. W.; Stellacci, F. *Spontaneous Assembly of Subnanometre-Ordered Domains in the Ligand Shell of Monolayer-Protected Nanoparticles*. *Nat. Mater.*, **2004**, *3*, 330-336.
126. Jackson, A. M.; Hu, Y.; Silva, P. J.; Stellacci, F. *From Homoligand- to Mixed-Ligand- Monolayer-Protected Metal Nanoparticles: A Scanning Tunneling Microscopy Investigation*. *J. Am. Chem. Soc.*, **2006**, *128*, 11135-11149.
127. DeVries, G. A.; Brunnbauer, M.; Hu, Y.; Jackson, A. M.; Long, B.; Neltner, B. T.; Uzun, O.; Wunsch, B. H.; Stellacci, F. *Divalent Metal Nanoparticles*. *Science*, **2007**, *315*, 358-361.
128. Verma, A.; Uzun, O.; Hu, Y.; Hu, Y.; Han, H.-S.; Watson, N.; Chen, S.; Irvine, D. J.; Stellacci, F. *Surface-Structure-Regulated Cell-Membrane Penetration by Monolayer-Protected Nanoparticles*. *Nat. Mater.*, **2008**, *7*, 588-595.
129. Lévy, R.; Shaheen, U.; Cesbron, Y.; Sée, V. *Gold Nanoparticles Delivery in Mammalian Cells: A Critical Review*. *Nano Rev.*, **2010**, *1*, 4889-4907.

130. Rosi, N. L.; Giljohann, D. A.; Thaxton, C. S.; Lytton-Jean, A. K. R.; Han, M. S.; Mirkin, C. A. *Oligonucleotide-Modified Gold Nanoparticles for Intracellular Gene Regulation*. *Science*, **2006**, 312, 1027-1030.
131. Giljohann, D. A.; Seferos, D. S.; Patel, P. C.; Millstone, J. E.; Rosi, N. L.; Mirkin, C. A. *Oligonucleotide Loading Determines Cellular Uptake of DNA-Modified Gold Nanoparticles*. *Nano Lett.*, **2007**, 7, 3818-3821.
132. Maiorano, G.; Sabella, S.; Sorce, B.; Brunetti, V.; Malvindi, M. A.; Cingolani, R.; Pompa, P. P. *Effects of Cell Culture Media on the Dynamic Formation of Protein–Nanoparticle Complexes and Influence on the Cellular Response*. *ACS Nano*, **2010**, 4, 7481-7491.
133. Nativo, P.; Prior, I. A.; Brust, M. *Uptake and Intracellular Fate of Surface-Modified Gold Nanoparticles*. *ACS Nano*, **2008**, 2, 1639-1644.
134. Krpetić, Z.; Saleemi, S.; Prior, I. A.; Sée, V.; Qureshi, R.; Brust, M. *Negotiation of Intracellular Membrane Barriers by TAT-Modified Gold Nanoparticles*. *ACS Nano*, **2011**, 5, 5195-5201.
135. Bastús, N. G.; Sánchez-Tilló, E.; Pujals, S.; Farrera, C.; López, C.; Giralt, E.; Celada, A.; Lloberas, J.; Puentes, V. *Homogeneous Conjugation of Peptides onto Gold Nanoparticles Enhances Macrophage Response*. *ACS Nano*, **2009**, 3, 1335-1344.
136. Pujals, S.; Bastús, N. G.; Pereiro, E.; López-Iglesias, C.; Puentes, V. F.; Kogan, M. J.; Giralt, E. *Shuttling Gold Nanoparticles into Tumoral Cells with an Amphipathic Proline-Rich Peptide*. *Chem. Bio. Chem.*, **2009**, 10, 1025-1031.
137. Ghosh, P.; Yang, X.; Arvizo, R.; Zhu, Z.-J.; Agasti, S. S.; Mo, Z.; Rotello, V. M. *Intracellular Delivery of a Membrane-Impermeable Enzyme in Active Form Using Functionalized Gold Nanoparticles*. *J. Am. Chem. Soc.*, **2010**, 132, 2642-2645.
138. Green, J. J.; Chiu, E.; Leshchiner, E. S.; Shi, J.; Langer, R.; Anderson, D. G. *Electrostatic Ligand Coatings of Nanoparticles Enable Ligand-Specific Gene Delivery to Human Primary Cells*. *Nano Lett.*, **2007**, 7, 874-879.
139. Sun, L.; Liu, D.; Wang, Z. *Functional Gold Nanoparticle–Peptide Complexes as Cell-Targeting Agents*. *Langmuir*, **2008**, 24, 10293-10297.
140. Xu, S.; Olenyuk, B. Z.; Okamoto, C. T.; Hamm-Alvarez, S. F. *Targeting Receptor-Mediated Endocytotic Pathways with Nanoparticles: Rationale and Advances*. *Adv. Drug Deliv. Rev.*, **2013**, 65, 121–138.
141. Chithrani, B. D.; Chan, W. C. W. *Elucidating the Mechanism of Cellular Uptake and Removal of Protein-Coated Gold Nanoparticles of Different Sizes and Shapes*. *Nano Lett.*, **2007**, 7, 1542-1550.
142. Schnitzer, J. E.; Oh, P. *Albondin-Mediated Capillary Permeability to Albumin. Differential Role of Receptors in Endothelial Transcytosis and Endocytosis of Native and Modified Albumins*. *J. Biol. Chem.*, **1994**, 269, 6072-6082.
143. (a) Doorley, G. W.; Payne, C. K. *Cellular Binding of Nanoparticles in the Presence of Serum Proteins*. *Chem. Commun.*, **2011**, 47, 466-468. (b) Doorley, G. W.; Payne, C. K. *Nanoparticles Act as Protein Carriers During Cellular Internalization*. *Chem. Commun.*, **2012**, 48, 2961-2963.

144. Zhu, Z.-J.; Posati, T.; Moyano, D. F.; Tang, R.; Yan, B.; Vachet, R. W.; Rotello, V. M.. *The Interplay of Monolayer Structure and Serum Protein Interactions on the Cellular Uptake of Gold Nanoparticles*. *Small*, **2012**, 8, 2659-2663.
145. Bhattacharyya, S.; Bhattacharya, R.; Curley, S.; McNiven, M. A.; Mukherjee, P. *Nanoconjugation Modulates the Trafficking and Mechanism of Antibody Induced Receptor Endocytosis*. *Proc. Natl. Acad. Sci. U.S.A.*, **2010**, 107, 14541-14546.

Introduction to Cationic Gold Nanoparticles



Cells regulate the entry of water-soluble molecules by their negatively charged hydrophobic plasma membrane, which limits drastically the delivery of polar molecules (*i.e.* peptides, nucleic acids and drugs) to intracellular targets.¹ This weak affinity is overcome in Nature by one type of small cationic peptides.² Polar mammalian defensins show spatially separated positively charged and hydrophobic regions, which allows them to insert themselves into the phospholipid membranes, so that their hydrophobic regions are buried within the lipid membrane interior and their cationic charged regions interact with anionic phospholipid head groups and water. Inspired by these natural molecular-based machineries, artificial Au NPs that mimic this cationic character on their surfaces has become an excellent strategy to efficiently deliver polar molecules into cells. The first illustrative examples were reported by Rotello and co-workers,^{3,4} who showed that 2 nm cationic Au NPs featuring quaternary ammonium functionalities were able to interact with the DNA phosphate backbones and efficiently transfect mammalian cells.

At present, the mechanism by which cationic NPs enter the cells and their related cytotoxicity are still under debate (see Chapter 4, Section 4.1.3). In principle, small cationic Au NPs (~ 2 nm) are able to penetrate the cell membrane through pore formation and are potentially toxic,⁵ whereas bigger NPs (~ 17 nm) adhere to the cell surface and apparently internalize via endocytosis.⁶ More information is still needed to determine the exact pathways of internalization for positively charged NPs. Essential to this understanding, however, it is the development of robust and scalable methods which enable the preparation of a rich catalog of cationic NPs, with different sizes, shapes and surface states, available for biological studies, especially when these are

determining factors in uptake (see Chapter 1, Section 1.4). Toward that end, scarce work has been done on the functionalization of NPs using cationic ligands by the scientific community, probably due to their difficult stabilization. Among these ligands, a few reports can be found using cationic lipids,^{7,8} synthetic cationic polymers such as poly(ethyleneimine) (PEI)⁹ or PAA,⁶ aminoalkanethiols¹⁰⁻¹² and quaternary ammonium salts,^{13,14} decorating the surface of Au NPs. Many of these syntheses suffer from poor monodispersity and are restricted to a certain ligand or NP size. These are current limitations for biological applications where the variation of these parameters is often necessary to optimize the way that NPs enter cells and how they influence the cell functions.^{15,16}

The next Chapters summarize and discuss the main existing synthetic routes to prepare cationic Au NPs and some of their biological applications. In such a context, the first part of this Thesis focuses on the exploration of two different methodologies for the preparation of cationic Au NPs of different sizes and surface states (Chapter 2 and 3), and the use of one of these strategies to design biologically relevant Au NPs functionalized with a cationic peptidic biomolecule (Chapter 4). In Chapter 2, a simple synthetic scheme involving the precise addition of two reducing agents (*i.e.* NaBH₄ and 11-amino-1-undecanethiol (AUT)) in aqueous solution is presented. Importantly, the result of combining two reducers was not just an intermediate effect (*i.e.* reduction with only AUT did not yield large NP sizes but rather small and polydisperse NPs) but they both act sequentially. First, NaBH₄ reduced a fraction of the Au⁺³ precursor to determine the number of Au seeds, which were then grown in mild conditions with AUT. Under optimized conditions, highly charged cationic Au NPs (ζ -potential $\sim +50$ mV at neutral pH) with sizes ranging from ~ 10 to 30 nm were obtained. Then, a more versatile phase transfer methodology is described in Chapter 3, which allowed the synthesis of high concentrations of a rich variety of cationic Au NPs (*i.e.* sizes ranging from ~ 4 to 13 nm and different functional ligands) with narrow size distributions. This method allowed the functionalization of Au NPs with cationic ligands bearing thiol groups by replacement of the alkylamine surfactant stabilizing the NPs in organic phase, facilitating their phase transfer into the aqueous phase. AUT was first employed as a case model ligand to optimize the synthetic procedure, which was then successfully applied in Chapter 4 for the conjugation of two identical peptidic biomolecules terminating in either positive (NH₃⁺) or negative (COO⁻) charged groups. This last

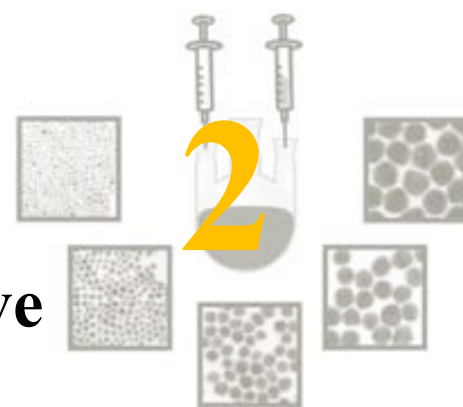
Chapter shows a complete characterization of the physicochemical properties of these Au NP bioconjugates in physiological medium. Mechanistic studies of the interaction of the prepared Au NP bioconjugates with human fibroblast cells (1BR3G) were also performed as there are no predictive models for the biological effects of Au NPs of 13 nm core with such high density of cationic biomolecules (normally they are mixed with stabilizers – e.g. PEG – on the Au NP surface in the reported studies in the literature). The positively charged NPs exhibited an exceptional uptake by fibroblast cells, with a predominant route of endocytosis and migration in endosomes towards the nucleus. Additionally, no toxicity was found for these Au NP bioconjugates, which is often a major obstacle in the development of new therapeutics.

References.

1. Conner, S. D.; Schmid, S. L. *Regulated Portals of Entry into the Cell*. *Nature*, **2003**, 422, 37-44.
2. Yang, D.; Biragyn, A.; Kwak L. W.; Oppenheim, J. J. *Mammalian Defensins in Immunity: More Than Just Microbicidal*. *Trends Immunol.*, **2002**, 23, 291-296.
3. McIntosh, C. M.; Esposito, E. A.; Boal, A. K.; Simard, J. M.; Martin, C. T.; Rotello, V. M. *Inhibition of DNA Transcription Using Cationic Mixed Monolayer Protected Gold Clusters*. *J. Am. Chem. Soc.*, **2001**, 123, 7626–7629.
4. Sandhu, K. K.; McIntosh, C. M.; Simard, J. M.; Smith, S. W.; Rotello, V. M. *Gold Nanoparticle-Mediated Transfection of Mammalian Cells*. *Bioconj. Chem.*, **2002**, 13, 3–6.
5. Goodman, C. M.; Mc Cusker, C. D.; Yilmaz, T.; Rotello, V. M. *Toxicity of Gold Nanoparticles Functionalized with Cationic and Anionic Side Chains*. *Bioconj. Chem.*, **2004**, 15, 897-900.
6. Cho, E. C.; Xie, J.; Wurm, P. A.; Xia, Y. *Understanding the Role of Surface Charges in Cellular Adsorption versus Internalization by Selectively Removing Gold Nanoparticles on the Cell Surface with a I2/KI Etchant*. *Nano Lett.*, **2009**, 9, 1080-1084.
7. Li, P.; Li, D.; Zhang, L.; Li, G.; Wang, E. *Cationic Lipid Bilayer Coated Gold Nanoparticles-Mediated Transfection of Mammalian Cells*. *Biomater.*, **2008**, 29, 3617-3624.
8. Zhang, L.; Sun, X.; Song, Y.; Jiang, X.; Dong, S.; Wang, E. *Didodecyldimethylammonium Bromide Lipid Bilayer-Protected Gold Nanoparticles: Synthesis, Characterization, and Self-Assembly*. *Langmuir*, **2006**, 22, 2838-2843.
9. Thomas, M.; Klibanov, A. M. *Conjugation to Gold Nanoparticles Enhances Polyethylenimine's Transfer of Plasmid DNA into Mammalian Cells*. *Proc. Natl. Acad. Sci. U.S.A.*, **2003**, 100, 9138–9143.

10. Niidome, T.; Nakashima, K.; Takahashi, H.; Niidome, Y. *Preparation of Primary Amine-Modified Gold Nanoparticles and their Transfection Ability into Cultivated Cells*. Chem. Commun., **2004**, 1978-1979.
11. Leroueil, P. R.; Berry, S. A.; Duthie, K.; Han, G.; Rotello, V.M.; McNerny, D. Q.; Baker, J. R.; Orr, B. G.; Banaszak-Holl, M. M. *Wide Varieties of Cationic Nanoparticles Induce Defects in Supported Lipid Bilayers*. Nano Lett., **2008**, 8, 420-424.
12. Lin, S.-Y.; Tsai, Y.-T.; Chen, C.-C.; Lin, C.-M.; Chen, C.-h. *Two-Step Functionalization of Neutral and Positively Charged Thiols onto Citrate-Stabilized Au Nanoparticles*. J. Phys. Chem. B, **2004**, 108, 2134-2139.
13. McIntosh, C. M.; Esposito, E. A.; Boal, A. K.; Simard, J. M.; Martin, C. T.; Rotello, V. M. *Inhibition of DNA Transcription Using Cationic Mixed Monolayer Protected Gold Clusters*. J. Am. Chem. Soc., **2001**, 123, 7626-7629.
14. Kalsin, A. M.; Kowalczyk, B.; Wesson, P.; Paszewski, M.; Grzybowski, B. A. *Studying the Thermodynamics of Surface Reactions on Nanoparticles by Electrostatic Titrations*. J. Am. Chem. Soc., **2007**, 129, 6664-6665.
15. Ferrari, M. *Nanogeometry: Beyond drug delivery*. Nat. Nano, **2008**, 3, 131-132.
16. Albanese, A.; Tang, P. S.; Chan, W. C. W. *The Effect of Nanoparticle Size, Shape, and Surface Chemistry on Biological Systems*. Ann. Rev. Biomed. Eng., **2012**, 14, 1-16.

Synthesis of Cationic Gold Nanoparticles by Competitive Reducers



Up to now, the synthesis and cationic functionalization of Au NPs has been greatly inspired by the pioneering Brust-Schiffrin's two-phase synthesis of monolayer protected Au NPs,¹ in which the gold precursor, hydrogen tetrachloroaurate (HAuCl₄), is reduced by sodium borohydride (NaBH₄) at the H₂O-toluene interface in the presence of an alkylthiol ligand stabilizing the NPs. Using this concept, cationic Au NPs are generally obtained in a single-phase system by NaBH₄ reduction of the gold precursor in the presence of the desired cationic ligand. These cationic ligands are normally thiolated molecules, such as 2-aminoethanethiol²⁻⁴ and tiocholine bromide,⁵ or amphiphilic surfactants, including cetyltrimethylammonium bromide (CTAB),⁶ didodecyldimethylammonium bromide (DDAB)⁷ and dimethyldioctadecylammonium bromide (DODAB).⁸ This methodology overcomes the major problem of instability in the formation of cationic Au NPs, since other common strategies, such as the universal Turkevich-Frens method^{9,10} based on citrate reduction of the gold precursor, and other derivations using tannic acid or ascorbic acid,^{11,12} render the stability of cationic Au NPs impossible due to the presence of negatively charged surfactants.¹³ NaBH₄ reduction is therefore a simple way to prepare cationic Au NPs due to their ready cationic functionalization without aggregating species in solution. Nevertheless, this method also offers many drawbacks as well. It is normally restricted to very small particle sizes (usually from 2 to 5 nm),^{1,5,7} or leads to rather polydisperse particles.^{4,8} In view of these drawbacks, a remaining current challenge is the development of new methods (see for example Chapter 3) or improving the existing ones to open up new avenues for synthesizing a richer catalog of stable, monodisperse cationic Au NPs with controlled sizes and surface functionalities.

In this Chapter, the above-mentioned method has been examined from a completely new point of view, considering that NaBH_4 and a cationic thiolated ligand (*i.e.*, 1-aminoundecane-11-thiol, AUT) are both used as independent reducing agents. Note that in this case, NaBH_4 and AUT are not supposed to interfere. Our observation is that the combination of both reducers does not simply result in an intermediate effect (*i.e.* reduction with only AUT did not yield large NP sizes but rather small and polydisperse NPs), but they really act sequentially in accordance to their chemical environment. In other words, in a first step, the fraction of Au^{+3} precursor reduced by NaBH_4 , which acts as a strong reducer, determines the number of seeds. In a second step, these seeds are grown by the AUT, acting as a weak reducer. By this methodology, precise size control of cationic Au NPs (from 10.3 to 28.2 nm) can be achieved in a two-step one-pot synthesis at room temperature and by separating the two reduction processes in time, mimicking standard seeded growth methods.

2.1. Introduction to the synthetic routes for preparing cationic Au NPs.

To date, there are basically three different synthetic methodologies that can be used to prepare cationic Au NPs. Two of them are based on the Brust-Schiffrin two-phase methodology.¹ In 1994, these authors reported a revolutionary new procedure for the facile synthesis of thiol-stabilized Au NPs by first transferring AuCl_4^- to toluene using tetraoctylammonium bromide (TOAB) as the phase transfer reagent, and then reducing it with NaBH_4 in the presence of dodecanethiol (Scheme 2.1; see a more detailed explanation in Chapter 3, Section 3.1.1). The resulting synthesized Au NPs are usually small (from 1.5 and 5.2 nm);¹⁴ this is due to the use of a large amount of thiolated ligands that strongly bind Au NPs and lower the free energy of the crystalline faces to which they bind, retarding the growth of those faces. Following this method, a wide variety of Au NPs with controlled small sizes have been synthesized by using a large number of reducing agents (e.g. NaBH_4 ,¹⁴ citrate⁶ and ascorbic acid⁶) and stabilizers, mainly thiolates (e.g. mercaptosuccinic acid,¹⁵ thiolated derivatives of PEG,¹⁶ tiopronin (N-2-mercaptopropionyl-glycine),¹⁷ CoA¹⁷ and glutathione)¹⁸ or amines (e.g. dioctylamine¹⁹ and dodecylamine),²⁰ due to their high affinity for Au surfaces (~ 50 Kcal/mol²¹ and 6 Kcal/mol,²² respectively). In such approaches, the particle diameter

was adjusted by varying the ratio of stabilizer to HAuCl_4 or the ratio of reducing agent to HAuCl_4 , although attempts to produce larger particles came at the cost of monodispersity.⁶ The reader is referred to some excellent reviews on this topic.^{21,23}

Inspired on this methodology, a first strategy to synthesize cationic NPs is the chemical reduction of the Au^{3+} precursor by a strong reducer (e.g. NaBH_4) in the presence of cationic ligands in water. Because of the concomitant Au^{3+} precursor reduction by the strong reducer and stabilization by the cationic ligand, this approach represents a simple way to synthesize stable cationic Au NPs without the need of using other species (e.g. negatively charged surfactants) that usually cause their agglomeration. For example, the universal Turkevich-Frens^{9,10} method provide citrate-stabilized Au NPs in which the direct negative citrate displacement by positively charged molecules causes multiple electrostatic bridging, leading to irreversible agglomeration of the NPs.¹³

A detailed literature search clearly reveals that this method is the most widely used for the synthesis of cationic Au NPs (Table 2.1). For example, the use of ligands such as thiocholine bromide (TCB)⁵ and DDAB⁷ produced cationic Au NPs of 2.7 and 5.5 nm in size, respectively, upon NaBH_4 reduction. This result contrasts with the larger sizes up to 29.0 and 33.6 nm obtained for cysteamine²⁴ and 2-aminoethanethiol² molecules, respectively. In this regard, it is worth to mention that the polydispersity of the reported materials is quite high and/or they are poorly characterized. Also note that the same reaction using 2-aminoethanethiol and NaBH_4 , at the same concentration and molar ratios, yielded the formation of cationic Au NPs with opposite low (standard deviation (σ) = 9%)² and high ($\sigma > 50\%$)⁴ monodispersity in size by two different authors. The cationic surfactant CTAB was shown to form 5.5 and 8 nm NPs with good monodispersity.⁶ In this case, ascorbic acid was used as a weak reducer and small Au NPs as seeds, although larger sizes were compromised with poor size distribution or multiple shape formation. In a particular case, multifunctional peptides were exploited to weakly reduce the AuCl_4^- and coat the surface of the NPs.²⁵ The reduction of AuCl_4^- by these peptides was attributed to their tyrosine residue, and the resulting Au NPs varied in charge, size, shape, aggregation state and packing density, depending on the peptidic amino acid sequence. The NP sizes ranged from 11.4 to 13.8 nm by using different peptides, with the particularity that the only NP bioconjugate with slightly

positive charge (ζ -potential of +3.44 mV) had a notably high polydispersity ($\sigma > 50\%$). In two other cases, the peptides yielded a good NP size distribution, with near-neutral ζ -potential values.

Size (nm) ^a , %SD	ζ -potential (mV)	Ligand	Reducer	Ref.
2.7 ± 0.4, 16 %	-	Thiocholine bromide (TCB)	NaBH ₄	5
5.5 ± 0.9, 16 %	-	DDAB	NaBH ₄	7
5.5 ± 0.6, 11 %	-	CTAB	Ascorbic Acid	6
8.0 ± 0.8, 10 %	-	CTAB	Ascorbic Acid	6
17 ± 2.5, 15 %	-	CTAB	Ascorbic Acid	6
12.8 ± 2.9, 23 %	+ 0.14 ^c	Peptide AYSSGAPMPPF ^d		23
13.3 ± 7.4, >50 %	+ 3.44 ^c	Peptide DYKDDDDK ^d		23
11.4 ± 1.2, 11 %	+ 0.10 ^c	Peptide DYKDDDDKPAYSSGAPMPPF ^d		23
13.8 ± 1.7, 12 %	+ 0.21 ^c	Peptide AYSSGAPMPPFPDYKDDDDK ^d		23
14.0 ± 4.0, 29 %	-	DODAB	NaBH ₄	8
29.0 ± 5.0, 17 %	+ 41.8	Cysteamine	NaBH ₄	22
33.6 ± 3.0, 9 %	+ 36.2 ± 15	2-Aminoethanethiol	NaBH ₄	2
10-48, > 50 %	+ 31.8 ± 8.2	2-Aminoethanethiol	NaBH ₄	4
47.5 ± 4.5, 9 %	+ 0.1 ± 0.2	2-Aminoethanethiol, mPEG-SH	NaBH ₄	3
2, -	-	TMA	NaBH ₄	27
2, -	+ 20 to +30	TTMA, TEG	NaBH ₄	29
17.1 ± 3.0, 18 %	-	11-Mercaptoundecylamine, thioctic acid	Sodium citrate	36
110.9 ^b	+ 11.8	Peptide CIPGNVG-PEG4-COOH	Sodium citrate	21

Table 2.1. Summary of synthetic approaches to obtain various cationic Au NPs and their respective size and ζ -potential values. ^a Sizes are based on TEM micrographs. ^b agglomerated AuNPs. ^c Note that these are indeed neutral or near-neutral ζ -potential values. We consider a negative charged NP when it is above -10 mV like proteins. ^d single letter amino acid code (A = alanine, Y = tyrosine, S = serine, P = proline, D = aspartic acid, K = lysine, M = methionine, F = phenylalanine, G = glycine).

A second general strategy to obtain cationic Au NPs is the ligand exchange of monolayer-protected Au NPs previously synthesized in organic solvent.¹ As shown in Figure 2.1, the replacement of the initial monolayer by the cationic ligand takes place through Murray place-exchange reaction.²⁶ This strategy has been widely used by Rotello and co-workers in order to conjugate cationic aminoalkanethiols,^{27,28} tetraalkylammonium salts,²⁹⁻³¹ and amino acids^{32,33} to Au NPs of 2 nm-in-size, which were then examined in a variety of therapeutic uses. In their studies, however, accurate

control on the NP size and size distribution was not presented. The size limitation from this method further confirms the need for more synthetic protocols in order to have access to stable cationic NPs of a wide range of sizes.

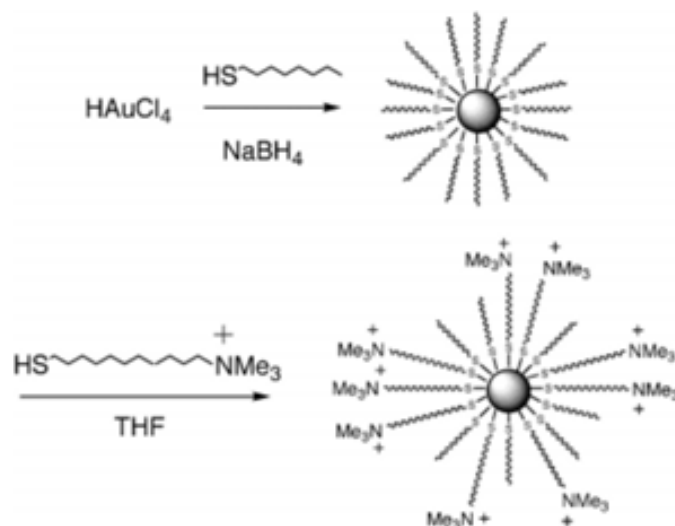


Figure 2.1. Schematic representation of the preparation of cationic Au NPs via Brust-Schiffrin synthesis (top) and Murray place-exchange reaction (bottom).

Finally, the third strategy to prepare cationic Au NPs is the already mentioned replacement of the citrate stabilizing molecules of Au NPs, synthesized through derivations of the traditional Frens-modified Turkevich method,^{9,10} by thiolated ligands. This method has the advantage of controlling the formation of Au NPs with larger sizes and good monodispersity. However, it has been demonstrated that this methodology produces immediate aggregation in the case of positively charged ligands due to the cross-linking effect of citrate.¹³ Indeed, several studies demonstrated the highly aggregating character of these systems, e.g. with mercaptoethylamine³⁵ or positively charged peptides.³⁶ Only in exceptional cases where the citrate was eliminated before the addition of cationic molecules, either by replacement with thioctic acid³⁷ or by centrifugation,³⁸ this method worked. Unfortunately, such approaches led to either mixed ligand Au NPs or unavoidable minor agglomeration effects, respectively.

Other examples use polymer coatings to confer the cationic character to Au NPs. Normally, these polymers bind electrostatically to the negatively charged Au NPs. For example, Xia and co-workers³⁸ used this strategy to functionalize citrate-capped Au NPs

of 17 nm in size with PAA, and used them for subsequent cellular uptake studies. This type of NPs has a different surface chemistry and is not included in this discussion.

2.2. Results and discussion

2.2.1. Independent control of nucleation and growth using different reducers at substoichiometric concentrations.

The importance of combining two reducers (NaBH_4 and AUT) with different reducing capacities in the synthesis of cationic Au NPs was explored. Briefly, the synthesis was performed by simultaneously injecting the two reducers onto the Au^{3+} precursor solution under vigorous stirring, in aqueous phase and at room temperature, obtaining Au NPs stabilized by AUT. Importantly, these synthetic conditions may be advantageous for a green and scalable production of cationic Au NPs. With this strategy, a series of identical reactions were performed in which the volume fraction of the stock solution of NaBH_4 was systematically increased under a fixed molar ratio of the other reagents; that is a Au:AUT: NaBH_4 molar ratio of 1:0.66:X, where X was varied from 0.11, 0.053, 0.026, 0.0132, 0.0066, 0.0033, 0.0016, 0.0008, 0.0004 to 0.0002 (Figure 2.2) by keeping a constant reaction volume. In these reactions, AUT was used in excess, whereas the NaBH_4 was employed in stoichiometric deficiency. In addition, the stoichiometric ratio Au:AUT was fixed to 1:0.66 because it was found to be the optimum for the formation of Au NPs. For such an amount of Au^{3+} precursor, addition of less AUT resulted in irreversible aggregation, sometimes even before the addition of NaBH_4 . On the contrary, under excess of AUT, nucleation was dramatically reduced probably due to the formation of stable AUT- Au^{+3} complexes.

Morphological characterization (Figure 2.2 and Figure 2.3-B) of the resulting cationic Au NPs showed that monomodal collections of NPs were only obtained with Au: NaBH_4 ratios between 1:0.053 and 1:0.0016, corresponding to particle sizes ranging from 10.3 ± 2.8 nm to 19.7 ± 2.6 nm. Within these two ratios, a decrease in NaBH_4 led to the formation of bigger particle sizes with increased monodispersity ($\sigma \sim 13$ %). In addition, the NPs were further characterized by UV-vis absorption spectroscopy, in which the effect of systematically decreasing the amount of NaBH_4 resulted in a red-

shift of the SPR peak from 523 to 553 nm (Figure 2.3-C). Considering that the SPR absorption peak is indicative of the particle size,³⁹ this shift confirmed a gradual increase of Au NPs diameter when reducing the NaBH₄ amount. The trend of size variation depending on the amount of NaBH₄ added was also confirmed by Dynamic Light Scattering (DLS) (Figure 2.3-A). However, a further comparison of absolute diameters measured with DLS to the data obtained from TEM was difficult because of the different nature of measurements (i.e. inorganic core diameter of single particles from TEM vs hydrodynamic diameter from an ensemble by DLS). Regarding DLS, bimodal size distributions could not be resolved neither by the general purpose nor the “*multiple narrow peak*” algorithm of the Malvern DTS software. The ζ -potential of the AUT-capped NPs was strongly positive (approx. + 50 mV at pH ~ 7 in all the cases), confirming the cationic nature of the NPs.

Closer monitoring of the Au NP formation and growth was also performed by recording a time series of absorption spectra for two selected reactions (Au:AUT:NaBH₄ 1:0.66:0.0066 and 1:0.66:0.0016, corresponding to reactions E and G from Figure 2.2, respectively). The absorption maximum and the position of the plasmon peak were plotted over time (Figure 2.4). The increasing absorption from the solutions over time, together with a red shift of the plasmon peak position, were indicative of NPs formation and growth. As expected, a maximum conversion rate, which corresponds to the maximum absorption and peak shift, was previously achieved for the addition of larger amounts of NaBH₄. This was in agreement with the formation of more nuclei, leading to smaller NP sizes, with a higher NaBH₄ content (Figure 2.2).

In view of these results, the controlled growth of NPs without significative new nucleation and with narrow size distributions can only be attributed to the existence of differentiated nucleation and growth mechanisms. In these mechanisms, NaBH₄ acts as the strong reducing agent which can immediately trigger nucleation of Au clusters, while AUT acts as the weak reducer and also as the stabilizing molecule which dictates the final NP size. Therefore, the initial fraction of Au⁺³ precursor reduced by NaBH₄ determines the number of seed particles, which are then grown larger by AUT present in the reaction mixture, by a slow reduction of the remaining Au³⁺ in solution.

PHASE I: # of nuclei / PHASE II: size of the NPs

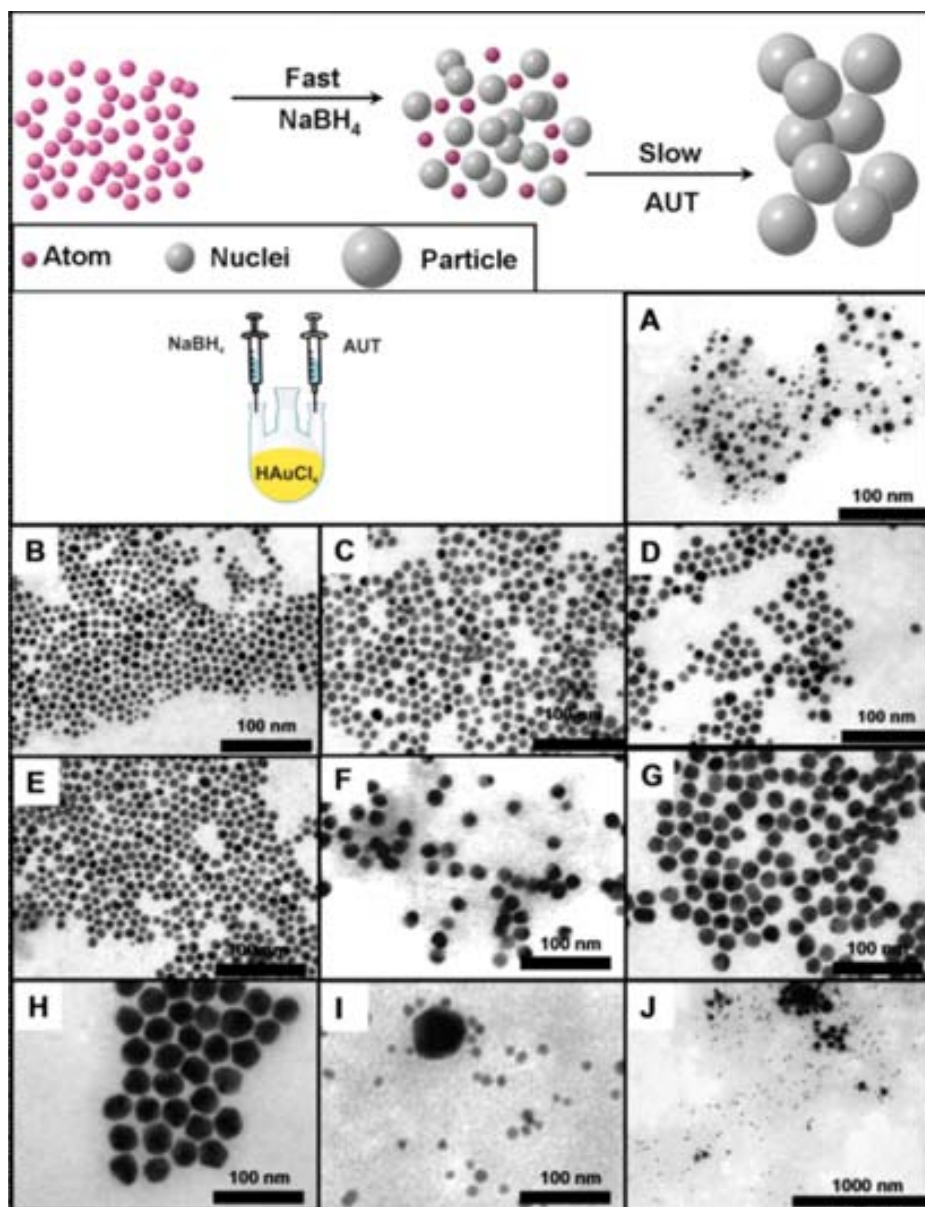


Figure 2.2. Schematic representation of the two-step - nucleation and growth - proposed mechanism for the formation of cationic Au NPs (top) and morphological (TEM) characterization of Au NPs synthesized with decreased volume fraction of a stock solution of NaBH₄ in a fixed molar ratio of the other reagents Au:AUT:NaBH₄ 1:0.66:X at room temperature (bottom). A) X = 0.11, B) X = 0.053, C) X = 0.026, D) X = 0.0132, E) X = 0.0066, F) X = 0.0033, G) X = 0.0016, H) X = 0.0008, I) X = 0.0004, J) X = 0.0002.

This hypothetical mechanism was fully confirmed with the obtained results at higher or lower Au:NaBH₄ ratios. In the presence of low NaBH₄ content (Au:NaBH₄ > 1:0.0016), the concentration of the strongest reducer was too low to avoid secondary nucleation. Indeed, as a consequence of the large concentration of Au⁺³ precursor in the

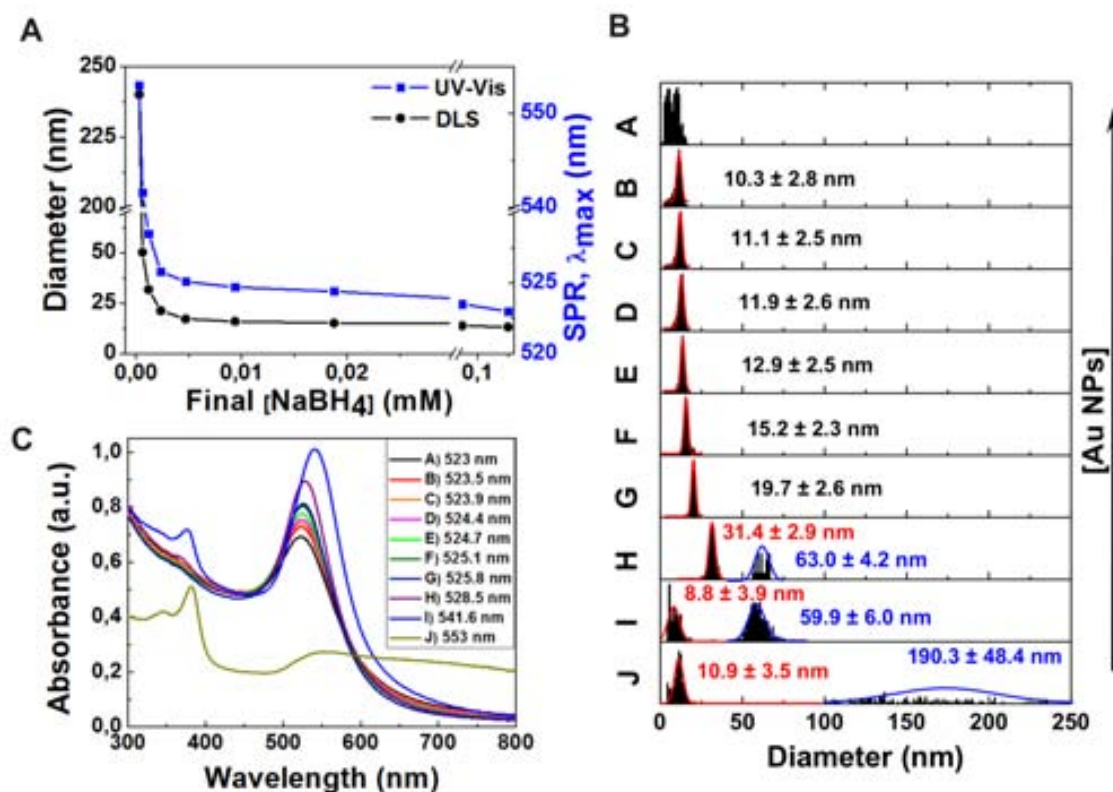


Figure 2.3. A, B) Morphological (DLS, TEM) and C) physical (UV-Vis absorbance) characterization of Au NPs synthesized with decreased volume fraction of a stock solution of NaBH₄ in a fixed molar ratio of the other reagents Au:AUT:NaBH₄ 1:0.66:X at room temperature. A) X = 0.11; B) X = 0.053; C) X = 0.026; D) X = 0.0132; E) X = 0.0066; F) X = 0.0033; G) X = 0.0016; H) X = 0.0008; I) X = 0.0004; J) X = 0.0002.

reaction mixture, the initial fraction reduced by NaBH₄ was also accompanied by a slow reduction of the remaining Au⁺³ salt by AUT. According to this, the nucleation of Au NPs was mainly divided in two stages that took place within several days: the nuclei produced first by NaBH₄ had a much longer time to grow, resulting into larger particles, whereas more nuclei were slowly and constantly produced by AUT. As a result, bimodal size distributions were obtained with a population of small particles (~ 10-30 nm) together with much larger Au NPs (between 60 and 200 nm; Figure 2.2-H,J). Importantly, the different polydispersity related to the different growth histories of each NP suggested the occurrence of two independent reduction processes.

For higher NaBH₄ content (Au:NaBH₄ < 1:0.11), faster homogeneous reduction than with AUT occurs, leading to a broad distribution of small particles (Figure 2.2-A). In most of the cases, the small clusters generated by an excess of NaBH₄ were not stable and caused the immediate precipitation of the samples.

Finally, it is worth to note that an excess of either NaBH_4 or AUT led to a broad distribution of small particles, suggesting a simultaneous and uncontrolled reduction of the Au^{+3} precursor (fast or slow, respectively) (Figure 2.2-A,J). Although one could argue that the excess of the weak reducer (*i.e.* AUT) would produce NPs of larger size, this was not observed in our case. We hypothesized that AUT molecules are capable of complexing the reduced Au^+ . These monomers in solution supported a continuous nucleation process, which resulted in samples being rich with very small NPs.

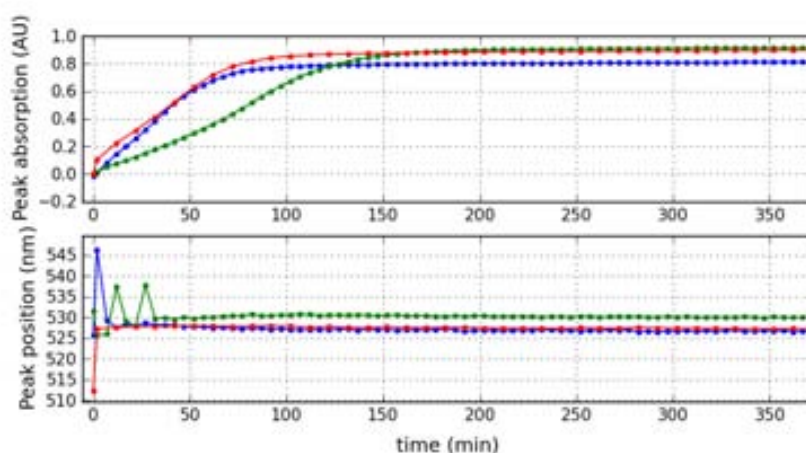


Figure 2.4. Time evolution of the UV-vis absorbance spectra of Au NPs synthesized under molar ratios of Au:AUT: NaBH_4 1:0.66:0.0066 (blue) and 1:0.66:0.0016 (green), and under addition of Au:AUT in a molar ratio = 1.5 to a seed solution of Au NP = 11.1 ± 2.5 nm (red).

2.2.2. Independent control of nucleation and growth using different reducers *via* seeded growth.

The two-step -nucleation and growth- mechanism proposed for the formation of cationic Au NPs in a one-pot synthesis was further confirmed when separating the two reduction processes in time mimicking standard seeding growth methods.^{6,40} In these syntheses, the formation of NP seeds and their growth are normally performed in different reactors. Therefore, by exploiting this same mechanism, preformed NPs from a first synthesis (Experiment C from Figure 2.2; Au:AUT: NaBH_4 1:0.66:0.026; Au NP

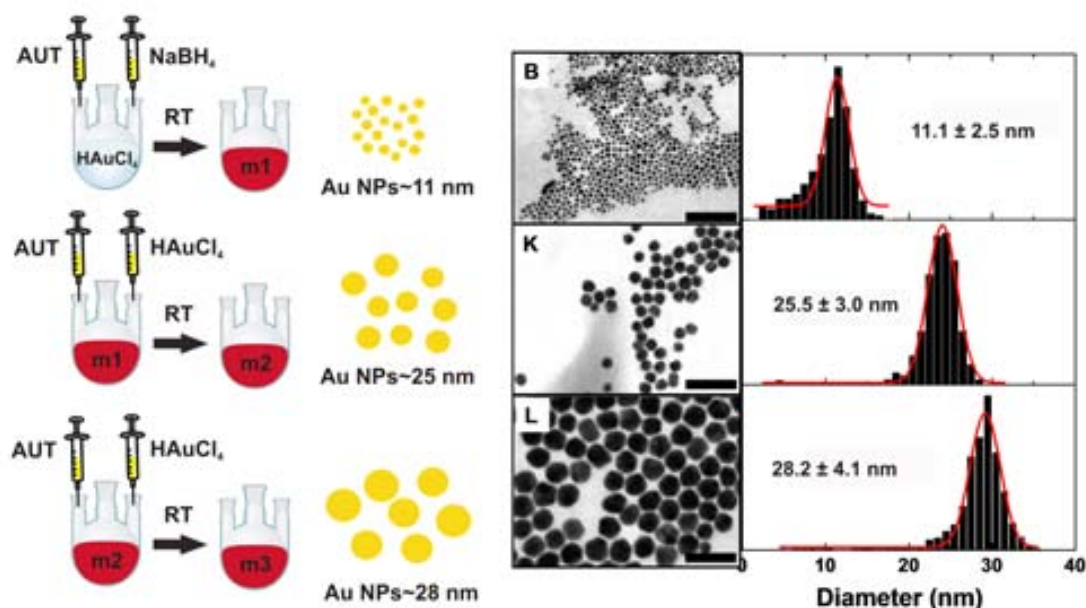


Figure 2.5. TEM characterization and size distribution measurements of Au NPs synthesized by addition of HAuCl_4 and AUT in a molar ratio Au:AUT = 1.5 to a seed solution of Au NP = $11.1 \pm 2.5 \text{ nm}$: B) As-synthesized seeds corresponding to experiment conditions C; K) addition of 7-fold excess of Au^{3+} ; L) addition of 26-fold excess of Au^{3+} . Scale bars are 100 nm.

size = $11.1 \pm 2.5 \text{ nm}$) were used as seeds for further growth by addition of fresh Au^{3+} precursor solution and AUT in a molar ratio Au:AUT = 1:0.66 at room temperature (Figure 2.5). Again, the synthetic conditions used are advantageous for the production of larger cationic Au NPs by a green and scalable seeding growth method. AUT was chosen for the subsequent seeding growth steps due to its weaker reducing capacity, favoring two important aspects in the kinetic control of the growth process: inhibition of new nucleation and slowing down of the reaction. Two different experiments were carried out in which the amount of Au added was 8- and 27-fold the amount of Au^{3+} used to prepare the initial Au NP seeds. These specific amounts of Au^{3+} were chosen with the aim to increase the original Au NP seeds by 2- and 3-fold, respectively (*i.e.* NP volume is proportional to the number of atoms and to radius³, then to increase the NP radius 2- and 3-fold, $2^3 = 8$ and $3^3 = 27$ x the number of atoms should be added), assuming that no additional nucleation occurs. Characterization by TEM (Figure 2.5) showed that the resulting Au NPs had diameters of $25.5 \pm 3.0 \text{ nm}$ and $28.2 \pm 4.1 \text{ nm}$, respectively, confirming the previous assumptions.

In addition, a closer monitoring of the Au NP growth was performed by recording a time series of absorption spectra for a seeded-growth reaction, where HAuCl_4 and AUT were added in a molar ratio $\text{Au:AUT} = 1:0.66$ to a seed solution of Au NP = 11.1 ± 2.5 nm (Figure 2.4). In this case, the increasing absorption from the solutions over time and the red shift of the plasmon peak position were similar to those found at the two-step one-pot synthesis of Au NPs using high amounts of NaBH_4 (Au:AUT:NaBH_4 1:0.66:0.0066). This again indicated that separating the nucleation and growth processes led to a similar kinetics of Au NP formation than on the two-step one-pot synthesis, in which the NaBH_4 determines the formation of the nuclei and AUT is responsible for a slow growth. Indeed, this second seeded-growth methodology shows a high kinetic control over the NP growth process. These results confirm that the formation of monodisperse Au NPs was mediated by a two-step mechanism where nucleation and growth processes were carried out separately due to the independent role of each reducing agent, either when they co-existed in solution or were separated in time.

2.3. Conclusions.

By combining two reducers (NaBH_4 and AUT) with different reducing capacities at precise sequence and ratios, size-control of Au NPs was achieved in a two-step one-pot synthesis at room temperature and by separating the two reduction processes in time, mimicking standard seeded growth methods. This methodologies provide new tools to functionalize NPs and obtaining refined materials such as size controlled cationic Au NPs. First, cationic Au NPs with sizes comprised between 10.3 and 19.7 nm with a high monodispersity were prepared by a two-step one-pot synthesis. In this synthesis, the NaBH_4 acted as a strong reducer and determined the number of seeds, whereas the AUT present in solution reduced slowly the Au^{+3} precursor, resulting in a controlled growth of the cationic Au NPs without significant new nucleation. The independent role of the two reducers was further confirmed by a seeding growth method, in which preformed Au NPs were grown larger (up to ~ 28 nm in size) by addition of fresh Au^{3+} precursor solution and AUT in a second injection. In this second methodology, the high kinetic control over the NP growth process was essentially due to the role of AUT: its weak reducing capacity and complexing abilities favoured the inhibition of new nucleation and

slowing down of the reaction. Overall, this study illustrates the importance of having the adequate combination and ratios of reducers to yield monomodal collections of size controlled Au NPs in a synthesis, where their monodispersity is related to an homogeneous growth. In addition, the outcome of this experimental research is a rich catalog of highly stable and monodisperse cationic Au NPs, with a range of sizes that is typically used for drug delivery and cellular uptake,⁴¹⁻⁴³ offering NP engineers with a new strategy to improve tools and develop processes/(nano)technology.

2.4. References.

1. Brust, M.; Walker, M.; Bethell, D.; Schiffrin, D. J.; Whyman, R. *Synthesis of Thiol-Derivatised Gold Nanoparticles in a Two-Phase Liquid-Liquid System*. J. Chem. Soc., Chem. Commun., **1994**, 801-802.
2. Niidome, T.; Nakashima, K.; Takahashi, H.; Niidome, Y. *Preparation of Primary Amine-Modified Gold Nanoparticles and their Transfection Ability into Cultivated Cells*. Chem. Commun., **2004**, 1978-1979.
3. Kawano, T.; Yamagata, M.; Takahashi, H.; Niidome, Y.; Yamada, S.; Katayama, Y.; Niidome, T. *Stabilizing of Plasmid DNA in Vivo by PEG-Modified Cationic Gold Nanoparticles and the Gene Expression Assisted with Electrical Pulses*. J. Control. Rel., **2006**, 111, 382-389.
4. Zhang, Y.; Liu, G.; Hou, C.; Chen, J.; Wang, J.; Pan, Y. *Preparation of Cationic Gold Nanoparticles and their Transfection Ability into Cultivated Cells*. Nanosci., **2007**, 1, 49-53.
5. Yonezawa, T.; Onoue, S.; Kimizuka, N. *Metal Coating of DNA Molecules by Cationic, Metastable Gold Nanoparticles*. Chem. Lett., **2002**, 31, 1172-1173.
6. Jana, N. R.; Gearheart, L.; Murphy, C. J. *Seeding Growth for Size Control of 5–40 nm Diameter Gold Nanoparticles*. Langmuir, **2001**, 17, 6782-6786.
7. Zhang, L.; Sun, X.; Song, Y.; Jiang, X.; Dong, S.; Wang, E. *Didodecyldimethylammonium Bromide Lipid Bilayer-Protected Gold Nanoparticles: Synthesis, Characterization, and Self-Assembly*. Langmuir, **2006**, 22, 2838-2843.
8. Li, P.; Li, D.; Zhang, L.; Li, G.; Wang, E. *Cationic Lipid Bilayer Coated Gold Nanoparticles-Mediated Transfection of Mammalian Cells*. Biomater., **2008**, 29, 3617-3624.
9. Turkevich, J.; Stevenson, P. C.; Hillier, J. *A Study of the Nucleation and Growth Processes in the Synthesis of Colloidal Gold*. Discuss. Farad. Soc., **1951**, 11, 55-75.
10. Frens, G. *Controlled Nucleation For Regulation of Particle Size in Monodisperse Gold Suspensions*. Nat. Phys. Sci., **1973**, 241, 20-22.

11. Hayat, M.A. *Colloidal Gold: Principles, Methods, and Applications*. Academic Press, San Diego, **1989**, Vol. 1, chap. 2.
12. Jana, N. R.; Gearheart, L.; Murphy, C. J. *Seeding Growth for Size Control of 5–40 nm Diameter Gold Nanoparticles*. *Langmuir*, **2001**, 17, 6782-6786.
13. Ojea-Jimenez, I.; Puentes, V. *Instability of Cationic Gold Nanoparticle Bioconjugates: The Role of Citrate Ions*. *J. Am. Chem. Soc.*, **2010**, 132, 5322-5322.
14. Hostetler, M. J.; Wingate, J. E.; Zhong, C.; Harris, J. E.; Vachet, R. W.; Clark, M. R.; Londono, J. D.; Green, S. J.; Stokes, J. J.; Wignall, G. D.; Glish, G. L.; Porter, M. D.; Evans, N. D.; Murray, R. W. *Alkanethiolate Gold Cluster Molecules with Core Diameters from 1.5 to 5.2 nm: Core and Monolayer Properties as a Function of Core Size*. *Langmuir*, **1998**, 14, 17-30.
15. Chen, S.; Kimura, K. *Synthesis and Characterization of Carboxylate-Modified Gold Nanoparticle Powders Dispersible in Water*. *Langmuir*, **1999**, 15, 1075-1082.
16. Kanaras, A. G.; Kamounah, F. S.; Schaumburg, K.; Kiely, C. J.; Brust, M. *Thioalkylated Tetraethylene Glycol: a New Ligand for Water Soluble Monolayer Protected Gold Clusters*. *Chem. Commun.*, **2002**, 2294-2295.
17. Templeton, A. C.; Chen, S.; Gross, S. M.; Murray, R. W. *Water-Soluble, Isolable Gold Clusters Protected by Tiopronin and Coenzyme A Monolayers*. *Langmuir*, **1998**, 15, 66-76.
18. Schaaff, T. G.; Knight, G.; Shafiqullin, M. N.; Borkman, R. F.; Whetten, R. L. *Isolation and Selected Properties of a 10.4 kDa Gold:Glutathione Cluster Compound*. *J. Phys. Chem. B*, **1998**, 102, 10643-10646.
19. Manea, F.; Bindoli, C.; Polizzi, S.; Lay, L.; Scrimin, P. *Expeditious Synthesis of Water-Soluble, Monolayer-Protected Gold Nanoparticles of Controlled Size and Monolayer Composition*. *Langmuir*, **2008**, 24, 4120-4124.
20. Leff, D. V.; Brandt, L.; Heath, J. R.; Leff, D. V. *Synthesis and Characterization of Hydrophobic, Organically-Soluble Gold Nanocrystals Functionalized with Primary Amines*. *Langmuir*, **1996**, 12, 4723-4730.
21. Love, J. C.; Estroff, L. A.; Kriebel, J. K.; Nuzzo, R. G.; Whitesides, G. M. *Self-Assembled Monolayers of Thiolates on Metals as a Form of Nanotechnology*. *Chem. Rev.*, **2005**, 105, 1103-1170.
22. Di Felice, R.; Selloni, A. *Adsorption Modes of Cysteine on Au(111): Thiolate, Amino-Thiolate, Disulfide*. *J. Chem. Phys.*, **2004**, 120, 4906-4914.
23. Daniel, M.-C.; Astruc, D. *Gold Nanoparticles: Assembly, Supramolecular Chemistry, Quantum-Size-Related Properties, and Applications toward Biology, Catalysis, and Nanotechnology*. *Chem. Rev.*, **2003**, 104, 293-346.
24. Kim, J-W.; Kim, J. H.; Chung, S. J.; Chung, B. H. *An Operationally Simple Colorimetric Assay of Hyaluronidase Activity using Cationic Gold Nanoparticles*. *Analyst*, **2009**, 134, 1291-1293.
25. Slocik, J. M.; Stone, M. O.; Naik, R. R. *Synthesis of Gold Nanoparticles Using Multifunctional Peptides*. *Small*, **2005**, 1, 1048-1052.

26. Hostetler, M. J.; Templeton, A. C.; Murray, R. W. *Dynamics of Place-Exchange Reactions on Monolayer-Protected Gold Cluster Molecules*. *Langmuir*, **1999**, 15, 3782-3789.
27. Kim, C.; Agasti, S. S.; Zhu, Z.; Isaacs, L.; Rotello, V. M. *Recognition-Mediated Activation of Therapeutic Gold Nanoparticles Inside Living Cells*. *Nat. Chem.*, **2010**, 2, 962-966.
28. Leroueil, P. R.; Berry, S. A.; Duthie, K.; Han, G.; Rotello, V.M.; McNerny, D. Q.; Baker, J. R.; Orr, B. G.; BanaszakHoll, M. M. *Wide Varieties of Cationic Nanoparticles Induce Defects in Supported Lipid Bilayers*. *Nano Lett.*, **2008**, 8, 420-424.
29. McIntosh, C. M.; Esposito, E. A.; Boal, A. K.; Simard, J. M.; Martin, C. T.; Rotello, V. M. *Inhibition of DNA Transcription Using Cationic Mixed Monolayer Protected Gold Clusters*. *J. Am. Chem. Soc.*, **2001**, 123, 7626-7629.
30. Kim, B.; Han, G.; Toley, B. J.; Kim, C.-k.; Rotello, V. M.; Forbes, N. S. *Tuning Payload Delivery in Tumour Cylindroids Using Gold Nanoparticles*. *Nat. Nanotechnol.*, **2010**, 5, 465-472.
31. Chompoosor, A.; Han, G.; Rotello, V. M. *Charge Dependence of Ligand Release and Monolayer Stability of Gold Nanoparticles by Biogenic Thiols*. *Bioconj. Chem.*, **2008**, 19, 1342-1345.
32. Ghosh, P. S.; Han, G.; Erdogan, B.; Rosado, O.; Krovi, S. A.; Rotello, V. M. *Nanoparticles Featuring Amino Acid-functionalized Side Chains as DNA Receptors*. *Chem. Biol. Drug Des.*, **2007**, 70, 13-18.
33. Ghosh, P. S.; Kim, C.-K.; Han, G.; Forbes, N. S.; Rotello, V. M. *Efficient Gene Delivery Vectors by Tuning the Surface Charge Density of Amino Acid-Functionalized Gold Nanoparticles*. *ACS Nano*, **2008**, 2, 2213-2218.
34. Pan, Y.; Leifert, A.; Ruau, D.; Neuss, S.; Bornemann, J.; Schmid, G.; Brandau, W.; Simon, U.; Jahnen-Dechent, W. *Gold Nanoparticles of Diameter 1.4 nm Trigger Necrosis by Oxidative Stress and Mitochondrial Damage*. *Small*, **2009**, 5, 2067-2076.
35. Bellino, M. G.; Calvo, E. J.; Gordillo, G. *Adsorption Kinetics of Charged Thiols on Gold Nanoparticles*. *Phys. Chem. Chem.Phys.*, **2004**, 6, 424-428.
36. Levy, R.; Thanh, N. T. K.; Doty, R. C.; Hussain, I.; Nichols, R. J.;Schiffrin, D. J.; Brust, M.; Fernig, D. G. *Rational and Combinatorial Design of Peptide Capping Ligands for Gold Nanoparticles*. *J. Am. Chem. Soc.*, **2004**, 126, 10076-10084.
37. Lin, S.-Y.; Tsai, Y.-T.; Chen, C.-C.; Lin, C.-M.; Chen, C.-h. *Two-Step Functionalization of Neutral and Positively Charged Thiols onto Citrate-Stabilized Au Nanoparticles*. *J. Phys. Chem. B*, **2004**, 108, 2134-2139.
38. Cho, E. C.; Xie, J.; Wurm, P. A.; Xia, Y. *Understanding the Role of Surface Charges in Cellular Adsorption versus Internalization by Selectively Removing Gold Nanoparticles on the Cell Surface with a I2/KI Etchant*. *Nano Lett.*, **2009**, 9, 1080-1084.
39. Link, S.; El-Sayed, M. A. *Size and Temperature Dependence of the Plasmon Absorption of Colloidal Gold Nanoparticles*. *J. Phys. Chem. B*, **1999**, 103, 4212-4217.
40. Bastús, N. G.; Comenge, J.; Puntès, V. *Kinetically Controlled Seeded Growth Synthesis of Citrate-Stabilized Gold Nanoparticles of up to 200 nm: Size Focusing versus Ostwald Ripening*. *Langmuir*, **2011**, 27, 11098-11105.

41. Krpetic, Z.; Nativio, P.; Prior, I. A.; Brust, M. *Acrylate-Facilitated Cellular Uptake of Gold Nanoparticles*. *Small*, **2011**, 7, 1982-1986.
42. Nativio, P.; Prior, I. A.; Brust, M. *Uptake and Intracellular Fate of Surface-Modified Gold Nanoparticles*. *ACS Nano*, **2008**, 2, 1639-1644.
43. Rosi, N. L.; Giljohann, D. A.; Thaxton, C. S.; Lytton-Jean, A. K. R.; Han, M. S.; Mirkin, C. A. *Oligonucleotide-Modified Gold Nanoparticles for Intracellular Gene Regulation*. *Science*, **2006**, 312, 1027-1030.

Synthesis of Cationic Gold Nanoparticles by Organic-Aqueous Phase Transfer



Water-based syntheses of cationically charged Au NPs are fraught with problems due to the ionic interactions between the growing NPs and the and the surfactants or polymers used to stabilize them (see also Chapter 2). When rethinking ways to obtain cationic NPs in biological environments, it is worth mentioning that, in contrast to aqueous protocols, organic synthetic methods usually produce higher quality nanocrystals with narrower dispersions and at high concentrations due to the highly efficient steric stabilization. The advantages of working in non-polar organic solvents can be combined with the benefits of working in aqueous solution (e.g. bioconjugation) by means of a phase transfer procedure.

Phase transfer protocols typically involve the synthesis and stabilization of the nanocrystals in the presence of an alkanethiol. Posterior surface functionalization of the NPs can be performed by partially exchanging thiolate ligands on the surface of the NPs.^{1,2} However, these surface modifications are not straightforward and yield mixed monolayers of ligands on the NPs surface (see Section 3.1.1). As an alternative to this, the current study deals first with the use of an alkylamine as both a weaker reducer for Au^{+3} precursor and a rather soft binding surfactant, so that NPs are produced under mild conditions. Then, the replacement at the interphase of alkylamine surfactants by aqueous-soluble thiol-containing ligands, which render hydrophilicity to the final NP conjugate, facilitates its transfer into the aqueous phase. This methodology overcomes the difficulties encountered in place-exchange reactions with alkanethiolate monolayers.

By taking advantage of this methodology, a simple organic-aqueous phase transfer process was optimized for the functionalization of Au NPs with cationic thiolated ligands in aqueous solution, employing a variety of nanocrystal sizes (4, 8 and 13 nm) with narrow size distributions. 11-amino-1-undecanethiol (AUT) was employed as a case model ligand to optimize the synthetic procedure. As proof of concept, this methodology was applied for the conjugation of two peptidic biomolecules terminating in positive and negative charged groups (Chapter 4). The main advantages from this strategy are that: i) it overcomes the aggregation difficulties observed for the conjugation of positively charged moieties in the presence of negatively charged stabilizers such as citrate,³ which crosslink the NPs, and ii) it produces high-quality nanocrystals with narrow dispersions and at high concentrations, in aqueous final dispersions having potential use for biological applications. Overall, the present chapter faces the rising demand of cationic Au NPs of different sizes and ligands (molecules and biomolecules) for biological applications.

3.1. Introduction.

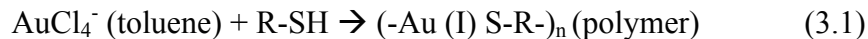
The next Section gives a brief overview of the organic synthetic methods used to prepare Au NPs in this Chapter. The as-synthesized Au NPs were then functionalized with cationic molecules by a phase transfer protocol. For a further understanding of this process, a description of the main phase transfer mechanisms is also provided.

3.1.1. Synthesis of Au NPs in organic solvents.

In contrast to aqueous protocols, organic synthetic methods generally produce higher-quality nanocrystals, with better size control, narrower dispersions, and in highly dense concentrations. Typically in these protocols, the reduction of metal ions is followed by stabilization with hydrophobic ligands, such as phosphine ligands⁴⁻⁶, organoamines,⁷⁻¹⁰ and alkanethiols.¹¹⁻¹³

The synthesis of Au NPs in non-polar organic solvents was pioneered by Schmid *et al.*¹⁴ in 1981 with the formation of phosphine-stabilized Au NPs of 1.4 nm in diameter

in benzene. The stabilization of Au NPs with alkanethiols was first reported in 1993 by Mulvaney and Giersig,¹⁵ who showed the possibility of using thiols with different chains lengths. However, the practical formation of stable, isolable alkanethiolate monolayer protected clusters (MPCs) in organic solvent was not demonstrated until 1994 by Brust and co-workers,¹¹ whose work had a considerable impact on the overall field. Basically, they combined the two-phase approach from Faraday¹⁶ with the alkanethiolate/Au chemistry to prepare in a simple, one step procedure, small clusters of Au atoms (with diameters ranging from 1.5 to 5.2 nm) with moderate monodispersity (standard deviation $\sigma \sim 10\%$ in diameter). Importantly, these NPs could be repeatedly isolated from and redispersed in common organic solvents without irreversible aggregation or decomposition, and they could be functionalized with ligands as stable organic molecules. In this strategy, AuCl_4^- is transferred into toluene using TOAB as a phase transfer reagent, and reduced by NaBH_4 at the H_2O -toluene interface in the presence of dodecanethiol (Figure 3.1-A). It is generally believed that prior to reduction with NaBH_4 , the precursor form Au(I) thiolate polymers with the dodecanethiol molecules, according to the following scheme:¹⁷



In contrast to this, a more recent study suggested that tetraalkylammonium metal complexes are the precursors of this two-phase reaction, whereas Au(I) thiolate polymers appear to be precursors of the one-phase reactions.¹⁸ The mechanism governing these reactions is consistent with a nucleation-growth-passivation process, in which both nucleation and growth can only occur at the interphase of the two liquid phases. The NP size can be controlled by simply varying the Au : thiol stoichiometry¹⁹⁻²¹ and other factors, such as the rate of reductant addition,^{20,22} temperature of reaction^{20,22} and quenching of the reaction after reduction.²² However, due to the high affinity of thiols for Au (Au-S bond ~ 50 Kcal/mol),²³ the growth process is hindered and the method is limited to the formation of very small NPs, typically between 1.5 and 5.2 nm in diameter.²⁰

Subsequent studies have shown that a wide range of alkanethiolate ligands can be employed in this same protocol,^{1,22,24,25} and also that the initial MPCs can be readily

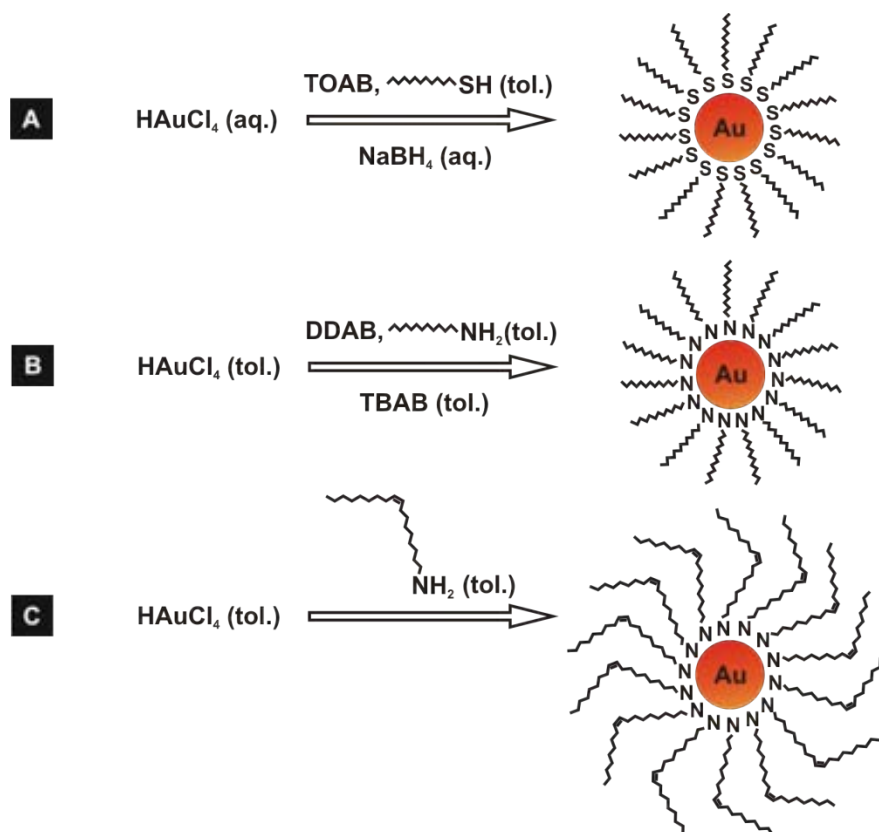


Figure 3.1. Reaction schemes of the organic synthetic methods followed in this Thesis for obtaining monodisperse Au NPs of different sizes and functionalities. A) Two-phase reduction with sodium borohydride in the presence of alkanethiols. B) One-phase reduction with TBAB and stabilization with aliphatic amines. C) One-phase reduction and stabilization with organoamines.

modified through ligand place-exchange reactions.^{2,12} For example, MPCs with alkanethiolate monolayers [(R-S)_mMPC] can be functionalized with R'-SH groups by the following reaction scheme:



The rate and equilibrium stoichiometry of reaction (Scheme 3.3) are controlled by the mole ratio of incoming R'-SH groups to R-S units on the MPCs, their relative steric bulk and R versus R' chainlengths.^{2,12,17} These surface modifications are not straightforward, since the initial MPCs are coated with a monolayer of strongly bound ligands (Au-S bond ~ 50 Kcal/mol).²³ In an attempt to obtain more versatile or ligand-replaceable NPs, Jana and Peng⁷ used weaker ligands (fatty acids or aliphatic amines) and weaker reducing agents (tetrabutylammonium borohydride (TBAB) and hydrazine) in a single-phase system (Figure 3.1-B). The resulting NPs had improved

monodispersity and sizes between 1.5 and 7 nm with TBAB and between 6 and 15 nm with hydrazine. The use of weak ligands (Au-N bond ~ 6 Kcal/mol)²⁶ allowed quite straightforward modification of the Au NPs surface by direct replacement with stronger ligands, such as thiols.²³

A superior method was later reported in which the synthesis of Au NPs of larger sizes (between 6 and 21 nm in diameter) with increased monodispersity (standard deviation $\sigma < 10\%$ in diameter) can be obtained in a one-pot synthesis.⁸ This method is based on the reduction of HAuCl₄ by an organoamine molecule, oleylamine (OLA), which in turn stabilizes the particles formed (Figure 3.1-C). As the amine reduces slowly and bind less strong to the Au surface than thiols, NPs can easily grow larger. The size of the NPs can be readily adjusted by varying the HAuCl₄/OLA stoichiometry,⁸ the reaction temperature^{9,27} or the solvent (and thus, the boiling point temperature).⁸

3.1.2. Phase transfer methods.

There exist a large number of recipes for the synthesis of Au NPs in polar (e.g. water) and non-polar organic solvents. Some advantages from water-based strategies include, for example, the possibility of functionalizing the NPs with a variety of ligand molecules and biomolecules (e.g. DNA, Abs, peptides, etc.). In an organic solution-based synthesis, the formation of NP bioconjugates is not possible, although a higher degree of control in the NP size and monodispersity is obtained, amongst other good quality features. Ideally, the combination of these two strategies would provide a whole range of sizes, shapes and chemical compositions of NPs available in the medium for the required applications. For example, Au NPs synthesized in aqueous phase with labile bound surfactants may be desirable in organic solution for catalytic activities.²⁸ Or oppositely, high quality Au nanocrystals produced in organic phase could be used in water-based biological applications.²⁹ This can be achieved by a phase transfer of the synthesized NPs from their original dispersion medium (water/organic solvent) to a second, non-miscible medium (organic solvent/water) in which the NPs are at first not able to disperse. In the case of NPs, phase transfer is even more challenging due to their large size compared to organic molecules.

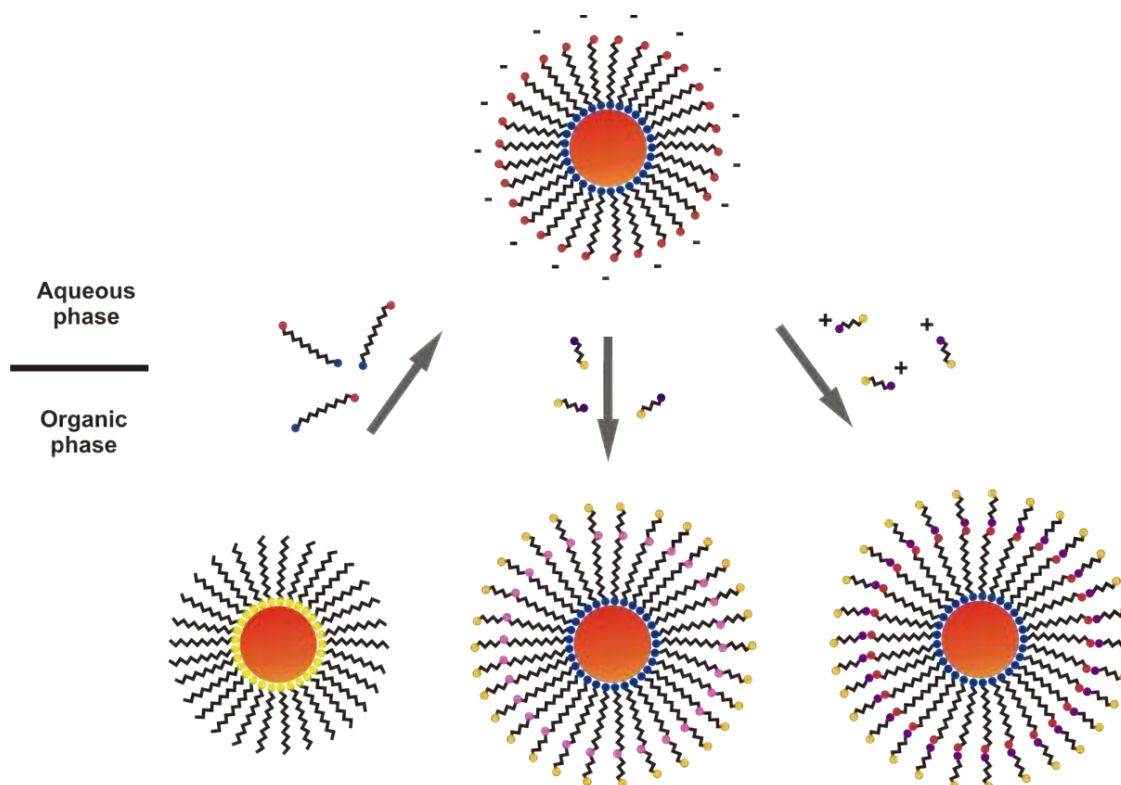


Figure 3.2. Representative scheme of different strategies for phase transfer of Au NPs. Left: ligand place-exchange; the incoming group has one head group (blue) binding the NP surface and a head group e.g. hydrophilic (red) pointing towards solution. Center: ligand modification; the additional ligand has a head group (violet) reacting e.g. covalently with the NP capping ligands and a head group e.g. hydrophobic (yellow) pointing towards solution. Right: addition of coating layers; a layer of molecules is adsorbed by one head group (violet) onto the NP capping ligands by electrostatic interactions, and a head group e.g. hydrophobic (yellow) provide colloidal stability.

Three common approaches for the phase transfer of NPs in the two directions, from aqueous to organic and from organic to aqueous phase, are: i) ligand place-exchange; ii) ligand modification; and iii) addition of coating layers (Figure 3.2). The key step in these approaches is to modify the NPs surface to provide them higher affinity for the desired phase, thus making them highly dispersible in this phase.

Phase transfer by ligand place-exchange reactions consists on modifying the hydrophilicity/hydrophobicity of NPs by replacing the ligand molecules that stabilize them in one phase (e.g. water) by other ligand molecules that allow transferring them to the second phase (e.g. an organic solvent) and their stabilization there (Figure 3.2, left). A prerequisite for the exchange to occur is that the new added ligands must have a higher binding affinity for the Au NPs surface than the original ligand molecules. Commonly used molecules include thiol groups (-SH), which bind strongly to the Au

surface (Au-S \sim 50 Kcal/mol),²³ thus replacing weaker bound ligands (e.g. amine capping ligands⁷ and other thiolated ligands).^{30,31} Alkylamines are also used in phase transfer to replace labile bound molecules, such as citrate.³²

Usually, the phase transfer from organic to aqueous phase occurs spontaneously since the molecules stabilizing the NPs in the aqueous phase (e.g. mercaptoundecanoic acid) are well-soluble in organic solvents. In this case, the place-exchange takes place at the organic phase where the NPs are initially dispersed.²⁹ However, the phase transfer from aqueous to organic phase is often more difficult, due to the poor water solubility of the molecules used to stabilize the NPs in organic phase (e.g. dodecanethiol). Hence, the ligand exchange takes place at the phase boundary.¹¹ In order to facilitate this transfer, various strategies have been used, such as the addition of acetone to decrease the surface tension³³ or a strong acid to neutralize charged NPs.³⁴

Another option is the ligand modification, in which the NPs are rendered hydrophilic/hydrophobic by chemical bonding with the adequate molecules to change their polarity (Figure 3.2, center). In this strategy, the original capping ligands are preserved onto the NPs, and a second layer is attached by chemical bonding, e.g. covalent interactions or complexation. For instance, hydrophilic mercaptoacetic acid functionalized Au NPs have been phase transferred by the incorporation of hydrophobic headgroups through a covalent amide coupling with the carboxy-terminated ligands.³⁵ Another example is the complexation of α -cyclodextrin (α -CD) with octadecanethiol (ODT) molecules rendering the Au NPs hydrophilic, which transferred spontaneously into an organic solvent by dislodging of the α -CD from the ODT molecules during shaking.³⁶

A third strategy is the addition of coating layers, which is based on the adsorption of a molecular layer on the original ligands stabilizing the NPs, thereby conferring a different polarity to the NPs (Figure 3.2, right). The new added layer is usually attached by weak electrostatic or hydrophobic interactions, preserving the native environment from the NPs since their original capping molecules are not replaced. This might be beneficial, for example, to prevent sensitive core materials from oxidation. A case study from Mayya *et al.*³⁷ used alkylamines to transfer Au NPs (6 and 12 nm in size) from an aqueous to an organic solution. These ligands interacted with the carboxylate and

sulfonate moieties on the Au NPs via acid-base pair formation, forming a hydrophobic layer that facilitated their transfer to organic phase. Other variations used quaternary ammonium salts (e.g. TOAB), which contain a hydrophobic part readily soluble in the organic phase and a hydrophilic part that interacts with the ligands on the surface of the NPs. Examples include the transfer of Au NPs bearing negatively charged carboxylate groups (e.g. mercaptosuccinic acid,^{38,39} glutathione³⁷ and N-(2-mercaptopropionyl)-glycine)³⁷ to organic solvents by electrostatic interaction with TOA⁺ molecules. This strategy was also employed for the transfer of dodecylamine-capped Au NPs to water by CTAB, which adsorbed onto the NPs and stabilized them in water by its positively charged ammonium moiety.⁴⁰ Other coating layers for the phase transfer of NPs are based on amphiphilic polymers^{41,42} or silica.^{43,44} Further reading can be found on some excellent reviews focused on the phase transfer of nanocrystals.^{45,46}

3.2. Results and discussion

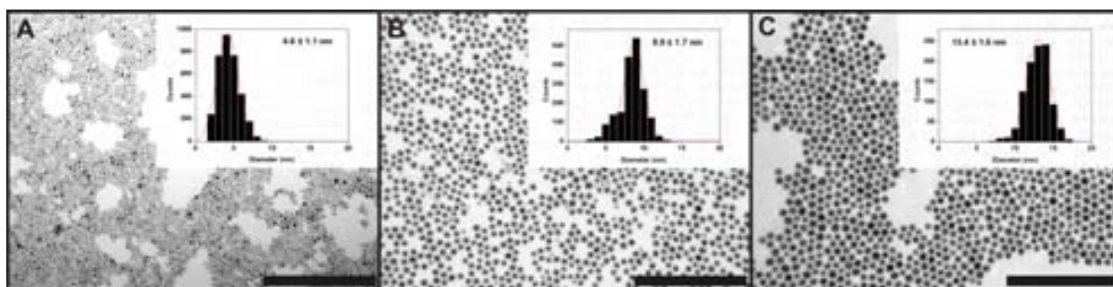
In this Chapter, the optimization of a phase-transfer methodology has allowed the successful preparation of cationic Au NPs with a variety of sizes, narrow size distributions and very high concentrations (e.g. concentrations of 3-4 mM of 13 nm NPs) in aqueous solution. This strategy takes advantage of well-known organic synthetic methods, in which the Au NPs are first synthesized. Then, intermediate transfer agents and solvents are employed in a precise sequence for an adequate phase transfer. As state above, AUT was chosen as a case model ligand to optimize the synthetic procedure, which was then successfully applied for the conjugation of two identical peptidic biomolecules terminating in either positive (NH₃⁺) or negative (COO⁻) charged groups (Chapter 4).

3.2.1. Preparation and characterization of Au NPs in the organic phase.

Different sizes of Au NPs (4, 8 and 13 nm) were initially synthesized in toluene and in the presence of alkylamine surfactants. The choice of these particle sizes was based on size-dependence studies reported in the literature, where phase transfer was 100 % successful for ~ 5 nm Au NPs but not for ~ 10 nm Au NPs, which accumulated at the

liquid-liquid interface and aggregated immediately.⁴⁷ The synthesis of 4 nm Au NPs was carried out by following the Brust-Schiffrin¹¹ protocol by NaBH_4 reduction in the presence of dodecylamine (Figure 3.3-A). Au NPs of 8 and 13 nm in diameter were prepared using oleylamine as both the reducer and surfactant simultaneously (Figure 3.3-B,C).⁹ Alternatively, 4 nm Au NPs were also firstly synthesized in aqueous phase upon NaBH_4 reduction in the presence of sodium citrate,⁴⁸ and then transferred into toluene using the amphiphilic ligand TOAB (Figure 3.3-D). Morphological analysis showed higher monodispersity of the Au NPs synthesized in organic phase when compared with aqueous synthetic routes. Further physicochemical characterization by UV-vis spectroscopy and DLS indicated a good stability of the resulting colloids (see below, Figure 3.5 and Table 3.1). All Au NPs were finally purified by eliminating the excess of the reagents remaining from the syntheses by centrifugation, and subsequently resuspended into more polar solvents such as chloroform (CHCl_3).

i) Synthesis in organic phase



ii) Synthesis in aqueous phase

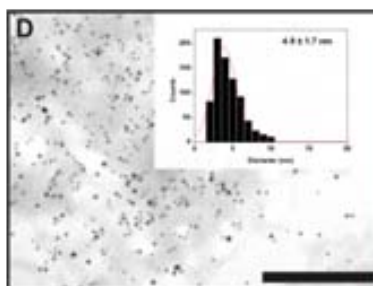


Figure 3.3. A-C) Representative TEM images of as-synthesized Au NPs in organic solvents; from left to right: 4.6 ± 1.1 nm dodecylamine-capped Au NPs in toluene, 8.9 ± 1.7 nm OLA-capped Au NPs in toluene, 13.4 ± 1.6 nm OLA-capped Au NPs in toluene. D) Representative TEM images of the synthesized Au NPs in aqueous phase after phase transfer to toluene; 4.9 ± 1.7 nm TOAB-Au NPs in toluene. Scale bars are 200 nm.

3.2.2. Phase transfer with a cationic alkanethiolate ligand.

The current study deals first with the use of an alkylamine as both a weaker reducer for Au^{+3} precursor and a rather soft binding surfactant, so that NPs are produced under mild conditions. Then, the replacement at the interphase of alkylamine surfactants by aqueous-soluble thiol-containing ligands, which render hydrophilicity to the final NP conjugate, facilitates its transfer into the aqueous phase (Figure 3.4-A). This methodology overcomes the difficulties encountered in place-exchange reactions with alkanethiolate monolayers (see Section 3.1.1).^{1,2}

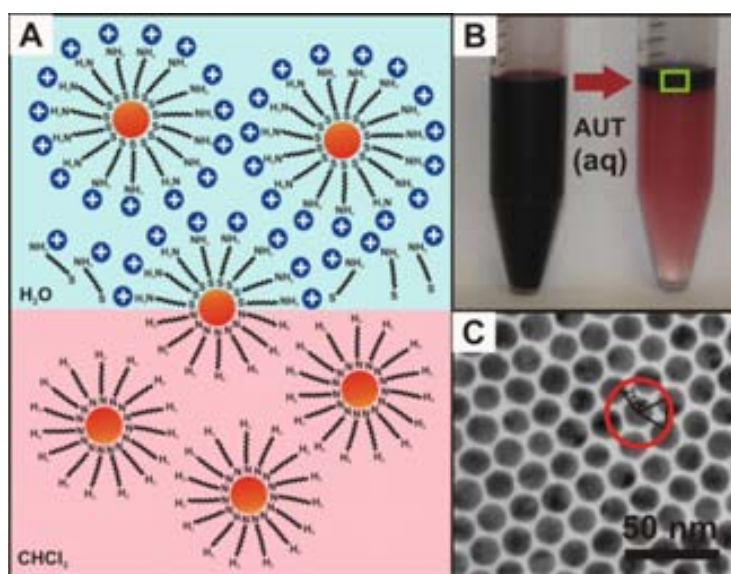


Figure 3.4. A) Schematic representation of the phase-transfer mechanism for the preparation of cationic Au NPs (drawn not to scale). B) View of highly concentrated Au NPs (~ 13 nm) suspended in chloroform (left) and after phase-transfer into an aqueous solution using AUT (right); inset of the cationic Au NPs. C) Representative TEM image of the cationic Au NPs in water showing a highly ordered compact hexagonal packing.

Initial studies were carried out with AUT, an aminoalkanethiol with a positive charge at neutral pH. As shown in Figure 3.4-B, Au NPs of ~ 13 nm in diameter could be successfully transferred from CHCl_3 into water by adding AUT at neutral pH, which led up to 15-fold concentrated samples (e.g. 3-4 mM of NPs). Such high concentrations are generally difficult to obtain by aqueous synthetic methods. For example, the traditional Turkevich-Frens^{49,50} method yields concentrations of ~ 2.6 nM of 17 nm NPs. Further concentration of these citrate-capped Au NPs requires tedious centrifugation steps, which may also induce aggregation effects. In addition, high

concentrations are desirable, since an effective dosage of Au NPs for cellular uptake studies is found for 5-6 nM of NPs,^{51,52} in which the NPs are incubated at a dilution factor of 5-10 to the cell culture media. TEM analysis of the cationic AUT-functionalized Au NPs in water showed similarity in particle size and size distribution in comparison to as-synthesized NPs (Figure 3.4-C), together with no sign of aggregation.

Surface functionalization of the Au NPs with AUT was followed by variations of the surface plasmon resonance (SPR) peak (Figure 3.5 and Table 3.1), whose absence of broadening further confirmed the stability of NPs after the phase transfer process. In most of the cases, a **blue-shift** about ~ 3 nm of the SPR peak was observed after phase transfer. This shift was indicative of a modification of the surface environment of the NP, probably as a consequence of the replacement of capping ligands. Only in the case of dodecylamine-capped Au NPs (4 nm, synthesized in organic phase), no significant variation of the SPR absorption peak was observed. This behaviour may be attributed to the similarity of the object before and after phase transfer. That is, both dodecylamine and AUT ligands may form a compact monolayer on the Au NP surface, whereas other bulkier ligands (e.g. OLA and TOAB) do not.

Hydrodynamic diameter measurements by DLS indicated a slight variation of $\sim 2 - 4$ nm in diameter in all the cases, which is due to the surface functionalization but also to the different nature of the solvents and the subsequent double layer formed. The positive surface charge of the conjugates (ζ -potential values between +23.6 and +45.6 mV) confirmed the new cationic coating of the NPs. In addition, the successful re-functionalization of Au NPs after the phase transfer process was demonstrated by FTIR spectroscopy, which is analyzed in Chapter 4 for the functionalization with cationic and anionic peptides (Figure 4.8). In those results, a proper elimination of the OLA capping molecules was observed.

The efficiency of the phase transfer was evaluated by employing different concentrations of AUT, both under a 0.5 molar defect over the estimated NPs complete

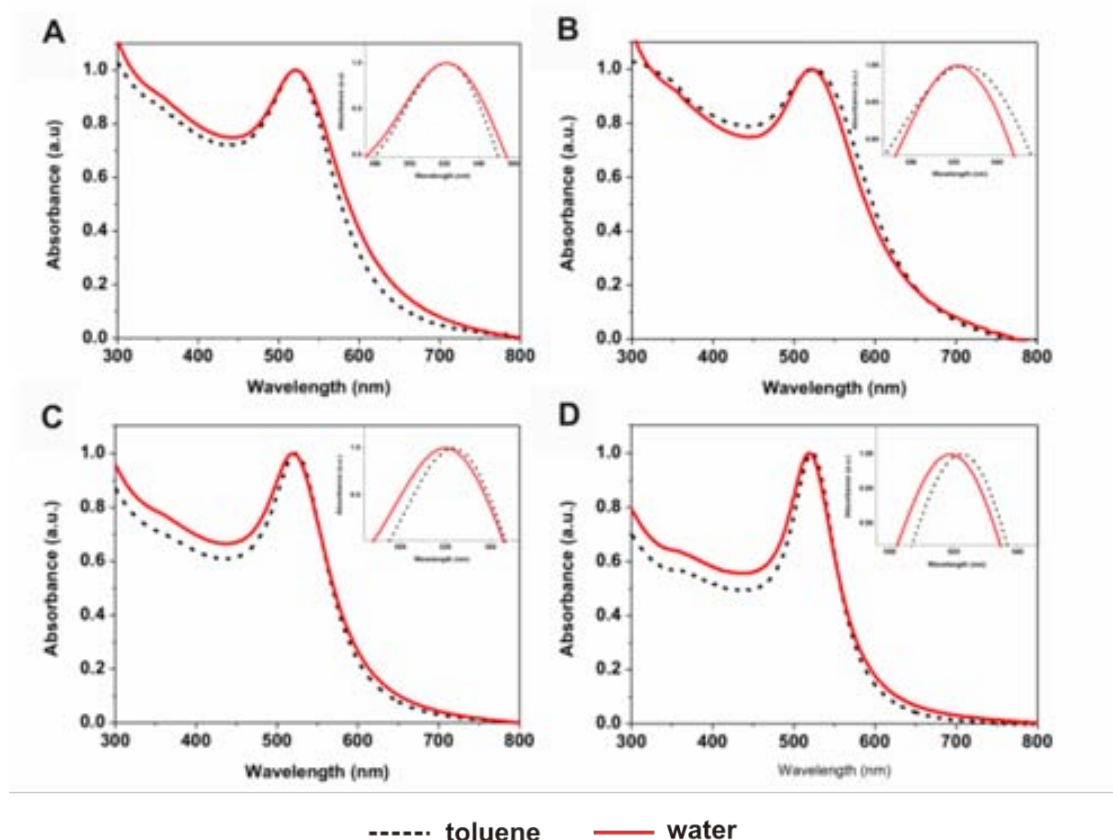


Figure 3.5. Normalized UV-vis absorption spectra of Au NPs before (dashed black line) and after phase transfer with AUT ligand (red line) employing different types of Au NPs: A) 4.6 ± 1.1 nm dodecylamine-capped Au NPs in toluene; B) 4.9 ± 1.7 nm TOAB-Au NPs in toluene after phase-transfer from aqueous solvent; C, D) OLA-capped Au NPs of 8.9 ± 1.7 nm and 13.4 ± 1.6 nm, respectively, in toluene.

Sample	λ_{\max} (nm)		Hydrodynamic Diameter in nm (Pdl)		ζ -Potential in mV (std. dev. in mV)
	before	after	before	after	after
Au NP (4 nm)	521.0	521.0	9.2 (0.2)	7.6 (0.5)	+43.0 (10.0)
Au NP (4 nm) aqueous	525.5	522.0	14.5 (0.5)	10.9 (0.5)	+23.6 (13.0)
Au NP (8 nm)	523.0	520.0	9.8 (0.2)	11.9 (0.8)	+45.6 (8.4)
Au NP (13 nm)	523.0	519.0	11.1 (0.2)	14.1 (0.5)	+24.3 (8.4)

Table 3.1. UV-vis wavelength of absorption maximum, number size by DLS and ζ -potential values of Au NPs transferred from CHCl_3 (before) into aqueous phase (after) with AUT.

coverage, and also under 1, 5 and 10-fold molar excess of AUT (Figure 3.6-A). In all cases, the Au NPs transferred well, but a defect of ligand made the NPs to immediately aggregate in the aqueous phase, as observed in the UV-vis absorbance spectra. This aggregation is probably due to the poor stabilization of the NP surface caused by the incomplete coating of the surface. A successful phase transfer to the aqueous layer was also obtained from Au NPs (~ 13 nm) dispersed in a set of different organic solvents (toluene, dichloromethane (DCM) and tetrahydrofuran (THF)) (Figure 3.6-B).

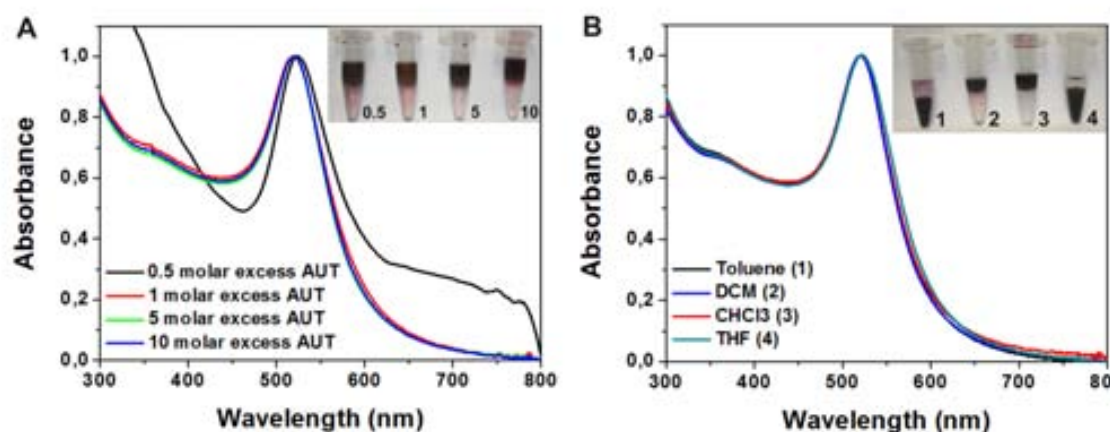


Figure 3.6. A) Normalized UV-vis absorption spectra of Au NPs (~ 13 nm) after phase transfer from chloroform into water and surface functionalization using 0.5, 1, 5 and 10-fold molar excess of AUT. (Inset) Images showing the phase transferred NPs. B) Normalized UV-vis absorption spectra of Au NPs (~ 13 nm) after phase transfer from a variety of solvents (toluene, DCM, CHCl_3 and THF) and surface functionalization using 50-fold molar excess of AUT. (Inset) Images showing the phase transferred NPs.

3.3. Conclusions.

A phase transfer methodology has been optimized in which alkylamines are used first to produce Au NPs in the organic phase, and the subsequent replacement of these ligands at the organic-aqueous liquid interface by a thiol-containing ligand (AUT) facilitates the transfer of NPs into the aqueous phase, even for NPs larger than 10 nm. This method has shown a great feasibility to yield functionalized positive Au NPs of different sizes (4, 8 and 13 nm) and high monodispersity. Other potential benefit from this strategy is that high concentrations of Au NPs are obtained by organic synthetic

routes, which in turn, can be increased in the phase transfer step. Such high concentration of cationic Au NPs might be greatly desirable, especially in the case of cell delivery where a high dosage of NPs is normally required. Finally, as opposite to the other existing methods, it can be applied to a wide range of sizes (we note that more organic synthetic methods should be explored) and it overcomes the aggregation difficulties observed for the conjugation of positively charged ligands in the presence of negatively charged stabilizers, such as citrate, especially critical in the case of Au.

3.4. References.

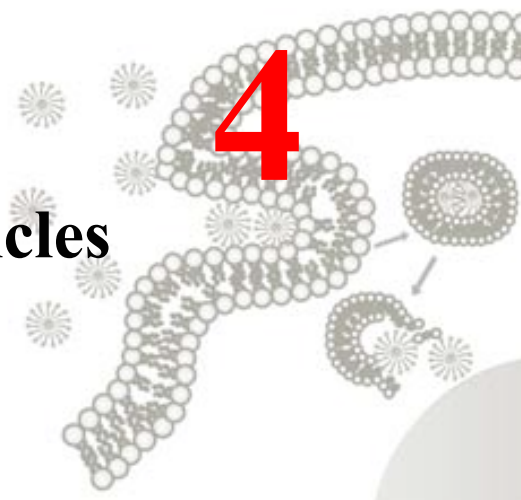
1. Badia, A.; Cuccia, L.; Demers, L.; Morin, F.; Lennox, R. B. *Structure and Dynamics in Alkanethiolate Monolayers Self-Assembled on Gold Nanoparticles: A DSC, FT-IR, and Deuterium NMR Study*. *J. Am. Chem. Soc.*, **1997**, 119, 2682-2692.
2. Hostetler, M. J.; Templeton, A. C.; Murray, R. W. *Dynamics of Place-Exchange Reactions on Monolayer-Protected Gold Cluster Molecules*. *Langmuir*, **1999**, 15, 3782-3789.
3. Ojea-Jimenez, I.; Puentes, V. *Instability of Cationic Gold Nanoparticle Bioconjugates: The Role of Citrate Ions*. *J. Am. Chem. Soc.*, **2010**, 132, 5322-5322.
4. Schmid, G.; Klein, N.; Korste, L.; Kreibitz, U.; Schönauer, D. *Large Transition Metal Clusters—VI. Ligand Exchange Reactions on $Au_{55}(PPh_3)_{12}Cl_6$ —the Formation of a Water Soluble Au_{55} Cluster*. *Polyhedron*, **1988**, 7, 605-608.
5. Weare, W. W.; Reed, S. M.; Warner, M. G.; Hutchison, J. E. *Improved Synthesis of Small ($d_{CORE} \approx 1.5$ nm) Phosphine-Stabilized Gold Nanoparticles*. *J. Am. Chem. Soc.*, **2000**, 122, 12890-12891.
6. Petroski, J.; Chou, M. H.; Creutz, C. *Rapid Phosphine Exchange on 1.5-nm Gold Nanoparticles*. *Inorg. Chem.*, **2004**, 43, 1597-1599.
7. Jana, N. R.; Peng X. *Single-Phase and Gram-Scale Routes toward Nearly Monodisperse Au and Other Noble Metal Nanocrystals*. *J. Am. Chem. Soc.*, **2003**, 125, 14280-14281.
8. Hiramatsu, H.; Osterloh, F. E. *A Simple Large-Scale Synthesis of Nearly Monodisperse Gold and Silver Nanoparticles with Adjustable Sizes and with Exchangeable Surfactants*. *Chem. Mater.*, **2004**, 16, 2509-2511.
9. Shen, C.; Hui, C.; Yang, T.; Xiao, C.; Tian, J.; Bao, L.; Chen, S.; Ding, H.; Gao, H. *Monodisperse Noble-Metal Nanoparticles and Their Surface Enhanced Raman Scattering Properties*. *Chem. Mater.*, **2008**, 20, 6939-6944.
10. Manea, F.; Bindoli, C.; Polizzi, S.; Lay, L.; Scrimin, P. *Expedition Synthesis of Water-Soluble, Monolayer-Protected Gold Nanoparticles of Controlled Size and Monolayer Composition*. *Langmuir*, **2008**, 24, 4120-4124.

11. Brust, M.; Walker, M.; Bethell, D.; Schiffrin, D. J.; Whyman, R. *Synthesis of Thiol-Derivatised Gold Nanoparticles in a Two-Phase Liquid-Liquid System*. J. Chem. Soc., Chem. Commun., **1994**, 801-802.
12. Ingram, R. S.; Hostetler, M. J.; Murray, R. W. *Poly-hetero- ω -functionalized Alkanethiolate-Stabilized Gold Cluster Compounds*. J. Am. Chem. Soc., **1997**, 119, 9175-9178.
13. Badia, A.; Gao, W.; Singh, S.; Demers, L.; Cuccia, L.; Reven, L. *Structure and Chain Dynamics of Alkanethiol-Capped Gold Colloids*. Langmuir, **1996**, 12, 1262-1269.
14. Schmid, G.; Pfeil, R.; Boese, R.; Bandermann, F.; Meyer, S.; Calis, G. H. M.; van der Velden, J. W. A. Au₅₅[P(C₆H₅)₃]₁₂Cl₆ - ein Goldcluster ungewöhnlicher Größe. Chem. Ber., **1981**, 114, 3634-3642.
15. Giersig, M.; Mulvaney, P. *Preparation of Ordered Colloid Monolayers by Electrophoretic Deposition*. Langmuir, **1993**, 9, 3408-3413.
16. Faraday, M. *Experimental Relations of Gold (and Other Metals) to Light*. Philos. Trans. R. Soc. London, **1857**, 147, 145-181.
17. Templeton, A. C.; Wuelfing, W. P.; Murray, R. W. *Monolayer-Protected Cluster Molecules*. Acc. Chem. Res., **1999**, 33, 27-36.
18. Goulet, P. J. G.; Lennox, R. B. *New Insights into Brust-Schiffrin Metal Nanoparticle Synthesis*. J. Am. Chem. Soc., **2010**, 132, 9582-9584.
19. Leff, D. V.; Ohara, P. C.; Heath, J. R.; Gelbart, W. M. *Thermodynamic Control of Gold Nanocrystal Size: Experiment and Theory*. J. Phys. Chem., **1995**, 99, 7036-7041.
20. Hostetler, M. J.; Wingate, J. E.; Zhong, C-J.; Harris, J. E.; Vachet, R. W.; Clark, M. R.; Londono, J. D.; Green, S. J.; Stokes, J. J.; Wignall, G. D.; Glish, G. L.; Porter, M. D.; Evans, N. D.; Murray, R. W. *Alkanethiolate Gold Cluster Molecules with Core Diameters from 1.5 to 5.2 nm: Core and Monolayer Properties as a Function of Core Size*. Langmuir, **1998**, 14, 17-30.
21. Whetten, R. L.; Khoury, J. T.; Alvarez, M. M.; Murthy, S.; Vezmar, I.; Wang, Z. L.; Stephens, P. W.; Cleveland, C. L.; Luedtke, W. D.; Landman, U. *Nanocrystal Gold Molecules*. Adv. Mater., **1996**, 8, 428-433.
22. Schaaff, T. G.; Shafigullin, M. N.; Khoury, J. T.; Vezmar, I.; Whetten, R. L.; Cullen, W. G.; First, P. N.; Gutiérrez-Wing, C.; Ascensio, J.; Jose-Yacamán, M. J. *Isolation of Smaller Nanocrystal Au Molecules: Robust Quantum Effects in Optical Spectra*. J. Phys. Chem. B, **1997**, 101, 7885-7891.
23. Love, J. C.; Estroff, L. A.; Kriebel, J. K.; Nuzzo, R. G.; Whitesides, G. M. *Self-Assembled Monolayers of Thiolates on Metals as a Form of Nanotechnology*. Chem. Rev., **2005**, 105, 1103-1170.
24. Porter, L. A.; Ji, D.; Westcott, S. L.; Graupe, M.; Czernuszewicz, R. S.; Halas, N. J.; Lee, T. R. *Gold and Silver Nanoparticles Functionalized by the Adsorption of Dialkyl Disulfides*. Langmuir, **1998**, 14, 7378-7386.
25. Johnson, S. R.; Evans, S. D.; Brydson, R. *Influence of a Terminal Functionality on the Physical Properties of Surfactant-Stabilized Gold Nanoparticles*. Langmuir, **1998**, 14, 6639-6647.

26. Di Felice, R.; Selloni, A. *Adsorption Modes of Cysteine on Au(111): Thiolate, Amino-Thiolate, Disulfide*. J. Chem. Phys., **2004**, 120, 4906-4914.
27. Pyrpassopoulos, S.; Niarchos, D.; Nounesis, G.; Boukos, N.; Zafiropoulou, I.; Tzitzios, V. *Synthesis and Self-Organization of Au Nanoparticles*. Nanotechnol., **2007**, 18, 485604.
28. Bonnemann, H.; Brinkmann, R.; Neiteler, P. *Preparation and Catalytic Properties of NR_4^+ -Stabilized Palladium Colloids*. Appl. Organomet. Chem., **1994**, 8, 361-378.
29. Gittins, D. I.; Caruso, F. *Biological and Physical Applications of Water-Based Metal Nanoparticles Synthesised in Organic Solution*. Chem. Phys. Chem., **2002**, 3, 110-113.
30. Templeton, A. C.; Hostetler, M. J.; Warmoth, E. K.; Chen, S.; Hartshorn, C. M.; Krishnamurthy, V. M.; Forbes, M. D. E.; Murray, R. W. *Gateway Reactions to Diverse, Polyfunctional Monolayer-Protected Gold Clusters*. J. Am. Chem. Soc., **1998**, 120, 4845-4849.
31. Simard, J.; Briggs, C.; Boal, A. K.; Rotello, V. M. *Formation and pH-Controlled Assembly of Amphiphilic Gold Nanoparticles*. Chem. Commun., **2000**, 1943-1944.
32. Karg, M.; Schelero, N.; Oppel, C.; Gradzielski, M.; Hellweg, T.; von Klitzing, R. *Versatile Phase Transfer of Gold Nanoparticles from Aqueous Media to Different Organic Media*. Chem. Eur. J., **2011**, 17, 4648-4654.
33. Gaponik, N.; Talapin, D. V.; Rogach, A. L.; Eychmüller, A.; Weller, H. *Efficient Phase Transfer of Luminescent Thiol-Capped Nanocrystals: From Water to Nonpolar Organic Solvents*. Nano Lett., **2002**, 2, 803-806.
34. Sarathy, K. V.; Kulkarni, G. U.; Rao, C. N. R. *A Novel Method of Preparing Thiol-Derivatised Nanoparticles of Gold, Platinum and Silver Forming Superstructures*. Chem. Commun., **1997**, 537-538.
35. McMahon, J. M.; Emory, S. R. *Phase Transfer of Large Gold Nanoparticles to Organic Solvents with Increased Stability*. Langmuir, **2006**, 23, 1414-1418.
36. Lala, N.; Lalbegi, S. P.; Adyanthaya, S. D.; Sastry, M. *Phase Transfer of Aqueous Gold Colloidal Particles Capped with Inclusion Complexes of Cyclodextrin and Alkanethiol Molecules into Chloroform*. Langmuir, **2001**, 17, 3766-3768.
37. Mayya, K. S.; Caruso, F. *Phase Transfer of Surface-Modified Gold Nanoparticles by Hydrophobization with Alkylamines*. Langmuir, **2003**, 19, 6987-6993.
38. Chen, S.; Yao, H.; Kimura, K. *Reversible Transference of Au Nanoparticles across the Water and Toluene Interface: A Langmuir Type Adsorption Mechanism*. Langmuir, **2001**, 17, 733-739.
39. Yao, H.; Momozawa, O.; Hamatani, T.; Kimura, K. *Stepwise Size-Selective Extraction of Carboxylate-Modified Gold Nanoparticles from an Aqueous Suspension into Toluene with Tetraoctylammonium Cations*. Chem. Mater., **2001**, 13, 4692-4697.
40. Swami, A.; Kumar, A.; Sastry, M. *Formation of Water-Dispersible Gold Nanoparticles Using a Technique Based on Surface-Bound Interdigitated Bilayers*. Langmuir, **2003**, 19, 1168-1172.

41. Pellegrino, T.; Manna, L.; Kudera, S.; Liedl, T.; Koktysh, D.; Rogach, A. L.; Keller, S.; Rädler, J.; Natile, G.; Parak, W. J. *Hydrophobic Nanocrystals Coated with an Amphiphilic Polymer shell: a General Route to Water Soluble Nanocrystals*. *Nano Lett.*, **2004**, *4*, 703-707.
42. Muir, B. W.; Moffat, B. A.; Harbour, P.; Coia, G.; Zhen, G.; Waddington, L.; Scoble, J.; Krah, D.; Thang, S. H.; Chong, Y. K.; Mulvaney, P.; Hartley, P. *Combinatorial Discovery of Novel Amphiphilic Polymers for the Phase Transfer of Magnetic Nanoparticles*. *J. Phys. Chem. C*, **2009**, *113*, 16615-16624.
43. Mulvaney, P.; Liz-Marzan, L. M.; Giersig, M.; Ung, T. *Silica Encapsulation of Quantum Dots and Metal Clusters*. *J. Mater. Chem.*, **2000**, *10*, 1259-1270.
44. Jana, N. R.; Earhart, C.; Ying, J. Y. *Synthesis of Water-Soluble and Functionalized Nanoparticles by Silica Coating*. *Chem. Mater.*, **2007**, *19*, 5074-5082.
45. Sastry, M. *Phase Transfer Protocols in Nanoparticle Synthesis*. *Curr. Sci.*, **2003**, *85*, 1735-1745.
46. Yang, J.; Lee, J. Y.; Ying, J. Y. *Phase Transfer and its Applications in Nanotechnology*. *Chem. Soc. Rev.*, **2011**, *40*, 1672-1696.
47. Cheng, W.; Wang, E. *Size-Dependent Phase Transfer of Gold Nanoparticles from Water into Toluene by Tetraoctylammonium Cations: A Wholly Electrostatic Interaction*. *J. Phys. Chem. B*, **2003**, *108*, 24-26.
48. Jana, N. R.; Gearheart, L.; Murphy, C. J. *Seeding Growth for Size Control of 5–40 nm Diameter Gold Nanoparticles*. *Langmuir*, **2001**, *17*, 6782-6786.
49. Turkevich, J.; Stevenson, P. C.; Hillier, J. *A Study of the Nucleation and Growth Processes in the Synthesis of Colloidal Gold*. *Discuss. Farad. Soc.*, **1951**, *11*, 55-75.
50. Frens, G. *Controlled Nucleation For Regulation of Particle Size in Monodisperse Gold Suspensions*. *Nat. Phys. Sci.*, **1973**, *241*, 20–22.
51. Nativo, P.; Prior, I. A.; Brust, M. *Uptake and Intracellular Fate of Surface-Modified Gold Nanoparticles*. *ACS Nano*, **2008**, *2*, 1639-1644.
52. Krpetić, Ž.; Saleemi, S.; Prior, I. A.; Sée, V.; Qureshi, R.; Brust, M. *Negotiation of Intracellular Membrane Barriers by TAT-Modified Gold Nanoparticles*. *ACS Nano*, **2011**, *5*, 5195-5201.

Bioconjugation of Cationic Peptides to Gold Nanoparticles for Cell Penetration



The ability of the cationic character to affect cellular uptake of a macromolecule has been known for many decades.¹ During the last ten years, this concept has been harnessed and applied to the development of NPs for intracellular delivery. As positively charged NPs interact with the negatively charged lipidic bilayer (membrane) of cells, they have the greatest efficiency in cell-membrane penetration and cellular internalization.^{2,3} Today, cationic Au NPs form the primary platform as synthetic carriers for drug and gene delivery. Some aspects such as their potential cytotoxicity⁴⁻⁶ and their modes of internalization,^{2,3,7,8} have become crucial topics of study associated with the biomedical application of these NPs. The importance of the colloidal stability of NPs during the biological studies^{9,10} and their interaction with serum proteins¹¹⁻¹⁴ has also been recognized, especially in the case of cationic NPs.^{9,11a}

Therefore, a great deal of effort is being made to better understand how cationic Au NPs interact with cells. Today, a remaining general shortcoming is the lack of generic protocols for the preparation of a rich catalog of cationic Au NPs with different sizes and functionalities. In the present Chapter, a phase transfer methodology (see Chapter 3) is proposed as a general approach for the synthesis of highly water-stable cationic Au NP bioconjugates of up to 13 nm core size. This NP size was particularly challenging, owing to the synthetic difficulties normally encountered by other methods (see Chapter 2, Section 2.1). Two peptidic biomolecules, bearing positive and negatively charged functional end groups, were used as a proof-of-concept of the phase transfer methodology. The effect of the surface charge of these Au NP bioconjugates was investigated in the cellular uptake on human fibroblast cells (1BR3G).

4.1. Introduction. Role of cationic charge in Au NPs internalization by cells.

This introduction aims to provide a brief research trajectory of the cation-mediated transport of Au NPs into cells, a discussion of their properties in extracellular media and an overview of the efforts done so far to determine their mechanism of cellular uptake.

4.1.1. Origins of cationic cellular uptake.

The potential of cationic molecules to enhance the uptake of macromolecules by cells has been well known for nearly 50 years. One of the earliest theories for targeting cancer cells involved the use of positively-charged polymers to deliver drugs.¹ This discovery gave birth to a new field of cationic drug delivery. Early work during the 60's and 70's demonstrated an increased uptake of proteins and small molecules by their complexation with cationic proteins (e.g. histone)¹⁵ or polyamino acids (e.g. polylysine, polyarginine and polyhistidine).¹⁵ However, the existing number of natural cationic molecules and macromolecules capable of cellular entry is rather small, so chemical cationization opened up new possibilities already in the 90's.¹⁶ In the same decade, the discovery of CPPs, short cationic peptides that are able to translocate the cell membrane without disruption, was the objective of many investigations. Some examples of CPPs that have been described include Tat, SAP, transportan, and polyarginines. For a more detailed description, the reader is referred to several interesting reviews on this topic.^{17,18}

Since then, many other studies have demonstrated the importance of the cationic character. For example, the complexation and transport of negatively charged DNA has been studied using a variety of systems, including peptides,¹⁹ liposomes with cationic lipids,²⁰ cationic polymers such as PEI²¹ or poly(L-lysine),²² poly(amidoamine) (PAMAM) dendrimers²³ and silica particles.²⁴ Rotello and co-workers²⁵ were the first to use cationic Au NPs as scaffolds for DNA binding, due to their charge-based interaction with the negatively charged DNA, demonstrating their transfection ability into a cultivated cell line.²⁶ This study revitalized the field of cation-mediated delivery and brought focus to cationic Au NPs as potential vehicles for macromolecular delivery.

Initially, Rotello and co-workers focused on the use of 2-nm-core cationic AuNPs as delivery vehicles for DNA.^{25,26} They found that these NPs were effective transfection agents, although having a major drawback of potential toxicity.⁴ This fact was attributed to the quaternary cationic ammonium moieties of the NPs, which interacted with the negatively charged bilayer of cells by promoting passive internalization of NPs and vesicle disruption.^{27,28} To improve the biocompatibility of these systems, they synthesized Au NPs featuring cationic amino acid headgroups.^{29,30} Amongst them, the NPs containing lysine residues showed to be a much more effective delivery vehicle with no concomitant toxicity. This was an important finding, since in that case the toxicity was proved to be dependent on the chemistry of the surface functional groups rather than directly related to their cationic character. We note that the chemical polarity, protein affinity, bioactivity, redox properties and other features from the NP surface, combined with surface charge (and local charge distribution) might be responsible for the observed biological effects.

Following studies exploited the use of cationic Au NPs as DNA transfection agents. To date, Niidome *et al.*³¹ employed aminoethanethiol-capped Au NPs of approximately 33 nm in diameter, showing a high transfection efficiency. Another study by Li *et al.*³² showed the potential use of cationic lipid-coated Au NPs of 14 nm in size for transfection. They also contributed elucidating the intracellular trafficking route of the DNA-Au NP bioconjugates by electron microscopy. The validity of these studies, however, may be questioned by the high polydispersity of their cationic Au NPs (see Chapter 2, Section 2.1). This may probably lead to confusing results (e.g. more than one internalization pathway or different cellular fates), since the interaction of NPs with biomolecules and cells is size dependent.^{33,34}

Similarly, cationic PEI-capped Au NPs of 15 nm in diameter were applied for complexation with negatively charged small interfering RNA (siRNA).³⁵ PEI-capped Au NPs mediated effective siRNA delivery, and resulted in remarkably efficient gene silencing in MDA-MB-435s (human breast carcinoma) cells when compared with PEI. Again, the excellent biological results were in contrast with the poor quality of the NPs and their characterization; the intrinsic polydispersity of the NPs could be clearly detected in TEM images.

In a recent work, Cho *et al.*² investigated the cellular uptake of polymer-coated cationic Au NPs of 17.7 ± 1.6 nm in diameter. Their studies showed that neutral and negatively charged Au NPs (*i.e.* citrate- and PVA-coated Au NPs) display a low affinity to interact with the cell membrane, whereas positively charged Au NPs (*i.e.* PAA-coated Au NPs) have a high cell-membrane binding affinity (Figure 4.1). These results further confirm the effect of the cationic character on the enhanced internalization of Au NPs. However, the toxicity tests carried out were not very realistic since an extremely low concentration was used (*i.e.* 0.027 nM of NPs) when comparing with similar studies (*i.e.* 5-6 nM of NPs).^{36,37} In this regard, it is well-known that the toxicity of NPs is dose-dependent.³⁸ In fact, already in the XVI century, Paracelso reached the conclusion that everything is poison and nothing is poison, *sola dosis facit venenum*.

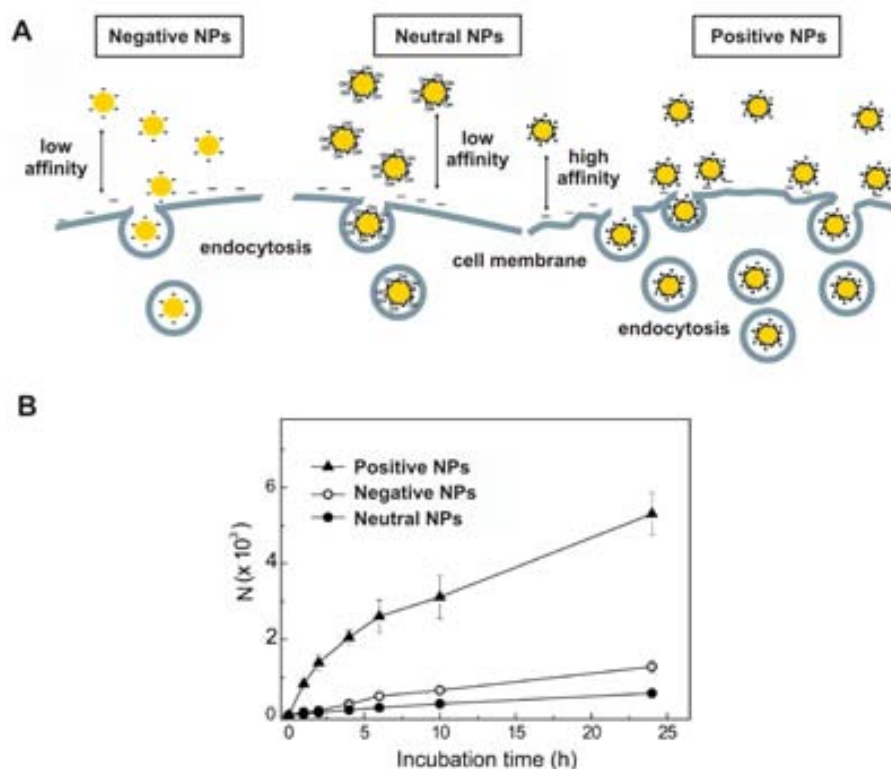


Figure 4.1. A) Schematics illustrating the interactions between Au NPs with different surface charges and SK-BR-3 cells. B) Time dependent profile for the uptake of Au NPs with different surface charges by SK-BR-3 cells. N is the number of Au NPs per cell. Image adapted from ref. 2.

Very recently, the use of cationic NPs for the delivery of proteins has also been investigated.³⁹ Specifically, cationic peptide-capped Au NPs (2.5 nm in diameter) using

a tetraethyleneglycol (TEG) linker to prevent protein denaturation were used for intracellular delivery of β -galactosidase (β -gal) (Figure 4.2-A); a challenging anionic, large size protein (465 kD). At first, the cationic Au NPs interacted with the anionic β -gal forming stable complexes. Then, the internalization of these complexes was favored by the electrostatic interactions of the peptide headgroup, composed of arginine, lysine and histidine residues, with the plasma membrane. Next, a potential escape from endosomes by the proton sponge imidazole group of histidine was suggested. And finally, the observed free delivery of β -gal into the cytosol (Figure 4.2-C) and concomitant restoration of its activity (Figure 4.2-B), was attributed to a ligand-place exchange procedure on the surface of the NPs by glutathione,⁴⁰ the main thiol component of the cell (concentration of approximately 5 mM in animal cells).

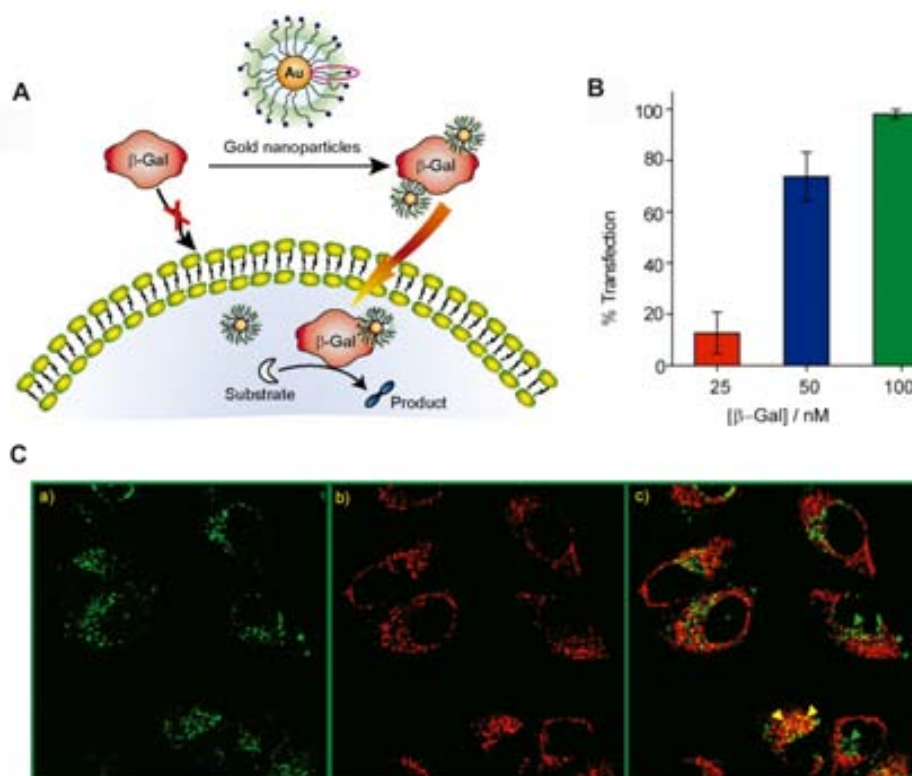


Figure 4.2. A) Schematic representation of the intracellular delivery of functional protein using cationic peptide-capped Au NPs. B) Dose-dependent protein delivery into HeLa cells at 2:1 NP / β -gal. C) Colocalization study using confocal laser scanning microscopy (CLSM) after protein transfection, at 2:1 NP / β -gal, of HeLa cells in the presence of FM 4-64 (a red endosome specific marker); (a, left) green fluorescence from FITC- β -gal, (b, center) red fluorescence from FM 4-64, and (c, right) overlap of the green and the red channels. In the merged image, green spots (shown with green arrowheads) are indicating proteins outside endosomes, while entrapped proteins inside endosomes appear as yellow dots (shown with yellow arrowheads). Image adapted from ref. 39.

4.1.2. Physicochemical properties of cationic NPs in the extracellular media.

When NPs enter biological fluids (e.g. cell culture media, CCM), their integrity can be compromised by the high ionic strength and the dense layer of proteins surrounding the NP surface.^{9,11} This may cause changes in the colloidal stability of the NPs and/or their physicochemical properties, which may fool analysis and ultimately vary the outcome of the intended biological applications. In addition, the NPs composition/surface charge are determinant factors to the adsorption of proteins,^{11,12,41} especially in the case of cationic NPs that interact with negatively charged proteins.^{11a} The composition of the adsorbed layer of proteins and the strength of these NP-protein interactions may ultimately affect the biocompatibility of nanomaterials and their internalization in cells.^{13,14,42,43}

The formation of a NP-protein corona is a key factor that constitutes the initial nano-bio interface interacting with cells, since it determines the surface properties, charges, resistance to aggregation and hydrodynamic size of NPs. Likewise, the nature of the particle surface (*i.e.* hydrophobicity, size, radius of curvature, charge, coatings that exert steric or electrosteric effects) will control which biomolecules interact with the NPs, and hence mediate their access to cells (Figure 4.3).⁴⁴ This notion was recently investigated by Casals *et al.* as a function of the NP charge.^{11a} They observed that cationic Au NPs (10 nm in diameter) featuring amine groups formed Au NP-protein unspecific aggregates driven by electrostatic interactions between the positively charged NPs and the negatively charged serum proteins. At first, the NPs underwent a fast adsorption of proteins (mostly albumin, the major component of plasma), and the formation of a *transient*-to-permanent protein corona was later observed. On the contrary, their anionic analogues featuring carboxylic groups did not show a stable protein corona formation; only loosely bound proteins were detected in contact with the NPs. More experimental evidence showed that cationic NPs are converted into anionic ones in biological media due to the adsorption of serum proteins.^{14,41,42}

Hence, a fundamental question that may arise is if cationic NPs have an enhanced cellular uptake as a direct result of their cationic charge or is their specific biological corona which promote endocytosis of these NPs. Specifically, does the serum protein bind to the cell with the NP or is it displaced at the cell surface by a higher affinity

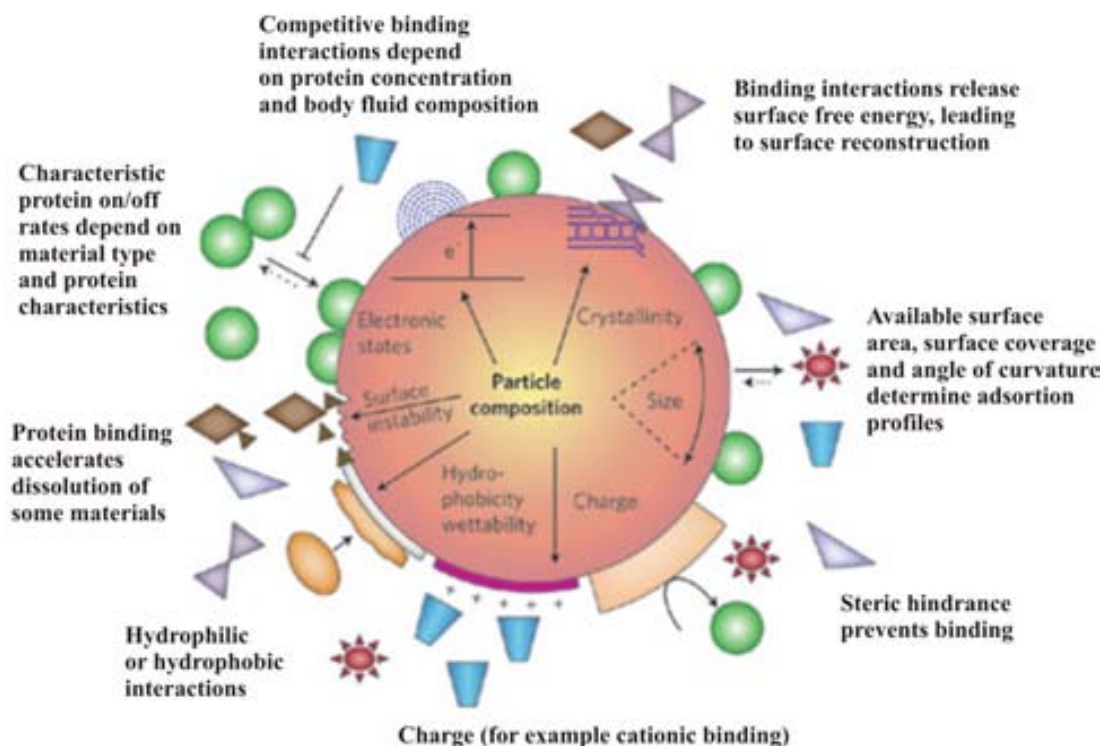


Figure 4.3. NP characteristics influencing the protein corona formation in a biological environment. Characteristic protein attachment/detachment rates, competitive binding interactions, steric hindrance by detergents and adsorbed polymers, and the protein profile of the body fluid lead to dynamic changes in the corona. Image extracted from ref. 44.

membrane protein? Recently, Doorley *et al.*¹⁴ showed by multi-colour fluorescence imaging the co-localization of serum proteins with amine-modified polystyrene spheres (200 nm in size) at the cell surface. They suggested that both bind as an anion complex to the plasma membrane, and that albumin, the most abundant protein adsorbed to NPs from serum,^{11a} could act as an endocytic ligand favoring NP uptake. Hence, according to this model, the surface charge is indeed a determinant factor in shaping NP-cell interactions, although mediated by the type, number, orientation and conformation from the adsorbed proteins. Herein, we note that the nature of the NP surface (e.g. hydrophobicity, size, radius of curvature and coatings that exert steric or electrosteric effects) will control which biomolecules interact with it and the kinetics of NP-protein association and dissociation. These dynamic changes strongly determine the NP-cell interactions. Undertaking a systematic study to elucidate the nature of such interactions should be required.

Another point which should be taken into consideration is the NP aggregation state during the cellular uptake experiments, especially in the case of cationic NPs whose instability has been observed during their interaction with the serum proteins.⁹ Indeed, Xia and co-workers¹⁰ demonstrated the importance of the NPs sedimentation and diffusion rate in cellular uptake by incubating the cells in upright and inverted configurations. The NPs transport properties significantly influenced the cellular uptake, especially in the case of large and/or heavy NPs, showing a much higher uptake for an upright configuration. This was attributed to the different NP dose resulting from sedimentation. Importantly, another study by Levy and co-workers⁴⁵ demonstrated that aggregated peptide-capped Au NPs revealed a different route of endocytosis: macropynocytosis. This route is the predominant form of bulk uptake of fluid and solid cargo into cytoplasmatic vacuoles. Overall, the aggregation state of NPs during the incubation experiments can influence primarily their cellular uptake, and also their route of endocytosis.

4.1.3. Mechanism of cation-mediated internalization of Au NPs.

Initial studies of cationic NPs internalization focused on the ability of these systems to cross cell membranes and target the nucleus. It is generally agreed that, in contrast to neutral and negatively charged NPs of the same size and shape, positively charged NPs are superior for cell-membrane penetration and cellular internalization.^{2,3} However, the debate on the internalization pathway of cationic Au NPs is still open, what can be inferred from the large differences found in the literature. For example, one of the current models defend that cationic NPs bind to negatively charged groups on the cell surface (e.g. sialic acid), following direct translocation across the plasma membrane by generation of transient holes.^{7,27,28} This process has been associated with cytotoxicity. A second widely accepted model suggests that the cationic charge promote stronger NP interactions with the anionic phospholipids composing the cell membrane, followed by endocytosis⁴⁶ and subsequent disruption of endosomal compartments by the **proton sponge effect**,^{47,48} that is, cationic NPs exhibit high buffering capacity in the lysosomal pH range of 5-7 due to presence of unprotonated amines. This leads to an increased influx of protons and chloride ions during endolysosomal acidification, resulting in an increased osmotic pressure in the vesicle. As a consequence, the passive diffusion of

water into the vesicle increases, leading to swelling and eventually rupture or leakage of the vesicle.

The first model is based on experimental evidence of the formation of membrane pores by their interaction with cationic NPs. A study from Leroueil *et al.*²⁷ concluded that hole formation in lipid bilayers by cationic NPs was a common property regardless of shape (spherical versus irregular), chemical composition (organic versus inorganic, such as Au and SiO₂ NPs), deformability (rigid versus flexible), charge density or size. Note that other studies have shown that uptake is determined by size, shape and surface state (see Chapter 1, Section 1.4). Pore-forming propensity in membranes by cationic NPs was confirmed as well by Zheng and co-workers.²⁸ They determined by dynamic simulation studies that highly charged cationic Au NPs (~2.2 nm core) penetrated the lipid membrane, causing membrane disruption and inducing an overt toxic effect on cells that compromised the transfection efficiency of Au NPs. However, at lower cationic coverage (~ 68%), Au NPs promoted a high transfection efficiency without concomitant toxicity. These results were in agreement with studies from Rotello and co-workers,²⁶ who found that Au NPs with a cationic coverage of 68% were the most effective and viable transfection vectors.

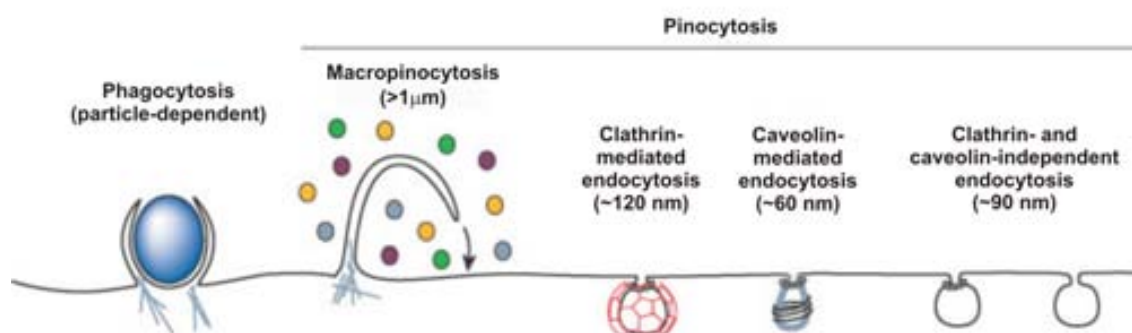


Figure 4.4. Different portals of entry into mammalian cells. Endocytic pathways differ with regard to the size of the endocytic vesicle, the nature of the cargo (ligands, receptors and lipids) and the mechanism of vesicle formation. Image extracted from ref. 49.

The second model reaffirms that cationic NPs are internalized by endocytosis. Although a variety of studies demonstrate a predominant endocytic route, there is no consensus on the endocytic pathway of cationic Au NPs (see Figure 4.4. for the main endocytic pathways in mammalian cells).⁴⁹ For example, Harush-Frenkel and co-workers⁴⁶ elucidated that cationic polymeric NPs (~90 nm in size) were internalized

rapidly in HeLa cells *via* a clathrin-mediated endocytosis pathway. When this pathway was blocked, the NPs activated a compensatory endocytosis pathway that resulted in an even higher accumulation of the NPs. Additionally, the uptake of PEI-capped superparamagnetic iron oxide NPs was related to clathrin- and caveolae-mediated endocytic pathways in HeLa, human epithelial BEAS-2B (bronchial) and HEP-G2 (liver hepatocellular) cells.⁵⁰ Another study confirmed as well a clathrin-mediated internalization process of cationic chitosan NPs in human epithelial CaCo-2 cells (colorectal adenocarcinoma).⁵¹

In these latter studies, it is important to note that cationic NPs exhibited different mechanisms of entry into various cells, which may be attributed to the NPs properties (e.g. size, polydispersity, shape, charge density, purity, aggregation/agglomeration state) but also to a number of factors, such as NP-protein interactions, NP-cell incubation conditions, type of cell culture media, cell types, cell generation, cell treatment, etc. Another important factor is that even though NPs display a certain size after synthesis, their incubation in physiological media during the *in vitro* studies might change their aggregation state, and together with the protein corona (see Section 4.1.2) are responsible to part of the dispersity/disparity of results.

Current research has been focused on the cytoplasmic and/or nuclear delivery of NPs. Qualitative observations showed that in most cases nanomaterials are endocytosed and confined in late endosomes or endolysosomes (membrane-bound vesicles), but cannot breach cell membrane barriers.^{13,52,53} This is an important barrier to success since many advanced nanomaterials, which are conceived to exert a biological effect, cannot operate without reaching the cytosolic machinery or the nucleus of the cell. Amongst synthetic nanomaterials, only cationic NPs^{35,39} or those fused to natural cell-penetrating motifs^{37,37,54} have shown an efficient transport into the cytosol and/or the nucleus.

If cationic NPs presumably enter into cells via an endocytic pathway and are delivered to the cytosol, they must at some point cross a bilayer (e.g. endosomal). Very recently, Rotello and co-workers³⁹ demonstrated the efficient delivery of β -gal into the cytoplasm by co-localization of the protein with an endosome-specific marker (see Section 4.1.1). Proteins were mainly localized outside the endosomes, and their enzymatic activity was preserved after delivery. However, how NPs undergo endosomal

escape and are released into the cytoplasm remains unclear. This process has been difficult to visualize and localize in live cells. Wang and co-workers³² showed that cationic lipid-coated Au NPs complexed with DNA were mainly accumulated inside the endosomes, albeit a few complexes were found in the cytoplasm near the endosome and in the nucleus. They suggested that the escapement from endosomes was a result of the interaction of the complex with the anionic lipid components in the endosomal membrane.

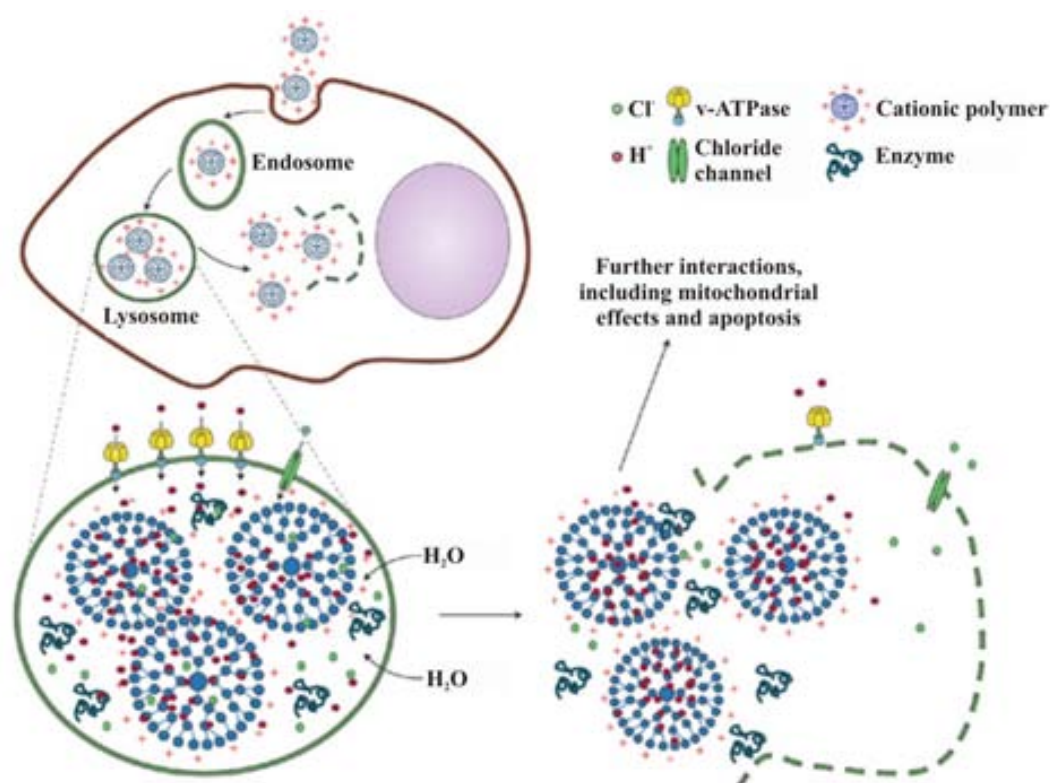


Figure 4.5. Schematics of the proton sponge effect mediated by cationic Au NPs, leading to lysosomal disruption and deposition of the cationic Au NPs in the cytoplasm. Image extracted from ref. 44.

At present, the most accepted mechanistic model to explain the escapement of cationic NPs from endosomes and their transport into the cytosol is based on the **proton sponge effect** (Figure 4.5).⁴⁴ Once these cationic NPs enter into an acidifying lysosomal compartment (pH = 5-6), the initially unsaturated amino groups are capable of sequestering protons that are supplied by the v-ATPase (proton pump). This process keeps the pump functioning and leads to the retention of one Cl⁻ ion and one water molecule per proton up to critical concentrations. Subsequent lysosomal swelling and rupture leads to particle deposition in the cytoplasm and the spillage of the lysosomal

content. This effect has been recently demonstrated in an interesting work from Irvine and co-workers,⁴⁷ who succeeded to cross the endolysosomal vesicles barrier by using cross-linked hydrogel NPs (~200 nm in size). These NPs were formed by a pH-sensitive core featuring tertiary amines with a pK_b of 7.0-7.3, and a pH-insensitive hydrophilic shell layer rich in primary amines. The NPs chemical composition allowed sequestering protons by their pH-sensitive core at the low endolysosomal pH, while the shell composition facilitated particle targeting, cell binding, and/or drug binding. The outcome was the disruption of the endosomes and efficient cytosolic delivery of both small molecules and macromolecules in dendritic cells. Similarly, Au NPs (15 nm-in-size) capped with a charge-reversal polymer (*i.e.* PEI/*cis*-aconitic anhydride functionalized PAA/ PEI) and siRNA underwent endosomal escape in HeLa cells by a pH-triggered charge reversion within the acidic intracellular organelles.⁴⁸ With occurrence of the charge-reversal, Au NPs exhibited a cationic charge (~ 20 mV) and the delivery of SiRNA, leading to a successful escape from endosomes and an efficient distribution of SiRNA over the cytoplasm. Other studies have also demonstrated this mode of endosomal escape.^{55,56}

4.2. Results and discussion.

4.2.1. Design of the peptidic biomolecules for functionalization.

Peptides were chosen as archetypical ligands because of their chemical properties analogous to those of proteins, their versatile chemistry that provides the functional groups found in the 20 natural amino acids, and their ability to form self-assembled monolayers at the surface of nanomaterials.⁵⁷ To study the effect of the surface charge of Au NPs on their interaction with biological systems, two peptidic biomolecules CIPGNVG-PEG-NH₂ and CIPGNVG-PEG-COOH were chosen (Figure 4.6). These ligands show identical core structures, and they only differ in the functional end groups that give the net surface charge at neutral pH. It is assumed that the differences in biological effect between these two peptidic biomolecules will be related to their surface charge and local charge distribution on the NP, in combination with other features, such as chemical polarity, protein affinity, etc. In particular, these biomolecules are of biological interest to stimulate collagen production. The choice of these type of

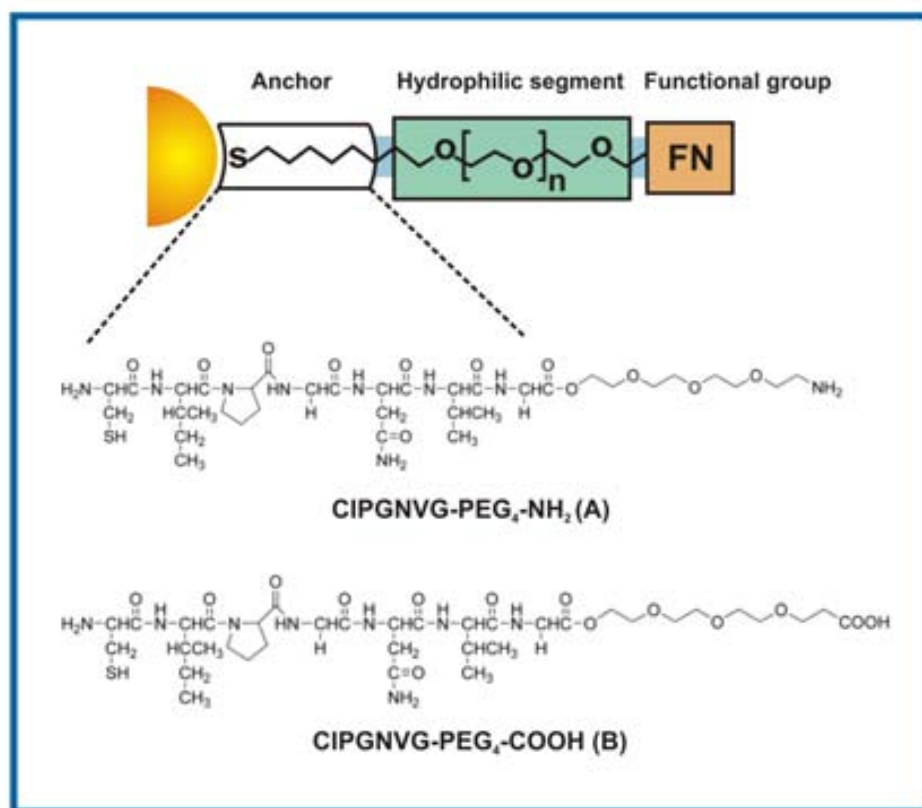


Figure 4.6. Schematics of the design and chemical formula of the selected peptidic biomolecules.

biomolecules was based on previous studies on positively charged biomolecules conjugated to Au NPs; in this case, they interacted electrostatically with the negatively charged citrate ions leading to irreversible aggregation.⁵⁸ We decided to employ the same ligands as proof of concept of the phase-transfer methodology developed (Chapter 3), and to provide robust and scalable methodologies for preparing cationic Au NPs.

The design of the peptide sequence took into account the need to have a strong affinity for Au-surfaces via Cys residues, where the SH group of the cysteine in the *N*-terminus provides a strong affinity for Au. In addition, as stated in the literature, amino groups also have a strong interaction with Au surfaces, which may exert a complementary effect with the thiol that strongly chemisorbs onto negatively charged NP surfaces.⁵⁹ The nonpolar side chains of the amino acid sequence give to the structure the ability to self-assemble into a dense layer that excludes water due to the hydrophobic repulsion. These hydrophobic interactions, together with the hydrogen bonding between the backbone amides, result in a very efficient packing of the

molecules on the NP surface. Such high molecule density on the NPs decreases the molecules mobility, avoiding an effective steric repulsion between Au NPs and compromising stability.⁶⁰ Due to the poor solubility of the peptides themselves, pegylation (PEG, MW = 220) was carried out at the C-terminus with the aim to provide the peptidic biomolecules with both a hydrophilic terminus and an enhanced stability in water.^{61,62} Since the main objective of these studies was to explore the effect of the terminal charge in the final NP bioconjugates, two different PEG termini were designed, ending in either acidic (-COOH) or amino (-NH₂) functionalities which, depending upon pH, would result in final negative or positive net charges, respectively.

4.2.2. Synthesis and physicochemical characterization of peptide-Au NP bioconjugates.

The versatility of the phase transfer methodology described in Chapter 3 with AUT as the case model ligand was further proved for the conjugation of the two identical peptidic biomolecules terminating in either positive (NH₃⁺) or negative (COO⁻) charged groups. As proof of concept, the selected cationic peptidic biomolecule was based on previous studies where the functionalization led to irreversible aggregation of the cationic peptide-capped Au NPs due to electrostatic interactions with the negatively charged surfactant stabilizing the Au NPs (*i.e.* citrate).⁵⁸ This effect was kinetically favoured in larger NP sizes, since a higher cooperative effect of multiple electrostatic bonds acting simultaneously led to higher effective affinities. For example, 8 nm and 16 nm Au NPs appeared to aggregate in less than one minute upon addition of the peptides, whereas 6 nm Au NPs were more resistant to aggregation. Given the sensitivity of size to aggregation, we selected a NP size of ~13 nm for our studies since it was more challenging to overcome this effect. In addition, previous studies have shown that NPs larger than 5 nm are difficult to transfer.⁶³ This size corresponds with the size range normally used for delivery and cellular uptake (10-to-15 nm Au NPs).^{36,53,64,65} Importantly, this size range can easily accommodate an increased and combined biological load while still able to penetrate and cross cell membranes.

Under the same reaction conditions as with AUT ligand (see Chapter 3), oleylamine-stabilized Au NPs of 13 nm in diameter could be transferred from

chloroform into water using 50-fold molar excess of peptidic biomolecules CIPGNVG-PEG-NH₂ or CIPGNVG-PEG-COOH (calculated by the number of Au atoms at the surface of the NP and assuming that each thiolated molecule occupies 21.4 Å² of the Au NP surface).^{66,67} Additionally for the peptidic biomolecules, a few drops of 0.1 M of either HCl or NaOH were required to form the respective charged compounds, followed by some additional mixing. The biphasic mixture was left stand on the bench for about 10-30 minutes, during which it could be observed how the red color of the organic solution was transferred into the aqueous layer (Figure 4.7-B). The resulting bioconjugates in the aqueous layer were exhaustively purified by dialysis in order to eliminate the excess of non-conjugating molecules.

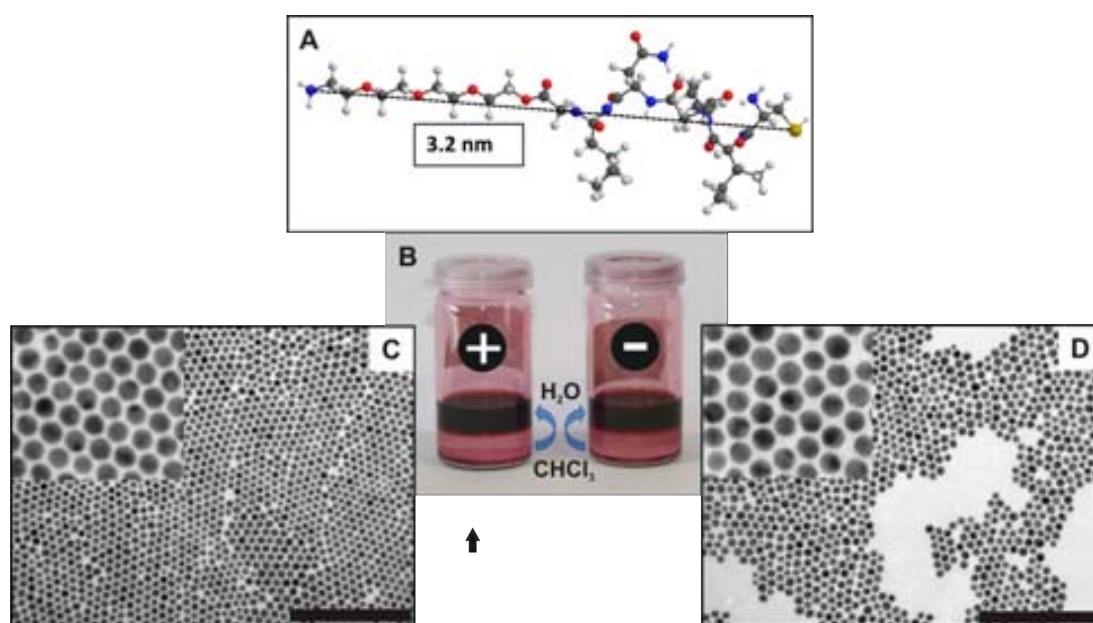


Figure 4.7. A) Minimum energy structure geometry of the peptidic biomolecule CIPGNVGPEG-NH₂ calculated using ChemBioDraw 3D. B) Representative image showing the efficient phase transfer of NPs from CHCl₃ into water with the peptidic biomolecules. C,D) Representative TEM images of Au NPs (~13 nm) functionalized with peptidic biomolecules CIPGNVGPEG-NH₂ (C) and CIPGNVG-PEG-COOH (D) after the phase transfer from CHCl₃ into the aqueous phase. Scale bars are 200 nm.

NP functionalization and stability of the bioconjugates were determined by TEM, UV-vis absorbance spectroscopy and DLS. Analysis by TEM showed the formation of ordered self-assembled monolayers of Au NPs, which is indicative of the high solubility and mobility of the NPs in solution⁶⁸ (Figure 4.7-C,D). The ordered arrangements of Au NPs have an interparticle spacing of 2-3 nm approximately, which is slightly below the limit of what would be expected for 2 x times the size of these biomolecules (~ 3.2 nm in a stretched form, Figure 4.7-A). Such an observation could be an effect of the drying

Sample	λ_{\max} (nm)		Hydrodynamic Diameter in nm (PDI)		ζ -Potential in mV
	Before	After	Before	After	(std. dev. in mV) After
Au-CIPGNVG-PEG-NH ₂	523.0	520.0	11.1 (0.2)	14.5 (0.3)	+10.0 (8.4)
Au-CIPGNVG-PEG-COOH		520.0		16.1 (0.3)	- 41.5 (5.6)

Table 4.1. UV-vis wavelength of absorption maximum, number size by DLS and ζ -potential values (at pH = 7.5) of Au NPs transferred from CHCl₃ (before) into aqueous phase (after) with the peptidic biomolecules CIPGNVG-PEG-NH₂ and CIPGNVG-PEG-COOH.

process of the samples on TEM grids and the subsequent packing and intermixing of the biomolecules at the NP-conjugates boundaries.

Similar to AUT conjugation, the UV-vis spectrum of Au NPs after phase-transfer and surface functionalization with the peptidic biomolecules showed a blue- shift of the SPR peak (~ 3 nm) for both negative and positive peptidic bioconjugates (Table 4.1). Hydrodynamic diameter measurements by DLS indicated an increase of ~ 3 and ~ 5 nm in diameter for the positive and negatively charged peptides, with respect to the volume size of oleylamine-stabilized Au NPs. ζ -potential measurements at neutral pH = 7.5 confirmed either the cationic or the anionic nature of bioconjugates Au NP-CIPGNVG-PEG-NH₃⁺ ($+ 10.0 \pm 8.4$) and Au NP-CIPGNVG-PEG-COO⁻ ($- 41.5 \pm 5.6$) respectively, whose absolute values indicated a dense packing of the ligands on the surface of the NPs (note that cationic Au NPs had a ζ -potential of $(+ 22.7 \pm 2.8$ mV in a 0.01M HCl aqueous solution).

The successful re-functionalization of Au NPs after the phase-transfer process was confirmed by FTIR spectroscopy (Figure 4.8). After the ligand exchange reaction, the band at 2912 cm⁻¹ corresponding to the C-H stretching mode next to the double bond of OLA capping molecules is clearly eliminated. At the same time, the band at 1740 cm⁻¹ corresponding to the amide groups of the peptidic sequences is detectable after the exchange reaction. Furthermore, the spectral change in the 1450-1680 cm⁻¹ region seems to support the presence of bands corresponding to the symmetric and asymmetric stretching modes in the carboxylate group of the peptidic biomolecule CIPGNVG-PEG-COOH.

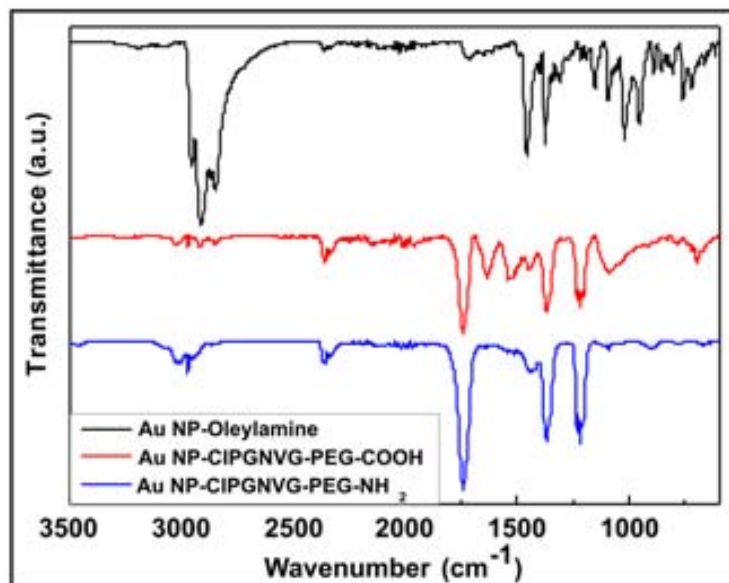


Figure 4.8. FTIR spectra of oleylamine-capped Au NPs before (black) and after the ligand exchange reaction with CIPGNVG-PEG-COOH (red) and CIPGNVG-PEG-NH₂ (blue) peptidic biomolecules.

It should be noted that the peptidic-capped Au NPs could be lyophilized and stored as a powder for further utilization. When resuspended in water, they display exactly the same UV-vis absorption spectrum as before freeze-drying. This is important since only a few nanobioconjugate preparations can be stored in the dry state and then redispersed in water without irreversible aggregation.⁶⁹

4.2.3. Stability and physicochemical properties of peptide-Au NP bioconjugates in physiological conditions.

Before the incubation of peptide-Au NP bioconjugates with cells, their stability in CCM was studied, since the formation of aggregates would render their application in cell culture pointless (see Section 4.1.2). In particular, the CCM used for the human dermal fibroblasts tested (1-BR3G line) contained Dulbecco's Modified Eagle Medium (DMEM) and 10 % of fetal bovine serum (FBS), which is a multicomponent fluid containing up to 1.8 mg/mL of glucose and 70 mg/mL of proteins, among which albumin is the most abundant (~ 51 % of total protein content) followed by globulins (~ 24 % of total protein content) and other proteins at much lower content (each < 0.3 %), such as hemoglobin. The stability of the peptide-Au NP bioconjugates was tested first

after incubating them in borate buffer solution (2 mM, pH 8.5) containing 10% FBS for 1 hour followed by dilution in CCM. No formation of aggregates could be observed after 24 hours (Figure 4.9). It should be also mentioned that both incubated bioconjugates with only DMEM led to complete aggregation after 5 hours (data not shown), which is due to the screening of the electrostatic repulsions between the charged termini of the peptidic chains and is in agreement with previous studies of bioconjugate stability as a function of the ionic strength.⁵⁸

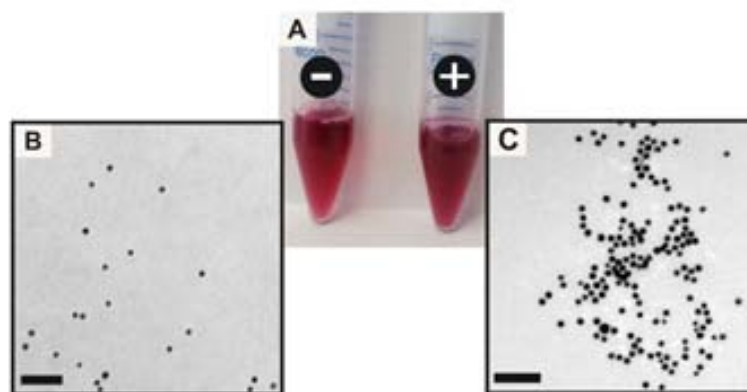


Figure 4.9. (A) View of Au NP-CIPGNVG-PEG-COO⁻ and Au NP-CIPGNVG-PEG-NH₃⁺ bioconjugates and TEM images of the Au NP-CIPGNVG-PEG-COO⁻ (B) and Au NP-CIPGNVG-PEG-NH₃⁺ (C) bioconjugates after 24 hours of incubation in CCM at a concentration of 5 nM NPs.

The evolution of the proteins adsorption from serum onto the NP surface was evaluated at different time intervals after centrifugation, to remove the unbound and loosely bound protein molecules, followed by subsequent resuspension in protein-free aqueous solution. The purification process was required to distinguish whether the adsorbed proteins were in equilibrium with the free proteins in solution, or whether they were irreversibly bound forming a stable protein corona, thus determining the biological identity of the Au NP bioconjugate. In this respect, it is necessary to mention that the achievement of a permanent and stable protein corona usually formed by a “hard” layer of slowly exchanging protein(s) and an outer loosely bound layer (the “soft” corona) is time-dependent.^{11,43} In the case of bare Au NPs, protein adsorption on the NP surface and formation of a stable “hard” corona was observed to be practically finished after 48 hours of incubation.^{11a} On the contrary, a faster absorption of proteins was observed on cationic Au NPs, driven by electrostatic interactions. The stability of the final hard protein corona was lower, indicating that the binding by coordinating bonds to the

Sample	λ_{\max} (nm)		Hydrodynamic Diameter in nm (Pdl)		ζ -Potential in mV (std. dev. in mV)	
	before	after	before	after	before	after
	Au-CIPGNVG-PEG-NH ₂	520.0	538.0	14.5 (0.3)	75.4 (0.5)	+10.0 (8.4)
Au-CIPGNVG-PEG-COOH	520.0	520.0	16.1 (0.3)	16.1 (0.3)	-41.5 (5.6)	-42.5 (5.8)

Table 4.2. UV-vis absorption maximum, number size by DLS and ζ -potential values of bioconjugates Au NP-CIPGNVG-PEG-NH₃⁺ and Au NP-CIPGNVG-PEG-COO⁻ diluted in H₂O (before) or after 24 hr incubation in CCM (after) at concentration of 5 nM of NPs. After incubation in CCM, samples were centrifuged (8000 rcf, 10 min), resuspended in milliQ H₂O and filtered using 0.2 μ m filters before the DLS and ζ -potential measurements were performed.

inorganic surface was stronger than the binding by electrostatic forces between organic molecules.^{11a}

UV-vis absorption spectroscopy allowed easy monitoring of the interaction of both bioconjugates Au NP-CIPGNVG-PEG-NH₃⁺ and Au NP-CIPGNVG-PEG-COO⁻ with serum proteins, since the SPR is highly sensitive to the NP environment (Figure 4.10, and Table 4.2). In the case of cationic bioconjugates, the absorbance spectra showed both an initial red-shift of the SPR peak of ~ 6 nm after 1 hour incubation in borate-FBS and of ~ 12 nm after 24 hours in CCM; both of them without any sign of Au NP aggregation. This is indicative of the formation of unspecific electrostatic interactions between the positively charged Au NP bioconjugates and the negatively charged abundant serum proteins (mostly albumin).^{11a} Similarly, after exposure of the cationic Au NP bioconjugates to CCM, DLS indicated an increase of ~ 61 nm in diameter, and the surface charge evolved nearby the serum average value (-37.5 mV). This data confirmed the coating of the particles with serum proteins (Figure 4.10 and Table 4.2). By contrast, in the same conditions, the anionic Au NP bioconjugates did not show variation of the SPR peak, significant increase of the hydrodynamic diameter or changes in the final surface charge, indicating the absence of interactions between these Au NP bioconjugates and the serum proteins. It should be noted that the ζ -potential of the anionic Au NP bioconjugate in borate buffer (pH = 8.5) at the initial time was -60.4 mV. After 24 hours of incubation in CCM (DMEM 10% FBS), this value reached -42.5 mV, which suggested that the proteins attached loosely to the NP surface by reducing its net surface charge. This is an interesting result since the presence of loosely bound proteins in the case of anionic Au NP bioconjugates are somehow responsible for the observed stability in CCM.

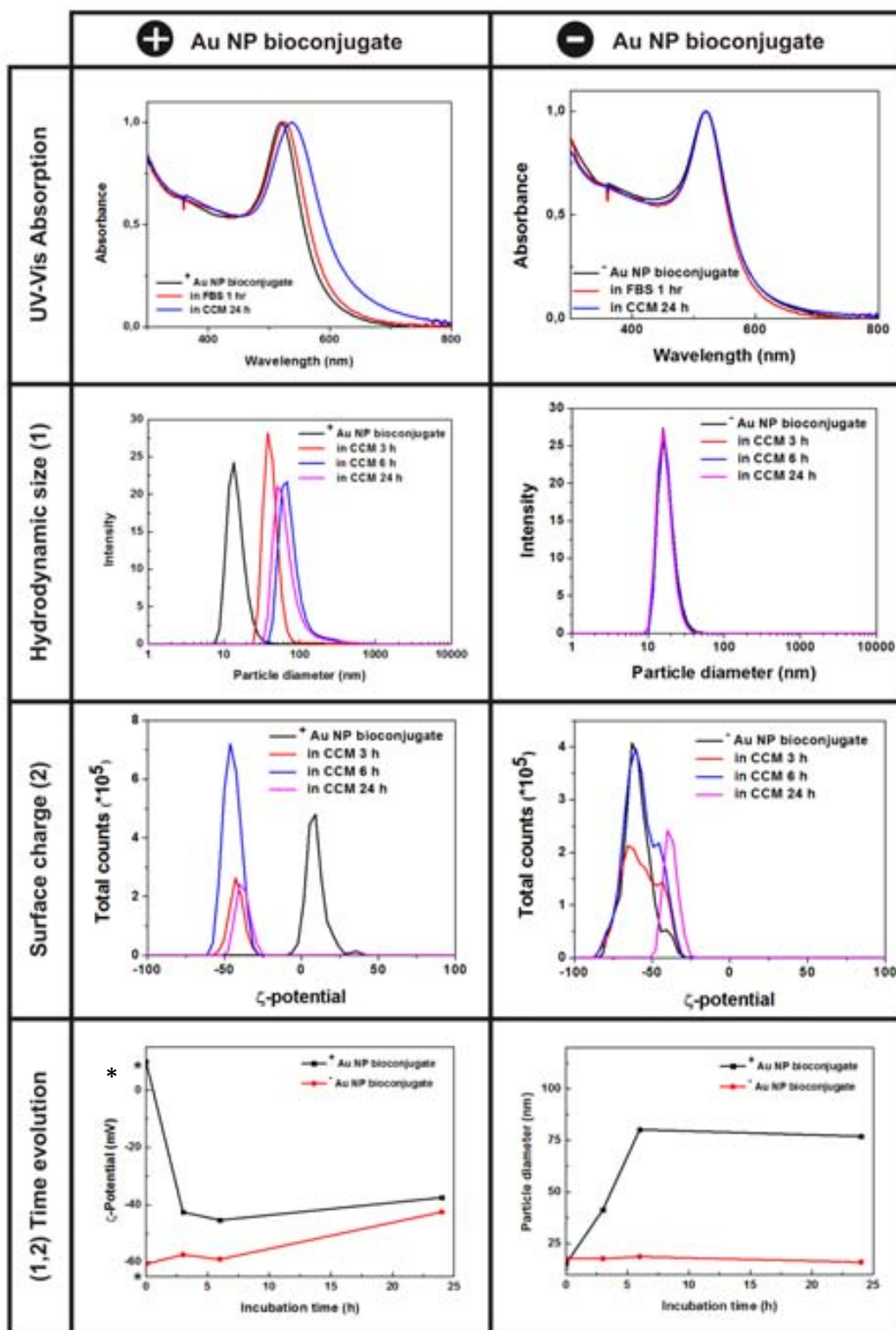


Figure 4.10. Normalized UV-vis absorption spectra, number size by DLS and ζ -potential values of Au NP-CIPGNVG-PEG-NH₃⁺ and Au NP-CIPGNVG-PEG-COO⁻ bioconjugates before* and after incubation in FBS and CCM at concentration of 5 nM of NPs. * Initial (t=0) ζ -potential and DLS measurements of the cationic Au NP bioconjugates correspond to neutral pH = 7.5, since this bioconjugate aggregated in only borate buffer (without FBS) at pH = 8.5. Anionic Au NP bioconjugates were measured in borate buffer at t=0.

4.2.4. *In vitro* toxicity, cellular uptake and intracellular fate of cationic peptide-Au NP bioconjugates.

The effect of the surface charge of these Au NP bioconjugates was investigated in the toxicity, cellular uptake and intracellular localization on human dermal fibroblasts (1BR3G).

To understand and evaluate the toxicity effects of the synthesized 13 nm peptide-Au NP bioconjugates, cell viability assessment was performed by a standard Trypan Blue exclusion assay carried out both after 3 and 24 hours of incubation with positive and negative Au NP bioconjugates at 5 nM of NPs (Figure 4.11-A). Trypan Blue is a diazo dye which selectively colour dead cells or tissues blue, whereas live cells or tissues with intact membranes do not absorb the compound. Comparative optical microscope images indicated that cells were alive, as indicated by the absence of blue color. In addition, the morphology of the cells was maintained and no major detachment occurred.

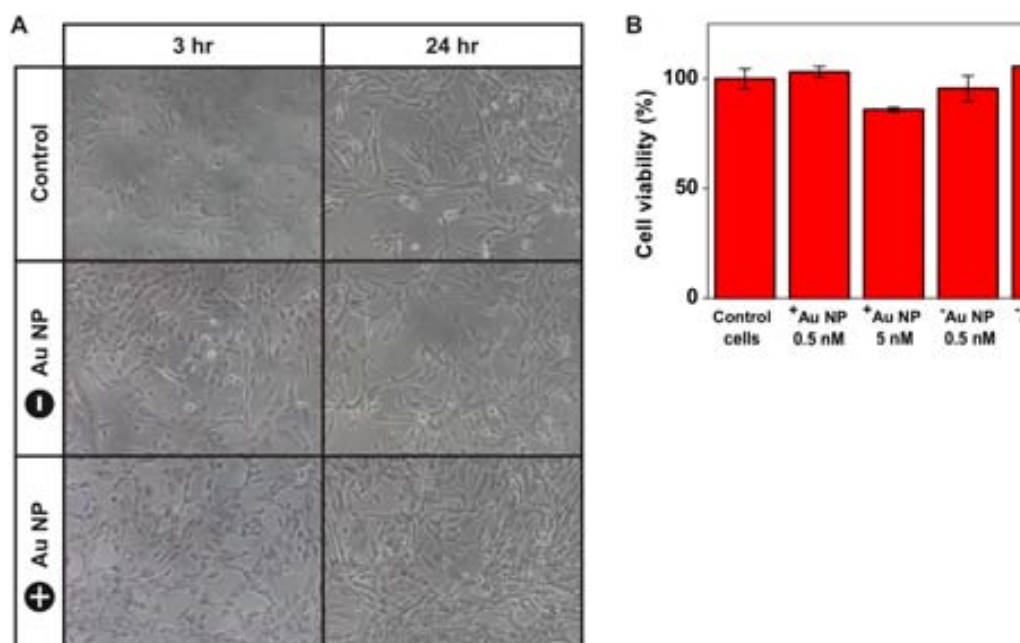


Figure 4.11. A) Toxicity of Au NP-CIPGNVG-PEG-NH₃⁺ and Au NP-CIPGNVG-PEG-COO⁻ bioconjugates at 5 nM of NPs in human fibroblast (1BR3G) cells as determined by Trypan Blue test and analyzed by comparative optical microscope images. Blue color determines dead cells. A) Toxicity of Au NP-CIPGNVG-PEG-NH₃⁺ and Au NP-CIPGNVG-PEG-COO⁻ bioconjugates at 0.5 nM and 5 nM of NPs in human fibroblast (1BR3G) cells as determined by XTT assay.

It is important to differentiate between cytotoxicity and cellular damage. NPs that show little or no cytotoxicity via several standard assays may be still able to cause serious cellular damage. For example, 13 nm citrate-capped Au NPs were not toxic according to an assay in skin cells, but the particles did apparently promote the formation of abnormal actin filaments, which led to decreases in cell proliferation, adhesion, and motility.⁶⁹ Based on these considerations, cell proliferation was also evaluated using the well-established (2,3-bis-(2-methoxy-4-nitro-5-sulphophenyl)-2H-tetrazolium-5-carboxanilide) (XTT) assay; a tetrazolium dye that is reduced to a soluble, brightly colored orange formazan derivative. XTT measures the respiratory activity of the cells and is related to cell proliferation (Figure 4.11-B). Importantly, after 24 hours of incubation with both positive and negative Au NP bioconjugates, none of the particles showed a significant toxicity at concentrations of 0.5 nM and 5 nM of NPs. Overall, there was no indication of any effects the NPs might have on cell metabolism or proliferation. This result is significant given the higher uptake in the case of cationic Au NP bioconjugates.

The intracellular uptake of the bioconjugates in 1BR3G cells was quantified by ICP-MS, which has very low detection limits for Au (18 parts-per-trillion, 10^{-12}) permitting a very rigorous quantification. Thus, 1BR3G cells were incubated for 30 minutes, 1 hour and 3 hours with two different concentrations (0.5 nM and 5 nM of Au NPs, corresponding to approx. 5 and 50 μg of Au respectively) of either Au NP-CIPGNVG-PEG-NH₃⁺ and Au NP-CIPGNVG-PEG-COO⁻ bioconjugates in serum-containing medium. The Au-content of both the NPs remaining in the incubation medium and the pellets of trypsinized cells was determined by ICP-MS. As anticipated from the higher affinity of cationic molecules for cell membranes, significantly all the cases showed a higher uptake of the cationic bioconjugates when compared with their anionic counterparts (Figure 4.12). The highest uptake (44.5 %) could be observed for 5 nM cationic Au NP bioconjugates after 3 hours, and a 10-fold dilution of the particles resulted in 31.5 % of uptake during the same incubation time. This contrasts with the maximum 5 % of uptake obtained in the best case of internalization with the anionic Au NP bioconjugates (incubation of 3 hours at 5 nM NP concentration). We assume that this technique may not distinguish between the internalized Au NPs and those attached on the outside of cell membranes. However, Au NPs have been recurrently seen to be endocytosed after interacting with the membrane of cells in a process of few hours.^{36,37}

Under this assumption, the estimated number of internalized/adsorbed cationic Au NP bioconjugates was 9.1×10^7 per cell,⁷¹ which is much higher than other reported values (approx. 2.0×10^5 NPs per cell for 15.5 nm Au NPs) using similar methods.⁷²

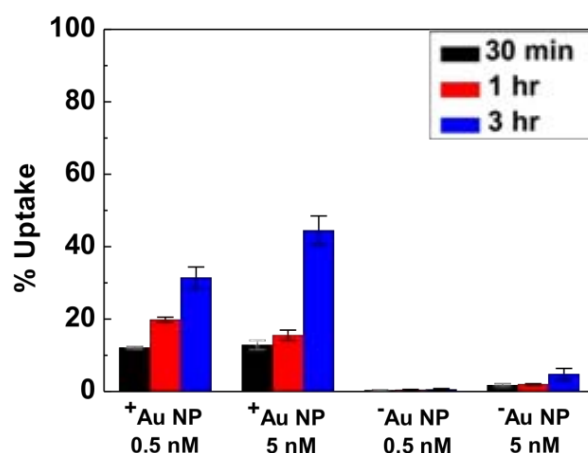


Figure 4.12. Intracellular Au-concentration as determined by ICP-MS as a function of time. Data represent the average of three independent experiments with standard deviation. Au NPCIPGNVG-PEG-NH₃⁺ and CIPGNVG-PEG-COO⁻ bioconjugates are named as ⁺Au NP and ⁻Au NP, respectively.

Confocal fluorescence microscopy was used to confirm and assess the enhanced uptake of the cationic Au NP bioconjugates in living cells. This technique is normally used to track fluorescently labelled molecules, but here the Au NPs were visualized by the scattered light when irradiated with a laser at 488 nm. While fibroblasts cells incubated with Au NP-CIPGNVG-PEG-COO⁻ presented low reflection signals (Figure 4.13-A), those incubated with Au NP-CIPGNVG-PEG-NH₃⁺ showed increased reflected light both attached outside of the cell membrane and accumulated in the cytoplasm (Figure 4.13-B). After optical sectioning (Figure 4.13-C,D) and spatial reconstruction of cells (Figure 4.13-E), confocal microscopy allowed to observe cationic Au NP bioconjugates homogeneously distributed throughout the cytoplasm. However, from the reconstructions it was difficult to confirm nuclear localization of the bioconjugates. In all the experiments, contrast phase and bright field were used to assess normal cell morphology, and nuclei were stained with 4',6-diamidino-2-phenylindole (DAPI). These results confirm that cationic Au NP bioconjugates bind more efficiently to cell membranes and induce higher levels of cellular uptake.

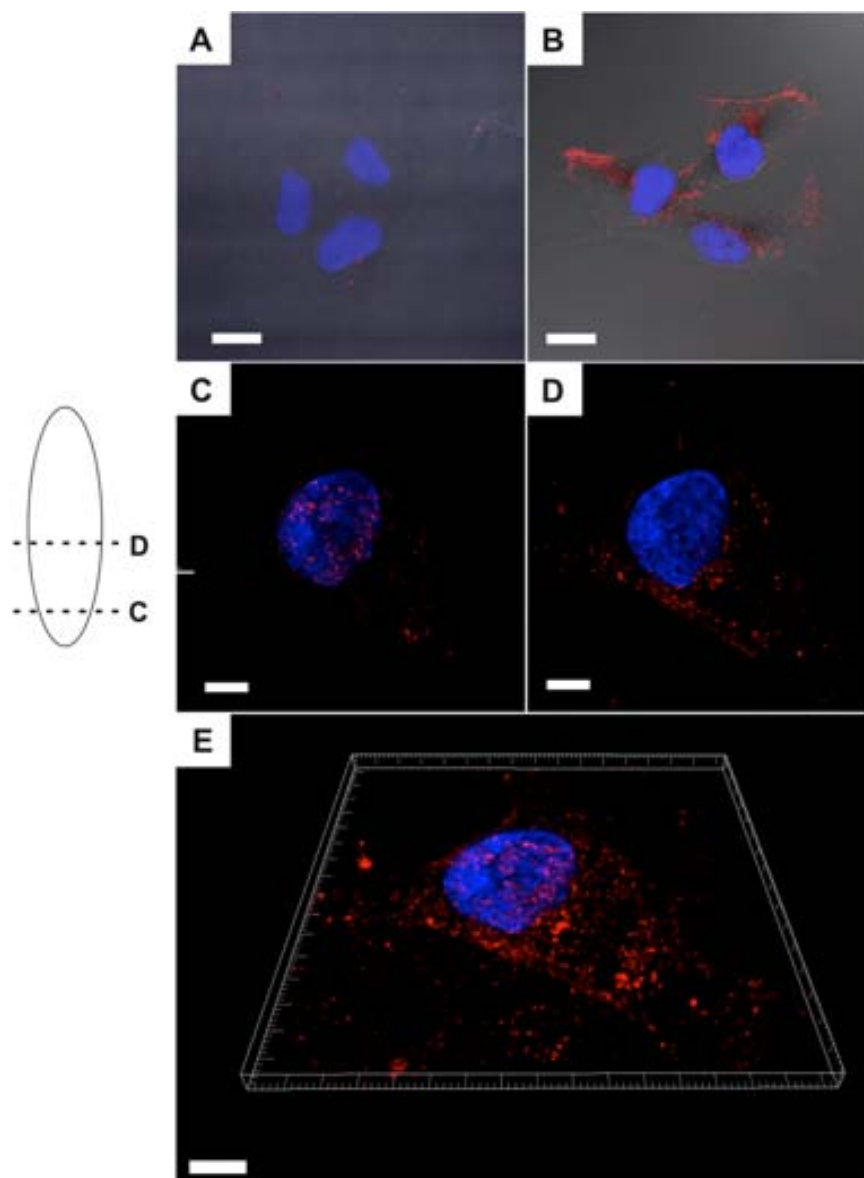


Figure 4.13. Confocal images of human fibroblast (1BR3G) cells incubated with Au NP-CIPGNVG-PEG-COO⁻ (A) and Au NP-CIPGNVG-PEG-NH₃⁺ (B-E) bioconjugates at 5 nM Au NP concentrations for 3 hours. Nuclei were stained with DAPI, showing blue fluorescence. The scattering from Au NPs is false-colored in red. A, B) Slides of 0.25 μm of the confocal fluorescence, reflectance, and differential interference contrast transmission images were obtained independently and then overlaid in a maximal projection mode. C, D) A schematic depicting the Z-axis of the images is shown (left). Clearly, as the Z-axis moves from top to bottom of the fibroblast cell, fluorescence spots are observed throughout the cell, indicating that the cationic Au NP bioconjugates are uniformly distributed throughout the cytoplasm. E) Spatial reconstruction from 0.25 μm sections. Scale bars are 20 μm (A,B) and 10 μm (C-E).

TEM was used as the main tool for the localization of the Au NPs inside the cells. Cationic and anionic Au NP bioconjugates were incubated with fibroblast cells for 3 hours at 37 °C and processed for TEM analysis. Note that dark-field contrast was

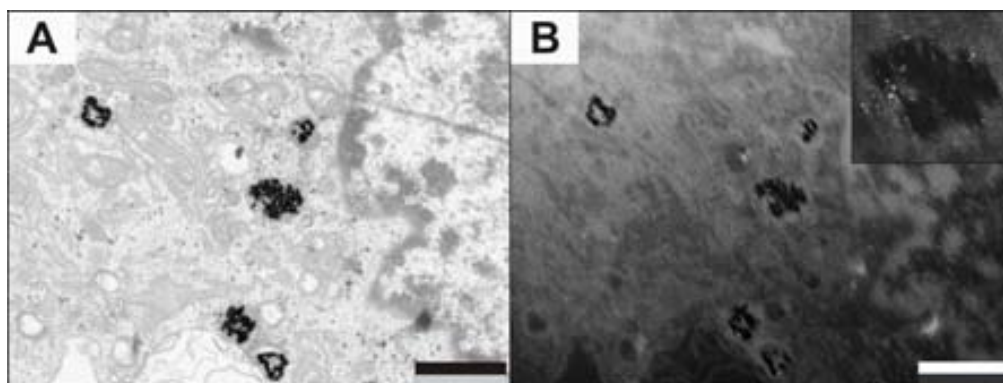


Figure 4.14. TEM images of human fibroblast (1BR3G) cells incubated with Au NP-CIPGNVG-PEG-NH₃⁺ bioconjugates at 5 nM NP concentration for 3 hours. A) Representative TEM image revealing internalization of cationic Au NP bioconjugates through endocytic vesicles. B) Dark-field imaging of the same area. In this operation mode, the electrons diffracted by the crystal planes of Au are imaged. As a result, the Au NPs whose crystals are aligned perpendicular to the e-beam appear bright while the rest of the sample scatters the electrons in a diffusive manner giving a grey background. Tilting the sample stage allow to easily distinguish the Au NPs from cellular features as ribosomes, which appear dark in the dark field imaging mode. Scale bars are 1 μm.

employed to unequivocally discriminate between Au NPs and the other features of the cell (Figure 4.14), accordingly to the high electronic density and crystallinity of Au. In agreement with ICP-MS and confocal studies, no significant uptake was observed for the anionic Au NP bioconjugates (Figure 4.15-A,B). On the contrary, cationic Au NP bioconjugates were found to be mainly confined to endocytic vesicles (Figure 4.15-C-F). This suggested that the predominant route of cellular uptake of the cationic Au NP bioconjugates was endocytosis, and that some of their cationic character and surface characteristics were maintained after interaction with the extracellular matrix, at least during the first hours of the *in vitro* experiment. It can be argued that with time, during the interaction of the bioconjugates with the physiological medium, interaction with serum proteins and a progressive “hardening” of the protein corona, aggregation or chemical modification of the functional groups, may deactivate these vectors. In our case, the positive surface charge of the Au NP bioconjugates may be the responsible for an increased interaction with the cell membrane, probably being attracted and attaching to it due to the intrinsic negative charge of the phospholipid bilayers. From there, it appears that NPs do not penetrate and cross the membrane but accumulate until the membrane is recycled and NPs internalized inside endosomes, as TEM reveals.

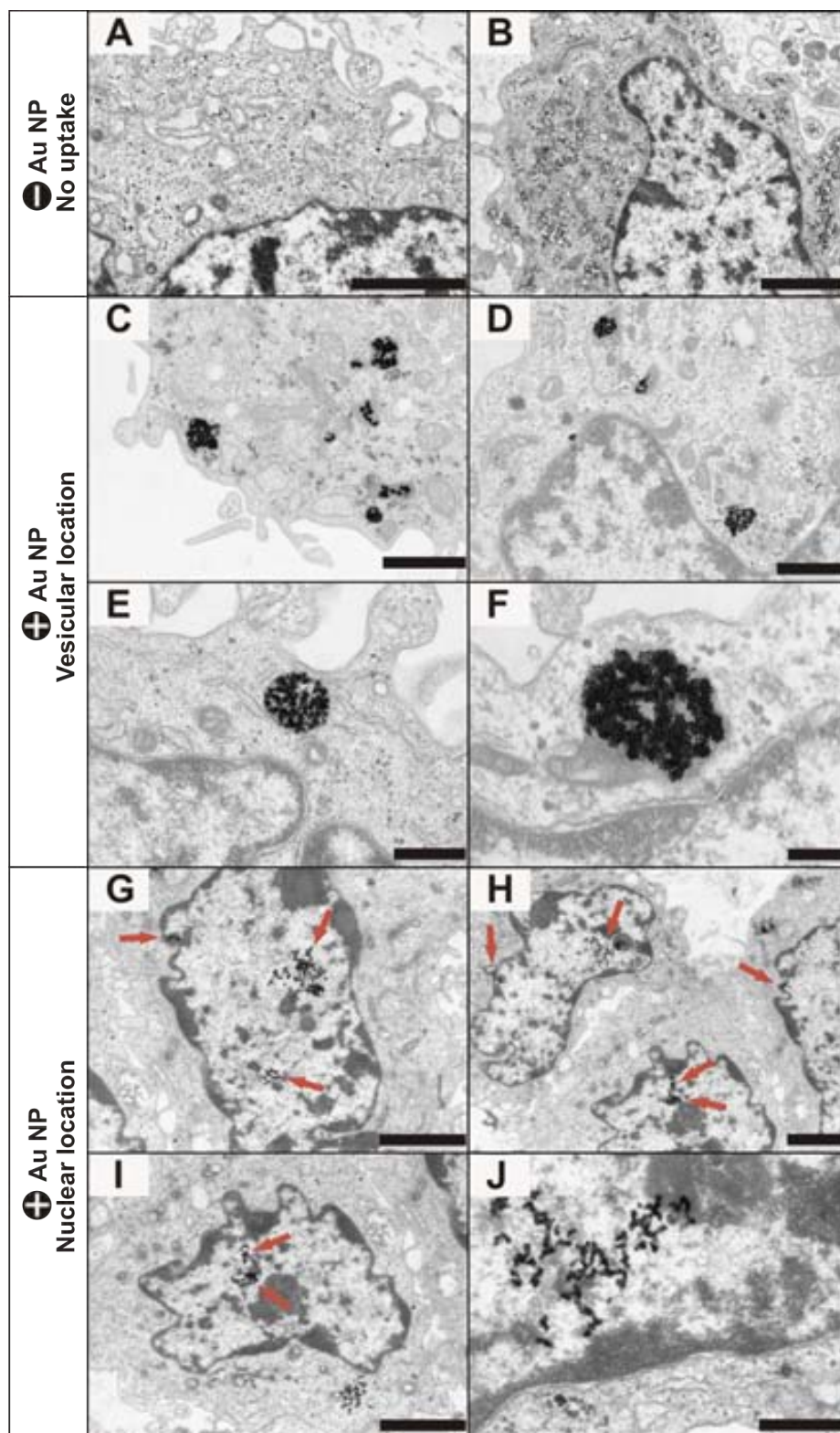


Figure 4.15. TEM images of human fibroblast (1BR3G) cells incubated with Au NPCIPGNVG-PEG-COO⁻ (A,B) an Au NP-CIPGNVG-PEG-NH₃⁺ (C-J) bioconjugates at 5 nM NP concentrations for 3 hr. (A, B) Cells incubated with Au NP-CIPGNVG-PEG-COO⁻ showing no NP uptake, (C-F) cells incubated with Au NP-CIPGNVG-PEG-NH₃⁺ showing NPs confined to endocytic vesicles, and (G-J) cells incubated with Au NPCIPGNVG-PEG-NH₃⁺ showing presence of NPs in the nucleus. Scale bars are 2 μm in A, B, G, H and I; 1 μm in C and D; 500 nm in E and J; and 200 nm in F.

Notably, the cationic Au NP bioconjugates within the endosomes show little stability against aggregation, which could be either due to ligand exchange reactions within the cell⁴⁰ or may be the result of the digestion of the ligand shell by proteases inside the endosome. Besides, a large proportion of the NPs seem to migrate towards the endoplasmic reticulum near the nucleus, and indeed, nuclear localization of the bioconjugates could also be observed (Figure 4.15-G-J), which suggested that the biomolecules were acting as nuclear vectors due to their positive charge. Apparently, inside the endosome, the cationic bioconjugates are still active, and may become even more positively charged in the acidic environment of the late endosomes/endolysosomes, resulting in membrane perturbation as in the case of proton sponges.^{44,47,48,55} This effect would justify the break of the endosome near the nucleus and the consequent penetration of the cationic Au NPs. Experiments to determine how these NPs escape from the endosomes and enter the nucleus are subject to an ongoing study.

4.3. Conclusions.

The phase transfer methodology developed in Chapter 3 has been successfully applied for the functionalization of 13 nm Au NPs with two peptidic ligands with identical chemical core structure but differing in their surface charge. Importantly, this method has shown to overcome the aggregation difficulties found for such cationic peptide-capped Au NPs in previous studies in our group. Another advantage is that large amounts of highly monodisperse and highly concentrated samples of Au NP bioconjugates have been obtained. The enhanced affinity for cell membranes and uptake of cationic Au NP bioconjugates over negative ones has been demonstrated in human dermal fibroblast cells. In addition, cationic Au NP bioconjugates showed a predominant route of endocytosis, and despite their high uptake rates, no toxicity was found after 24 h. The nuclear localization observed for the cationic Au NP bioconjugates upholds promising applications in gene delivery, where oligonucleotides are loaded onto the particles and are carried into the cells with potentially higher efficiency than unbound DNA. Ongoing work focuses on elucidating the mechanism of endosomal escape and nuclear entry.

4.4. References.

1. Kornguth, S. B.; Stahmann, M. A.; Anderson, J. W. *Effect of Polylysine on the Cytology of Ehrlich Ascites Tumor Cells*. Exp. Cell Res., **1961**, 24, 484-494.
2. Cho, E. C.; Xie, J.; Wurm, P. A.; Xia, Y. *Understanding the Role of Surface Charges in Cellular Adsorption versus Internalization by Selectively Removing Gold Nanoparticles on the Cell Surface with a I2/KI Etchant*. Nano Lett., **2009**, 9, 1080-1084.
3. Arvizo, R. R.; Miranda, O. R.; Thompson, M. A.; Pabelick, C. M.; Bhattacharya, R.; Robertson, J. D.; Rotello, V. M.; Prakash, Y. S.; Mukherjee, P. *Effect of Nanoparticle Surface Charge at the Plasma Membrane and Beyond*. Nano Lett., **2010**, 10, 2543-2548.
4. Goodman, C. M.; Mc Cusker, C. D.; Yilmaz, T.; Rotello, V. M. *Toxicity of Gold Nanoparticles Functionalized with Cationic and Anionic Side Chains*. Bioconj. Chem., **2004**, 15, 897-900.
5. Leroueil, P. R.; Hong, S.; Mecke, A.; Baker, J. R.; Orr, B. G.; Banaszak Holl, M. M. *Nanoparticle Interaction with Biological Membranes: Does Nanotechnology Present a Janus Face?* Acc. Chem. Res., **2007**, 40, 335-342.
6. Rivera-Gil, P.; Jimenez De Aberasturi, D.; Wulf, V.; Pelaz, B.; Del Pino, P.; Zhao, Y.; De La Fuente, J. M.; Ruiz De Larramendi, I.; Rojo, T.; Liang, X-J.; Parak, W. J. *The Challenge to Relate the Physicochemical Properties of Colloidal Nanoparticles to Their Cytotoxicity*. Acc. Chem. Res., **2013**, 46, 743-749.
7. Moghadam, B. Y.; Hou, W-C.; Corredor, C.; Westerhoff, P.; Posner, J. D. *Role of Nanoparticle Surface Functionality in the Disruption of Model Cell Membranes*. Langmuir, **2012**, 28, 16318-16326.
8. Harush-Frenkel, O.; Rozentur, E.; Benita, S.; Altschuler, Y. *Surface Charge of Nanoparticles Determines Their Endocytic and Transcytotic Pathway in Polarized MDCK Cells*. Biomacromol., **2008**, 9, 435-443.
9. Nafee, N.; Schneider, M.; Schaefer, U. F.; Lehr, C-M. *Relevance of the Colloidal Stability of Chitosan/PLGA Nanoparticles on their Cytotoxicity Profile*. Int. J. Pharma., **2009**, 381, 130-139.
10. Cho, E. C.; Zhang, Q.; Xia, Y. *The Effect of Sedimentation and Diffusion on Cellular Uptake of Gold Nanoparticles*. Nat. Nano, **2011**, 6, 385-391.
11. (a) Casals, E.; Pfaller, T.; Duschl, A.; Oostingh, G. J.; Puentes, V. *Time Evolution of the Nanoparticle Protein Corona*. ACS Nano, **2010**, 4, 3623-3632. (b) Casals, E.; Pfaller, T.; Duschl, A.; Oostingh, J.; Puentes, V. F. *Hardening of the Nanoparticle-Protein Corona in Metal (Au, Ag) and Oxide (Fe₃O₄, CoO, and CeO₂) Nanoparticles*. Small, **2011**, 7, 3479.
12. Lundqvist, M.; Stigler, J.; Cedervall, T.; Berggård, T.; Flanagan, M. B.; Lynch, I.; Elia, G.; Dawson, K. *The Evolution of the Protein Corona around Nanoparticles: A Test Study*. ACS Nano, **2011**, 5, 7503-7509.
13. Chithrani, B. D.; Ghazani, A. A.; Chan, Warren C. W. *Determining the Size and Shape Dependence of Gold Nanoparticle Uptake into Mammalian Cells*. Nano Lett., **2006**, 6, 662-668.

14. (a) Doorley, G. W.; Payne, C. K. *Cellular Binding of Nanoparticles in the Presence of Serum Proteins*. Chem. Commun., **2011**, 47, 466-468. (b) Doorley, G. W.; Payne, C. K. *Nanoparticles Act as Protein Carriers During Cellular Internalization*. Chem. Commun., **2012**, 48, 2961-2963.
15. Ryser, H.J.; Hancock, R. *Histones and Basic Polyamino Acids Stimulate the Uptake of Albumin by Tumor Cells in Culture*. Science, **1965**, 150, 501-503.
16. Pardridge, W. M.; Triguero, D.; Buciak, J. L. *Tissue Uptake of Immunoglobulin-G is Greatly Enhanced Following Cationization of the Protein*. Clin. Res., **1990**, 38, A133-A133.
17. Pujals, S.; Fernández-Carneado, J.; López-Iglesias, C.; Kogan, M. J.; Giralt, E. *Mechanistic Aspects of CPP-Mediated Intracellular Drug Delivery: Relevance of CPP Self-Assembly*. Biochim. Biophys. Acta-Biomem., **2006**, 1758, 264-279.
18. Heitz, F.; Morris, M. C.; Divita, G. *Twenty Years of Cell-Penetrating Peptides: from Molecular Mechanisms to Therapeutics*. Br. J. Pharm., **2009**, 157, 195-206.
19. Singh, D.; Bisland, S. K.; Kawamura, K.; Gariépy, J. *Peptide-Based Intracellular Shuttle Able To Facilitate Gene Transfer in Mammalian Cells*. Bioconj. Chem., **1999**, 10, 745-754.
20. Colin, M.; Harbottle, R. P.; Knight, A.; Kornprobst, M.; Cooper, R. G.; Miller, A. D.; Trugnan, G.; Capeau, J.; Coutelle, C.; Brahimi-Horn, M. C. *Liposomes Enhance Delivery and Expression of an RGD-Oligolysine Gene Transfer Vector in Human Tracheal Cells*. Gene Therapy, **1998**, 5, 1488-1498.
21. Coll, J-L.; Chollet, P.; Brambilla, E.; Desplanques, D.; Behr, J-P.; Favrot, M. *In Vivo Delivery to Tumors of DNA Complexed with Linear Polyethylenimine*. Human Gene Therapy, **1999**, 10, 1659-1666.
22. Perales, J. C.; Ferkol, T.; Molas, M.; Hanson, R. W. *An Evaluation of Receptor-Mediated Gene Transfer Using Synthetic DNA-Ligand Complexes*. Eur. J. Biochem., **1994**, 226, 255-266.
23. Tang, M. X.; Redemann, C. T.; Szoka, F. C. *In Vitro Gene Delivery by Degraded Polyamidoamine Dendrimers*. Bioconj. Chem., **1996**, 7, 703-714.
24. Kneuer, C.; Sameti, M.; Bakowsky, U.; Schiestel, T.; Schirra, H.; Schmidt, H.; Lehr, C-M. *A Nonviral DNA Delivery System Based on Surface Modified Silica-Nanoparticles Can Efficiently Transfect Cells in Vitro*. Bioconj. Chem., **2000**, 11, 926-932.
25. McIntosh, C. M.; Esposito, E. A.; Boal, A. K.; Simard, J. M.; Martin, C. T.; Rotello, V. M. *Inhibition of DNA Transcription Using Cationic Mixed Monolayer Protected Gold Clusters*. J. Am. Chem. Soc., **2001**, 123, 7626-7629.
26. Sandhu, K. K.; McIntosh, C. M.; Simard, J. M.; Smith, S. W.; Rotello, V. M. *Gold Nanoparticle-Mediated Transfection of Mammalian Cells*. Bioconj. Chem., **2002**, 13, 3-6.
27. Leroueil, P. R.; Berry, S. A.; Duthie, K.; Han, G.; Rotello, V. M.; Mc Nerny, D. Q.; Baker, J. R.; Orr, B. G.; Banaszak Holl, M. M. *Wide Varieties of Cationic Nanoparticles Induce Defects in Supported Lipid Bilayers*. Nano Lett., **2008**, 8, 420-424.
28. Lin, J.; Zhang, H.; Chen, Z.; Zheng, Y. *Penetration of Lipid Membranes by Gold Nanoparticles: Insights into Cellular Uptake, Cytotoxicity, and Their Relationship*. ACS Nano, **2010**, 4, 5421-5429.

29. Ghosh, P. S.; Han, G.; Erdogan, B.; Rosado, O.; Krovi, S. A.; Rotello, V. M. *Nanoparticles Featuring Amino Acid-functionalized Side Chains as DNA Receptors*. Chem. Biol. Drug Des., **2007**, *70*, 13-18.
30. Ghosh, P. S.; Kim, C.-K.; Han, G.; Forbes, N. S.; Rotello, V. M. *Efficient Gene Delivery Vectors by Tuning the Surface Charge Density of Amino Acid-Functionalized Gold Nanoparticles*. ACS Nano, **2008**, *2*, 2213-2218.
31. Niidome, T.; Nakashima, K.; Takahashi, H.; Niidome, Y. *Preparation of Primary Amine-Modified Gold Nanoparticles and their Transfection Ability into Cultivated Cells*. Chem. Commun., **2004**, 1978-1979.
32. Li, P.; Li, D.; Zhang, L.; Li, G.; Wang, E. *Cationic Lipid Bilayer Coated Gold Nanoparticles-Mediated Transfection of Mammalian Cells*. Biomater., **2008**, *29*, 3617-3624.
33. Chithrani, B. D.; Ghazani, A. A.; Chan, W. C. W. *Determining the Size and Shape Dependence of Gold Nanoparticle Uptake into Mammalian Cells*. Nano Lett., **2006**, *6*, 662-668.
34. Jiang, W.; KimBetty, Y. S.; Rutka, J. T.; Warren, C. W. C. *Nanoparticle-Mediated Cellular Response is Size-Dependent*. Nat. Nano, **2008**, *3*, 145-150.
35. Song, W.-J.; Du, J.-Z.; Sun, T.-M.; Zhang, P.-Z.; Wang, J. *Gold Nanoparticles Capped with Polyethyleneimine for Enhanced siRNA Delivery*. Small, **2010**, *6*, 239-246.
36. Nativo, P.; Prior, I. A.; Brust, M. *Uptake and Intracellular Fate of Surface-Modified Gold Nanoparticles*. ACS Nano, **2008**, *2*, 1639-1644.
37. Krpetić, Ž.; Saleemi, S.; Prior, I. A.; Sée, V.; Qureshi, R.; Brust, M. *Negotiation of Intracellular Membrane Barriers by TAT-Modified Gold Nanoparticles*. ACS Nano, **2011**, *5*, 5195-5201.
38. Soenen, S. J.; Manshian, B.; Montenegro, J. M.; Amin, F.; Meermann, B.; Thiron, T.; Cornelissen, M.; Vanhaecke, F.; Doak, S.; Parak, W. J.; De Smedt, S.; Braeckmans, K. *Cytotoxic Effects of Gold Nanoparticles: A Multiparametric Study*. ACS Nano, **2012**, *6*, 5767-5783.
39. Ghosh, P.; Yang, X.; Arvizo, R.; Zhu, Z.-J.; Agasti, S. S.; Mo, Z.; Rotello, V. M. *Intracellular Delivery of a Membrane-Impermeable Enzyme in Active Form Using Functionalized Gold Nanoparticles*. J. Am. Chem. Soc., **2010**, *132*, 2642-2645.
40. (a) Hong, R.; Han, G.; Fernández, J. M.; Kim, B.-J.; Forbes, N. S.; Rotello, V. M. *Glutathione-Mediated Delivery and Release Using Monolayer Protected Nanoparticle Carriers*. J. Am. Chem. Soc., **2006**, *128*, 1078-1079. (b) Han, G.; Chari, N. S.; Verma, A.; Hong, R.; Martin, C. T.; Rotello, V. M. *Controlled Recovery of the Transcription of Nanoparticle-Bound DNA by Intracellular Concentrations of Glutathione*. Bioconj. Chem., **2005**, *16*, 1356-1359.
41. Schulze, C.; Kroll, A.; Lehr, C.-M.; Schäfer, U. F.; Becker, K.; Schnekenburger, J.; Schulze Isfort, C.; Landsiedel, R.; Wohlleben, W. *Not Ready to Use - Overcoming Pitfalls when Dispersing Nanoparticles in Physiological Media*. Nanotoxicol., **2008**, *2*, 51-61.
42. García-Fernández, L.; Ojea-Jiménez, I.; Lorenzo, J.; Puentes, V. F. *Facile Preparation of Cationic Gold Nanoparticle-Bioconjugates for Cell Penetration and Nuclear Targeting*. ACS Nano, **2012**, *6*, 7692-7702.

43. (a) Lynch, I.; Salvati, A.; Dawson, K. A. *Protein-Nanoparticle Interactions: What does the Cell See?* Nat. Nanotechnol., **2009**, 4, 546. (b) Walczyk, D.; Baldelli-Bombelli, F.; Monopoli, M. P.; Lynch, I.; Dawson, K. A. *What the Cell “Sees” in Bionanoscience*. J. Am. Chem. Soc., **2010**, 132, 5761.
44. Nel, A. E.; Madler, L.; Velegol, D.; Xia, T.; Hoek, E. M. V.; Somasundaran, P.; Klaessig, F.; Castranova, V.; Thompson, M. *Understanding Biophysicochemical Interactions at the Nano-Bio Interface*. Nat. Mater., **2009**, 8, 543-557.
45. Lévy, R.; Shaheen, U.; Cesbron, Y.; Sée, V. *Gold Nanoparticles Delivery in Mammalian Cells: A Critical Review*. Nano Rev., **2010**, 1, 4889-4907.
46. Harush-Frenkel, O.; Debotton, N.; Benita, S.; Altschuler, Y. *Targeting of Nanoparticles to the Clathrin-Mediated Endocytic Pathway*. Biochem. Biophys. Res. Commun., **2007**, 353, 26-32.
47. Hu, Y.; Litwin, T.; Nagaraja, A. R.; Kwong, B.; Katz, J.; Watson, N.; Irvine, D. J. *Cytosolic Delivery of Membrane-Impermeable Molecules in Dendritic Cells Using pH-Responsive Core-Shell Nanoparticles*. Nano Lett., **2007**, 7, 3056-3064.
48. Guo, S.; Huang, Y.; Jiang, Q.; Sun, Y.; Deng, L.; Liang, Z.; Du, Q.; Xing, J.; Zhao, Y.; Wang, P. C.; Dong, A.; Liang, X-J. *Enhanced Gene Delivery and siRNA Silencing by Gold Nanoparticles Coated with Charge-Reversal Polyelectrolyte*. ACS Nano, **2010**, 4, 5505-5511.
49. Conner, S. D.; Schmid, S. L. *Regulated Portals of Entry into the Cell*. Nature, **2003**, 422, 37-44.
50. Huth, S.; Lausier, J.; Gersting, S. W.; Rudolph, C.; Plank, C.; Welsch, U.; Rosenecker, J. *Insights Into the Mechanism of Magnetofection Using PEI-Based Magnetofectins for Gene Transfer*. J. Gene Med., **2004**, 6, 923-936.
51. Ma, Z.; Lim, L.Y. *Uptake of Chitosan and Associated Insulin in Caco-2 Cell Monolayers: a Comparison Between Chitosan Molecules and Chitosan Nanoparticles*. Pharm. Res., **2003**, 20, 1812-1819.
52. Shukla, R.; Bansal, V.; Chaudhary, M.; Basu, A.; Bhonde, R. R.; Sastry, M. *Biocompatibility of Gold Nanoparticles and Their Endocytotic Fate Inside the Cellular Compartment: A Microscopic Overview*. Langmuir, **2005**, 21, 10644-10654.
53. Krpetić, Ž.; Nativo, P.; Sée, V.; Prior, I. A.; Brust, M.; Volk, M. *Inflicting Controlled Nonthermal Damage to Subcellular Structures by Laser-Activated Gold Nanoparticles*. Nano Lett., **2010**, 10, 4549-4554.
54. El-Sayed, A.; Khalil, I. A.; Kogure, K.; Futaki, S.; Harashima, H. *Octaarginine- and Octalysine-modified Nanoparticles Have Different Modes of Endosomal Escape*. J. Biol. Chem., **2008**, 283, 23450-23461.
55. Yezhelyev, M. V.; Qi, L.; O'Regan, R. M.; Nie, S.; Gao, X. *Proton-Sponge Coated Quantum Dots for siRNA Delivery and Intracellular Imaging*. J. Am. Chem. Soc., **2008**, 130, 9006-9012.
56. Dominska, M.; Dykxhoorn, D. M. *Breaking Down the Barriers: siRNA Delivery and Endosome Escape*. J. Cell Sci., **2010**, 123, 1183-1189.
57. Lévy, R. *Peptide-Capped Gold Nanoparticles: Towards Artificial Proteins*. Chem.Bio.Chem., **2006**, 7, 1141-1145.

58. Ojea-Jimenez, I.; Puentes, V. *Instability of Cationic Gold Nanoparticle Bioconjugates: The Role of Citrate Ions*. *J. Am. Chem. Soc.*, **2010**, 132, 5322-5322.
59. Zhang, J.; Chi, Q.; Nielsen, J. U.; Friis, E. P.; Andersen, J. E. T.; Ulstrup, J. *Two-Dimensional Cysteine and Cystine Cluster Networks on Au(111) Disclosed by Voltammetry and in Situ Scanning Tunneling Microscopy*. *Langmuir*, **2000**, 16, 7229-7237.
60. Pale-Grosdemange, C.; Simon, E. S.; Prime, K. L.; Whitesides, G. M. *Formation of Self-Assembled Monolayers by Chemisorption of Derivatives of Oligo(ethylene glycol) of Structure HS(CH₂)₁₁(OCH₂CH₂)_mOH on gold*. *J. Am. Chem. Soc.*, **1991**, 113, 12-20.
61. Kanaras, A. G.; Kamounah, F. S.; Schaumburg, K.; Kiely, C. J.; Brust, M. *Thioalkylated Tetraethylene Glycol: A New Ligand for Water Soluble Monolayer Protected Gold Clusters*. *Chem. Commun.*, **2002**, 20, 2294-2295.
62. Doty, R. C.; Tshikhudo, T. R.; Brust, M.; Fernig, D. G. *Extremely Stable Water-Soluble Ag Nanoparticles*. *Chem. Mater.*, **2005**, 17, 4630-4635.
63. Cheng, W.; Wang, E. *Size-Dependent Phase Transfer of Gold Nanoparticles from Water into Toluene by Tetraoctylammonium Cations: A Wholly Electrostatic Interaction*. *J. Phys. Chem. B*, **2003**, 108, 24-26.
64. Krpetic, Z.; Nativo, P.; Prior, I. A.; Brust, M. *Acrylate-Facilitated Cellular Uptake of Gold Nanoparticles*. *Small*, **2011**, 7, 1982-1986.
65. Rosi, N. L.; Giljohann, D. A.; Thaxton, C. S.; Lytton-Jean, A. K. R.; Han, M. S.; Mirkin, C. A. *Oligonucleotide-Modified Gold Nanoparticles for Intracellular Gene Regulation*. *Science*, **2006**, 312, 1027-1030.
66. Based on electron diffraction studies of monolayers of alkanethiolates on Au(111) surface, which show a calculated area per molecule of 21.4 Å² (ref. 67), the maximum surface density of 13 nm Au NPs would correspond to approximately 2150 AUT molecules per NP.
67. Sellers, H.; Ulman, A.; Shnidman, Y.; Eilers, J. E. *Structure and Binding of Alkanethiolates on Gold and Silver Surfaces: Implications for Self-Assembled Monolayers*. *J. Am. Chem. Soc.*, **1993**, 115, 9389-9401.
68. Puentes, V. F.; Gorostiza, P.; Aruguete, D. M.; Bastus, N. G.; Alivisatos, A. P. *Collective Behaviour in Two-Dimensional Cobalt Nanoparticle Assemblies Observed by Magnetic Force Microscopy*. *Nat. Mater.*, **2004**, 3, 263-268.
69. Levy, R.; Thanh, N. T. K.; Doty, R. C.; Hussain, I.; Nichols, R. J.; Schiffrin, D. J.; Brust, M.; Fernig, D. G. *Rational and Combinatorial Design of Peptide Capping Ligands for Gold Nanoparticles*. *J. Am. Chem. Soc.* **2004**, 126, 10076-10084.
70. Pernodet, N.; Fang, X.; Sun, Y.; Bakhtina, A.; Ramakrishnan, A.; Sokolov, J.; Ulman, A.; Rafailovich, M. *Adverse Effects of Citrate/Gold Nanoparticles on Human Dermal Fibroblasts*. *Small*, **2006**, 2, 766-773.
71. The measured concentration of Au³⁺ was divided by the number of Au atoms per NP to obtain the concentration of AuNPs in solution. The number of Au atoms per NP was calculated using the NP

diameter, the density of bulk Au, and the molecular weight of Au; the value was 6×10^4 Au atoms per NP.

72. Elbakry, A.; Zaky, A.; Liebl, R.; Rachel, R.; Goepferich, A.; Breunig, M. *Layer-by-Layer Assembled Gold Nanoparticles for siRNA Delivery*. *Nano Lett.*, **2009**, *9*, 2059-2064.

Introduction to the Controlled Bioconjugation of Antibodies on Gold Nanoparticles



Antibodies (Abs) are one of the most important classes of biological agents to be combined with inorganic NPs for basic research and applications that make use of their directed specificity, high affinity and large availability. Their chemical coupling to NPs impart them additional functions, such as target recognition,^{1,2} therapeutic activity,^{3,4} and additional stability.⁵ As well, the NPs provide unique platforms that confer multivalent capacity⁶⁻⁸ and increased stability in addition to their physicochemical properties.^{9,10} All these benefits have made Ab-NP bioconjugates promising candidates for a wide variety of applications, ranging from targeted drug delivery, tissue repair, contrast agents for magnetic resonance imaging (MRI), sensing, cell sorting, bioseparation, enzyme immobilization, immunoassays, transfection (e.g. gene delivery) to purification.¹¹

The unique structural characteristics of Abs supply a number of choices for modification and conjugation schemes.¹² However, the range of bioconjugate chemistries used to functionalize them with NPs has lagged behind the multitude of biological applications proposed (see Chapter 5, Section 5.1.4). Main drawbacks from currently used strategies are that they lack from chemical specificity, orientation of the Abs on the NPs surface or control over the number of surface-bound Abs. These, in turn, are important parameters that define the Abs performance and the overall functionality of the Ab-NP bioconjugate, and would allow quantification and improve reproducibility. In particular, the design of Ab-NP bioconjugates has an increased significance in mediating biological effects, such as their interactions with their cell surface receptors (see Chapter 6, Section 6.2). Recent studies have shown that Abs

undergo different endocytic pathways when bound to the surface of Au NPs or free in solution, probably due to the different presentation of Abs to the cell.¹³ In addition, the size of Ab-Au NP bioconjugates has been observed to be critical in cellular uptake, proliferation and signalling processes, due to the curvature-dependent Abs density on the NPs.¹⁴ The ligand coverage of the NPs, and thus the strength of the ligand/receptor interactions, has also been identified as a crucial parameter in endocytic processes.^{15,16} As expected, these findings suggest that the biological response depends on fine structural features beyond the NP bioconjugate composition.

The need to achieve a greater control in the display of Abs on NPs makes us to focus the second part of this Thesis in the development and study of an efficient synthetic route that allows the controlled formation of Ab-NP bioconjugates; that is, with controlled architecture, conformation and therefore performance. This goal is especially important for biomedical applications in which scientists have started imaging the development of new tools for a controlled addressing of cell transmembrane receptors. The strategy described herein is based on the derivatization of Abs before conjugation to the NP rather than the standard approach of functionalizing the NP before attaching it to the Abs. This reaction scheme provides a controlled binding of Abs to Au NPs through strong Au-S interactions, resulting in an optimum Ab orientation for maximizing the recognition capability of the bioconjugates and a well-defined number of Abs per NP. Such synthetic control is demonstrated by the formation of rationally designed NP superstructures based on specific Ab-antigen interactions (Chapter 5), and it is used to explore and manipulate specific cellular receptor interactions with Au NPs coupled to a biologically relevant monoclonal Ab (Chapter 6). Thus, in Chapter 5, it is presented a complete physicochemical characterization of a covalent and site-directed coupling of Abs to Au NPs through a heterobifunctional linker, which opens up the possibility to better control the orientation and number of Abs on the Au NPs surface. As proof of concept, a series of Ab-Au NP bioconjugates with well-defined structures have been prepared to direct the assembly of NPs into complex superstructures (*i.e.* dimers, trimers and satellite-shaped assemblies), further proving the preserved activity of the Ab molecules after coupling. This type of NP superstructures have been largely studied with DNA due to its controlled conjugation to NPs,^{17,18} but attempts to use specific Ab-antigen interactions have only resulted in the formation of large aggregates.¹⁹ In addition, in Chapter 6, this site-directed chemistry

has been explored for the bioconjugation of Au NPs with the anti-epidermal growth factor receptor (EGFR) Ab Cetuximab (IMC-225, trade name Erbitux), a monoclonal Ab of wide importance in cancer therapeutics.²⁰ Importantly, it is demonstrated that the molecular interactions between EGF cell-surface receptors in an epidermoid cancer cell line (A431) and the Cetuximab-Au NP bioconjugates are strictly dependent on the Ab-NP structure. By controlling the local concentration of Abs and orientation/presentation of the ligands to the cell surface, the NP-membrane receptor binding, receptor distribution, receptor endocytosis and recycling, and subsequent intracellular signal transduction, have been precisely tuned. These results show that the formation of Ab-NP structures with controlled morphology and stability is essential to explore complex cell behaviours.

References

1. El-Sayed, I. H.; Huang, X.; El-Sayed, M. A. *Surface Plasmon Resonance Scattering and Absorption of anti-EGFR Antibody Conjugated Gold Nanoparticles in Cancer Diagnostics: Applications in Oral Cancer*. *Nano Lett.*, **2005**, 5, 829-834.
2. Patra, C. R.; Bhattacharya, R.; Wang, E.; Katarya, A.; Lau, J. S.; Dutta, S.; Muders, M.; Wang, S.; Buhrow, S. A.; Safgren, S. L.; Yaszemski, M. J.; Reid, J. M.; Ames, M. M.; Mukherjee, P.; Mukhopadhyay, D. *Targeted Delivery of Gemcitabine to Pancreatic Adenocarcinoma Using Cetuximab as a Targeting Agent*. *Cancer Res.*, **2008**, 68, 1970-1978.
3. Adams, G. P.; Weiner, L. M. *Monoclonal Antibody Therapy of Cancer*. *Nat. Biotech.*, **2005**, 23, 1147-1157.
4. Yokoyama, T.; Tam, J.; Kuroda, S.; Scott, A. W.; Aaron, J.; Larson, T.; Shanker, M.; Correa, A. M.; Kondo, S.; Roth, J. A.; Sokolov, K.; Ramesh, R. *EGFR-Targeted Hybrid Plasmonic Magnetic Nanoparticles Synergistically Induce Autophagy and Apoptosis in Non-Small Cell Lung Cancer Cells*. *PLOS ONE*, **2011**, 6, e25507.
5. Goy-López, S.; Juárez, J.; Alatorre-Meda, M.; Casals, E.; Puntos, V. F.; Taboada, P.; Mosquera, V. *Physicochemical Characteristics of Protein-NP Bioconjugates: The Role of Particle Curvature and Solution Conditions on Human Serum Albumin Conformation and Fibrillogenesis Inhibition*. *Langmuir*, **2012**, 28, 9113-9126.
6. Jiang, W.; KimBetty, Y. S.; Rutka, J. T.; Chan Warren, C. W. *Nanoparticle-Mediated Cellular Response is Size-Dependent*. *Nat. Nano*, **2008**, 3, 145-150.
7. Huang, Y.-F.; Liu, H.; Xiong, X.; Chen, Y.; Tan, W. *Nanoparticle-Mediated IgE-Receptor Aggregation and Signaling in RBL Mast Cells*. *J. Am. Chem. Soc.*, **2009**, 131, 17328-17334.

8. Wang, J.; Tian, S.; Petros, R. A.; Napier, M. E.; DeSimone, J. M. *The Complex Role of Multivalency in Nanoparticles Targeting the Transferrin Receptor for Cancer Therapies*. *J. Am. Chem. Soc.*, **2010**, 132, 11306-11313.
9. Eck, W.; Nicholson, A. I.; Zentgraf, H.; Semmler, W.; Bartling, S. *Anti-CD4-targeted Gold Nanoparticles Induce Specific Contrast Enhancement of Peripheral Lymph Nodes in X-ray Computed Tomography of Live Mice*. *Nano Lett.*, **2010**, 10, 2318-2322.
10. Haun, J. B.; Devaraj, N. K.; Hilderbrand, S. A.; Lee, H.; Weissleder, R. *Bioorthogonal Chemistry Amplifies Nanoparticle Binding and Enhances the Sensitivity of Cell Detection*. *Nat. Nano.* **2010**, 5, 660-665.
11. Arruebo, M.; Valladares, M.; González-Fernández, A. *Antibody-Conjugated Nanoparticles for Biomedical Applications*. *J. Nanomater.*, **2009**, 1-24.
12. Hermanson, G. T. *Bioconjugate Techniques*, 2nd ed., Academic Press, San Diego, **2008**.
13. Bhattacharyya, S.; Bhattacharya, R.; Curley, S.; McNiven, M. A.; Mukherjee, P. *Nanoconjugation Modulates the Trafficking and Mechanism of Antibody Induced Receptor Endocytosis*. *Proc. Natl. Acad. Sci. U.S.A.*, **2010**, 107, 14541-14546.
14. Jiang, W.; KimBetty, Y. S.; Rutka, J. T.; Chan Warren, C. W. *Nanoparticle-Mediated Cellular Response is Size-Dependent*. *Nat. Nano.* **2008**, 3, 145-150.
15. Maus, L.; Dick, O.; Bading, H.; Spatz, J. P.; Fiammengo, R. *Conjugation of Peptides to the Passivation Shell of Gold Nanoparticles for Targeting of Cell-Surface Receptors*. *ACS Nano*, **2010**, 4, 6617-6628.
16. Vácha, R.; Martinez-Veracoechea, F. J.; Frenkel, D. *Receptor-Mediated Endocytosis of Nanoparticles of Various Shapes*. *Nano Lett.*, **2011**, 11, 5391-5395.
17. Mirkin, C. A.; Letsinger, R. L.; Mucic, R. C.; Storhoff, J. J. *A DNA-Based Method for Rationally Assembling Nanoparticles into Macroscopic Materials*. *Nature*, **1996**, 382, 607-609.
18. Alivisatos, A. P.; Johnsson, K. P.; Peng, X.; Wilson, T. E.; Loweth, C. J.; Bruchez, M. P.; Schultz, P. G. *Organization of 'Nanocrystal Molecules' Using DNA*. *Nature*, **1996**, 382, 609-611.
19. Shenton, W.; Davis, S. A.; Mann, S. *Directed Self-Assembly of Nanoparticles into Macroscopic Materials Using Antibody-Antigen Recognition*. *Adv. Mater.*, **1999**, 11, 449-452.
20. Li, S.; Schmitz, K. R.; Jeffrey, P. D.; Wiltzius, J. J. W.; Kussie, P.; Ferguson, K. M. *Structural Basis for Inhibition of the Epidermal Growth Factor Receptor by Cetuximab*. *Cancer Cell*, **2005**, 7, 301-311.

Controlled Display of Antibodies on Gold Nanoparticles:

5

Biomolecular Orientation and Ratio of Bioconjugation

Numerous straightforward physicochemical methods have been proposed to couple and functionalize various types of NPs with Abs. Some examples are summarized in this Chapter and in some excellent reviews on this topic.^{1,2} Nevertheless, despite the apparent importance of bioconjugating Abs to nanoparticulate systems, **the preparation of physicochemically well-defined bioconjugates and the optimization of the Ab bioconjugation chemistry are still limiting factors to their progress in practical biomedical applications.** In this regard, it has been recently recognized that the ability to prepare NP bioconjugates in a controlled manner is highly desirable. It is paramount in obtaining bioconjugates with well-defined and reproducible properties.³

In this Chapter, a site-directed chemistry has been thoroughly studied to obtain an improved control in the preparation of Ab-Au NP bioconjugates, including control over Ab binding ratio, orientation on the NP surface and functionality. In these bioconjugates, the mobility of the Abs and the separation distance between the Abs and the NP are advantageous to their interaction with molecular receptors. Opposite to conventional covalent strategies that require multiple NP-functionalization steps,⁴⁻⁸ the Abs are first chemically modified with an heterobifunctional linker for their direct coupling onto Au NPs. This strategy opens up the possibility to better control the orientation, number and binding capacity of such Ab molecules on Au NPs. In addition, by avoiding intermediate steps of functionalization, we have gained in stability and reproducibility, since the conditions required for the chemistry of reactive groups are

often not compatible with colloidal stability of the NPs or structure integrity of the Abs. Such high degree of control has been especially critical in creating a series of Ab-Au NP bioconjugates for their rational assembly into complex superstructures, which, to our knowledge, remains a challenge faced by nanoparticle-based materials chemistry using Ab-antigen cross-links. Importantly, the formation of these novel Ab-based superstructures opens the door to employ proteins with additional functionality when compared to DNA-based superstructures.⁹⁻¹¹ Such structures have been considered paradigmatic/paramount in the nanobiotechnology field.

5.1. Introduction.

The following Section presents a description of the functions and classes of Ab molecules, and in particular, a structural description of the immunoglobulin G (IgG). The main approaches exploiting its unique structural characteristics to the bioconjugation with NPs are discussed. Finally, an additional part describes the synthetic methods used in this Thesis to prepare aqueous monodisperse Au NPs of different sizes for the Ab bioconjugation studies.

5.1.1. Antibody functions and isotypes.

Abs, also referred to as immunoglobulins (Igs), are glycoproteins found in plasma and extracellular fluids that comprise one of the principal effectors of the adaptive (humoral) immune system. They are produced in the body by a special type of white blood cells called B-lymphocytes, or simply B-cells. When a foreign substance (referred to as pathogen/antigen) enters the body, B-cells undergo a rearrangement in their genes to produce Ab molecules which are capable of interacting with the antigen in a highly specific manner; that is, the antigen-binding sites on the surface of the B-cell bind a small region of the pathogen called the “epitope”, which has a complementary shape. Through such interactions, Abs are involved in a number of biological effects (Figure 5.1),¹² such as: i) neutralizing toxic substances (“toxins”) of microbial origin; ii) agglutinating (*i.e.* cause to clump) bacteria and other microbes; iii) tagging the microbes (a process called “opsonization”) such that certain immune effector cells (such as

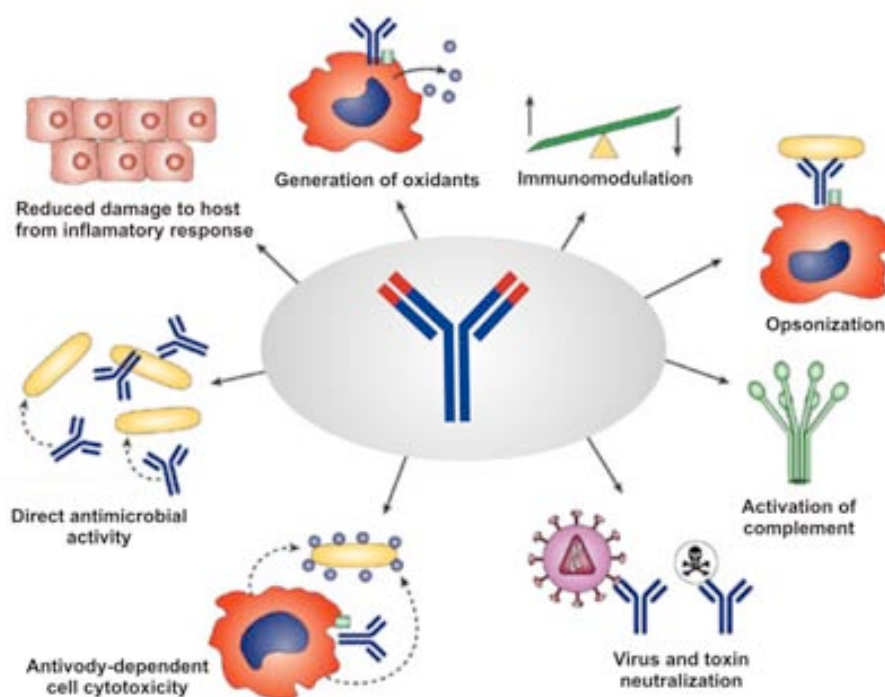


Figure 5.1. Different biological effects of Abs. Image adapted from ref. 12.

macrophages, dendritic cells and neutrophils) can recognize and destroy the microbes by internalizing, via a process called “phagocytosis”, and breaking them down; iv) inducing certain immune effector cells (such as neutrophils, basophils, eosinophils, mast cells and cytotoxic T and Natural Killer lymphocytes) to release potent antimicrobial molecules (via a process called “degranulation”) that can destroy invading microbes; v) directly killing certain microbes by interfering with their uptake of essential substances, or damaging their outer membrane; vi) activating certain serum proteins (called “complement”) to form a complex that can poke holes into the membrane of certain bacteria, causing them to lyse (*i.e.* be destroyed by dissolution).

In mammals, there exist five different Ab classes or isotypes with similar composition but different chemistries (Table 5.1): IgG, IgA, IgM, IgD and IgE. The Ig class determines both the type and the temporal nature of the immune response. In addition, IgA and IgG isotypes present different subclasses (IgA1 and IgA2; IgG1, IgG2, IgG3 and IgG4), each having different functions. All Igs within one class share about 90% homology, but only 60% among classes. They are all made of basic Y-shaped structural units; each with two large heavy chains and two small light chains (further description in Section 5.1.3). Their heavy chains differ in primary structure,

carbohydrate content, and antigenic properties amongst Ab classes, whereas light chain types are the same for all classes (*i.e.* either lambda (λ) or kappa (κ)). In addition, all Igs contain two or more carbohydrate chains, usually linked to their heavy chains. Light chains are usually free of carbohydrate components. Because of its relative abundance (approximately 75% of human serum Igs) and excellent specificity toward antigens, IgG is the principle Ab used in immunological research and clinical diagnostics. For this reason, IgG molecules have been chosen in this Thesis for NP functionalization studies; further details on IgG structure are described in Section 5.1.3.






	IgG	IgA (dimer only)	IgM	IgD	IgE
					
Form	Monomer	Dimer, Monomer	Pentamer	Monomer	Monomer
Number of antigen binding sites	2	4,2	10	2	2
Molecular Weight (kDa)	150	160	950	180	190
Carbohydrates (%)	3	7.5	12	12	12
No. of Oligosaccharide Chains per Constant Region	1	5	-	3	6
Percentage of Total Antibody in Serum (%)	80	13	6	1	0.002
Average Half-Life in Serum (Days)	23	6	5	3	2,5
Biological Function	Long-term immunity; memory Abs; neutralizes toxins; opsonizes; fixes complement.	Secretory Ab; on mucous membranes	Produced at first response to antigen; can serve as B-cell receptor	Receptor on B-cells	Ab of allergy; worm infections

Table 5.1. Characteristics of the Ig classes. Adapted from The McGraw-Hill Companies, Inc. and ref. 13 and 14.

5.1.2. Polyclonal and monoclonal antibodies.

The immune response to an antigen generally involves the activation of multiple B-cells, all of which target a specific site or epitope on that antigen. As a result, a large number of Abs are produced with different specificities and epitope affinities, which are known as **polyclonal antibodies** (PAbs). For production purposes, pAbs are generally purified from the serum of immunized animals where the antigen of interest stimulates the B-lymphocytes to produce a diverse range of Igs specific to that antigen. In contrast, **monoclonal antibodies** (MAbs) represent a single B lymphocyte generating Abs to one specific epitope. B cells can be fused with myeloma cells with the resulting immortal hybridomas, each producing a unique MAb. The main differences between PAbs and MAbs, which can be either advantages or disadvantages, are listed in Table 5.2. In this Thesis, PAbs have been employed to optimize the Ab-NP bioconjugation strategy (Chapter 5), since they are commonly found in nature, carbohydrate-rich and inexpensive. Further, MAbs have been used to explore the interactions between MAb-NP bioconjugates and their specific cell membrane receptors (Chapter 6), due to its high specificity and homogeneity.

Monoclonal Abs	Polyclonal Abs
Homogeneous and consistent	Heterogeneous and can be batch to batch variability
Monospecificity	Recognizes multiple epitopes on any one antigen
Sensitive to small structural changes in an epitope	Small structural changes in an epitope are not significant to its function
Susceptible to small changes of pH and salt concentration	Stable over a broad range of pH and salt concentration
Can be generated as a constant and renewable source by hybridomas	Generated using multiple animals
Generated at higher concentration and purity (~50-200 mg/ml generated as ascites)	Obtained at much lower concentration and purity (~5-20 mg/ml Ig in polyclonal sera)
Expensive to produce, high technology	Inexpensive to produce, low technology

Table 5.2. Main differences between polyclonal and monoclonal Abs.

5.1.3. Immunoglobulin G (IgG) structure.

IgG is one of the most abundant proteins in the blood serum (~10 mg/ml).¹³ It is composed of four polypeptide chains: two identical large or heavy chains (H) of about 50-60 kDa, and two small or light chains (L) of about 23 kDa linked by noncovalent interactions as well as a number of disulfide bonds (Figure 5.2). The heavy chains are disulfide-bonded to each other in the hinge region, and then branch to interact separately with the light chains by disulfide-bonds, forming a “Y” shaped molecule. The number of disulfide bonds and the length and flexibility of the hinge region differ amongst IgG subclasses. The arms of the “Y” contain the sites where two antigens can bind, and they

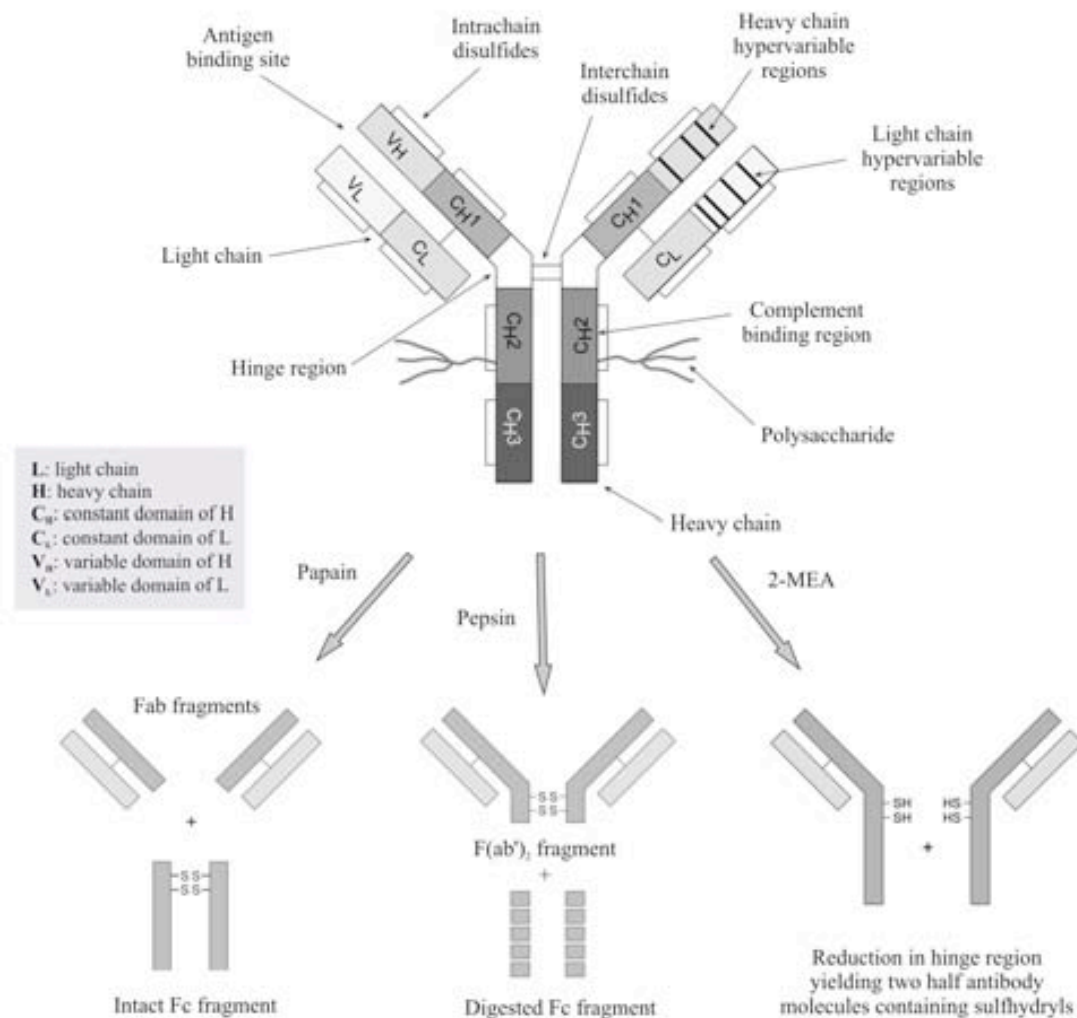


Figure 5.2. Schematic representation of the structure of an IgG (top) and common strategies used for the fragmentation of Abs (bottom). Two common fragmentation strategies are proteolytic digestion (e.g. with papain and pepsin) and reduction of disulfides (e.g. with 2-MEA). Image adapted from ref. 17.

are referred to as Fab (fragment antigen binding) regions. It is composed of one constant and one variable domain from each H and L chain of the Ab. The variable domains of L and H (V_H , V_L) present most of the variability in amino acid sequence. Importantly, the unique orientation of these domains in three-dimensional space creates a binding site of high affinity for a particular antigen, due to both structural complementarity as well as the combination of van der Waals, ionic, hydrophobic, and hydrogen bonding forces, which may be created at each point of contact. The base of the “Y”, called the Fc (fragment crystallizable) region, is composed of two H chains containing two constant domains. Polysaccharides or carbohydrate chains are typically attached to the asparagine 297 (ASN-297) residue from the C_H2 domain within the Fc region¹⁵ (Figure 5.3).

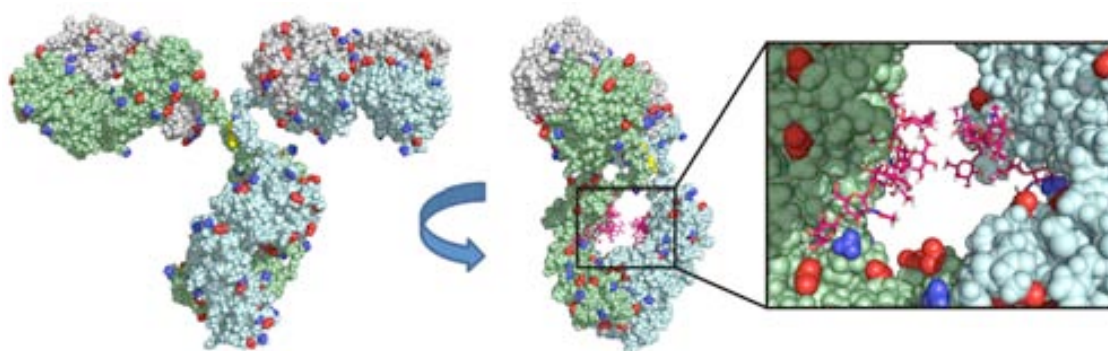


Figure 5.3. Crystal structure of an IgG (Protein Data Bank, PDB 1IGT), showing the position of carbohydrate residues in the asparagine 297 (ASN-297) residue from the C_H2 domain within the Fc region (pink). Light and heavy chains from the Ab are colored grey and green-blue, respectively. Nitrogen and oxygen atoms are colored dark blue and red, and sulfur atoms are colored yellow.

IgG molecules possess a number of functional groups suitable for conjugation to NPs. The most abundant ones are amine (e.g. lysine ϵ -amine and N-terminal α -amine groups) and carboxylate groups (e.g. C-terminal end, aspartic acid and glutamic acid residues), which are uniformly distributed throughout the surface topology of Abs. These may be exploited to covalently couple Ab molecules to the surface of NPs (e.g. *via* EDC/NHS chemistry), albeit cross-linking of molecules to the antigen-binding sites as well as random orientation of the Ab molecules on the NPs surface may decrease their antigen binding activity.

A more efficient strategy to preserve the activity of Abs is to use functional groups that are present in limiting quantities and only at discrete sites on the molecule, usually chosen to be distant from the antigen binding sites. In this regard, carbohydrate chains are especially suitable since they are typically attached to the Fc region.¹⁵ Thus, they can serve as specific sites for conjugation to NPs, e.g. through mild oxidation of the polysaccharide sugar residues to generate aldehyde groups for coupling with a hydrazide-containing molecule^{16,17} By coupling through its carbohydrate chains, the IgG molecule can be oriented so that its bivalent binding potential for antigen remains accessible.

Ab fragments can also be produced by cleavage of the disulfides in the hinge region that hold the heavy chains together (Figure 5.2, bottom). Common strategies that produce Ab fragments (*i.e.* Fab, Fc, F(ab')₂ and Fab') are consisted on proteolytic digestion (e.g. with pepsin or papain) and reduction of disulfides (e.g. by using 2-mercaptoethylamine (2-MEA)).¹⁷ Such fragments expose sulfhydryl groups which can bind to the NPs, however, they are limited by structural rigidity on the NP surface and its decreased avidity. Note that bivalency of Abs is essential to regulate cell functions, e.g. receptor dimerization and inhibiting tumor cell proliferation.¹⁸ Smaller Ab fragments can also be engineered, such as single monomeric variable Ab domains, called nanobodies, and single-chain variable fragments (scFv), which are fusion proteins of V_H and V_L of IgGs, connected with a short linker peptide.

5.1.4. Antibody-NP bioconjugation strategies.

In general, IgG molecules are coupled to NPs via four major strategies, which are mainly based on: i) adsorption through electrostatic, hydrophobic and Van der Waals interactions), ii) covalent coupling through their amine/carboxylate groups, iii) binding with bacterial proteins such as protein A (pA) or G (pG), and iv) covalent coupling through their polysaccharide chains. Advantages and limitations from these methods are discussed below.

Since 1971 the coupling of Abs to Au NPs has been extensively used to label biological samples for imaging in electron microscopy.¹⁹ This typical *immunogold* is

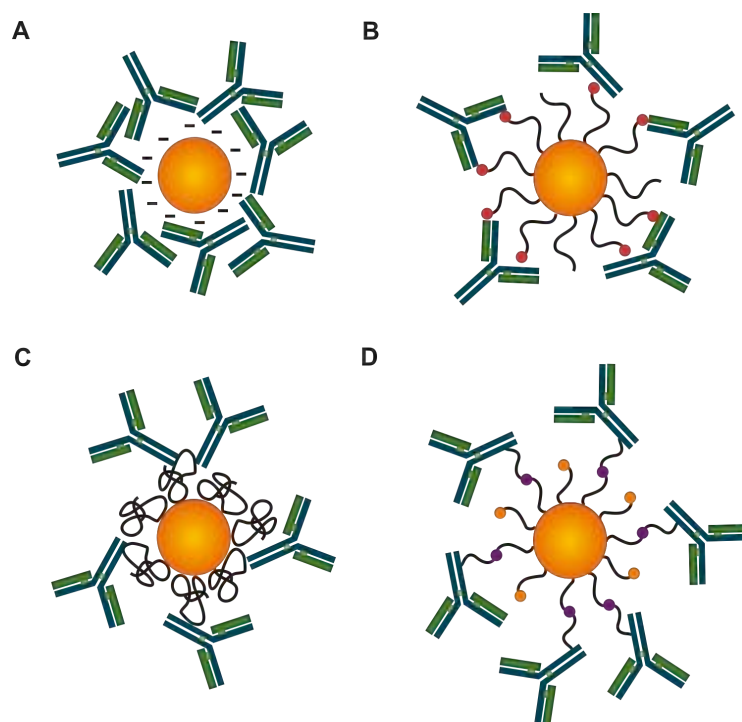


Figure 5.4. Schematic representation of the general strategies used for the coupling of Abs onto Au NPs. A) Adsorption of Abs through electrostatic, hydrophobic and Van der Waals interactions. B) Activation of carboxylic terminal groups from the NPs (red) and coupling to primary amines from Abs. C) Functionalization of NPs with proteins (pA or pG) having a high binding affinity for the Abs' Fc region. D) Oxidation of oligosaccharide chains of Abs for the addition of functional groups (violet) and reaction with functional groups in the NPs (orange).

formed by physisorption of Abs onto Au NPs via electrostatic, hydrophobic and Van der Waals interactions, leading to a random orientation of the Abs immobilized on the NPs (Figure 5.4-A). Its simplicity of preparation has been the motive of many applications in biodiagnostics and targeted therapy.²⁰⁻²³ By this method, however, quantitative data of the amount of protein to be added and the composition of the final product are scarce. For instance, the optimum protein concentration required to stabilize a given solution of NPs is typically determined by an inaccurate NaCl titration method.²⁴ For example, the minimum protein concentration at which 10% NaCl does not cause NP aggregation is determined to be the optimal, although an excess over the minimum has been observed to increase the NP bioconjugate functionality,^{25,26} probably due to the fact that a complete NPs coverage is not needed to stabilize them.²⁷ Another important limitation of this approach is that the adsorbed Abs may undergo a competitive displacement by high affinity proteins and blood components in the *in vitro* and *in vivo* applications.^{28,29}

Covalent coupling of Abs generally overcomes such limitations. Two important benefits from covalent binding are an increased Ab stability and a better control over available protein binding sites. Some of these methods are based on the use of Ab fragments.³⁰⁻³² For example, carboxylate-modified poly(lactic-co-glycolic acid) (PLGA) NPs were preactivated by using the common EDC/NHS coupling chemistry, and then coupled to Fab' rhuMAbHER2 or anti-CD25 Ab fragments through their amino groups.³¹ In a more sophisticated conjugation, Ackerson *et al.*³² mutated scFv Ab fragments to present an exposed cysteine residue for a pseudocovalent binding to Au NPs. However, the binding of intact IgGs is generally more challenging, since the utility and effectiveness of these biomolecules is often dependent on their bivalent capacity,^{18,33} in addition of the needed Ab mobility and flexibility to properly function. Typical IgG coupling chemistries make use of their reactive amine groups, mainly lysine ϵ -amine and N-terminal α -amine groups, or carboxylate groups from the C-terminal end as well as aspartic acid and glutamic acid residues. The most common example of this approach is the EDC/NHS coupling chemistry; for example to bind the primary amines from the lysine residues of Abs with carboxy-terminated NPs.^{6,8,34} Other examples include the introduction of epoxy³⁴ and cyano³⁵ groups on the NPs that interact with amino groups on the Abs (note that epoxy groups can also interact with other nucleophilic groups, such as hydroxyl and thiol moieties). These strategies have been extensively used, although two main drawbacks limit the efficiency of this method: on one hand, since the Abs are linked to the NPs in a random orientation, a certain percentage of their antigen binding sites can be occluded (Figure 5.4-B); on the other hand, controlling the number of Abs attached to Au NPs is quite difficult since both Au NPs and Abs possess multiple functional groups capable to interact with each other.

A third strategy is based on the capping of Au NPs by pA or pG from the bacterial cell wall of *Staphylococcus aureus*, which are well-known to bind the Ab' Fc portion with high affinity.^{36,37} Some examples include the immobilization of pA onto Au NPs via N-succinimidyl 3-(2-pyridyldithio)propionate (SPDP) to orient the binding of anti-cotinine Abs,⁵ and the direct adsorption of pA on the surface of Au NPs for binding studies of human IgG.⁷ Although this method provides an oriented coupling of the Abs upon binding to pA or pG (Figure 5.4-C), the number of conjugated Abs per NP can vary as a function of both, the number and orientation of the pA or pG molecules on the

NP surface and the available reactive sites containing each protein; e.g. up to 2-3 IgG can be bound in one pA with high affinity (10^{10} - 10^{11} M⁻¹).^{7,38,39} In addition, the affinity of pA for Au NP is very low since it exhibited marked desorption,⁴⁰ and only at very high protein concentrations NPs stability is reached in physiological media. Therefore, controlled Ab loading is not possible.

Finally, an excellent strategy used for an oriented covalent coupling of Abs is the oxidation of oligosaccharide chains from the Abs' Fc region to produce reactive aldehyde groups, which are suitable for coupling with amine or hydrazide-containing molecules by hydrazone ligation. Some examples include the biotinylation¹⁷ or maleimide modification⁴¹ of intact Abs after mild periodate treatment. Later on, the modified Abs can be linked to NPs by, for example, biotin-streptavidin interactions⁴ or Diels-Alder chemistry,⁴¹ leading to oriented configurations (*i.e.* with the Fab region available for binding; Figure 5.4-D). Other promising chemistries that can address this challenge include click chemistry (e.g. tetrazine ligation),⁴² Staudinger ligation (azide-phosphine)⁴³ and metal-affinity coordination (e.g. *via* histidine (His) residues).³⁵

Although these chemistries are highly selective, there still remains the need to produce NP bioconjugates with a controlled display of Abs that can offer liable and reproducible properties. In this Thesis, research efforts have been focused on the study of a site-directed chemistry (*i.e.* hydrazone ligation) to prepare Ab-Au NP bioconjugates in a controlled manner. A key aspect here has been to modify the Ab prior attachment to the NP. Importantly, the previous modification of Abs' polysaccharide chains with a thiolated linker allowed to better control their coupling to Au NPs (*i.e.* through Au-S interactions), and as well monitoring the binding so as to obtain "calibration" curves. This was paramount in obtaining controlled superstructures versus large and randomly formed aggregates. Further details are discussed in Section 5.2.

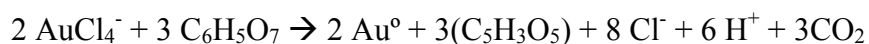
5.1.5. Synthesis of different sized citrate-capped Au NPs.

Citrate-capped Au NPs of a range of sizes (from 9 to 30 nm) were employed in this Chapter as citrate molecules can be easily replaced by a thiolated linker attached to the Abs. The classical citrate reduction method, developed by Turkevich *et al.*⁴⁴ and later

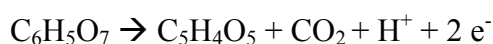
refined by Frens,⁴⁵ was used to produce modestly monodisperse particles ($10 < \sigma < 15\%$ in diameter) in the 10-20 nm diameter range. Larger sizes can also be obtained in one step by the reduction of Au^{3+} by citrate, but it usually comes at the cost of monodispersity, concentration, shape and reproducibility.⁴⁶ For this reason, the synthesis of monodisperse Au NPs of larger sizes (up to 30 nm) was done following a seeding growth method developed in our group.⁴⁷

The first structural studies of Au NPs using electron microscopy were done by Turkevich *et al.* in 1951.⁴⁴ They examined the preparation of various Au NP solutions, describing for the first time the nucleation and growth mechanisms in the formation of gold colloids. Amongst all the synthetic reactions examined in their study, the preparation of which they termed the “standard” sodium citrate solution received special attention because it yielded highly reproducible and spherical colloids. Following their guidelines, in 1973, Frens⁴⁵ performed a systematic study of the citrate-mediated synthesis, producing spherical Au NPs in the range of 16 nm to 150 nm in diameter. The size of the resulting particles was controlled by adjusting the ratio of Au salt to the reducing/stabilizing agent, with larger ratios leading to larger diameters (although with high polydispersity). Today, these conditions have become the cornerstone of a large amount of posterior colloidal synthetic methods developed for obtaining Au NPs. The reader is referred to exhaustive and excellent reviews for detailed information on Au NPs synthesis.^{48,49}

Nowadays, this citrate reduction synthesis remains one of the most popular methods to produce Au NPs. It represents a good model system which includes only three starting materials: auric acid, sodium citrate and water (Figure 5.5-A). The overall reaction scheme is as follows:



The initial step of this multiple process is the oxidation of citrate to yield dicarboxy acetone:



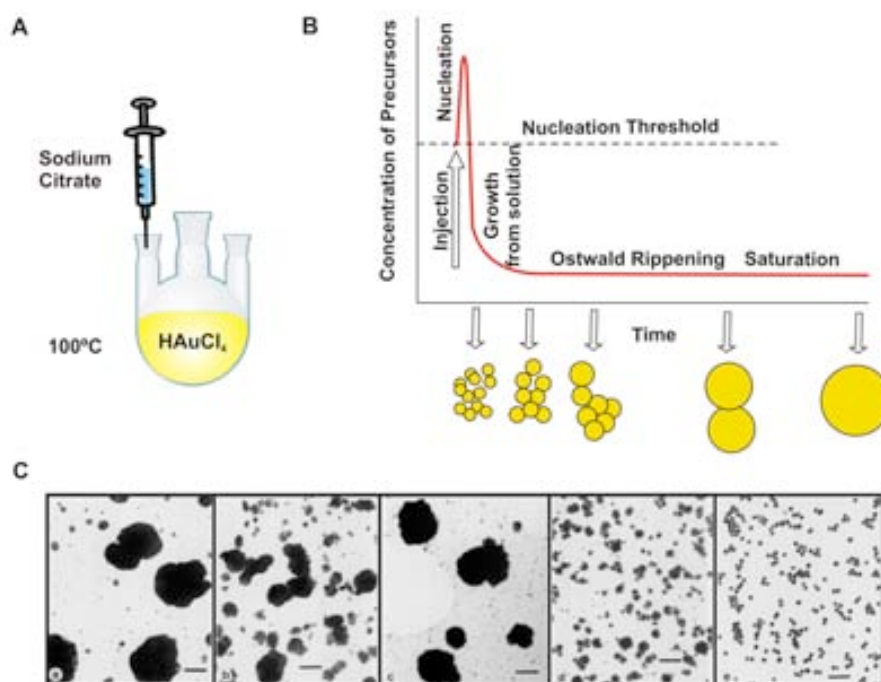
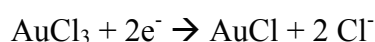


Figure 5.5. A) Experimental setup for the synthesis of Au NPs by citrate reduction. B) Schematic representation of LaMer and Dinegar⁵³ proposed Au NPs formation mechanism by a nucleation-growth process. C) TEM images showing the mechanism of Au NPs formation proposed by Chow and Zukowski,⁵¹ in which the initial period of nucleation is followed by the formation of large aggregates or “protoparticles” that evolve into small NPs.

Then, Au³⁺ is reduced in solution to Au⁺, which forms a multimolecular complex with the formed dicarboxy acetone:



And finally, there is a disproportionation of aurous species to Au atoms:



A more detailed discussion can be found on ref. 50. In this synthesis, citrate acts as a reducer and also as a capping agent, conferring stability to the colloid by electrostatic repulsion. To date, the reaction parameters of this synthesis have been largely explored, including for example the reagents concentration,^{45,51} the reaction temperature⁵¹ and the reaction pH.⁵² Furthermore, there is a substantial amount of information in the literature regarding the NPs formation mechanism. Initially, the mechanism suggested by

Turkevich *et al.*⁴⁴ was complemented with the classic studies from LaMer and Dinegar,⁵³ which described the production of monodisperse colloids *via* a temporally discrete nucleation event followed by a slower controlled growth on the existing nuclei (Figure 5.5-B). Later, Chow and Zukoski⁵¹ demonstrated that the initial period of nucleation favored the formation of large aggregates, resulting from the reduction of Au^{3+} by citrate, which evolved during the course of the reaction to produce small monodisperse particles. (Figure 5.5-C) Further studies by Liz-Marzán and co-workers⁵⁴ supported this reaction mechanism by electrochemical measurements, which showed drastic changes in particle charge and redox potential during the particle formation, and concluded that the reduction of Au(III) to Au(I) is the rate limiting step in both nucleation and growth phases. In contrast, Pong *et al.*⁵⁵ proposed a modified growth mechanism in which the small nuclei formed by citrate-mediated thermal reduction of chloroauric acid initially self-assemble into a network of nanowires. Then, as these nanowires increase in diameter with increasing Au deposition, small fragments break off from these structures before the final spherical particles are formed.

The synthesis of large (from 20 to 200 nm), monodisperse and stable colloidal Au NPs has also been the focus of many investigations. When using the common citrate reduction method, difficulties in controlling the nucleation and growth steps occurring at intermediate stages of particle formation generally results in a broad particle size distribution. An alternative approach to Turkevich-Frens method^{44,45} is seeding growth. Typically in this strategy, the growth and nucleation steps are independent. First, small NPs are synthesized, and they are used as seeds or nucleation centers for the preparation of larger size NPs. For instance, Brown *et al.*⁵⁶ studied the formation of colloidal Au NPs with diameters between 30 and 100 nm based on the colloidal Au surface-catalyzed reduction of Au^{3+} by NH_2OH . However, by the third growth step, this procedure also yields a significant number of shapes that are different from spheres. Other approaches use sodium borohydrate or ascorbic acid as reductants and CTAB as the stabilizer, producing NPs with diameters between 5 and 40 nm and 12 and 180 nm, respectively.^{57,58} Some drawbacks from these synthesis are that multiple shapes are obtained and the complete removal of CTAB after synthesis is not possible, thus rendering the NPs toxic and impeding any further surface functionalization. More recently, Perrault *et al.*⁵⁹ proposed hydroquinone as a weak reductant to produce NPs in the size regime of 50 to 200 nm in diameter, resulting in a decrease of the quality of the

synthesized NPs (polydispersity and low shape stability), and the production of hazardous benzoquinone.

A recent study from our group⁴⁷ has overcome these difficulties, providing a simple synthetic scheme controlling the growth kinetics to produce non-toxic Au NPs with a large range of available sizes (from 10 to 200 nm), very monodisperse size distributions, and stabilized by SC, an easy-to-exchange ligand (Figure 5.6). Besides, postsynthetic cleanup steps are not necessary in this method. Briefly, it consists on the formation of Au NP seeds by the classical Turkevich-Frens method^{44,45} and the subsequent use of these seeds for the growth of NPs with further addition of Au salts and citrate. Importantly, the reactions containing Au NP seeds are developed at a lower temperature (90 °C) than the initial reaction (100 °C) to avoid new nucleation. By adjusting the amount of Au NP seeds and the concentration of Au³⁺ injected into the solution, the growth of successive generations of spherical particles with increasing sizes up to 200 nm is possible. Sodium citrate, as a buffer, is added to each growth step in order to

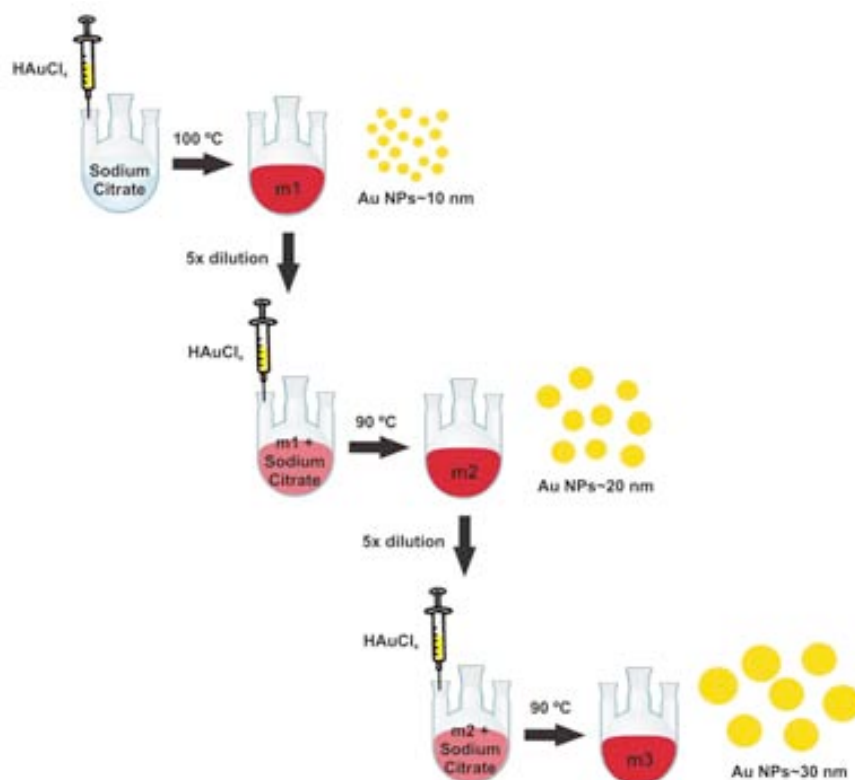


Figure 5.6. Schematic representation of the step-by-step seeding growth method followed in this Thesis for the obtention of large and monodisperse Au NPs. The NPs can be grown by subsequent reduction steps up to 200 nm.⁴⁷

compensate the decrease in pH after Au^{3+} addition. By using this synthetic approach, reproducible NP sizes of high monodispersity were obtained in this Thesis, which was fundamental for the preparation of controlled Au NP bioconjugates.

5.2. Results and discussion.

5.2.1. Controlled formation of antibody-Au NP bioconjugates by a site-directed chemistry.

A site-directed chemistry targeting Ab polysaccharide chains was explored for the conjugation of different Abs on Au NPs of various sizes, controlling their binding number and orientation. With this aim, a set of different polyclonal Abs, including anti-rabbit IgG from goat, anti- BSA IgG from rabbit and rabbit IgG from bovine serum,

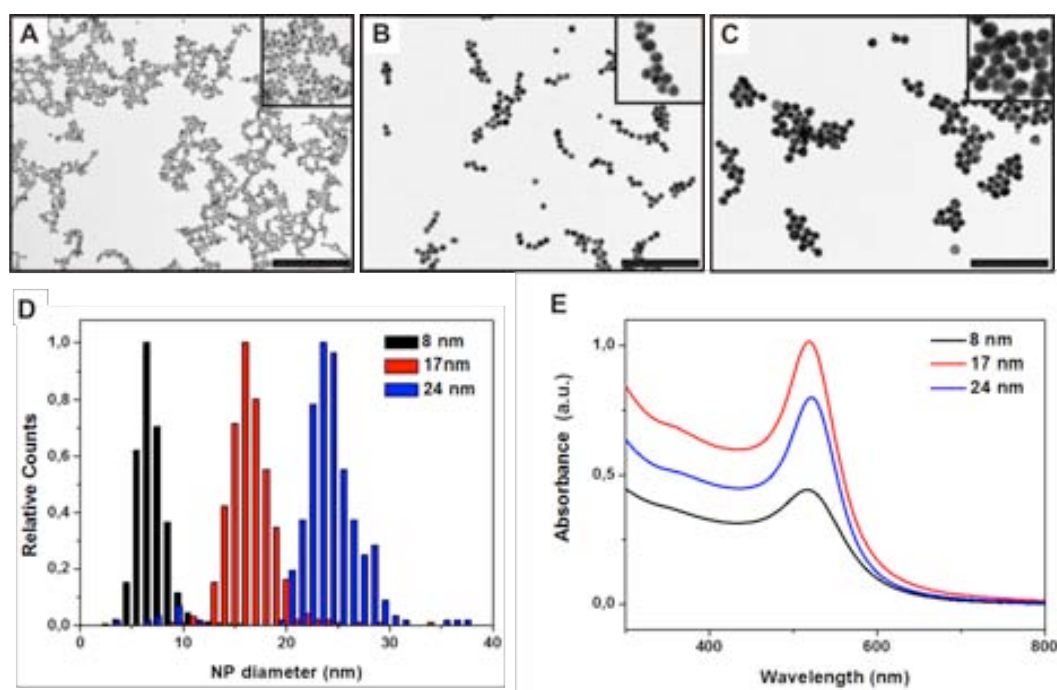


Figure 5.7. TEM and UV-Vis spectroscopic characterization of the citrate-capped Au NPs of different sizes prepared for the bioconjugation studies. A,B) Representative TEM images of the Au NPs of 7.9 ± 1.5 nm and 17.1 ± 2.4 nm in diameter prepared by the classical citrate reduction method. C) Representative TEM images of the Au NPs of 24.0 ± 3.8 nm in diameter prepared by the kinetically controlled seeding growth method developed in our group. D) NPs size analysis and size distribution measured by Image J from various TEM images. E) UV-Vis absorption spectra from the synthesized Au NPs. Different NPs are at different concentrations. Scale bars correspond to 200 nm.

were chosen. In parallel, Au NPs of 7.9 ± 1.5 nm and 17.1 ± 2.4 nm in diameter were prepared by citrate reduction of HAuCl_4 ,^{44,45} whereas kinetically controlled seeding growth synthesis was used to obtain larger Au NPs of 24.0 ± 3.8 nm in diameter (Figure 5.7).⁴⁷

All synthesized Au NPs were then purified by centrifugation and redispersed in borate buffer 2 mM at pH = 8.5, to ensure deprotonation of citrate molecules and at the same time to move away from the Abs isoelectric point (pI) (Figure 5.8). This is the pH of net electrical neutrality for a protein, wherein any electrically induced repulsive or attractive forces are balanced. It has been demonstrated that proteins can be made to adsorb maximally at or near their pI,⁶⁰ and that increasing the pH beyond the pI range results in a decreased percentage of protein bound onto Au NPs.²⁴ Thus, by working at pH = 8.5 (*i.e.* more than 2 units above the pI from the chosen Abs) we wanted to minimize the unspecific adsorption of Abs onto Au NPs (e.g. via electrostatic, hydrophobic and Van der Waals interactions). Here it is important to mention that **the conditions required for the chemistry of reactive groups need to be compatible with colloidal stability of the NPs and structure integrity of the Abs**. This redispersion step was fundamental because such Au NPs required being stabilized in a low ionic strength surfactant, avoiding any potential aggregation when mixed with

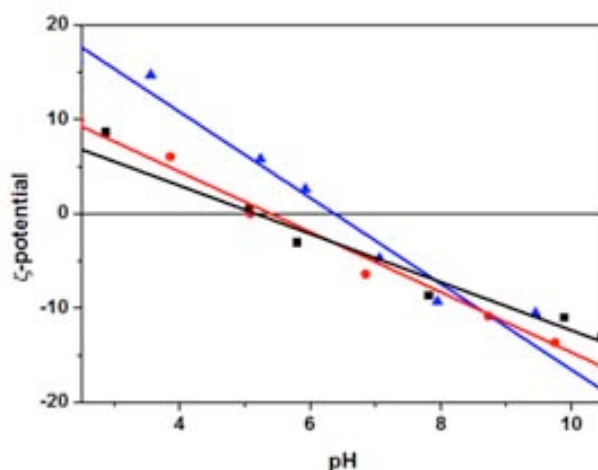


Figure 5.8. ζ -potential measurements from goat anti-rabbit IgG (blue triangles), rabbit anti-BSA IgG (red circles) and bovine IgG (black squares) in PBS solution (10 mM, pH = 7) at a concentration of 1 mg/ml. The samples were titrated with NaOH/HCl (0.01M and 0.1M) in a range of pH from 2.5 to 10.5. Experimental data was fitted to a linear regression ($R^2 = 0.986$ for goat anti-rabbit IgG; $R^2 = 0.986$ for rabbit anti-BSA IgG and $R^2 = 0.954$ for bovine IgG), from which the estimated pIs (ζ -potential = 0) corresponded to ~ 6.4 , 5.4 and 5.2, respectively.

buffered saline solutions (e.g. phosphate buffered saline or PBS, (4-(2-hydroxyethyl)-1-piperazineethanesulfonic acid or HEPES) of Abs during the bioconjugation reaction. At the same time, the final conjugation medium needed to meet the conditions (*i.e.* ionic strength and pH) required for the stabilization of Abs. Note that macromolecules have a very strong tendency to aggregation as soon as their environment changes; one clear example of this is amyloidogenesis or prion aggregation, which are very sensitive to the physicochemical environment.

Once Au NPs were prepared, the selected Abs were conjugated onto these NPs by employing a covalent, site-directed reaction that uses an organic linker to selectively bridge them, forming well-defined Ab-linker-Au NP bioconjugates. Here it is important to note that opposite to conventional covalent strategies that require multiple NP-functionalization steps,⁴⁻⁸ the Abs were first chemically modified with the linker for their direct coupling onto Au NPs, opening up the possibility to better control the orientation, number and binding capacity of Ab molecules on Au NPs (Figure 5.9). The formation of these bioconjugates started with the modification of the polysaccharide chains from the Fc region of the Abs by using periodate oxidation under mild conditions.¹⁷ As shown in Figure 5.10-A, this mild oxidation reaction allows breaking the bond between two adjacent carbons not involved in the glycosidic linkage and creating a pair of aldehydes at the two free tips of each broken monosaccharide ring. These aldehyde groups serve then to link the Abs to the Au NPs through the use of a specific organic linker.^{61,62} This organic linker is 22-(3,5-bis((6-

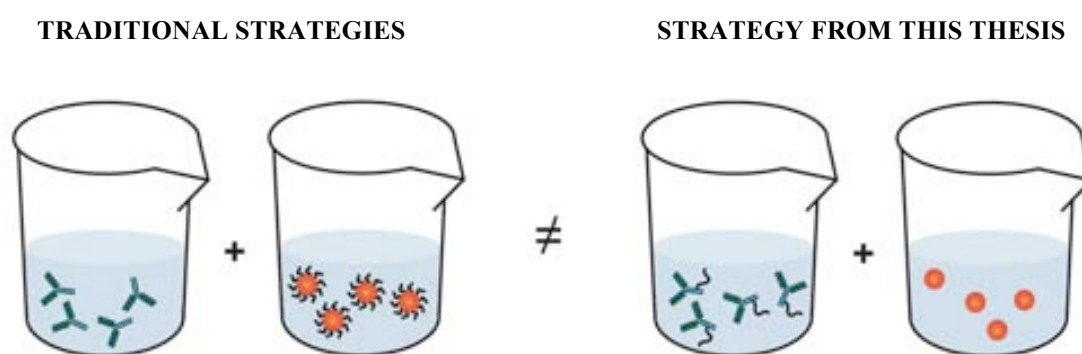


Figure 5.9. Conventional strategies use previous NP functionalization steps and the chemistry of reactive groups is performed in the presence of both, Au NPs and Abs, which might not be compatible with colloidal stability of the NPs or structure integrity of the Abs (left). In this Thesis, previous reactive chemistry on the Abs and further functionalization with naked Au NPs was advantageous to the formation of well-defined Ab-linker-Au NP bioconjugates (right).

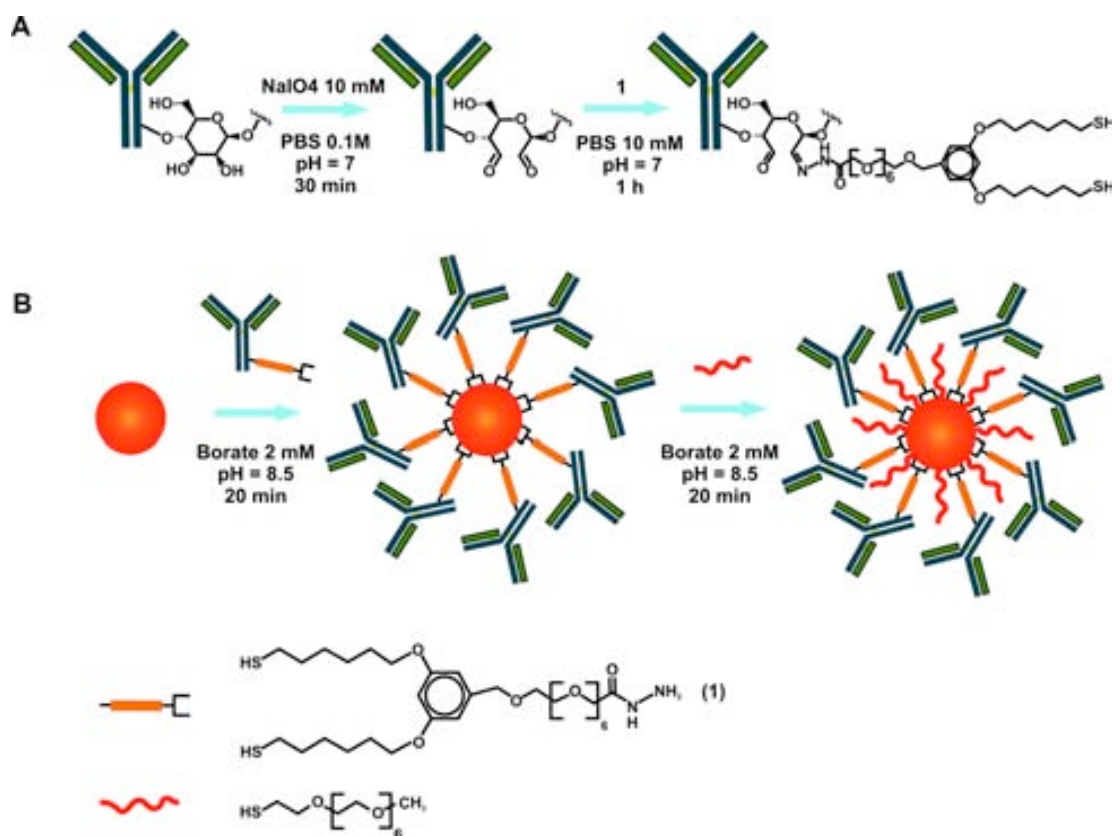


Figure 5.10. Schematic representation of the self-assembly of Ab-1-Au NP bioconjugates from reactions between the Au NPs and the modified Ab-1. A) The hydrazide group located at one PEG termini from the linker **1** is easily accessible to aldehydes from oxidized Abs to form a stable hydrazone bond. B) Thiol groups from the other PEG termini of the linker **1** enable a covalent coupling to Au NPs through strong Au-S linkages. SH-PEG chains (MW 356.48) are used to protect the AuNPs remaining surface against inespecific adsorption or ionic destabilization.

mercaptohexyl)oxy)phenyl)-3,6,9,12,15,18,21-heptaodocosanic hydrazide (hereafter called linker **1**), which contains two thiol-terminated chains able to interact with the Au NPs and one hydrazide-PEG-terminated chain able to form a stable hydrazone bond with the pre-formed aldehyde groups of the Abs (Figure 5.10-A,B).

A key aspect for controlling the number of Abs attached per NP is to control the number of molecules of linker **1** that are bound to each Ab. It is obvious that the optimum number of linker **1** per Ab must be one, because the formation of well-defined Ab-1 pairs avoids the possibility that one Ab can interact with more than one Au NP. To achieve this level of control, it was crucial to oxidize only one site per Ab. This first oxidation step was optimized according to Wolfe and Hage,⁶³ who showed the possibility to control the number of oxidized sites from one to eight groups per Ab by

Ab	Mol LyCH/mol Ab			Average
	Experiment 1	Experiment 2	Experiment 3	
Goat anti-rabbit IgG	0.8	0.7	1.0	0.9 ± 0.1
Rabbit anti-BSA IgG	0.8	0.6	0.6	0.7 ± 0.1
Bovine IgG	0.9	0.9	0.8	0.9 ± 0.1

Table 5.3. Determination of labelling sites per Ab under the optimized oxidation conditions (oxidation time = 30 minutes; solution pH = 7; NaIO₄ concentration = 10 mM; and reaction temperature = RT) with LYCH, which reacts with the aldehyde groups of the Abs to form fluorescent Ab-LYCH conjugates.

varying the different oxidation conditions, including the oxidation time, solution pH, periodate concentration and reaction temperature. With this purpose, prior incubation with NPs, the selected Abs were oxidized using the following optimized conditions: oxidation time = 30 minutes; solution pH = 7; periodate concentration = 10 mM; and reaction temperature = room temperature (RT). The mixture was stirred so as to ensure homogenization of the solution and a statistic biodistribution of one oxidized site for the different Abs. A fluorescent hydrazide-containing dye, Lucifer Yellow cabohydrazide (LYCH), was added after this reaction in order to measure the degree of oxidation. Similar to linker **1**, LYCH reacts with the aldehyde groups of the Abs to form fluorescent Ab-LYCH conjugates.¹⁷ This reaction was performed by adding 20 µl of an aqueous solution of 10 mM LYCH (250-fold molar excess with respect to the Abs) into 100 µl of a PB solution (pH = 7) of 1 mg/ml of oxidized Abs. The resulting mixture was stirred for 1 hour under dark conditions at RT. Synthesized Ab-LYCH conjugates were then purified by dialysis (three cycles of 3 hours), and studied by spectrofluorometry and UV-Vis spectroscopy to determine the concentration of LYCH and Ab, respectively. Importantly, an estimated coupling of approximately one LYCH molecule per Ab was observed for all three Abs (Table 5.3), indicating that one site per Ab was oxidized under the given oxidation conditions. Under the purification conditions used, the level of nonspecifically bound LYCH was approximately 0.01-0.02 mol of LYCH per mol of Ab. This amount was almost two orders of magnitude lower than the total amount of LYCH measured for the oxidized Ab samples.

The reaction of the oxidized Abs with linker **1** was performed under similar conditions used for LYCH. That is, 2 µl of an ethanolic solution of 50 mg/ml linker **1** was added into 100 µl of a PB solution (pH = 7) of 1 mg/ml of Abs. The resulting

mixture was then stirred for 1 hour under dark conditions at RT, and the synthesized Ab-1 pairs were then simultaneously purified and concentrated in a 40 mM HEPES buffer solution at pH = 8.5 using ultracentrifugation filter tubes.

The bioconjugation of Ab-1 with synthesized Au NPs was finally done by adding an HEPES solution of Ab-1 into a borate solution of Au NPs. The resulting mixture was left to react for 20 minutes under stirring at RT to ensure the efficient formation of Ab-1-Au NP bioconjugates. In fact, the bioconjugation reaction between Ab-1 pairs and Au NPs was proved to be completed within approximately one minute by UV-Vis spectroscopy (see Figure 5.11-B,C). To test this, the reaction between 7.9 ± 1.5 nm Au NPs and goat anti-rabbit Ab-1 in a 3x molar excess with respect to the expected maximum NP-coverage (see calculation in Section 5.2.2) was analyzed by UV-Vis spectroscopy. Interestingly, after mixing both components, the characteristic SPR peak from Au NPs immediately shifted towards higher wavelengths, reaching a saturation value after ~ 1 minute of reaction (Figure 5.11-B,C). This fast reaction rate is characteristic from a pseudocovalent binding of thiolated molecules on Au NPs.⁶⁴ In addition, this shift is indicative of a modification in the surface environment of the NP, probably due to the coupling of Ab-1 with Au NPs through Au-S bonds. Finally, once Ab-1-Au NP bioconjugates were synthesized, the remaining reactive surface of the NPs was passivated with short SH-PEG molecules (MW 356.48) to prevent unspecific adsorption or ionic destabilization; e.g. in cell culture media. Note that the SH-PEG molecules are unlikely to replace 1-Abs due to its shorter length, low packing density, and monothiol anchoring (versus dithiol anchoring of linker 1).⁶⁵

Following this methodology, a series of goat anti-rabbit Ab-1-Au NP conjugates with varying NP size (7.9 ± 1.5 nm, 17.1 ± 2.4 nm and 24.0 ± 3.8 nm in diameter) were systematically prepared by adding different Ab/NP ratios. In a typical experiment, goat anti-rabbit Ab-1-Au NP conjugates with increasing Ab/NP ratios were prepared by stepwise addition of goat anti-rabbit Ab-1 into a colloidal solution of Au NPs under the above-mentioned reaction conditions. All three reactions were again monitored by UV-Vis spectroscopy after each stepwise addition of Ab-1. As shown in Figure 5.11-D-F, a constant evolution of the SPR peak towards longer wavelengths, an increase of its absorbance and no detectable peak broadening was observed after each addition. These observations indicated an increase in the attachment of Abs onto Au NPs and the

formation of stable goat anti-rabbit Ab-1-Au NP bioconjugates. For the three NP sizes, however, a maximum red shift of the SPR peak was reached as the ratio of goat anti-rabbit Ab-1/NP was further increased, indicating NP surface saturation (Table 5.4). As expected, this surface saturation was reached using a lower amount Ab-1 (Ab-1/NP ratio = ~ 15) for the smaller 7.9 ± 1.5 nm NPs. In addition, a more dramatic shift of the SPR peak per nm^2 was observed for the smaller NP size (Figure 5.11-F), in agreement with the larger SPR peak shifts found in small NPs, tips and hot spots.^{66,67} On the contrary, larger amounts of Ab-1 were necessary to reach this surface saturation for larger 17.1 ± 2.4 nm and 24.0 ± 3.8 nm NPs (Ab-1/NP ratios of ~ 50 and ~ 80 , respectively), also accompanied with a less pronounced shift in their SPR peak.

In agreement with these results, an increase in the hydrodynamic diameter of the NPs was also measured by DLS after each goat anti-rabbit Ab-1 addition (Figure 5.11-G). This size increase was associated to higher Ab-1/NP ratios, reaching a saturation value of ~ 10 nm, in which further addition of Abs did not result in size changes. The saturation Ab-1/NP ratios for the three NP sizes correlated well with that from the UV-Vis spectroscopy measurements, thus indicating a maximum loading of goat anti-rabbit Ab-1 at these ratios (Table 5.4). The size increase has shown to be consistent and independent from the original NP size, which indicates the controlled and repeated coupling pattern of Abs onto Au NPs. As an extended configuration of the Abs was not expected due to the chemical linkage of **1** on the side chains of the Abs' Fc region, the maximum size increase of ~ 10 nm measured by DLS was attributed to fully covered NPs by Abs at a tilted angle (Figure 5.11-A). In addition, such DLS increase corresponded to a single monolayer on the NP surface, indicating no Abs denaturation and their consequent aggregation. We note that the polydispersity index obtained from these DLS measurements (≤ 0.3 , *i.e.* value derived from the second-order coefficient of the cumulant analysis) did not significantly increase following conjugation, indicating that the variance of the distribution is unchanged. Furthermore, gel electrophoresis of these Ab-1-Au NP bioconjugates (Figure 5.11-G, inset) indicated that the attachment of each Ab molecule resulted in a change in the bioconjugate size. At the same time, their size distribution (or charge distribution) was sufficiently narrow in order to result in a sharp band in the agarose gel. This suggests that the observed size increase was caused by a homogeneous change in particle size resulting from the coupling of Abs,⁶⁸ in which dispersion/homogenization was faster than conjugation.

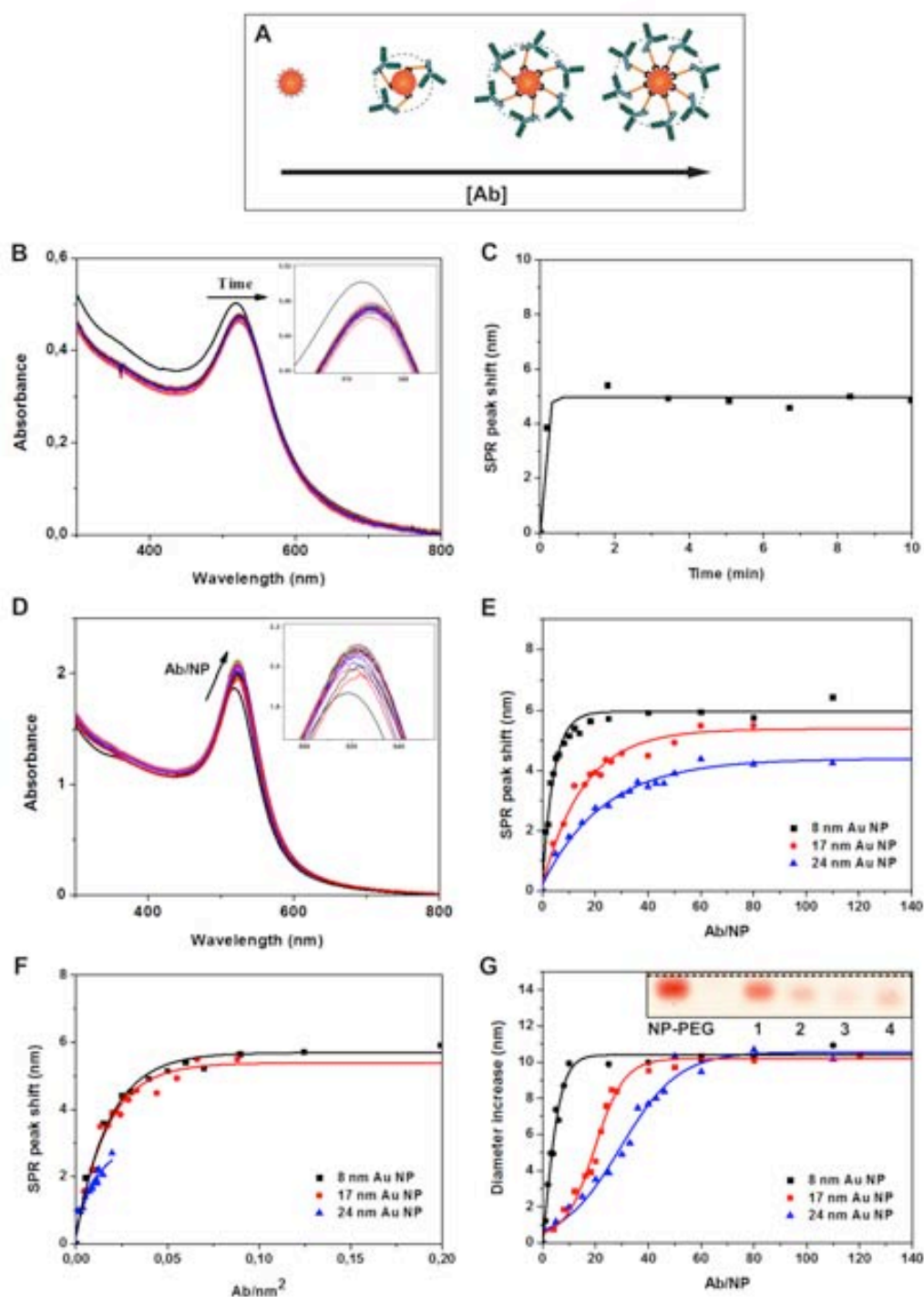


Figure 5.11. A) Schematic diagram of the bioconjugate configuration as a function of number of Abs attached onto the Au NPs, showing the controlled formation of Ab-1-Au NP bioconjugates. B,C) UV-Vis study of the reaction rate between 8 nm Au NPs and goat anti-rabbit Ab-1 (Ab-1/NP ratio of 50 in solution). Data was fitted to Boltzmann eq. ($R^2 = 0.94$). D) UV-Vis spectra of 17 nm Au NPs with increasing goat anti-rabbit Ab-1/NP ratio. E,F) SPR peak shift for different NP sizes (8 nm:black squares, 17 nm:red circles and 24 nm:blue triangles) with increasing goat anti-rabbit Ab-1/NP ratio, represented as a function of the Ab-1/NP ratio in solution or Ab/nm². Data was fitted to Boltzmann eq. ($R^2 = 0.98$, $R^2 = 0.97$, and $R^2 = 0.97$ for 8, 17 and 24 nm Au NPs respectively in graph E; $R^2 = 0.98$, $R^2 = 0.97$, and $R^2 = 0.90$ for 8, 17 and 24 nm Au NPs respectively in graph F). G) Increase in hydrodynamic diameter (volume value) of different NP sizes with increasing goat anti-rabbit Ab-1/NP ratio. Inset: gel electrophoresis of Ab-1-Au NP bioconjugates with approx. 1, 2, 3 and 4 Ab molecules bound (samples 1 to 4) and NP-PEG conjugate as control.

NP size ^a (nm)	η	SPR peak shift (nm)	Hydrodynamic diameter increase (nm)
7.9 ± 1.5	15	5.7	9.9
17.1 ± 2.4	50	5.5	10.3
24.0 ± 3.8	80	4.2	10.7

Table 5.4. Physicochemical characteristics of goat anti-rabbit Ab-1-Au NP bioconjugates at NP surface saturation conditions. Stoichiometry (Ab-1/NP ratio in solution), η , wavelength of maximum absorption peak shift and hydrodynamic diameter increase (volume value).^a Values obtained by analyzing ~ 300 Au NPs from TEM images.

As a control experiment, the coupling of Abs onto Au NPs was done using the traditional strategy of adsorption (see Section 5.1.4). However, the coupling of native (non-modified) goat anti-rabbit Abs to Au NPs at the same conditions used in our previous experiments resulted in larger shifts of the SPR peak, with a continuous decrease in its absorbance and broadening of the peak (Figure 5.12-B,C). These observations clearly indicated the formation of large aggregates, probably due to the

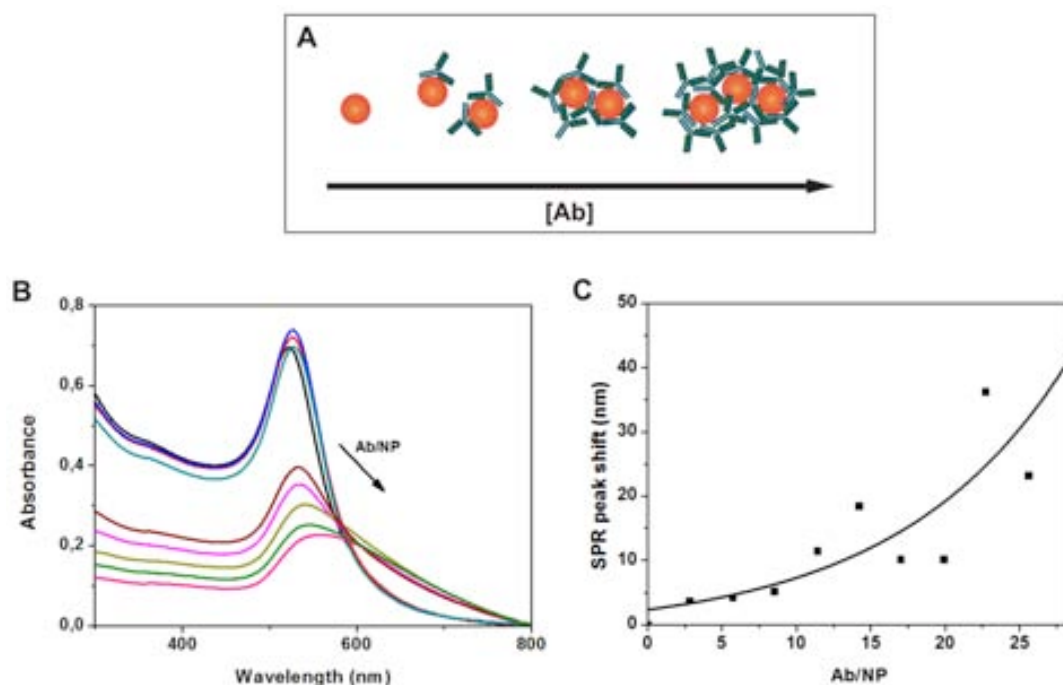


Figure 5.12. A) Representative schematic diagram of the bioconjugate configuration as a function of number of native goat anti-rabbit Abs adsorbed onto the Au NPs, leading to the formation of uncontrolled large aggregates. UV-visible spectra (B) and SPR peak shift (C) of 17.1 ± 2.4 nm Au NPs with increasing native goat anti-rabbit Ab/NP ratio. Data was fitted to exponential growth equation ($R^2 = 0.76$).

lower affinity of Abs for the Au NP surface leading to an inefficient stabilization of the NPs and their aggregation. The formation of aggregates was further observed by DLS, from which a large size increase (> 700 nm) was measured after 24 hours.

To further confirm the controlled display of Abs on Au NPs, the same coupling strategy was employed with IgGs from different species. With this aim, a number of rabbit anti-BSA Ab-1-Au NP and bovine Ab-1-Au NP bioconjugates were synthesized by stepwise additions of rabbit anti-BSA Ab-1 and bovine Ab-1, respectively, on 7.9 ± 1.5 nm Au NPs. The trend evolution of both SPR peak and hydrodynamic size after each addition was similar to that observed for the goat anti-rabbit Ab. A red shift of the SPR peak was clearly observed for both Abs (Figure 5.13-A), although they had small differences in their maximum peak shift that could be attributed to their differences in glycosylation, and thus, to their 1 binding efficiency. However, the NPs size was equally increased after coupling the different Abs (Figure 5.13-B), reaching a maximum increase of ~ 10 nm in diameter (volume value) at the maximum loading ratio (Ab/NP ratio ~ 15). These results confirmed a repeated coupling pattern that can only be due to an ordered arrangement of the Abs on the Au NPs surface. Overall, the controlled loading of a series of Abs onto Au NPs was demonstrated.

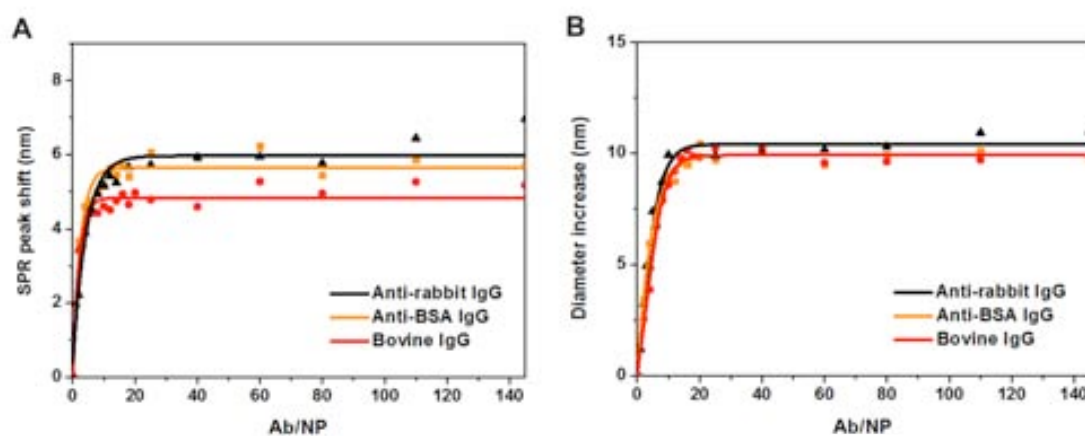


Figure 5.13. A) SPR peak shift of 7.9 ± 1.5 nm Au NPs with increasing goat anti-rabbit Ab-1/NP ratio (black triangles), rabbit anti-BSA Ab-1/NP ratio (orange squares) and bovine Ab-1/NP ratio (red circles). Data was fitted to Boltzmann equation ($R^2 = 0.99$ for goat anti-rabbit Ab, $R^2 = 0.91$ for rabbit anti-BSA Ab and $R^2 = 0.94$ for bovine Ab). B) Hydrodynamic diameter (volume value) of 7.9 ± 1.5 nm Au NPs with increasing goat anti-rabbit Ab-1/NP ratio (black triangles), rabbit anti-BSA Ab-1/NP ratio (orange squares) and bovine Ab-1/NP ratio (red circles). Data was fitted to Boltzmann equation ($R^2 = 0.98$ for goat anti-rabbit Ab, $R^2 = 0.99$ for rabbit anti-BSA Ab and $R^2 = 0.99$ for bovine Ab).

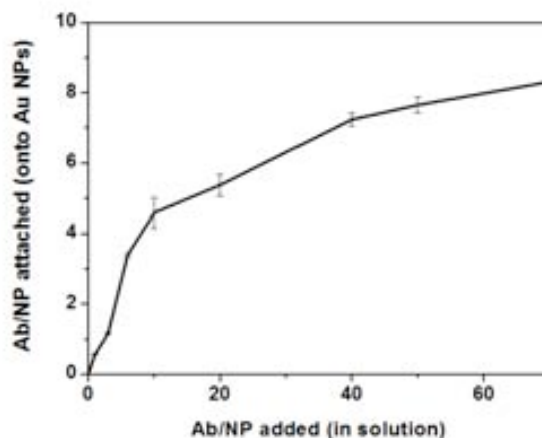


Figure 5.14. Quantification of Abs covalently attached to 17.1 ± 2.4 nm Au NPs. Goat anti-rabbit Ab-1 were labelled with Alexa Fluor 488. Then, AlexaFluor 488-Ab-1 were added to the Au NPs at different ratios, and the fluorescence emission intensity from unbound AlexaFluor 488-Ab-1 was measured. The average amount of attached Abs to NPs was determined by subtracting the unbound AlexaFluor 488-Ab-1 from total.

Ab/NP added in solution	Ab/NP attached	Conjugation efficiency (%) ^a
1	0.6 ± 0.0	60.0
3	1.2 ± 0.0	40.0
6	3.4 ± 0.0	56.7
10	4.6 ± 0.4	46.0
20	5.4 ± 0.3	27.0
40	7.2 ± 0.2	18.0
50	7.6 ± 0.2	15.2

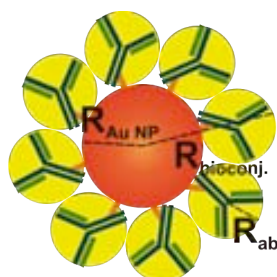
Table 5.5. Determination of the Ab-1-NP conjugation efficiency. ^a Conjugation efficiency was calculated from the number of Ab molecules attached to the NP divided by the total Abs added in solution.

From the measurements done so far, the amount of Abs used in the conjugation (Ab/NP ratio in solution) can only be correlated to a certain percentage of Ab coverage density on the Au NPs. However, **this value cannot be correlated to the “real” number of Abs that is conjugated on each Au NP**, since modifications of the SPR peak or DLS are greater for the first arriving Ab (to the NP surface) than the last ones. To gain further understanding on the conjugation efficiency and determine the number

of Abs covalently attached to the 17.1 ± 2.4 nm Au NPs, the Ab-1 pairs were labeled with the fluorescent dye Alexa Fluor 488, according to the manufacturer's instructions. Alexa Fluor 488 has a tetrafluorophenyl ester moiety that reacts efficiently with primary amines on the Abs to form a stable dye-Ab conjugate. The Abs were subsequently added to the Au NPs at different ratios, forming AlexaFluor 488-Ab-1-Au NP bioconjugates. Centrifugation of the samples was then used to separate the pellet containing the AlexaFluor 488-Ab-1-Au NPs conjugates from the supernatant containing unbound AlexaFluor 488-Ab-1. The fluorescence emission intensity of the supernatant, for excitation and emission wavelengths of 494 and 519 nm, respectively, was measured to determine the concentration of the AlexaFluor 488-Ab-1. Finally, the average amount of attached Abs to NPs was determined by subtracting the unbound AlexaFluor 488-Ab-1 from total (Figure 5.14 and Table 5.5). Measurements were done from duplicate experiments and two different sample fractions. From these results, the efficiency of conjugation was calculated as the number of Ab-1 attached to the NP divided by the total Ab-1 added in solution. As can be observed in Table 5.5, the initially bound Abs posed a strong repulsive barrier for the late incoming Abs, thus limiting the loading avidity, especially when reaching NP surface saturation ratios.

5.2.2. Theoretical calculations of the loading of antibodies on Au NPs.

The total number of Abs than can be attached to a single Au NP depends on the surface area of the NP compared with the Ab fingerprint. An estimate of the maximum theoretical number of Abs (N_{\max}) that can be packed on the surface of each spherical Au NP can be derived from steric considerations using the following equation:⁶⁹



$$N_{\max} = 0.65 (R_{\text{bioconjugate}}^3 - R_{\text{AuNP}}^3) / R_{\text{Ab}}^3 \quad (5.1)$$

where $R_{\text{bioconjugate}}$ is the radius of the Ab-1-Au NP bioconjugate ($R_{\text{AuNP}} + R_{\text{Ab}}$), R_{AuNP} is the radius of the Au NP, and R_{Ab} is the radius of the IgG. In this model, it is assumed

that the Abs are close-packed as spheres around a central Au NP, and the linker **1** is considered to have no steric effect on packing due to its flexible conformation and relatively small size. Equation 5.1 takes account of the filling factor of hard spheres and adjusts the volume ratios by a factor of 0.65.⁷⁰ The value of the radius of the IgG (R_{Ab}) was calculated from the following equation:⁷¹

$$R_{Ab} \approx 0.81 \times M_r^{1/3} (\text{\AA}) \quad (5.2)$$

where M_r is the molecular weight of the IgG (~150.000 g/mol). This equation gives a reasonably accurate estimate from the radius of compact globular proteins. Thus, an estimate of an IgG radius of ~ 4.36 nm is derived from equation 5.2, which is consistent with DLS measurements (increase of 10 nm in diameter at maximum Ab loading, Figure 5.11-G). By using the values $R_{AuNP} = 8.5$ and $R_{bioconjugate} = 12.86$ (for Au NPs of 17.1 nm), an estimate of N_{max} per NP of 11.8 is derived from equation 5.1 (Table 5.6). This estimate compares well with the experimental value derived from the fluorescence spectroscopy data shown in Figure 5.14 and Table 5.5, in which the maximum number of attached Abs on a 17.1 ± 2.4 nm Au NP (at the saturation Ab-1/NP ratio of ~50) is $\sim 7.6 \pm 0.2$. Estimated N_{max} values derived from equation 5.1 for 7.9 and 24.0 nm Au NPs are 4.1 and 20.8 Ab molecules per Au NP (Table 5.6). Nonetheless, this theoretical number is subject to a slight error since Abs have an Y-shape that is not optimum for packing.

NP size ^a (nm)	N_{max} theoretical	η	N_{max} experimental
7.9 ± 1.5	4.1	15	-
17.1 ± 2.4	11.8	50	7.6
24.0 ± 3.8	20.8	80	-

Table 5.6. Theoretical number of maximum Ab molecules on Au NP, N_{max} theoretical; stoichiometry (Ab-1/NP ratio), η ; and experimental number of maximum Ab molecules on Au NP, N_{max} experimental.^a Values obtained by analyzing ~ 300 Au NPs from TEM images.

5.2.3. Rational design and formation of antibody-Au NP superstructures.

To demonstrate that Ab-1-Au NP bioconjugates developed in this Chapter retain the biological activity and recognition capabilities of Abs, a series of bioconjugates made of Abs that can be specifically recognized (through Ab-antigen interaction) was designed and used to create well-defined NP superstructures. In fact, the controlled formation of NP-biomolecule superstructures is currently attracting the attention of many scientists, who have created beautiful arrangements by using for example DNA hybridization⁷²⁻⁷⁷ and peptide bonds.⁷⁸ Thus far, however, attempts to use specific Ab-antigen interactions have only resulted in the formation of large aggregates.⁷⁹ In this Thesis, the formation of Ab-1-Au NP bioconjugates with controlled number and orientation of Abs wants to be used to rationally design well-defined NP superstructures (dimers, trimers and satellite-shaped superstructures) based on the specific Ab-antigen interactions of two or more of such bioconjugates.

Initially, the formation of dimers built up from connecting 7.9 ± 1.5 nm and 17.1 ± 2.4 nm Au NPs was evaluated (Figure 5.15, strategy 1). For this configuration, rabbit anti-BSA Ab-1 and goat anti-rabbit Ab-1 were coupled to the 7.9 ± 1.5 nm and 17.1 ± 2.4 nm Au NPs, respectively, with an Ab-1/NP ratio of 3 in solution, corresponding to an Ab-1/NP ratio of 1.2 (NP1 and NP2, respectively; see Table 5.7). A short thiolated PEG (MW 356.48) was added at 3-fold molar excess over the estimated complete NPs coverage, to passivate the remaining NPs surface. Then, an equimolar stoichiometric amount of NP1 and NP2 bioconjugates were mixed under slow agitation at 4 °C overnight. Afterwards, a gentle centrifugation step (5000 g, 5 minutes) was employed to separate the formed NP superstructures from individual (unbound) bioconjugates. The collected pellet was visualized under TEM, revealing the successful formation of the desired NP1-NP2 dimers (Figure 5.15-A,B). The correct formation of these dimers confirmed the specific recognition between the goat anti-rabbit IgG' Fab and its epitope present in the rabbit anti-BSA IgG' Fc region, further proving that the synthesized bioconjugates fully retain their biological activity. A much fewer number of dimers and trimers composed of equally sized NPs were also observed (~ 26.2 %, Table 5.7), probably due to unspecific interactions between the same types of Abs (e.g. NP1-NP1).

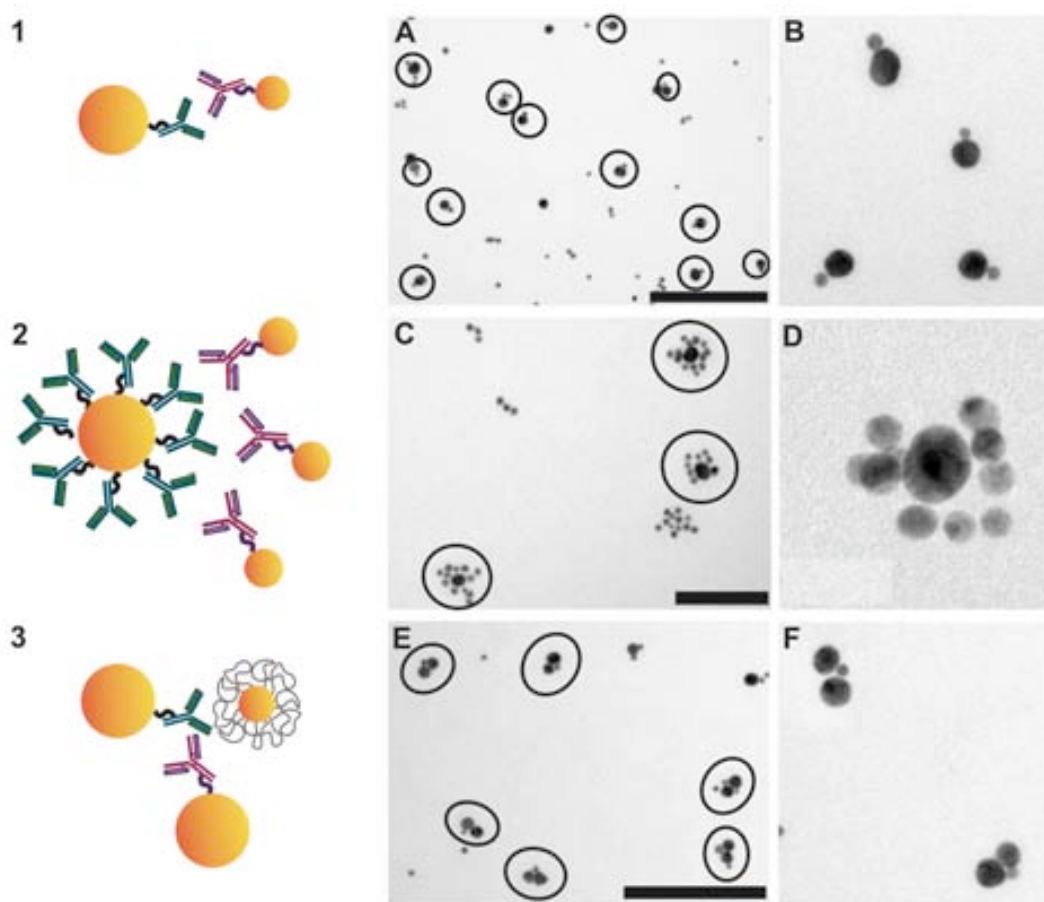


Figure 5.15. (1-3) Schematic illustration describing the formation of NP assemblies by specific Ab-antigen interactions. A,B) TEM images of the formed dimers by recognition between NP1 and NP2. C,D) TEM images of the formed satellite-shaped assemblies by recognition between NP1 and NP3. E,F) TEM images of the formed trimeric superstructures by double Ab-antigen recognition, first between NP4 and NP5 which form dimers, and later adding NP2 bioconjugates that recognize the NP5 component of the dimer. Scale bars are 100 nm (C) and 200 nm (A,E).

Sample	NP size	Ab-1/NP ratio*	Protein/Ab
NP1	7.9 ± 1.5	1	Rabbit anti-BSA IgG
NP2	17.1 ± 2.4	1	Goat anti-rabbit IgG
NP3	17.1 ± 2.4	8	Goat anti-rabbit IgG
NP4	7.9 ± 1.5	-	BSA
NP5	17.1 ± 2.4	1	Rabbit anti-BSA IgG

Table 5.7. Core size and composition of the Au NP bioconjugates used to the formation of dimers, trimers and satellite-shaped assemblies.*Note that this value correspond to the expected ratio of Ab-1 onto the Au NP according to previous experiments with AlexaFluor 488-Ab-1 (see Section 5.2.1).

In a next step, satellite-shaped NP superstructures were designed (Figure 5.15, strategy 2). In this case, goat anti-rabbit Ab-1 were coupled to 17.1 ± 2.4 nm Au NPs up to a saturation ratio (**NP3**, Ab-1/NP ratio ~ 8). In parallel, rabbit anti-BSA Ab-1 were again coupled to 7.9 ± 1.5 nm Au NPs with an Ab-1/NP ratio of 3 in solution (**NP1**, Ab-1/NP ratio ~ 1). The two bioconjugates, NP1 and NP3, were mixed in an excess (100x) of the NP1 bioconjugates, and the resulting mixture was gently stirred at 4 °C overnight. Again, a soft centrifugation step was used to purify the NP superstructures from individual bioconjugates, and the pellet was collected for TEM analysis. The correct formation of **NP1-NP3 satellite-shaped assemblies** was clearly observed by TEM (Figure 5.15-C,D). It is important to highlight here that the relative number of 7.9 ± 1.5 nm Au NPs surrounding the 17.1 ± 2.4 nm ones was 9 ± 1 , which is in good agreement with previous results (Figure 5.14 and Table 5.5) where the maximum number of attached Abs on the 17.1 ± 2.4 nm Au NPs was ~ 8 . Figure 5.16 shows different snapshots of a 3D tomography TEM characterization of one of such NP1-NP3 satellite-shaped superstructures, illustrating their three-dimensionality.

Finally, more complex ternary NP superstructures that involve controlling two different Ab-antigen interactions were synthesized (Figure 5.15, strategy 3). These trimeric superstructures were designed by first creating BSA-Au NP bioconjugates (**NP4**, 7.9 ± 1.5 nm) using the traditional strategy of adsorption (BSA was added using an excess of 100 x to ensure a complete NP coverage), and adding them to 17.1 ± 2.4 nm Au NPs coupled to rabbit anti-BSA at Ab-1/NP ratio of 3 in solution (**NP5**, ~ 1 Ab-1/NP ratio). NP4 and NP5 were mixed at stoichiometric concentration of the NPs, and it was left to react for 2 hours at RT under slow agitation. The resulting mixture was allowed to react with NP2 bioconjugates, which recognize the rabbit anti-BSA Ab component of the dimer (in NP5) to form the **NP2-NP4-NP5 trimeric superstructures**. The resulting new mixture was gently stirred overnight at 4°C, and a soft centrifugation step (5000 g, 5 min) was then performed for separating the superstructures. TEM characterization of the resulting pellet showed the predominant assembly of NP2-NP4-NP5 trimeric superstructures (Figure 5.15-E,F), thus confirming the possibility to control two different Ab-antigen interactions.

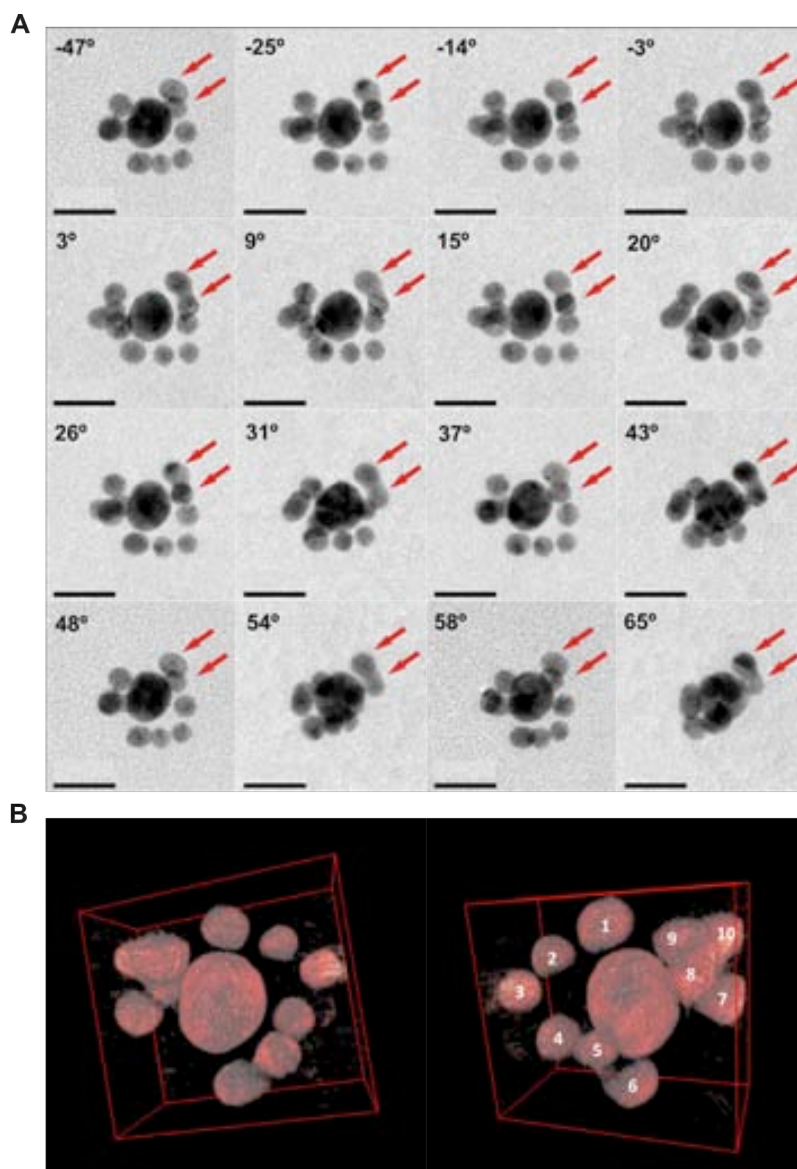


Figure 5.16. A) Representative bright field (BF) TEM images from tilt series (from -69° to 65°) of a satellite-shaped NP assembly based on specific Ab-antigen interactions between NP1 and NP3. There are 10 Au NPs of 7.9 ± 1.5 nm surrounding the bigger 17.1 ± 2.4 nm Au NPs. Notice that the two NPs marked with red arrows suffer a live process of coalescence during the 1 hour and 45 minutes tilt process. They start as separated NPs (see tilt images from -47° to -14°) and fuse when reaching approximately -3° (half of the process, approximately after 55 minutes under beam exposure). B) Front and back 3D reconstruction of the satellite system. Scale bars are 20 nm.

To verify that the assembled NP superstructures were formed through specific Ab-antigen interactions, a statistical analysis considering more than 100 NPs (either isolated NPs or composing a superstructure) was carried out. Table 5.7 shows the resulting percentages for the three different reactions, confirming a good yield of formation (52.6 %, 48.7 % and 43.4 % of dimers, satellite-shaped superstructures and trimers, respectively) of all the desired superstructures. Interestingly, these yields were

found to be a good approximation when compared with other strategies that use complementary DNA strands,⁸⁰ which are smaller and facile to orient on the NP surface.

Strategy	Percentage of isolated Au NPs		Percentage of architectures (%) ^a			
	7.9 nm	17.1 nm	Dimer	Satellite-shaped	Trimer	Others
1	15.2	6.9	52.6	-	-	26.2
2	35.8	-	-	48.7	-	15.5
3	32.7	6.2	-	-	43.4	29.5

Table 5.7. Statistical analysis of TEM images from NP assemblies. ^a The percentage of designed architectures is calculated by dividing the number of Au NPs used in assembling designed architectures by the total number of Au NPs. Other architectures, such as dimers and trimers of equally sized NPs, are also formed probably due to unspecific interactions between the same Abs, or during sample preparation (drying).

5.3. Conclusions

The chemoselective ligation between linker **1** and the polysaccharide residues from the Abs' Fc region resulted in a site-directed and pseudocovalent binding of Abs to Au NPs, obtaining a higher control of the NP/biomolecule ratio and biomolecular orientation compared to other multiple NP functionalization strategies. This control was possible due to the high affinity of the thiolated linker **1** for Au, which favoured the attachment of **1**-Ab molecules to the NPs by Au-S bonds with respect to ionic or hydrophobic interactions. In addition, a maximum exposure of Ab epitopes to their molecular receptors was achieved by this strategy, together with an advantageous mobility of the Abs in solution thanks to the PEGylated linker, which are crucial factors to optimize the NP-Ab bioconjugate function. Worth to note, the mild aqueous conditions used in the oxidation process avoided significant loss of the specific functionality from Abs, which was later demonstrated by the controlled formation Ab-directed NP superstructures. A key aspect in the formation of these NP superstructures was the control of physicochemical parameters from the Ab-NP conjugates by UV-Visible spectroscopy and DLS. From these results, we gained further understanding on

the biomolecule orientation and the Ab/NP ratio, which was fundamental for the preparation of well-defined NP-Ab conjugates for their self-assembly into two- and three-dimensional NP superstructures. To our knowledge, the formation of this kind of superstructures using Ab-antigen cross-links remains a challenge faced by NP-based materials chemistry. Hence, this study opens the door to employ proteins additional functionality when compared to DNA-based superstructures. The high control achieved on the directional conjugation of Ab molecules on Au NPs under the chosen set of conditions can be extended to create complex and multiple functional delivery systems. Thus, by taking advantage of the previous chemical modification of Abs, an appropriate linker can provide a covalent and site-specific linkage of Abs to other nanoparticulate systems used for imaging, diagnostics or targeted delivery of chemotherapeutic agents, amongst others. The present study paves the way for a more sophisticated engineering of the Ab-NP interface and opens up new expecting possibilities for the application of these potential materials in the biological and medical fields, such as the generation of strong optical hotspots for diagnosis.

5.4. References.

1. Arruebo, M.; Valladares, M.; González-Fernández, A. *Antibody-Conjugated Nanoparticles for Biomedical Applications*. *J. Nanomater.*, **2009**, 1-24.
2. Nobs, L.; Buchegger, F.; Gurny, R.; Allémann, E. *Current Methods for Attaching Targeting Ligands to Liposomes and Nanoparticles*. *J. Pharm. Sci.*, **2004**, 93, 1980-1992.
3. Algar, W. R.; Prasuhn, D. E.; Stewart, M. H.; Jennings, T. L.; Blanco-Canosa, J. B.; Dawson, P. E.; Medintz, I. L. *The Controlled Display of Biomolecules on Nanoparticles: A Challenge Suited to Bioorthogonal Chemistry*. *Bioconj. Chem.*, **2011**, 22, 825-858.
4. Varshney, M.; Yang, L.; Su, X.-L.; Li, Y. *Magnetic Nanoparticle-Antibody Conjugates for the Separation of Escherichia coli O157:H7 in Ground Beef*. *J. Food Protec.*, **2005**, 68, 1804-1811.
5. Leggett, R.; Lee-Smith, E. E.; Jickells, S. M.; Russell, D. A. *"Intelligent" Fingerprinting: Simultaneous Identification of Drug Metabolites and Individuals by using Antibody-Functionalized Nanoparticles*. *Angew. Chem. Int. Ed.*, **2007**, 46, 4100-4103.
6. Eck, W.; Craig, G.; Sigdel, A.; Ritter, G.; Old, L. J.; Tang, L.; Brennan, M. F.; Allen, P. J.; Mason, M. D. *PEGylated Gold Nanoparticles Conjugated to Monoclonal F19 Antibodies as Targeted Labeling Agents for Human Pancreatic Carcinoma Tissue*. *ACS Nano*, **2008**, 2, 2263-2272.

7. Jans, H.; Liu, X.; Austin, L.; Maes, G.; Huo, Q. *Dynamic Light Scattering as a Powerful Tool for Gold Nanoparticle Bioconjugation and Biomolecular Binding Studies*. *Anal. Chem.*, **2009**, 81, 9425-9432.
8. Di Pasqua, A. J.; R. E. Mishler; Y. L. Ship; J. C. Dabrowiak; T. Asefa. *Preparation of Antibody-Conjugated Gold Nanoparticles*. *Mater. Lett.*, **2009**, 63, 1876-1879.
9. Mirkin, C. A.; Letsinger, R. L.; Mucic, R. C.; Storhoff, J. J. *A DNA-Based Method for Rationally Assembling Nanoparticles into Macroscopic Materials*. *Nature*, **1996**, 382, 607-609.
10. Alivisatos, A. P.; Johnsson, K. P.; Peng, X. G.; Wilson, T. E.; Loweth, C. J.; Bruchez, M. P.; Schultz, P. G. *Organization of 'Nanocrystal Molecules' using DNA*. *Nature*, **1996**, 382, 609-611.
11. Seeman, N. C. *Feature DNA in a material world*. *Nature*, **2003**, 421, 427-431.
12. Casadevall, A.; Dadachova, E.; L. Pirofski. *Passive Antibody Therapy for Infectious Diseases*. *Nat. Rev. Micro.*, **2004**, 2, 695-703.
13. Nezlin, R. *The Immunoglobulins: Structure and Function*. Elsevier Inc., **1998**.
14. Berg, J. M.; Tymoczko, J. L.; Freeman, L. S. *Biochemistry, 6th edition*. W.H. Freeman, **2006**.
15. Kaneko, Y.; Nimmerjahn, F.; Ravetch, E. V. *Anti-inflammatory Activity of Immunoglobulin G Resulting from Fc Sialylation*. *Science*, **2006**, 313, 670-673.
16. Wolfe, C. A. C.; Hage, D. S. *Studies on the Rate and Control of Antibody Oxidation by Periodate*. *Anal. Biochem.*, **1995**, 231, 123-130.
17. Hermanson, G. T. *Bioconjugate Techniques, 2nd edition*. Elsevier Inc., **2008**.
18. Fan, Z.; Lu, Y.; Wu, X.; Mendelsohn, J. *Antibody-Induced Epidermal Growth Factor Receptor Dimerization Mediates Inhibition of Autocrine Proliferation of A431 Squamous Carcinoma Cells*. *J. Biol. Chem.*, **1994**, 269, 27595-27602.
19. Faulk, W. P.; Taylor, G. M. *An Immunocolloid Method for the Electron Microscope*. *Immunochem.*, **1971**, 8, 1081-1083.
20. Sokolov, K.; Follen, M.; Aaron, J.; Pavlova, I.; Malpica, A.; Lotan, R.; Richards-Kortum, R. *Real-Time Vital Optical Imaging of Precancer Using Anti-Epidermal Growth Factor Receptor Antibodies Conjugated to Gold Nanoparticles*. *Cancer Res.*, **2003**, 63, 1999-2004.
21. Patra, C. R.; Bhattacharya, R.; Wang, E.; Katarya, A.; Lau, J. S.; Dutta, S.; Muders, M.; Wang, S.; Buhrow, S. A.; Safgren, S. L.; Yaszemski, M. J.; Reid, J. M.; Ames, M. M.; Mukherjee, P.; Mukhopadhyay, D. *Targeted Delivery of Gemcitabine to Pancreatic Adenocarcinoma Using Cetuximab as a Targeting Agent*. *Cancer Res.*, **2008**, 68, 1970-1978.
22. Jiang, W.; Kim Betty, Y. S.; Rutka, J. T.; Chan Warren, C. W. *Nanoparticle-Mediated Cellular Response is Size-Dependent*. *Nat. Nano*, **2008**, 3, 145-150.
23. Bhattacharyya, S.; Bhattacharya, R.; Curley, S.; McNiven, M. A.; Mukherjee, P. *Nanoconjugation Modulates the Trafficking and Mechanism of Antibody Induced Receptor Endocytosis*. *Proc. Natl. Acad. Sci. U.S.A.*, **2010**, 107, 14541-14546.

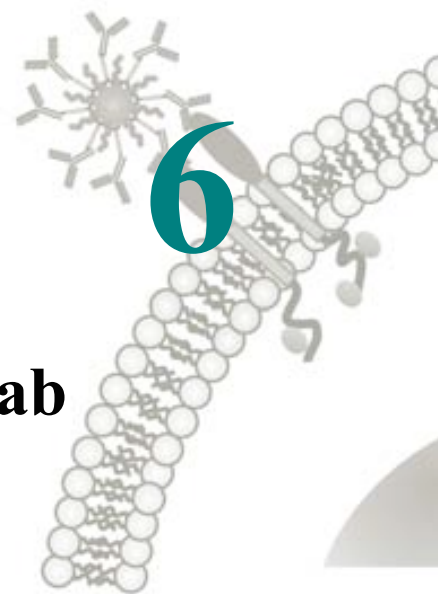
24. Geoghegan, W. D. *The Effect of Three Variables on Adsorption of Rabbit IgG to Colloidal Gold*. J. Histochem. Cytochem., **1988**, 36, 401-407.
25. Tokuyasu, K.T. *Present State of Immunocytochemistry*. J. Histochem. Cytochem., **1983**, 31, 164-167.
26. Tinglu, G.; Ghosh, A.; Ghosh, B.K. *Subcellular Localization of Alkaline Phosphatase in Bacillus Licheniformis 749/C by Immunoelectron Microscopy with Colloidal Gold*. J. Bacteriol., **1984**, 159, 668-677.
27. Ardao, I.; Comenge, J.; Benaiges, M. D.; Álvaro, G.; Puentes, V. F. *Rational Nanoconjugation Improves Biocatalytic Performance of Enzymes: Aldol Addition Catalyzed by Immobilized Rhamnulose-1-Phosphate Aldolase*. Langmuir, **2012**, 28, 6461-6467.
28. Casals, E.; Pfaller, T.; Duschl, A.; Oostingh, G. J.; Puentes, V. *Time Evolution of the Nanoparticle Protein Corona*. ACS Nano, **2010**, 4, 3623-3632.
29. Dobrovolskaia, M. A.; Patri, A. K.; Zheng, J.; Clogston, J. D.; Ayub, N.; Aggarwal, P.; Neun, B. W.; Hall, J. B.; McNeil, S. E. *Interaction of Colloidal Gold Nanoparticles with Human Blood: Effects on Particle Size and Analysis of Plasma Protein Binding Profiles*. Nanomedicine: Nanotech. Biol. Med., **2009**, 5, 106-117.
30. Mamot, C.; Drummond, D. C.; Greiser, U.; Hong, K.; Kirpotin, D. B.; Marks, J. D.; Park, J. W. *Epidermal Growth Factor Receptor (EGFR)-Targeted Immunoliposomes Mediate Specific and Efficient Drug Delivery to EGFR- and EGFRvIII-overexpressing Tumor Cells*. Cancer Res., **2003**, 63, 3154-3161.
31. Chen, H.; Gao, J.; Lu, Y.; Kou, G.; Zhang, H.; Fan, L.; Sun, Z.; Guo, Y.; Zhong, Y. *Preparation and Characterization of PE38KDEL-Loaded Anti-HER2 Nanoparticles for Targeted Cancer Therapy*. J. Control. Rel., **2008**, 128, 209-216.
32. Ackerson, C. J.; Jadzinsky, P. D.; Jensen, G. J.; Kornberg, R. D. *Rigid, Specific, and Discrete Gold Nanoparticle/Antibody Conjugates*. J. Am. Chem. Soc., **2006**, 128, 2635-2640.
33. Garrido, G.; Tikhomirov, I. A.; Rabasa, A.; Yang, E.; Gracia, E.; Iznaga, N.; Fernández, L. E.; Crombet, T.; Kerbel, R. S.; Pérez, R. *Bivalent Binding by Intermediate Affinity of Nimotuzumab: A Contribution to Explain Antibody Clinical Profile*. Cancer Biol. Ther., **2011**, 11, 373-382.
34. Puertas, S.; Batalla, P.; Moros, M.; Polo, E.; del Pino, P.; Guisán, J. M.; Grazú, V.; de la Fuente, J. M. *Taking Advantage of Unspecific Interactions to Produce Highly Active Magnetic Nanoparticle-Antibody Conjugates*. ACS Nano, **2011**, 5, 4521-4528.
35. Fuentes, M.; Mateo, C.; Guisán, J. M.; Fernández-Lafuente, R. *Preparation of Inert Magnetic Nanoparticles for the Directed Immobilization of Antibodies*. Biosens. Bioelec., **2005**, 20, 1380-1387.
36. Deisenhofer, J. *Crystallographic Refinement and Atomic Models of a Human Fc Fragment and its Complex with Fragment B of Protein A from Staphylococcus Aureus at 2.9- and 2.8-Å Resolution*. Biochem., **1981**, 20, 2361-2370. (Protein data bank file 1FC1).
37. Sauer-Eriksson, A. E.; Kleywegt, G. J.; Uhlén, M.; Jones, T. A. *Crystal Structure of the C2 Fragment of Streptococcal Protein G in Complex with the Fc Domain of Human IgG*. Structure, **1995**, 3, 265-278. (Protein data bank file 1FCC).

38. Akerström, B.; Björck, L. *A Physicochemical Study of Protein G, a Molecule with Unique Immunoglobulin G-Binding Properties*. *J. Biol. Chem.*, **1986**, 261, 10240-10247.
39. Yang, L.; Biswas, M. E.; Chen, P. *Study of Binding between Protein A and Immunoglobulin G Using a Surface Tension Probe*. *Biophys. J.*, **2003**, 84, 509-522.
40. Horisberger, M.; Clerc, M. F. *Labelling of Colloidal Gold with Protein A*. *Histochem.*, **1985**, 82, 219-223.
41. Shi, M.; Wosnick, J. H.; Ho, K.; Keating, A.; Shoichet, M. S. *Immuno-Polymeric Nanoparticles by Diels–Alder Chemistry*. *Angew. Chem. Int. Ed.*, **2007**, 119, 6238-6243.
42. Haun, J. B.; Devaraj, N. K.; Hilderbrand, S. A.; Lee, H.; Weissleder, R. *Bioorthogonal Chemistry Amplifies Nanoparticle Binding and Enhances the Sensitivity of Cell Detection*. *Nat. Nano*, **2010**, 5, 660-665.
43. Vugts, D. J.; Vervoort, A.; Stigter-van Walsum, M.; Visser, G. W. M.; Robillard, M. S.; Versteegen, R. M.; Vulders, R. C. M.; Herscheid, J. D. M.; van Dongen, G. A. M. S. *Synthesis of Phosphine and Antibody–Azide Probes for in Vivo Staudinger Ligation in a Pretargeted Imaging and Therapy Approach*. *Bioconj. Chem.*, **2011**, 22, 2072-2081.
44. Turkevich, J.; Stevenson, P. C.; Hillier, J. *A Study of the Nucleation and Growth Processes in the Synthesis of Colloidal Gold*. *Discuss. Farad. Soc.*, **1951**, 11, 55-75.
45. Frens, G. *Controlled Nucleation For Regulation of Particle Size in Monodisperse Gold Suspensions*. *Nat. Phys. Sci.*, **1973**, 241, 20–22.
46. Kimling, J.; Maier, M.; Okenve, B.; Kotaidis, V.; Ballot, H.; Plech, A. *Turkevich Method for Gold Nanoparticle Synthesis Revisited*. *J. Phys. Chem. B*, **2006**, 110, 15700-15707.
47. Bastús, N. G.; Comenge, J.; Puntès, V. *Kinetically Controlled Seeded Growth Synthesis of Citrate-Stabilized Gold Nanoparticles of up to 200 nm: Size Focusing versus Ostwald Ripening*. *Langmuir*, **2011**, 27, 11098-11105.
48. Daniel, M.-C.; Astruc, D. *Gold Nanoparticles: Assembly, Supramolecular Chemistry, Quantum-Size-Related Properties, and Applications toward Biology, Catalysis, and Nanotechnology*. *Chem. Rev.*, **2003**, 104, 293-346.
49. Saha, K.; Agasti, S. S.; Kim, C.; Li, X.; Rotello, V. M. *Gold Nanoparticles in Chemical and Biological Sensing*. *Chem. Rev.*, **2012**, 112, 2739-2779.
50. Kumar, S.; Gandhi, K. S.; Kumar, R. *Modeling of Formation of Gold Nanoparticles by Citrate Method*. *Ind. Eng. Chem. Res.*, **2006**, 46, 3128-3136.
51. Chow, M. K.; Zukoski, C. F. *Gold Sol Formation Mechanisms: Role of Colloidal Stability*. *J. Coll. Int. Sci.*, **1994**, 165, 97-109.
52. Ji, X.; Song, X.; Li, J.; Bai, Y.; Yang, W.; Peng, X. *Size Control of Gold Nanocrystals in Citrate Reduction: The Third Role of Citrate*. *J. Am. Chem. Soc.*, **2007**, 129, 13939-13948.
53. LaMer, V. K.; Dinegar, R. H. *Theory, Production and Mechanism of Formation of Monodispersed Hydrosols*. *J. Am. Chem. Soc.*, **1950**, 72, 4847-4854.

54. Rodríguez-González, B.; Mulvaney, P.; Liz-Marzán, L. M. *An Electrochemical Model for Gold Colloid Formation via Citrate Reduction*. *Phys. Chem.*, **2007**, 221, 415-426.
55. Pong, B.-K.; Elim, H. I.; Chong, J.-X.; Ji, W.; Trout, B. L.; Lee, J.-Y. *New Insights on the Nanoparticle Growth Mechanism in the Citrate Reduction of Gold(III) Salt: Formation of the Au Nanowire Intermediate and Its Nonlinear Optical Properties*. *J. Phys. Chem. C*, **2007**, 111, 6281-6287.
56. Brown, K. R.; Natan, M. J. *Hydroxylamine Seeding of Colloidal Au Nanoparticles in Solution and on Surfaces*. *Langmuir*, **1998**, 14, 726-728.
57. Jana, N. R.; Gearheart, L.; Murphy, C. J. *Seeding Growth for Size Control of 5–40 nm Diameter Gold Nanoparticles*. *Langmuir*, **2001**, 17, 6782-6786.
58. Rodríguez-Fernández, J.; Pérez-Juste, J.; García de Abajo, F. J.; Liz-Marzán, L. M. *Seeded Growth of Submicron Au Colloids with Quadrupole Plasmon Resonance Modes*. *Langmuir*, **2006**, 22, 7007-7010.
59. Perrault, S. D.; Chan, W. C. W. *Synthesis and Surface Modification of Highly Monodispersed, Spherical Gold Nanoparticles of 50–200 nm*. *J. Am. Chem. Soc.*, **2009**, 131, 17042-17043.
60. Norde, W. *Adsorption of Proteins from Solution at the Solid-Liquid Interface*. *Adv. Coll. Int. Sci.*, **1986**, 25, 267-340.
61. Kumar, S.; Aaron, J.; Sokolov, K. *Directional Conjugation of Antibodies to Nanoparticles for Synthesis of Multiplexed Optical Contrast Agents with Both Delivery and Targeting Moieties*. *Nat. Protoc.*, **2008**, 3, 314-320.
62. Kumar, S.; Harrison, N.; Richards-Kortum, R.; Sokolov, K. *Plasmonic Nanosensors for Imaging Intracellular Biomarkers in Live Cells*. *Nano Lett.*, **2007**, 7, 1338-1343.
63. Wolfe, C. A. C.; Hage, D. S. *Studies on the Rate and Control of Antibody Oxidation by Periodate*. *Anal. Biochem.*, **1995**, 231, 123-130.
64. Amigo, J. M.; Bastús, N. G.; Hoen, R.; Vázquez-Campos, S.; Varón, M.; Royo, M.; Puentes, V. *Analysis of Time-Dependent Conjugation of Gold Nanoparticles with an Antiparkinsonian Molecule by using Curve Resolution Methods*. *Anal. Chim. Acta*, **2011**, 683, 170-177.
65. Tang, Z.; Xu, Bin; Wu, B.; Germann, M. W.; Wang, G. *Synthesis and Structural Determination of Multidentate 2,3-Dithiol-Stabilized Au Clusters*. *J. Am. Chem. Soc.*, **2010**, 132, 3367–3374.
66. Dondapati, S. K.; Sau, T. K.; Hrelescu, C.; Klar, T. A.; Stefani, F. D.; Feldmann, J. *Label-free Biosensing Based on Single Gold Nanostars as Plasmonic Transducers*. *ACS Nano*, **2010**, 4, 6318-6322.
67. Hrelescu, C.; Sau, T. K.; Rogach, A. L.; Jäckel, F.; Laurent, G.; Douillard, L.; Charra, F. *Selective Excitation of Individual Plasmonic Hotspots at the Tips of Single Gold Nanostars*. *Nano Lett.*, **2011**, 11, 402-407.
68. Sperling, R. A.; Pellegrino, T.; Li, J. K.; Chang, W. H.; Parak, W. J. *Electrophoretic Separation of Nanoparticles with a Discrete Number of Functional Groups*. *Adv. Func. Mater.*, **2006**, 16, 943-948.

69. Mattoussi, H.; Mauro, J. M.; Goldman, E. R.; Anderson, G. P.; Sundar, V. C.; Mikulec, F. V.; Bawendi, M. G. *Self-Assembly of CdSe–ZnS Quantum Dot Bioconjugates Using an Engineered Recombinant Protein*. *J. Am. Chem. Soc.*, **2000**, 122, 12142-12150.
70. Cebula, D. J.; Ottewill, R. H.; Ralston, J.; Pusey, P. N. *Investigations of Microemulsions by Light Scattering and Neutron Scattering*. *J. Chem. Soc., Faraday Trans. 1*, **1981**, 77, 2585-2612.
71. Hagel, L. *Gel Filtration: Size Exclusion Chromatography. Protein Purification*. John Wiley & Sons, Inc., **2011**, 51-91.
72. Mirkin, C. A.; Letsinger, R. L.; Mucic, R. C.; Storhoff, J. J. *A DNA-Based Method for Rationally Assembling Nanoparticles into Macroscopic Materials*. *Nature*, **1996**, 382, 607-609.
73. Alivisatos, A. P.; Johnsson, K. P.; Peng, X.; Wilson, T. E.; Loweth, C. J.; Bruchez, M. P.; Schultz, P. G. *Organization of 'Nanocrystal Molecules' Using DNA*. *Nature*, **1996**, 382, 609-611.
74. Mucic, R. C.; Storhoff, J. J.; Mirkin, C. A.; Letsinger, R. L. *DNA-Directed Synthesis of Binary Nanoparticle Network Materials*. *J. Am. Chem. Soc.*, **1998**, 120, 12674-12675.
75. Fu, A.; Micheel, C. M.; Cha, J.; Chang, H.; Yang, H.; Alivisatos, A. P. *Discrete Nanostructures of Quantum Dots/Au with DNA*. *J. Am. Chem. Soc.*, **2004**, 126, 10832-10833.
76. Lee, J. H.; Wernette, D. P.; Yigit, M. V.; Liu, J.; Wang, Z.; Lu, Y. *Site-Specific Control of Distances between Gold Nanoparticles Using Phosphorothioate Anchors on DNA and a Short Bifunctional Molecular Fastener*. *Angew. Chem. Int. Ed.*, **2007**, 46, 9006-9010.
77. Ohshiro, T.; Zako, T.; Watanabe-Tamaki, R.; Tanaka, T.; Maeda, M. *A Facile Method Towards Cyclic Assembly of Gold Nanoparticles Using DNA Template Alone*. *Chem. Commun.*, **2010**, 46, 6132-6134.
78. Li, X.; Yi, G.; Renguo, X.; Jiaqi, Z.; Wensheng, Y.; Tiejin, L. *Three-Dimensional Assembly of Au Nanoparticles Using Dipeptides*. *Nanotechnol.*, **2002**, 13, 725-728.
79. Shenton, W.; Davis, S. A.; Mann, S. *Directed Self-Assembly of Nanoparticles into Macroscopic Materials Using Antibody–Antigen Recognition*. *Adv. Mater.*, **1999**, 11, 449-452.
80. Hui, Y.; Changqing, Y.; Chi-Hung, T.; Junjie, Z.; Mengsu, Y. *DNA-Directed Self-Assembly of Gold Nanoparticles into Binary and Ternary Nanostructures*. *Nanotechnol.*, **2007**, 18, 015102.

Targeting the Epidermal Growth Factor Receptor by Rationally Designed Cetuximab Antibody-Gold Nanoparticle Bioconjugates



Monoclonal antibody (MAb) drugs are a relatively new innovation in medical treatment. Most of the MAbs approved by the US Food and Drug Administration (FDA) for clinical applications in oncology have come in the last decade.^{1,2} Thus far, many attempts have been made to improve their efficacy, but there still remain serious troubles for their practical use, such as causing side effects or difficulty in targeting the tumours. Therefore, there is a mandatory need to vehiculate those therapeutic agents in order to fully take advantage of their therapeutic power. Recent experimental evidences show that NPs can be excellent carriers of MAbs, and in turn, they can still load other components such as chemotherapeutic drugs,³⁻⁶ thus increasing their therapeutic efficacy. Yet, the potentiality of MAb-NP bioconjugation or “nanoconjugation” is not only consisted on providing targeted delivery vehicles, as it has been generally believed,⁷ but also controlling the degree of cellular response.⁸⁻¹³ In this sense, it has been observed that Cetuximab MAb-NP bioconjugation alters the mechanism governing the endocytosis of its specific receptor, probably due to the different Ab presentation to the cell and/or the presence of the NP, hence mediating a different cellular fate from that of the free MAb.¹⁰ The size of Herceptin MAb-NP bioconjugates has also been observed to play an important role in their specific cell receptor interactions and uptake, thus controlling proliferation and the extent of other cellular functions.¹¹ In a similar way, peptides specific to endothelial-expressed

receptors have improved their ability to induce angiogenesis when conjugated to NPs, mainly due to the presentation of the peptide on a structured scaffold which provide an optimum interaction with cell receptors.¹² Other parameters such as ligand coverage density of the NPs and the strength of the ligand/receptor interaction have also been identified to have a crucial role in receptor-mediated endocytic processes,^{13,14} providing novel means to modulate cellular behaviours. In addition to all this benefits, NP bioconjugates can passively accumulate in the tumour by the enhanced permeability and retention (EPR) effect; tumor vessels are usually abnormal in form and with wide fenestrations where NPs can penetrate and be retained due to the lack of effective lymphatic drainage.

This Chapter aims to provide further insight on how a rational design of the MAb-NP bioconjugates can tune molecular events that eventually regulate and modulate the cell response. To that end, Au NPs have been functionalized with Cetuximab MAbs at a well-defined orientation and coverage density through the site-directed chemistry developed in Chapter 5. The attachment of Cetuximab MAbs onto Au NPs in a controlled manner has allowed the formation of different multivalent NPs, which can selectively control specific interactions between Cetuximab and the epidermal growth factor receptor (EGFR); a receptor tyrosine kinase overexpressed in the used squamous cancer cell line (A431), as in other cancer cells.¹⁵ Herein, it is shown that NPs with a different presentation of surface-coupled Abs can regulate molecular processes, such as NP-membrane receptor binding, receptor distribution, receptor endocytosis and recycling, and subsequent intracellular signal transduction, to a different extent. These results show that the Cetuximab-Au NP bioconjugates may elicit different biological responses due to the modification in the local concentration of Abs and orientation/presentation of the ligands to the cell surface than those produced by different concentration of the free MAb.

6.1. Background and overview. Targeted Therapy of the Epidermal Growth Factor Receptor (EGFR) by Cetuximab Monoclonal Antibodies.

Members from the EGFR family regulate many cellular processes, including cell survival, growth, proliferation or differentiation, by ligand-activated signalling.

Perturbation of this signalling (e.g. by receptor overexpression, mutation/truncation or activation by excessive autocrine growth factor expression) has been correlated to cancer.¹⁵⁻¹⁸ Indeed, the key role of EGFR has been identified in many human cancers, such as breast, colon, head, neck, kidney and lung.¹⁹ For this reason, blocking EGFR has become a promising target for cancer therapy, leading to the development of a wide range of anticancer therapeutics towards this receptor.^{15,20,21} Anti-EGFR MABs are one of the most successful molecular-targeted drugs for cancer treatment. Amongst them, Cetuximab was already approved by the FDA in 2004 for the treatment of advanced colorectal cancer. The primary mechanism of Cetuximab is to bind EGFR with high affinity, thus preventing ligand binding and its ensuing receptor activation.²² In this Section, a comprehensive view of the receptor structure and function and its inactivation mechanism by Cetuximab is given.

6.1.1. EGFR structure and function

The EGFR is a 170-kDa trans-membrane glycoprotein that belongs to the tyrosine kinase family of receptors, and it is part of the ErbB/HER family of receptors: EGFR itself (ErbB1), ErbB2 (HER2/*neu*), ErbB3 (HER3), and ErbB4 (HER4). Each of these receptors comprises three domains: a large extracellular region (EC), a lipophilic transmembrane (TM) segment, and an intracellular (IC) domain (Figure 6.1).²³ The extracellular region contains two homologous domains involved in ligand binding (domains I and III; L1 and L3) and two cysteine-rich domains (domains II and IV; CR2 and CR4). The TM domain separates the EC and IC regions of the receptor. The IC region is composed of a juxtamembrane (JM) region, a tyrosine kinase (TK) domain, and a C-terminal (CT) regulatory region. CT domain contains tyrosine residues that modulate EGFR-mediated signal transduction upon phosphorylation.

The EC region from the receptor can bind high-affinity ligands. In particular, six mammalian ligands have been identified that bind to EGFR, including epidermal growth factor (EGF), transforming growth factor- α (TGF α), amphiregulin, heparin-binding EGF-like growth factor, betacellulin and epiregulin.²⁴ The binding of these ligands alters the spatial arrangement of the receptor domains (Figure 6.2).²² Most of

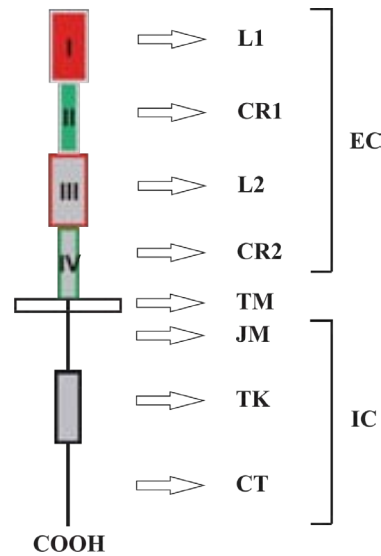


Figure 6.1. Schematic representation of EGFR structure. The EGFR is composed of three domains: the EC domain, the lipophilic TM segment and an IC domain. The EC domain consists of four sub-domains (I-IV, numbered from distal end to membrane), also known as L1/L2 and CR1/CR2. The TM domain is followed by the IC domain, which has a JM region, a TK region and a CT domain, responsible for recruitment and phosphorylation of proteins in pathways that are activated by EGFR. EGFR: Epidermal growth factor receptor; EC: Extracellular; L: Large domain; CR: Cystein-rich; TM: Transmembrane; IC: Intracellular; JM: Juxtamembrane; TK: Tyrosine kinase; CT: Carboxyl terminal.

the unliganded EGFRs (about 95%) exist in a compact autoinhibited conformation, in which domain II is tethered with domain IV (Figure 6.2-A). In the 5% remaining unliganded receptors, this tether is broken and the EGFR adopts an untethered or extended conformation (Figure 6.2-B). Ligands bind preferentially to this extended form, interacting with domain I and III and stabilizing the receptor in a conformation in which domain II is exposed and the receptor can dimerize (Figure 6.2-C-D). The EGFR dimerization is entirely receptor-mediated, with no contacts between the two growth factor molecules in the dimeric complex. For instance, the distance between the two ligands in the back-to-back dimer configuration was found to be approximately 8 nm, clearly indicating that the ligand is not involved in cross-linking the receptor dimer.^{25,26}

Importantly, this ligand-induced dimerization is also responsible for the increase in receptor tyrosine kinase activity, leading to cross- or transphosphorylation of key tyrosine residues in the CT domain.^{27,28} The phosphorylation at these residues creates high-affinity docking sites for the recruitment of intracellular signaling proteins (*i.e.*

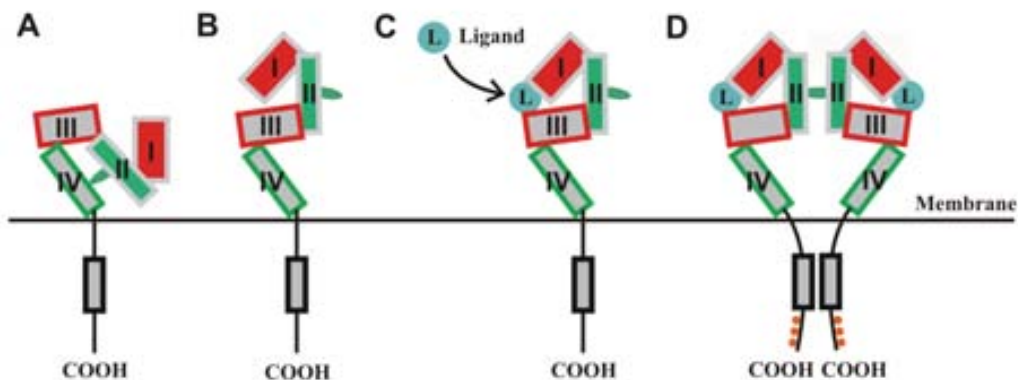


Figure 6.2. Mechanism of ligand-induced EGFR dimerization. Cartoon representation of the domains of the extracellular region of EGFR; domain I in red, domain II in green, domain III in gray with red border, domain IV in gray with green border, ligand in cyan and phosphorylated tyrosine residues in orange. A) Tethered monomer; B) untethered monomer; C) ligand stabilized extended conformation; D) ligand induced activated dimer.

SH2- and PTB-containing signalling proteins), which in turn, become phosphorylated and thereby activated.²⁹ These intracellular phosphorylation events can activate a number of signal transduction cascades that lead the signal towards the nucleus, resulting in growth and survival benefits towards the cell (Figure 6.3).¹⁸ The intracellular signalling pathways activated by the EGFR include the mitogen-activated protein kinase/extracellular signal-regulated kinase (MAPK/ERK), the phosphatidylinositol 3 kinase/AKT (PI3K/AKT), the phospholipase C gamma /protein kinase C (PLC- γ /PKC) and the signal transducer and activator of transcription (STAT) pathways, which regulates cell transformation, proliferation and survival.^{30,31} MAPK/ERK and PI3K/AKT pathways have been thought to be the two dominant signalling pathways derived from EGFR stimulation. The reader is referred to a few excellent reviews on this topic.^{16,32}

The major physiological portal of EGFR cell internalization are clathrin-coated pits (Figure 6.4).^{33,34} Shortly after binding, the EGF-EGFR complexes have been localized in clathrin-coated regions of the plasma membranes.³⁵ The clathrin coat rapidly dissociates from these vesicles in order for the vesicle to fuse with early endosomes, where EGF and EGFR accumulate rapidly after endocytosis.³⁶ Importantly, the EGF-EGFR complexes remain intact in the early endosomes, as the mildly acidic pH (6.0-6.5) from these compartments is not sufficient to cause their dissociation.³⁷ Therefore, receptors in endosomes remain dimerized and tyrosine

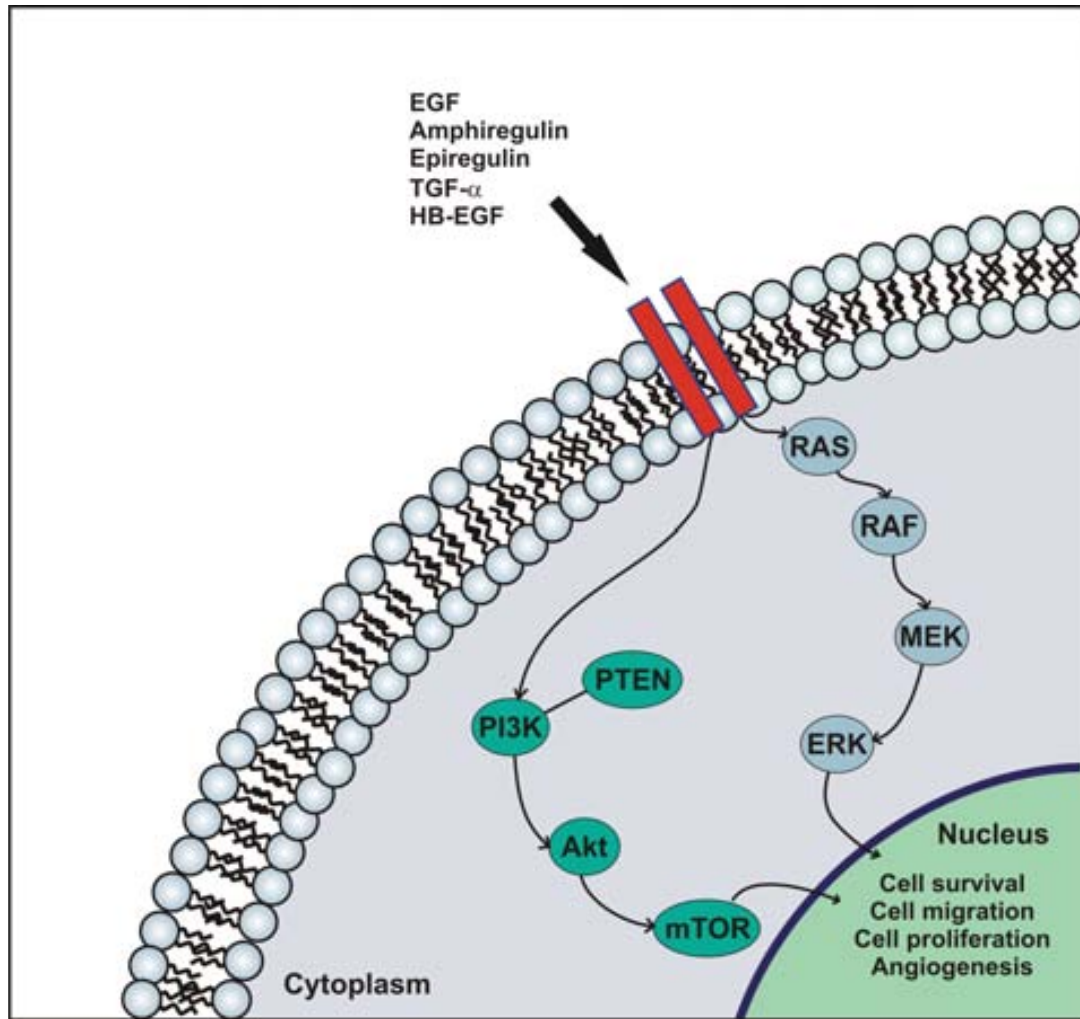


Figure 6.3. Representative scheme of the main EGFR signaling pathways. Ligands bind to ErbB receptors (red) leading to their dimerization and activation of a network of signalling pathways: PI3K/AKT (green) and MAPK/ERK (blue) pathways. These pathways lead the signal towards the nucleus where cell survival, cell migration, cell proliferation and angiogenesis are regulated.

phosphorylated.³⁸ Then, early endosomes can either recycle to the cell surface³⁹ or proceed through formation of multivesicular bodies (MVBs) and late endosomes.⁴⁰ Recycling continues in MVBs, albeit at lower rates than from early endosomes.³⁹ Finally, MVBs containing EGF-EGFR complexes fuse with primary lysosomal vesicles.⁴¹ At the low pH level of ~ 5 showing these compartments, EGF-EGFR complex dissociates³⁷ and both, ligand and receptor, are degraded by the lysosomal proteases (*i. e.* cathepsin B).⁴¹⁻⁴³ A few studies have also localized the EGF receptor in the endoplasmatic reticulum (ER) and the nucleus.^{44,45} For instance, Lin *et al.* suggested for the first time that the nuclear fraction of the receptor and its ligand were involved in gene expression.⁴⁴ However, how the receptor is translocated to the nucleus remains unclear.

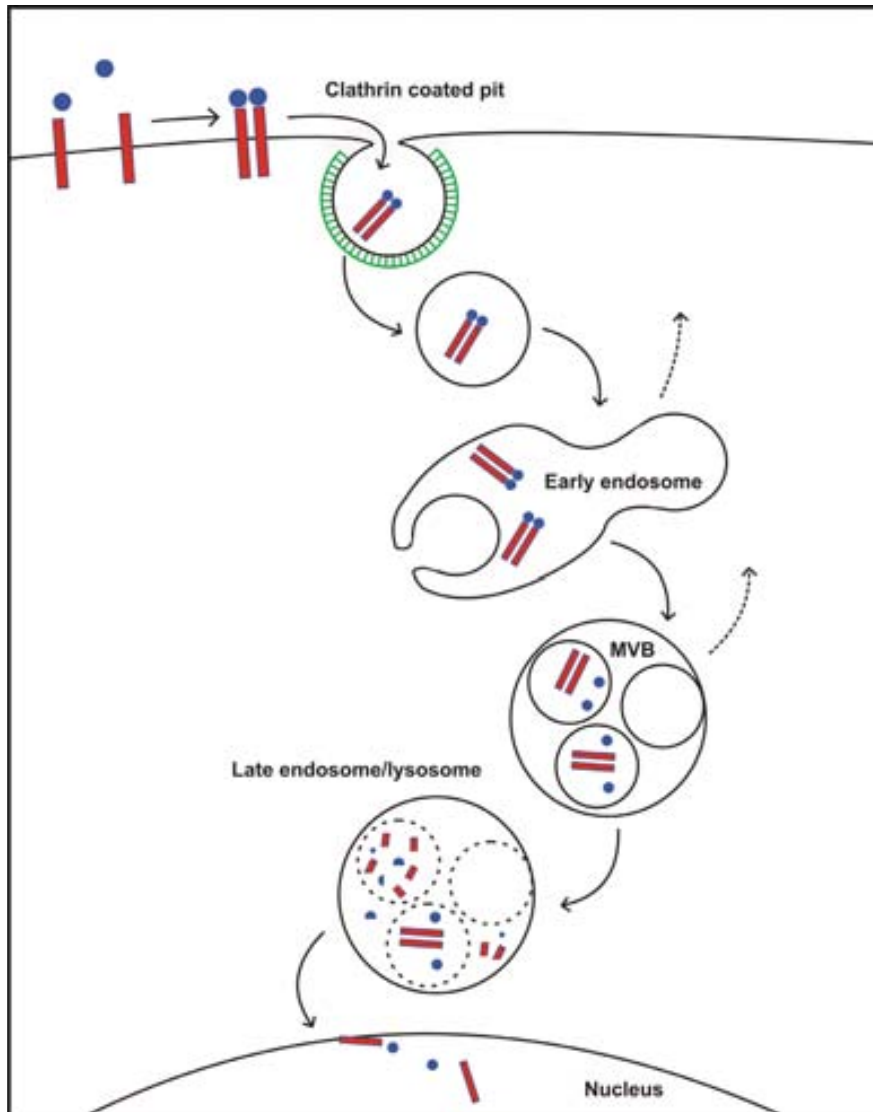


Figure 6.4. Schematic of EGFR trafficking upon ligand binding. Ligand-EGFR complex is predominantly internalized in clathrin-coated pits and accumulates into early endosomes. Then, early endosomes can either recycle to the cell surface (dashed arrow) or proceed through formation of late endosomes and MVBs. MVBs continue to recycle (dashed arrow). Sorting of MVBs leads the receptor to lysosomes that contain proteolytic enzymes, where EGF and EGFR undergo degradation. A fraction of EGFR and EGF have also been localized in the ER and the nucleus.

6.1.2. Binding of Cetuximab Monoclonal Antibody to EGFR.

The first therapeutics to target the EGFR EC domain have been MAbs (e.g. Cetuximab) directed against the ligand-binding region of the EGFR. Cetuximab, formerly named IMC C225 and first marketed in Australia as Erbitux (Merck-Serono),

is a chimeric human-murine IgG1 MAb which binds to EGFR with high affinity (approx. 5 to 10x superior to that from endogenous ligands), thus blocking it and preventing its activation.²² As one of several new cancer biotherapies, Cetuximab is in advanced-stage development for the treatment of various solid tumors. In 2004, it was approved by the U.S. Food and Drug Administration (FDA) for its use in patients with metastatic colorectal cancer, followed by European-wide approval. In 2006, it was also approved, alone or in combination with cisplatin and radiation, for patients with head and neck squamous cell carcinoma. Furthermore, Cetuximab is currently being evaluated in patients with non-small cell lung carcinoma and pancreatic cancer. Today, more than 40 countries have been approved to use Cetuximab, and thousands of patients have been treated with this drug.

Recent studies have demonstrated that the MAb Cetuximab binds to a site in the region III of the EGFR EC domain, covering an epitope that partially overlaps the EGF binding site on that domain (Figure 6.5).²² Specifically, the tyrosine Y102 from the complementarity determining region (CDR) H3 of FabC225 occupies approximately the same position on the surface of EGFR as does an essential leucine side chain (L47) from EGF. In addition, the V_H region of FabC225 sterically blocks

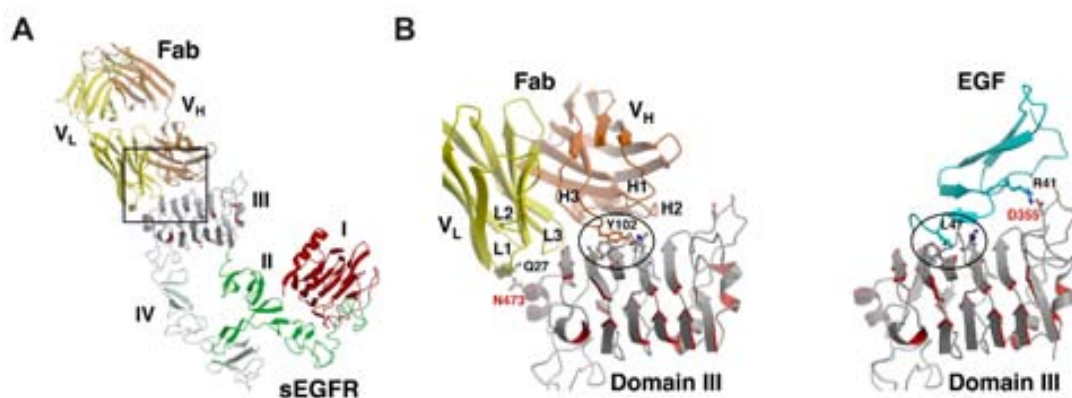


Figure 6.5. Crystal structure of FabC225-EGFR and EGF-EGFR complexes. A) Cetuximab binds to domain III of a tethered EGFR molecule; both V_H and V_L of Cetuximab participate in the interaction with domain III, with all contacts coming from the CDRs of FabC225. Inset shown in figure B. B) Detailed view of the interactions of domain III of EGFR with Fab C225 and EGF. Tyrosine Y102 of FabC225 occupies the same binding pocket as L47 of EGF. Image adapted from ref. 22.

domain I from occupying the position observed in EGF-bound structures.

The binding of Cetuximab to domain III keeps the receptor in a tethered or autoinhibited conformation (*i.e.* with intramolecular interactions between domains II and IV; see Section 6.1.1, Figure 6.2). This prevents the receptor from adopting the extended conformation required for ligand binding, and thus, its ligand-induced dimerization and activation. In contrast, it has been demonstrated that due to the bivalency of Cetuximab MAb, it has the ability to crosslink two receptor molecules. Such mechanistic event involves receptor dimerization in an inactive state (*i.e.* without receptor phosphorylation), and it has been shown to be essential to inhibit tumour cells growth.⁴⁶ Similarly, crosslinking of two EGFR molecules by the MAb Zalutumumab (*i.e.* a MAb directed against domain III of EGFR) has been identified by tomography analyses.⁴⁷ In such complexes, the intracellular kinase domains are separated to an extent that result incompatible with the induction of signalling. Specifically, the two kinase domains are oriented relatively far from each other, 17-32 nm, compared with 1-2 nm observed for EGF-bound dimers.

Hence, Cetuximab-induced receptor dimerization has been demonstrated to play a key role in the inhibition of cell proliferation and EGFR down-regulation.⁴⁶ By this mechanism, the MAbs can block the receptor tyrosine kinase activity, thus inhibiting the phosphorylation of key tyrosine residues in the CT domain. As a result, the inhibition of phosphorylation events prevents the activation of the main EGFR signal transduction pathways, MAPK/ERK and PI3K/AKT (see Section 6.1.1), which modulate cellular transcription and cell cycle progression.¹⁸

Despite ligand dimerization and activation of EGFR are primary events for the EGF-EGFR complex to be internalized by the cell (see Section 6.6.1), Cetuximab does not require such circumstances. Cetuximab-EGFR complexes are internalized by the cell without tyrosine kinase activation.⁴⁸ In addition, the internalization process is slow compared with ligand-dependent internalization.⁴⁹ The intracellular fate of these complexes is also different than that of EGF-EGFR complexes. Most of the internalized Cetuximab-EGFR complex is recycled to the cell surface.⁴⁹ Unlike the receptor complex with EGF, Cetuximab-EGFR targeting endosomes is not dissociated

by the low pH levels showing these compartments.²² Whether any of the Cetuximab-internalized receptor is trafficked to the lysosome is not known directly. However, some data suggests that the receptor is degraded in the lysosomes since slow down-regulation has been observed.^{46,49,50} Additionally, a recent study demonstrated that Cetuximab induces EGFR trafficking to the ER, and ultimately to the nucleus.⁴⁸ The mechanism by which Cetuximab-EGFR complex escape the lysosome and enters the nucleus, as well as how this influences the biological response of cells, still remains to be explored.

6.2. Cellular receptor-mediated interactions with Au NP bioconjugates.

Ligand-mediated receptor clustering that alters intracellular signalling is ubiquitous in nature (see Section 6.1.1). Nevertheless, the effects of aggregation of receptors caused by an inhibitor of signal transduction, such as receptor-specific MAbs, remain to be fully elucidated. A few number of examples in the literature have demonstrated that MAbs can efficiently crosslink cell surface receptors and alter intracellular signalling and downstream events.^{46,47,51} Some of these studies have identified the formation of receptor dimers by their interaction with MAbs (e.g. Cetuximab⁴⁶ and Zalutumumab),⁴⁷ resulting in inhibition of cell signalling which promotes cell proliferation, amongst other cellular functions. Increased receptor crosslinking has been observed by a combination of two MAbs, in which synergistic effects lead to a higher receptor down-regulation.⁵¹ While it is possible to produce receptor clustering and alter cellular functions with MAbs, the extent of this mechanism is limited since MAbs are organic molecules with only two receptor binding sites.

In this regard, multivalent ligands provide valuable tools to investigate important receptor-ligand interactions. Multivalent ligands have shown to crosslink the membrane receptors more efficiently to regulate signalling processes.⁵² However, naturally occurring ligands are often scarce, structurally heterogeneous, or complex (e.g. a viral surface). NPs can act as synthetic multivalent ligands by providing multiple receptor interaction sites. Amongst other advantages, NPs can be synthesized

with a controlled size and shape and a chemically defined surface. By modulating these properties, the degree of receptors crosslinking and subsequent cell responses may be precisely controlled. Additionally, the fate of the receptors may be altered; for example, recycling of receptors may be decreased thanks to the NPs.

In particular, NPs coated with MAbs could potentially function as advanced multivalent ligands that are capable of crosslinking cell surface receptors and, in turn, further manipulate the cells response. For instance, the bioconjugation of Cetuximab MAbs with Au NPs (5 nm in size) was observed to enhance Cetuximab-induced EGFR endocytosis in PANC-1, AsPC-1, and MiaPaca-2 (human pancreatic cancer) cells, also altering this mechanism from clathrin mediated endocytosis (CME) to clathrin independent (CI) endocytosis.¹⁰ This effect was probably due to an increased capability of Cetuximab-Au NP bioconjugates for multiple binding to EGF receptors. Additionally, Chan and co-workers¹¹ examined the interactions of Herceptin MAb-functionalized Au NPs, of sizes ranging from 2 to 100 nm, with their ErbB2 receptors in SK-BR-3 (human breast cancer) cells (Figure 6.6). They found that NPs with diameter of 40-50 nm entered the cells much more efficiently than other sizes, inducing a greater receptor down-regulation, a decrease in downstream protein expression and a growth inhibition. This effect was attributed to their unique size for maximum interaction with ErbB2 receptors. They hypothesized that smaller NP bioconjugates (~2 nm) had a decreased effect due to their lower binding avidity, which led to a higher dissociation from the receptors. The lower efficiency of the larger NP bioconjugates (~70 nm) was attributed to their extremely high local concentration of Abs. Such high concentration limited the process of membrane wrapping due to the depletion of receptors in the area of binding. Note that differences in colloidal stability and NP concentration amongst the different NP sizes (for the same Ab concentration) might artefactually increase/decrease cell effects. Based on this study, Yokoyama *et al.*⁵³ investigated the effect of Cetuximab-NP bioconjugates in the size range of 40-50 nm. The bioconjugates showed greater levels of apoptosis and autophagy in HCC827 and H520 (non-small cell lung cancer) cells than unconjugated Cetuximab MAbs, probably due to a multivalent enhancement effect.

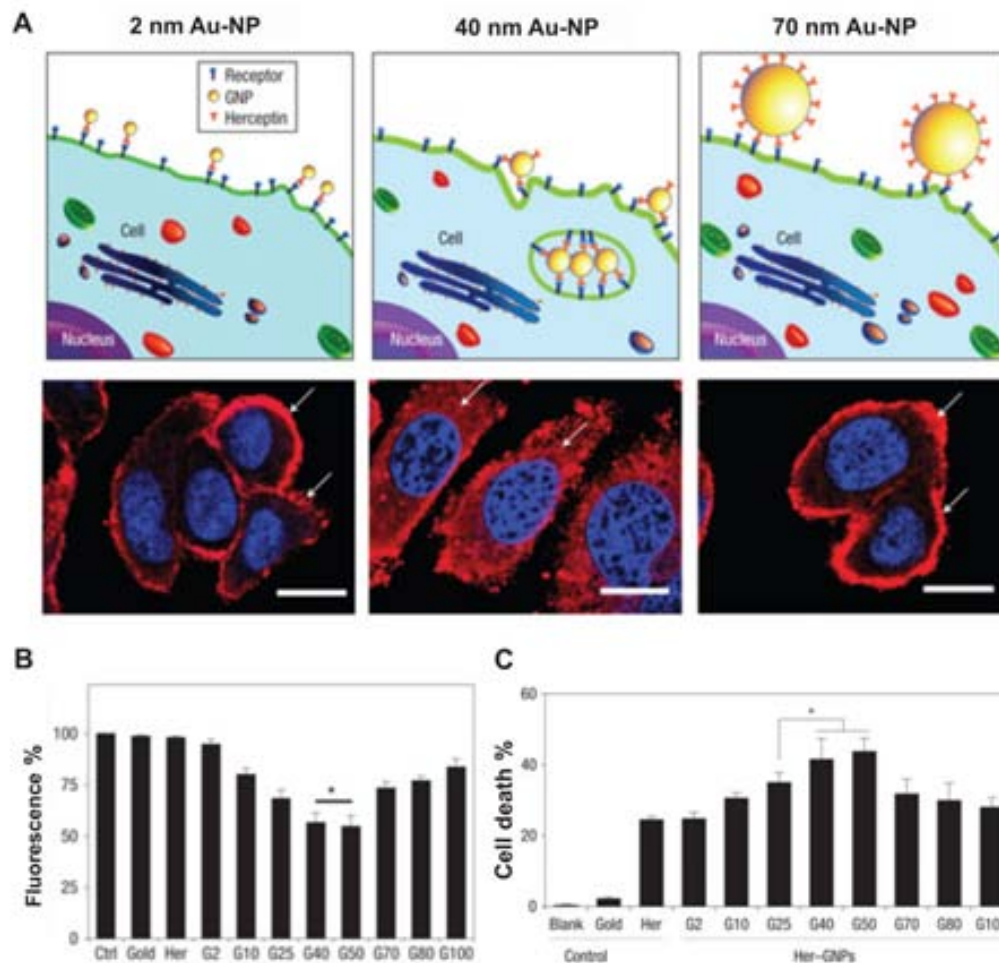


Figure 6.6. A) Illustration demonstrating binding of Herceptin-Au NP bioconjugates (G2, G40, G70 for 2, 40, 70 nm diameter) to ErbB2 receptors on the cell surface. G40 interacts with the receptors more efficiently due to its unique size and propensity for endocytosis. Lower panel: fluorescence images of the cellular distribution of ErbB2 (red) after treatment with fluorescently-labeled G2, G40, and G70. Note that only in the case of G40 treatment, NPs redistributed from the cell surface to the cytoplasm due to efficient endocytosis. B) Increase in relative fluorescence intensity following NP uptake was found to correlate with (C) subsequent cell death. Nuclei are stained blue, scale bar = 10 mm, * $p < 0.05$, error bars \pm sd, $n = 4$. Image adapted from reference 11.

Similarly, peptide-NP bioconjugates specific to endothelial-expressed receptors that control angiogenesis have shown to influence on the gene expression profile of hypoxia-related and angiogenic genes in HUVEC (human umbilical vein endothelial) cells. This influence was mainly due to the presentation of the peptide on a structured scaffold, which provided an optimum interaction with cell receptors.¹² In the same line, Maus *et al.*¹³ found a large increase in cell binding affinity of receptor-specific peptide-Au NP bioconjugates of approximately 10^3 x times when compared to the free

peptide. They attributed this effect to the multivalency of these Au NP bioconjugates, and suggested that even in the case of relatively weak ligand-receptor interaction, efficient receptor targeting can be reached with low Au NP concentrations (below 1 nM).

Further evidence of this multivalent effect of NPs was demonstrated by Huang *et al.*⁸ These authors found that the NP size and surface ligand density played key regulatory roles in the process of membrane Ab-receptor (IgE-FcεRI) binding and cross-linking, which, in turn, modulated degranulation and the consequent release of chemical mediators on RBL-2H3 (rat basophilic leukemia) cells. In their studies, Au NPs of 19.8 nm in size modified with thiolated dinitrophenyl (DNP) were effective cross-linkers of IgE-FcεRI complexes for cell activation, but only in the case of highly grafted DNP density. By decreasing the surface density of DNP on Au NPs such that the spacing of two DNPs became distant, they speculated that the antigen-mediated clustering of IgE-FcεRI complexes would then be precluded, thereby inhibiting an immune response. In addition, recent dynamic simulation studies by Vácha *et al.*¹⁴ identified the surface ligand density of NPs and the strength of the ligand/receptor interaction to have a crucial role in endocytic processes. In our studies with different local concentration and optimum orientation/presentation of Cetuximab MAbs, while no unique EGF receptor blocking effects have been observed, a significant change on receptor recycling after binding has also been detected. Avoiding receptor recycling evidently improves the biological/therapeutic effects of blocking EGFR.

6.3. Results and discussion

Recent observations highlight the importance of bioconjugating MAbs onto NPs and the NP characteristics (e.g. size) to their interactions with cell surface receptors (Section 6.1.3).^{10,11} In such studies, however, the MAbs are simply adsorbed onto the NPs leading to random configurations, and therefore, to a non-controlled multivalency with reversible binding (see Chapter 5, Section 5.1.4). The question on the biological effect produced by NPs with different Abs density was still open. In the present Chapter, a more delicate study has been performed, in which equally sized Au NPs

have been loaded in a controlled manner with MAbs, eventually obtaining a well-controlled orientation and number of MAbs to interact with cell surface receptors. To that end, the site-directed chemistry developed in Chapter 5 has been explored for the bioconjugation of Au NPs of 17.2 ± 1.8 nm-in-size with the EGFR MAb Cetuximab, a MAb of wide importance in cancer therapeutics (see Section 6.1.2).^{15,22} The choice of this particular NP size was based on the following considerations: i) they can be easily synthesized in water by the classical citrate reduction method with fairly good monodispersity,^{54,55} ii) they exhibit good colloidal stability when compared with large NP sizes (e.g. 50 nm),⁵⁶ and iii) it represents an optimum size to accommodate an increased and combined biological load while still being able to penetrate and cross cell membranes.⁵⁷⁻⁵⁹ The evidence of loading control has been based on the linearity of SPR evolution and calibrated NP saturation, as previously shown in Chapter 5 with a number of PABs. The interaction of Cetuximab-1-Au NP bioconjugates of varying multivalency with EGFR and how this influences the receptor intracellular pathway and subsequent cell signalling has been explored in a human epidermoid cancer cell line (A431), which specially overexpresses EGFR.

6.3.1. Synthesis of Cetuximab-1-Au NP bioconjugates by controlling the orientation and number of antibodies onto Au NPs.

The synthesis of Cetuximab-1-Au NP bioconjugates was done following the same steps already optimized in Chapter 5: i) Au NPs synthesis; ii) formation of Cetuximab-1 pair; iii) formation of Cetuximab-1-Au NP bioconjugates; and iv) Au NP surface passivation and purification.

Following this methodology, Au NPs of 17.2 ± 1.8 nm in diameter were first synthesized by variations of the traditional citrate reduction method (Figure 6.7-A,B).^{54,55} These NPs were used as-synthesized for the coupling of Cetuximab-1 pairs. Briefly, the oligosaccharide chains of Cetuximab MAbs, mainly located in the Ab' Fc region, were selectively oxidized to generate aldehyde groups. Then, these Abs were reacted with a hydrazide-containing linker molecule (**1**), resulting in the formation of a stable hydrazone bond with the formed aldehydes by chemoselective ligation (see

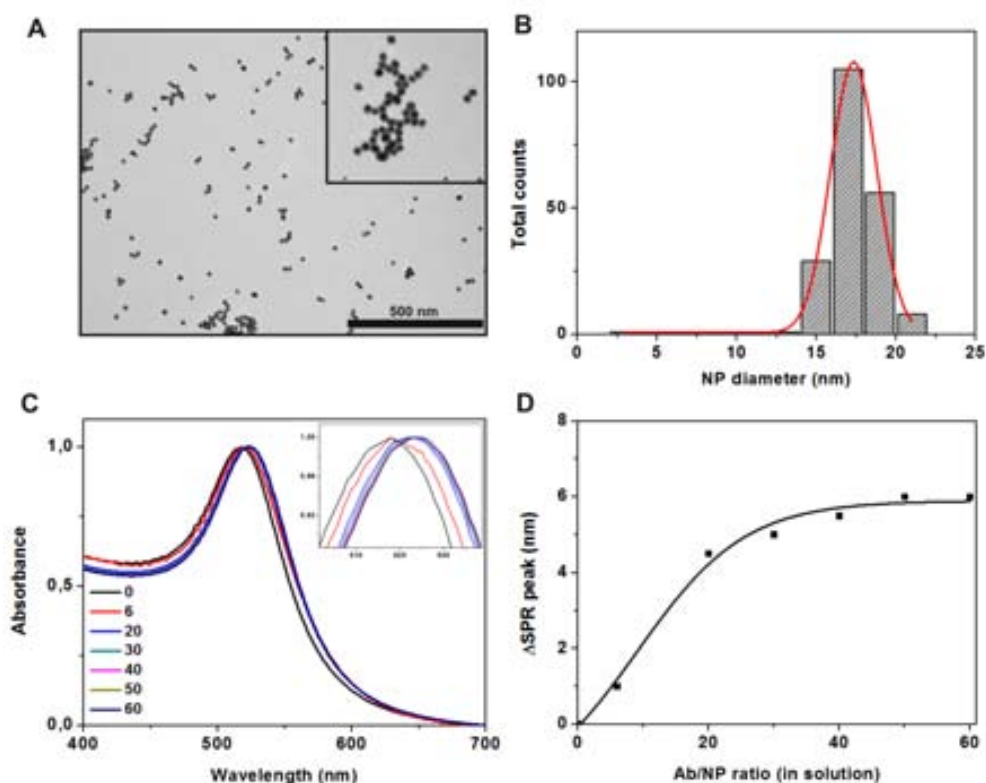


Figure 6.7. Characterization of the synthesized 17.2 ± 1.8 nm Au NPs and their bioconjugation with Cetuximab MAbs. A) Representative TEM image of the synthesized Au NPs and B) their size distribution. C) SP absorption bands of the NPs (normalized) with increasing amount of Cetuximab MAbs in solution (MAb/NP ratio in solution from 0 to 60), showing a red shift (inset). D) Shift of the SPR peak from the Au NPs upon conjugation with Cetuximab MAbs. Experimental data was fitted to Boltzmann equation ($R^2 = 0.984$).

Chapter 5, Figure 5.10). The linker **1** provided accessible dithiol groups to the Abs, which facilitated their spontaneous adsorption from solution on the surface of Au NPs in an oriented and controlled manner by forming strong Au-S bonds.^{60,61} The preferential binding of SH- groups to Au (~ 50 Kcal/mol)⁶² allowed the facile replacement of the citrate capping molecules on the NPs by Cetuximab-**1** pairs. The PEGylated linker **1**, in turn, may act as spacer arm leaving certain mobility to the Abs and conferring strong stability to the NP-Ab bioconjugate in water.^{63,64}

In the process of the chemical modification of Cetuximab, it was crucial to control the number of molecules of linker **1** that are bound to each MAb, since the formation of well-defined Cetuximab-**1** pairs avoids the possibility that one Cetuximab MAb can interact with more than one Au NP. Therefore, the selected Cetuximab MAb was

Mol LyCH/mol Cetuximab			
Experiment 1	Experiment 2	Experiment 3	Average
1.1	1.3	1.5	1.3 ± 0.2

Table 6.1. Determination of labelling sites in Cetuximab MAb under the optimized oxidation conditions (oxidation time = 30 minutes; solution pH = 7; periodate concentration = 10 mM; and reaction temperature = RT) with LYCH, which reacts with the aldehyde groups of the Cetuximab MAb to form fluorescent Cetuximab-LYCH conjugates.

oxidized following the optimized conditions found in Chapter 5: oxidation time = 30 minutes; solution pH = 7; periodate concentration = 10 mM; and reaction temperature = room temperature (RT). To ensure the efficient oxidation of one reaction site in Cetuximab MAb, a fluorescent hydrazide-containing dye (LYCH) was added after the oxidation reaction (for more details see Chapter 5, Section 5.2.1). Similar to linker **1**, LYCH reacts with the aldehyde groups of the Cetuximab MAbs to form fluorescent Cetuximab-LYCH conjugates.⁶⁵ MAb-LYCH conjugates were studied by spectrofluorometry and UV-Vis spectroscopy to determine the concentration of LYCH and Cetuximab, respectively. Importantly, an estimated coupling of nearly one LYCH molecule per Cetuximab MAb was obtained (Table 6.1), indicating that approximately one site per MAb was oxidized under the given oxidation conditions. In control experiments, under the purification conditions used the level of nonspecifically bound LYCH was found to be approximately 0.01-0.02 mol of LYCH per mol of Cetuximab. This amount was almost two orders of magnitude lower than the total amount of LYCH measured for the oxidized Cetuximab samples.

The reaction of the oxidized Cetuximab MAbs with linker **1** was performed under similar conditions used for LYCH (for more details see Chapter 5, Section 5.2.1). The synthesized Cetuximab-**1** pairs were then simultaneously purified and concentrated in a 40 mM HEPES buffer solution at pH = 8.5 using ultracentrifugation filter tubes. The bioconjugation of Cetuximab-**1** with the synthesized Au NPs was finally done by adding an HEPES solution of Cetuximab-**1** into a borate solution of Au NPs. The resulting mixture was left to react for 20 minutes under stirring at RT to ensure the efficient formation of Cetuximab-**1**-Au NP bioconjugates.

The binding of Cetuximab-1 to Au NPs was next monitored by taking advantage of the inherent optical properties of Au NPs. As Au NPs have a strong SPR band absorbance in the visible spectrum, particle aggregation, surface modification and changes in the surrounding dielectric medium can be measured as either a peak broadening or peak shift in the absorbance spectra.⁶⁶ Increasing amounts of Cetuximab-1 were added to the NPs, and the resulting Au NP bioconjugates were analyzed by UV-vis spectrophotometry (Figure 6.7-C,D). An evolution of the SPR peak to longer wavelengths was observed with increasing Cetuximab-1/NP ratio, until it reached a maximum constant value that was attributed to NP surface saturation. For instance, a Cetuximab-1/NP ratio (in solution) ≥ 50 revealed a maximum SPR peak shift of ~ 6 nm. Notably, these values fitted well to those obtained with other Ab systems (see Section 5.2.1, Chapter 5), indicating the efficacy and reproducibility of the conjugation process. Furthermore, no broadening of the SPR peak was observed, which was indicative of the high stability of the formed Cetuximab-1-Au NP bioconjugates.

The SPR values obtained were used as a reference for the preparation of Cetuximab-1-Au NP bioconjugates of a known coverage density of MAbs. In further experiments, a Cetuximab-1/NP ratio of 50 (in solution) was used to obtain the maximum coverage density of the NPs, and ratios of 20 and 6 were used for lower coverage densities. The amount of MAbs added in solution was correlated to the number of MAbs on the NPs. This is particularly important to their interaction with cell surface receptors. To this end, goat anti-rabbit-1 Abs were used as a model system to label with a fluorescent dye (*i.e.* AlexaFluor 488) and add to the NPs at different ratios (Chapter 5, Section 5.2.1). The bioconjugates prepared with Ab-1/NP ratios (in solution) of 6, 20 and 50 were quantified to have ~ 3 , 6 and 8 Abs on the NPs surface.

Herein, it is important to note that the addition of native (non-modified) Cetuximab MAbs onto Au NPs at the same conditions led to irreversible aggregation of the NPs within a few minutes (Figure 6.8), probably due to the lower affinity of Abs for the Au NP surface that is not sufficient to prevent Au NP aggregation. At lower concentrations (10x dilution of the Au NPs, ~ 1.8 nM Au NPs), this effect was less

significant, and stability was observed for ratios up to ~ 50 Ab/NP after 1 hour of incubation.

Finally, a short SH-PEG (MW = 356.48) was added to the bioconjugates to passivate the Au NP surface and avoid unspecific interactions with the cell surface and extracellular proteins or biomolecules, or with the linked Abs themselves. The SH-PEG molecules, in turn, are smaller than the linker **1** molecules, which may allow the mobility and maximum exposure of MAbs on the bioconjugate configuration. Note that these are important features to an efficient Ab-antigen binding. The samples were immediately dialyzed by using 300 kDa cellulose ester membranes. In particular, 10 ml of each bioconjugate was dialyzed against 5 L of PBS, in 2 cycles of 2 hours and a third cycle overnight at 4°C. In parallel, a control Ab (goat anti-rabbit IgG) was likewise purified to confirm the successful release of free Abs across the dialysis membrane. After the purification step, the samples were preserved in PBS 0.1% (w/v) BSA.

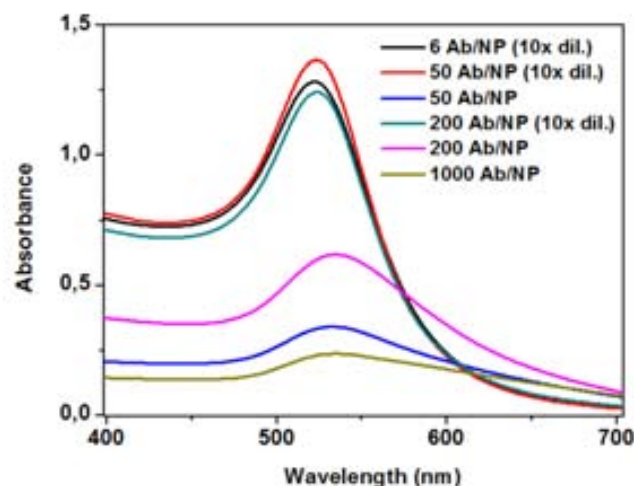


Figure 6.8. UV-visible spectra of 17.2 ± 1.8 nm Au NPs with increasing native goat anti-rabbit Ab/NP ratio (in solution) at the same concentration used for the previous experiments (~ 18 nM Au NPs) and a dilution of 10 x times (~ 1.8 nM Au NPs) after 1 hour of incubation.

6.3.2. Binding of Cetuximab-1-Au NP bioconjugates to EGFR.

The attachment of multiple Cetuximab molecules onto the Au NP surface allows the formation of multivalent engineered nanoparticles for crosslinking surface EGF receptors. To test this hypothesis, the binding capacity of Cetuximab-1-Au NP bioconjugates to EGFR was analyzed *in vitro* in a human epidermoid cancer cell line (A431) that expresses abnormally high levels of EGFR (1.2×10^6 receptors/cell) and it is normally used as a positive control for EGFR expression.^{46,67,68} With this aim, plasma membrane sheets from A431 cells were prepared, fixed, and incubated with Ab-1-Au NP bioconjugates by optimizing the method from Prior *et al.* (see Annex I: materials and methods).^{69,70} Cells were incubated either with Cetuximab-1-Au NP bioconjugates with a different loading of Abs (3, 6 and 8 Cetuximab MAbs attached onto 17.2 ± 1.8 nm Au NPs; hereafter named as **NPC3**, **NPC6** and **NPC8**, respectively) or unspecific Ab-1-Au NP bioconjugates (8 goat anti-rabbit PABs attached onto 17.2 ± 1.8 nm Au NPs; hereafter named as **NPAR**) at a concentration of ~ 7.5 nM of NPs for 25 minutes at 4°C to avoid receptor-mediated internalization.⁷¹

Areas of these plasma membrane sheets were visualized under TEM, allowing the interactions between the bioconjugates and EGFR to be screened, and providing a detailed monitoring of the distribution of EGF receptors in different regions of the plasma membrane (Figure 6.9-A). Image analysis from the resulting 2-D spatial maps describing cell surface microdomain distributions revealed that the binding efficiency of the Cetuximab-1-Au NP bioconjugates was much greater in the case of NPC8 than NPC6 and NPC3 (Figure 6.9-B), as expected. The observed increase in binding of NPC8 with EGF receptors suggests that the maximized Cetuximab MAbs loading on the NP, and thus, its higher multivalent capacity is probably enhancing its possibility of interaction with multiple EGF receptors. In contrast, NPC3 bioconjugates showed the lowest binding to the cell membrane due to their reduced Ab density. Worth to note, equivalent concentrations of Abs (e.g. 2 x concentrated NPC3 versus NPC6) did not reach the same NP labelling efficiency. In this regard, we hypothesized that membrane bound NPC3 bioconjugates had steric effects, reducing further NP membrane binding. NPC6 and NPC8 bioconjugates, however, had multivalent effects that increased their binding efficiency. The use of unspecific bioconjugates (NPAR)

similar in composition to NPC8 showed a minimal level of interaction with the cell membrane. This result confirms that the binding of Cetuximab-1-Au NP bioconjugates to the cell membrane was mainly due to NP-receptor interactions.

As well, the specific functionality of Cetuximab-1-Au NP bioconjugates opened the possibility to study the distribution of EGF receptors in different regions of the plasma membrane. With this aim, membrane binding interactions of Cetuximab-1-Au NP bioconjugates with different Cetuximab loading (NPC3, NPC6 and NPC8) were compared by a combined TEM-statistical approach. Briefly, areas of the plasma membrane sheets were selected (800 x 800 nm) from TEM images and processed for determining the (x,y) coordinates of all Au NPs using Image J. Subsequent analysis of the NP coordinates was done using Ripley's univariate K-function, a statistic tool for point pattern analysis. A macro that carries out the analysis function was gently provided by Prior *et al.*^{69,70} The K-function is expressed as a linear transformation by the equation:

$$L(r) - r = \text{sqrt} [(K(r) / \pi) - r] \quad (6.1)$$

Values of L(r)-r above 1.0 (normalization of 99% confidence interval (C.I.)) indicate significant clustering within the defined x-axis radius (r). Values below -1.0 indicate significant dispersal. And no deviation outside the C.I. indicates a random pattern. Ripley's K-function analysis determined the extent of clustering within the Au NP patterns in the obtained plasma membrane sheets, showing large clustering for NPC8 and NPC6 and a random pattern for NPC3 (Figure 6.9-C). Interestingly, these results gave a consistent picture of the spatial regulation of EGF receptors on the plasma membrane. A more clustered Au NP pattern was observed for higher multivalent NPs, from NPC6 to NPC8. This effect was attributed to the capacity of these NP bioconjugates to induce multiple EGFR crosslinking. In addition, it may have significant implications in the internalization process, which is strongly dependent on the inter NP-distance⁷² and the diffusion rate of receptors⁷³ on the plasma membrane.

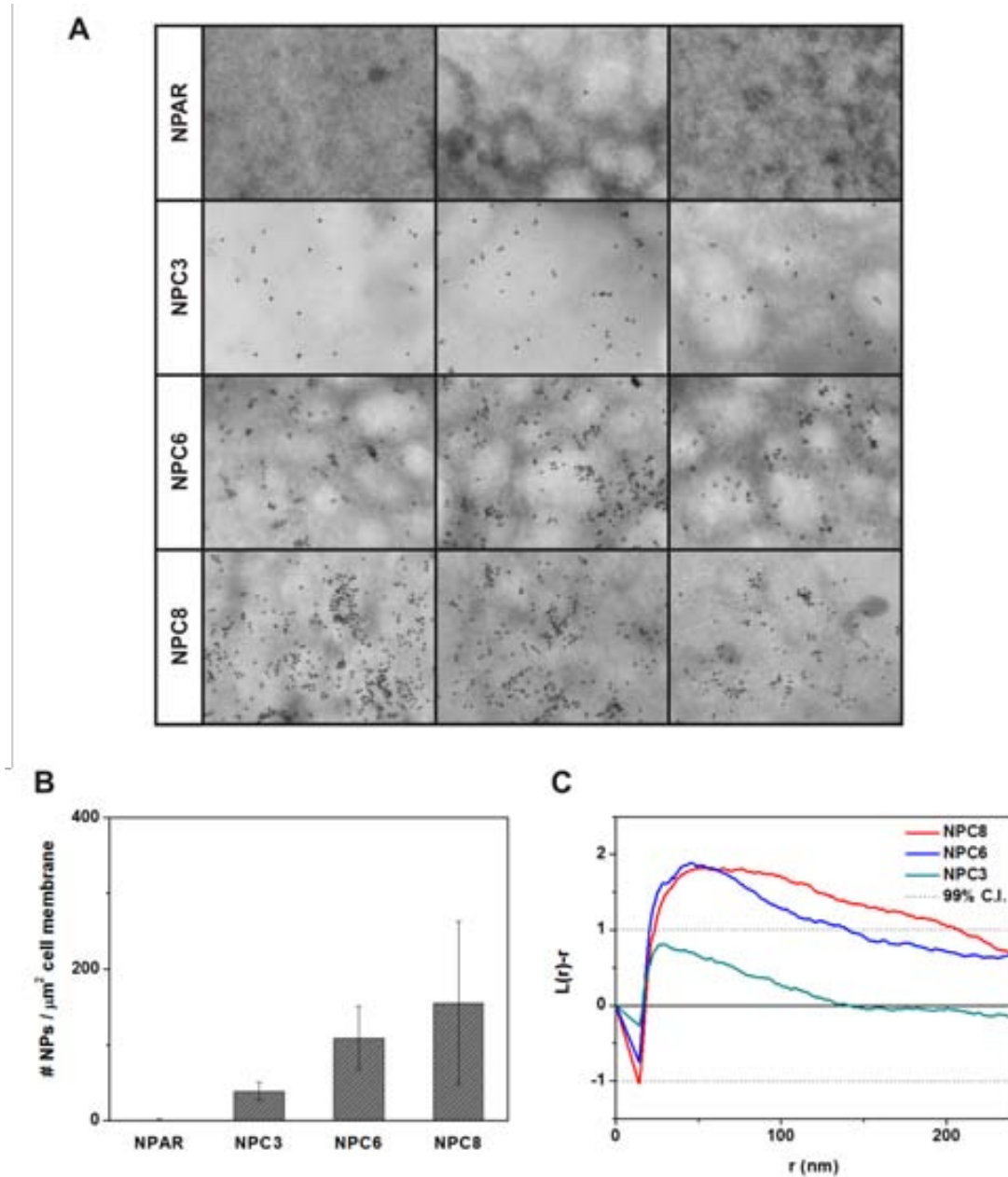


Figure 6.9. TEM analysis of plasma membrane sheets from 431 cells after incubation with Cetuximab-1-Au NP (NPC3, NPC6 and NPC8) and NPAR bioconjugates at 7.5 nM of NPs for 25 minutes at 4°C. A) Representative TEM images of plasma membrane sheets. B) Mean number of Au NPs present in the plasma membranes measured from an area of 800 x 800 nm² in a total of 10 TEM images from different cells. C) Ripley's K-function analysis (eq. 6.1); this function determined the extent of clustering within the Au NP patterns, showing large clustering for NPC8 and NPC6 and a random pattern for NPC3.

6.3.3. Blockade of EGF ligand binding to EGFR.

The next interesting aspect from the use of these Cetuximab-1-Au NP bioconjugates was their potential to block EGF ligand binding to EGFR in comparison to the unconjugated Cetuximab (see Section 6.1.2).²² Importantly, the blockade of EGF binding is advantageous in the treatment of tumors that rely heavily upon EGFR receptor signalling as a growth-promoting signal.^{16,18} Thus, EGF binding studies were performed after incubation of Cetuximab (8 nM) and Ab-1-Au NP bioconjugates (NPC3, NPC6, NPC8 and NPAR; 2, 4 and 8 nM NPs) for 2 hours at 37 °C. Treated cells were stimulated for 15 minutes with 20 ng/ml of Alexa Fluor 555-EGF complex (a fluorescent dye-EGF conjugate) and immediately fixed (see Annex I: materials and methods). Coverslips were mounted with medium containing 4',6-diamidino-2-phenylindole (DAPI); a fluorescent stain that binds strongly to adenine-thymine (A-T) rich regions in DNA and is typically used for nucleus staining.

Fluorescence optical microscopy analysis confirmed that the cells treated with free Cetuximab did not show binding or internalization of Alexa Fluor 555-EGF (Figure 6.10-C), indicating the efficacy of Cetuximab to block the EGF binding site of the receptor. Similarly, cells treated with NPC6 and NPC8 bioconjugates exhibited no ligand binding or uptake. In contrast, a significant intracellular localization of Alexa Fluor 555-EGF complex was found in cells treated with NPC3 bioconjugates (Figure 6.10-J-L) when compared to the maximum ligand uptake in cells treated with NPAR bioconjugate or non-treated cells (Figure 6.10-M-O). These differences in ligand uptake may be attributed to the relative binding efficiency of the bioconjugates. Since higher multivalent NPs have shown to bind more efficiently to EGFR (see Section 6.3.2), a decreased number of free EGF receptors may be available for binding. In addition, the NP-bound receptors may undergo internalization and down-regulation,^{48,49,68} which in turn, decrease further possibilities of EGF for binding. It was hypothesized that in the case of NPC3, a lower receptor blocking effect was probably due to its steric hindrance (*i.e.* resulting in a lower binding of NPs), especially when compared to the free Ab.

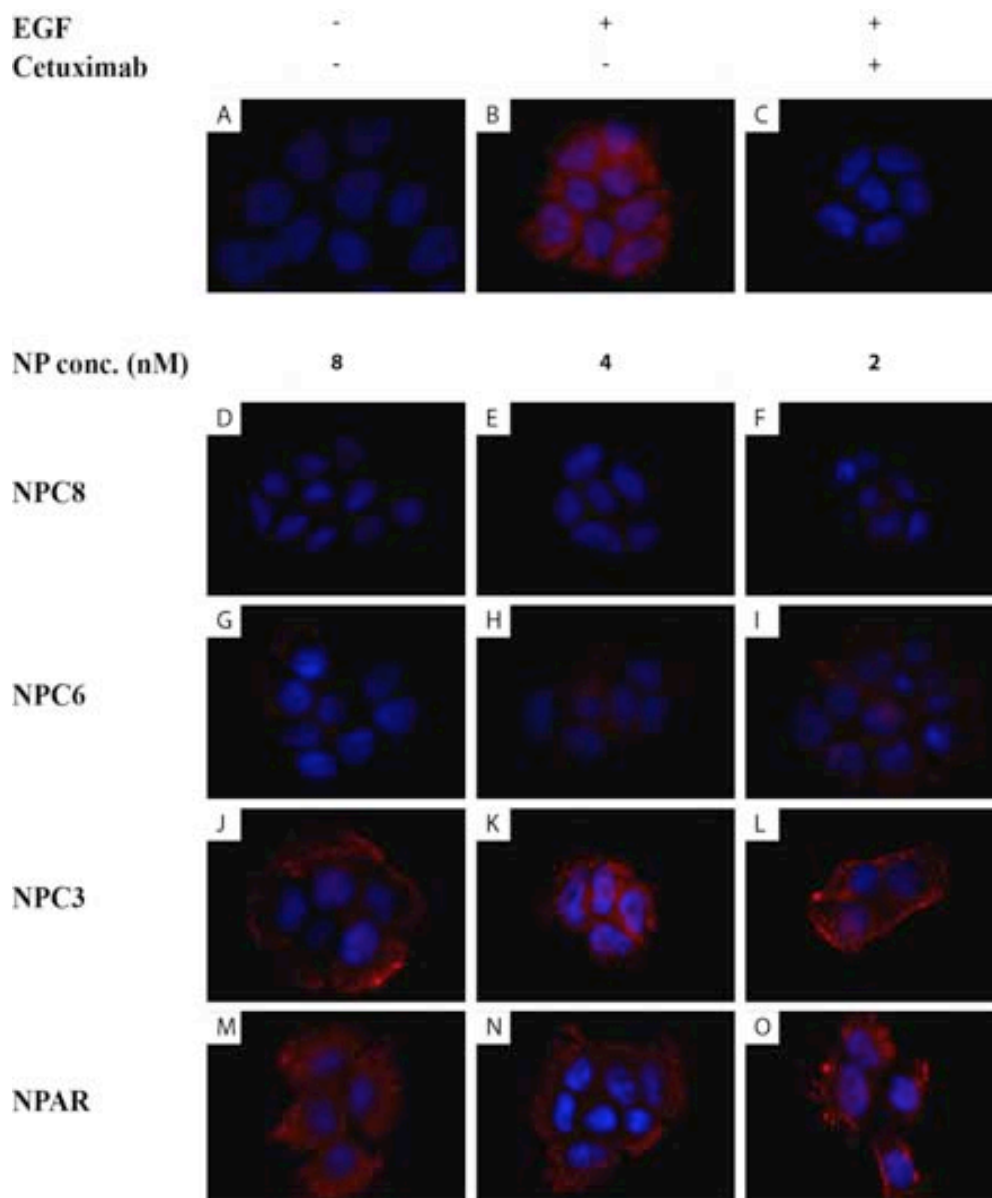


Figure 6.10. Alexa Fluor 555-EGF binding and internalization studies in A431 cells after incubating Cetuximab at 8 nM concentration and Cetuximab-1-Au NP (NPC3, NPC6 and NPC8) and NPAR bioconjugates at concentrations of 2, 4 and 8 nM of NPs for 2 hours at 37 °C. Nuclei were stained with DAPI.

The presence of Au NPs was confirmed by dark field optical microscopy (Figure 6.11). This technique allows visualizing Au NPs due to their strong light scattering properties.^{74,75} Indeed, Au NPs scattered orange-yellow light in cells treated with the Cetuximab-1-Au NP bioconjugates, whereas NPAR bioconjugates were not detected as expected from their minimal interaction with cells (Figure 6.9-A,B). The scattering

images show differences between the Cetuximab-1-Au NP bioconjugates, which may be attributed to their differences in position in the cell.⁷⁵

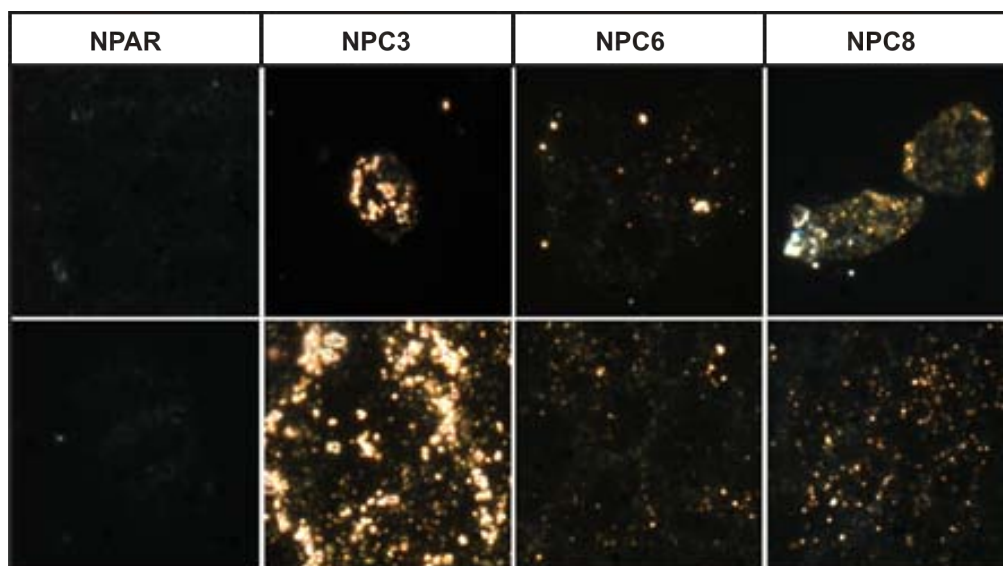


Figure 6.11. Dark field optical microscopy analysis of A431 cells after incubating Cetuximab-1-Au NP (NPC3, NPC6 and NPC8) and NPAR bioconjugates at a concentration of 8 nM NPs for 2 hours at 37 °C. Au NPs scattered orange-yellow light in cells treated with all three Cetuximab-1-Au NP bioconjugates, whereas NPAR bioconjugates were not detected due to their minimal interactions with the cells. Differences in scattering between the Cetuximab-1-Au NP bioconjugates may be attributed to the bioconjugate position in the cell.

6.3.4. Uptake and intracellular fate of Cetuximab-1-Au NP bioconjugates.

To test of the multivalency of the Cetuximab-1-Au NP bioconjugates have significant implications in their internalization process, the intracellular uptake of these bioconjugates was tested. Serum-starved A431 cells were incubated for 3 hours at 37 °C with Cetuximab-1-Au NP (NPC3, NPC6 and NPC8) and NPAR bioconjugates at 4.5, 9 and 13.5 nM of NPs (corresponding to approximately 112, 224 and 335 ppm of Au, respectively). After the incubation time, the medium of the cells and the trypsinized pellets were collected to analyze the Au content of both by ICP-MS (see Annex I: Materials and Methods). As anticipated from the higher binding affinity of NPC8 for cell membranes (see Section 6.3.2), all the cases significantly showed a higher uptake of the NPC8 bioconjugates when compared with the lower multivalent NPC6 and NPC3 bioconjugates (Figure 6.12). The highest uptake was

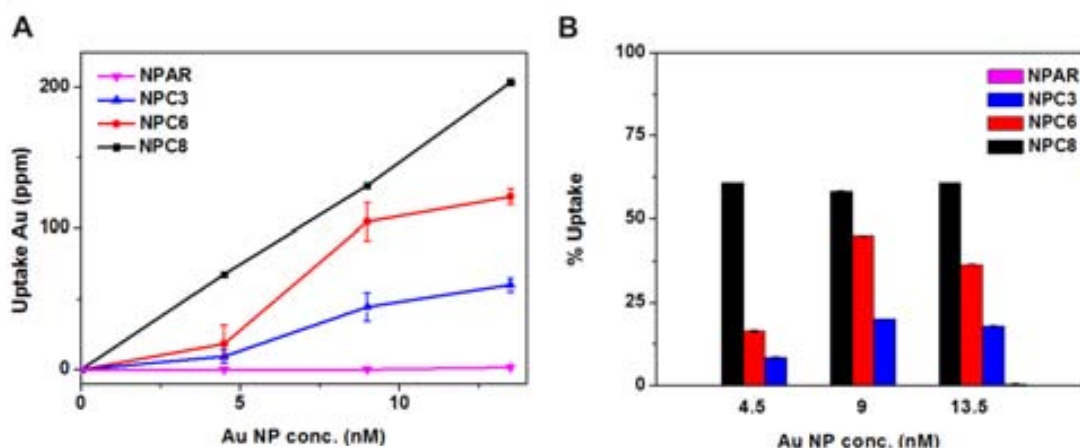


Figure 6.12. Cellular uptake of Cetuximab-1-Au NP bioconjugates (NPC3, NPC6 and NPC8) and anti-rabbit Ab-1-Au NP bioconjugates (NPAR) after 3 hours of incubation at 37°C measured by ICP-MS. A) Total Au uptake (in ppm). B) Uptake rate (%) over the initial Au NP incubation.

observed for NPC8 bioconjugates at the maximum concentration used (~ 204 ppm Au, 61 % uptake). Importantly, a 3-fold dilution of the NPs resulted in the same uptake efficiency (~ 68 ppm Au, 61 % uptake). This observation contrasts with the lower internalization efficiency reached by NPC6 and NPC3 (~ 122 ppm Au, 36 % uptake and ~ 60 ppm Au, 18% uptake, respectively), in which a 3-fold dilution of the NPs resulted in a further decreased uptake (~ 18 ppm Au, 18 % uptake and ~ 9 ppm Au, 8 % uptake). As expected, the highest dose of NPAR showed a minimal uptake (~ 2 ppm Au, 0.5 % uptake). Such low level of unspecific uptake further confirmed that the Cetuximab-1-Au NP bioconjugates were mainly internalized by specific NP-EGFR interactions. Overall, ICP-MS analysis revealed that the endocytosis of Cetuximab-1-Au NP bioconjugates was enhanced by a higher loading of Cetuximab Abs on the NPs (NPC8 > NPC6 > NPC3).

To further confirm the differences in intracellular uptake of the Cetuximab-1-Au NP bioconjugates, TEM was used as a tool to locate the Au NPs inside the cells and discriminate between the internalized bioconjugates and those attached to the cell membrane. Serum-starved A431 cells were incubated either with Cetuximab-1-Au NP (NPC3, NPC6 and NPC8) or NPAR bioconjugates at a concentration of ~ 9 nM NPs for 3 hours and 24 hours at 37 °C. After incubation, the cells were immediately processed for TEM analysis (see Annex I: Materials and Methods).

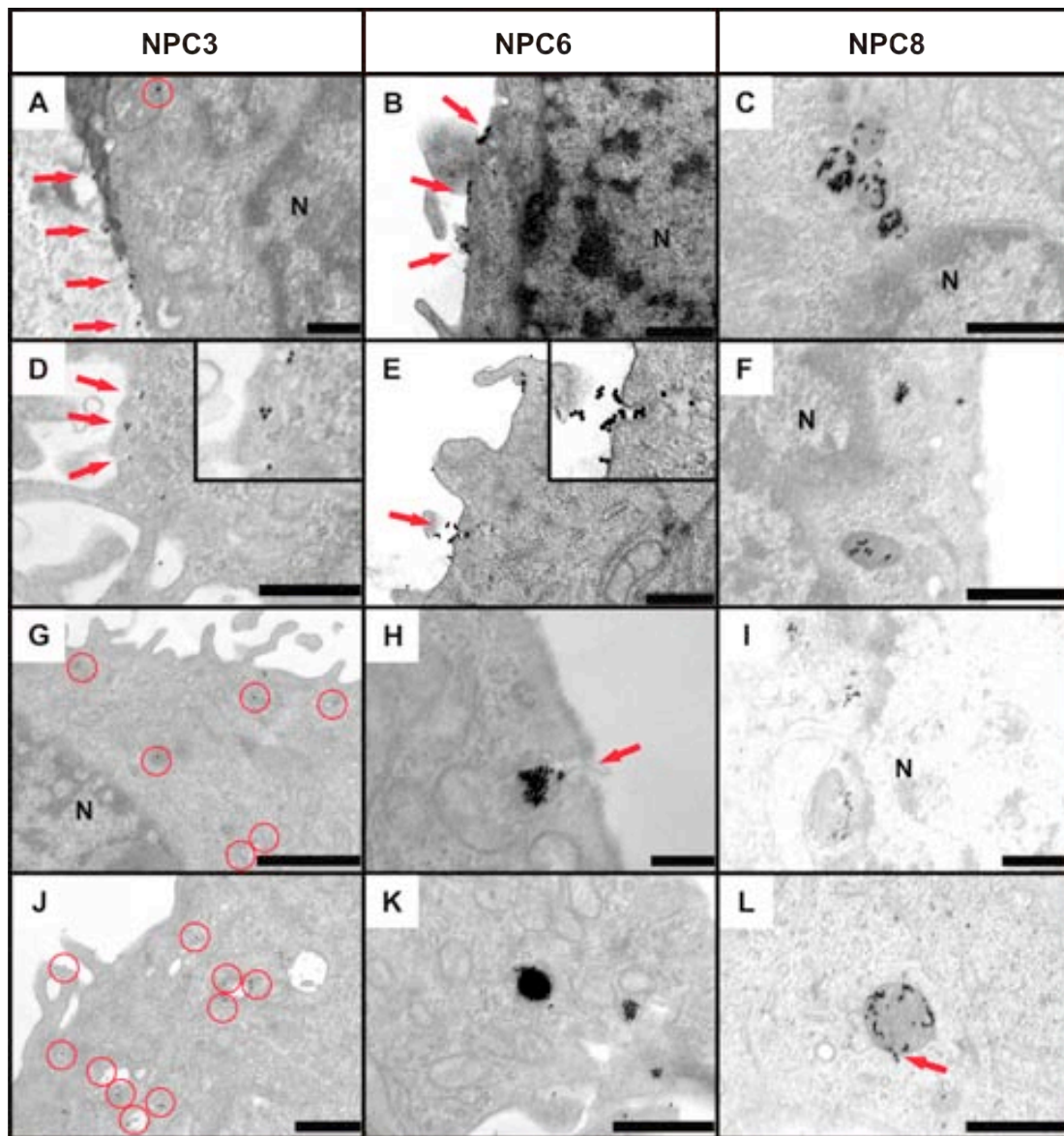


Figure 6.13. Representative TEM images showing the cellular uptake of Cetuximab-1-Au NP bioconjugates (NPC3, NPC6 and NPC8) after 3 hours of incubation at 37°C. Au NPs with a high loading of Abs clustered into a close packed aggregate on the membrane (B) and internalized as a whole (E, H), whereas Au NPs with lower multivalency bound to the membrane separated from each other (A, D) and internalized independently (G, J). The observed uptake was consistent with a receptor-mediated endocytosis of the bioconjugates; NPC3 and NPC6 bioconjugates were partially localized in the plasma membrane (A, B), followed by membrane invagination and vesicle formation (D, E, H); NPC6 bioconjugates were also present within endosomes and MVBs (K); NPC8 bioconjugates were located in late endosomes in the vicinity of the nucleus (C, F, I). Note that the NPs were observed to escape the endosome (L), which could be a possible mechanism for the observed nuclear localization (Figure 6.11). Scale bars are 200 nm (A, H), 500 nm (B-F, I-L) and 1 μ m (G). Circles indicate internalized Au NPs, and arrows indicate Au NPs bound to the plasma membrane and membrane invagination (except in L where arrow indicates endosome rupture).

As anticipated from quantitative Au analysis by ICP-MS (Figure 6.12), TEM images revealed that NPC3 bioconjugates showed the lowest uptake after 3 hours, whereas an enhanced internalization was found for NPC6 and NPC8 bioconjugates (Figure 6.13). Interestingly, while Au NPs with a high loading of Cetuximab MAbs clustered into a close packed aggregate on the membrane (Figure 6.13-B) and internalized as a whole (Figure 6.13-E,H), Au NPs with lower multivalency bound to the membrane separated from each other (Figure 6.13-A,D) and internalized independently (Figure 6.13-G,J). Such effect was directly related to NP uptake by theoretical simulations. Yue *et. al.*⁷² demonstrated that small NPs were difficult to internalize due to the high local membrane deformation required, whereas multiple NPs clustered to facilitate the wrapping process and reduce the energy cost associated with membrane deformation. Thus, this cooperative effect might contribute to the increased uptake of higher multivalent bioconjugates. After prolonged incubation time (24 hours), all three bioconjugates were densely packed inside endosomes (Figure 6.14). In the case of NPAR, no NPs were found inside the cells after 24 hours, which is in reasonable agreement with the low concentration of Au detected by ICP-MS (Figure 6.12). Overall, these results suggested again that a maximized density of Abs on the NPs presented an optimal interaction with EGF receptors for NP uptake. Such increased uptake is probably due to the higher capacity of these bioconjugates for multivalent crosslinking of membrane receptors, which may potentially increase the rate of NP wrapping.^{72,73} Additionally, these observations were broadly consistent with the Au NP pattern distribution found in plasma membrane sheets (see Section 6.3.2).

Besides uptake, our second focus was the intracellular fate of the bioconjugates. After 3 hours of incubation, TEM images showed the binding of NPC3 and NPC6 bioconjugates with the plasma membrane (Figure 6.13-A, B), followed by membrane invagination and vesicle formation (Figure 6.13-D, E, H). In addition, NPC6 bioconjugates were present within endosomes, showing a more advanced stage in the internalization process (Figure 6.13-K). Only NPC8 seemed to migrate towards late endosomes near the ER, in the vicinity of the nucleus (Figure 6.13-C, F, I).

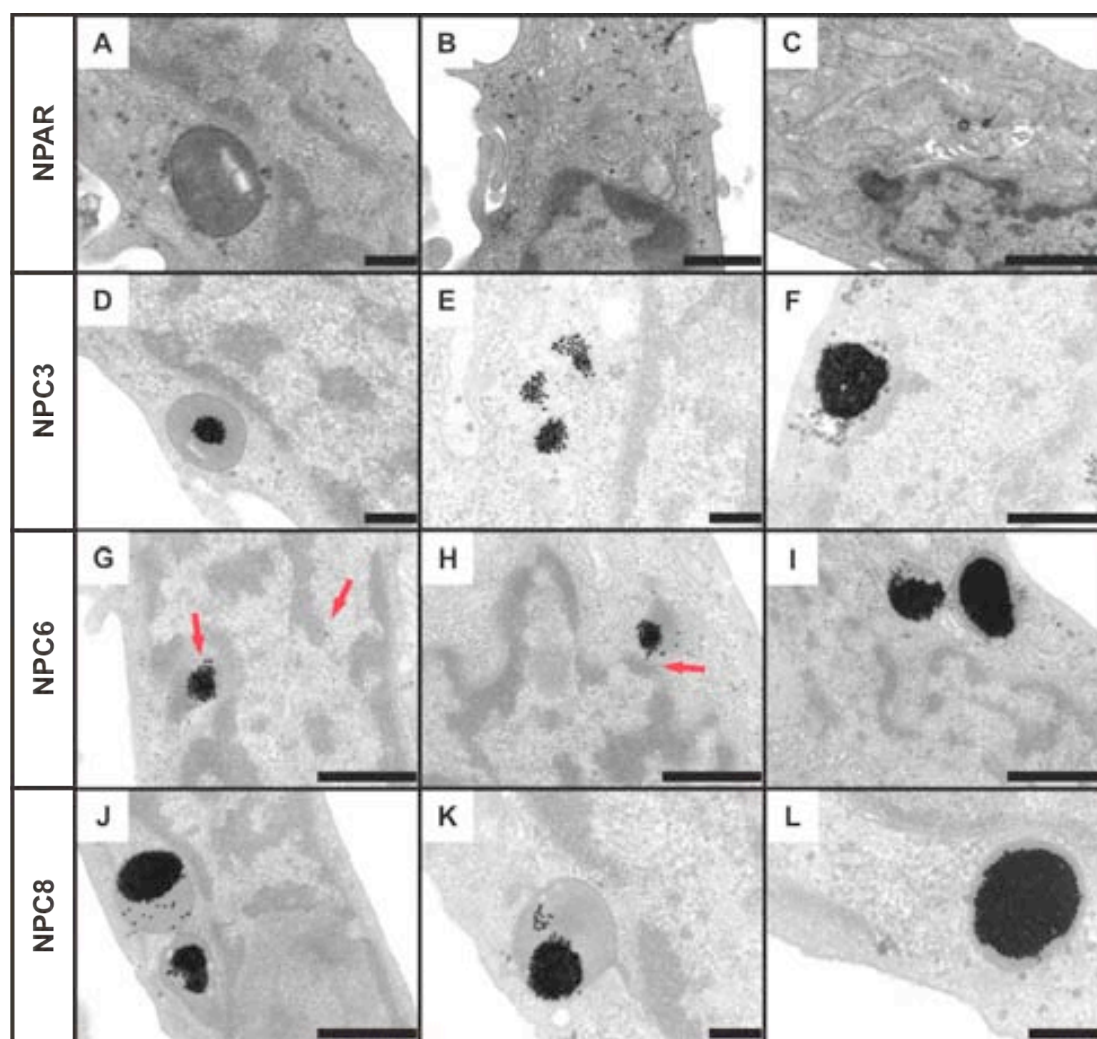


Figure 6.14. Representative TEM images showing the cellular uptake of Cetuximab-1-Au NP bioconjugates (NPC3, NPC6 and NPC8) and NPAR after 24 hours of incubation at 37°C. Cetuximab-1-Au NP bioconjugates showed to be accumulated in late endosomes near the nucleus, and occasionally, nuclear localization was found (G). Arrows indicate localization of the bioconjugates in the perinuclear region and in the nucleus. NPAR bioconjugate was not detected inside the cells.

After prolonged incubation of the Cetuximab-1-Au NP bioconjugates for 24 hours, they showed a predominant accumulation in late endosomes near the nucleus (Figure 6.14), and occasionally, nuclear localization was found (Figure 6.14-G). Interestingly, these observations were consistent with a receptor-mediated endocytosis of the bioconjugates (see Sections 6.1.1 and 6.1.2), despite different internalization rates were clearly observed for the Cetuximab-1-Au NP bioconjugates. According to TEM analysis after 3 hours of incubation, a faster endocytosis of such bioconjugates was observed with a higher loading of oriented Cetuximab Abs on the NPs (NPC8 >

NPC6 > NPC3). At prolonged incubation times, however, a similar intracellular fate of the bioconjugates was found.

6.3.5. Inhibition of ligand-induced EGFR tyrosine kinase activation and signalling downstream.

Since the primary mechanism of Cetuximab to inhibit tumor cell proliferation is to block ligand binding to EGFR and thus ligand-stimulated signalling (see Section 6.1.2), it was of substantial interest to investigate the potential of Cetuximab-1-Au NP bioconjugates to elicit different responses on EGFR signalling pathways. The biological pathways obtained after receptor blocking and stimulation were then analyzed. WB analysis was performed to explore the phosphorylation of key tyrosine residues in the CT domain of EGFR and the subsequent phosphorylation of its main signaling transduction pathways, MAPK/ERK and PI3K/AKT (see Annex I, Materials and Methods). A431 cells were serum-starved for 24 hours, and incubated for 2 hours at 37 °C with serum-free medium containing free Cetuximab at the maximum concentration used in the NPs (18.2 µg/ml), and Cetuximab-1-Au NP (NPC3, NPC6 and NPC8) and NPAR bioconjugates at a concentration of ~ 15 nM NPs. The treated cells were rinsed 3x with PBS and stimulated for 15 minutes with 20 ng/ml of EGF diluted in serum-free medium. Cells were again rinsed 3x with cold PBS and processed for WB.

As expected, WB analysis showed a high EGFR phosphorylation in the tyrosine residue 1045 (pEGFR 1045) after stimulation of the cells with EGF ligand (Figure 6.15). Incubations with Cetuximab-1-Au NP bioconjugates previous to stimulation with EGF led to a marked reduction in pEGFR 1045. Remarkable inhibitory effects (~ 50 %) were obtained with all three Cetuximab-1-Au NP bioconjugates, showing a higher efficiency in blocking the receptor than unbound Cetuximab. As expected, no significant inhibition was observed in NPAR-treated cells. A marked inhibitory effect was also observed on MAPK/ERK and PI3/AKT signal transduction pathways. NPC8 and NPC6 greatly inhibited AKT cascade by reducing its phosphorylation up to ~ 90 %, and phosphorylation of p44/42 MAPK was significantly reduced up to ~ 49 % and

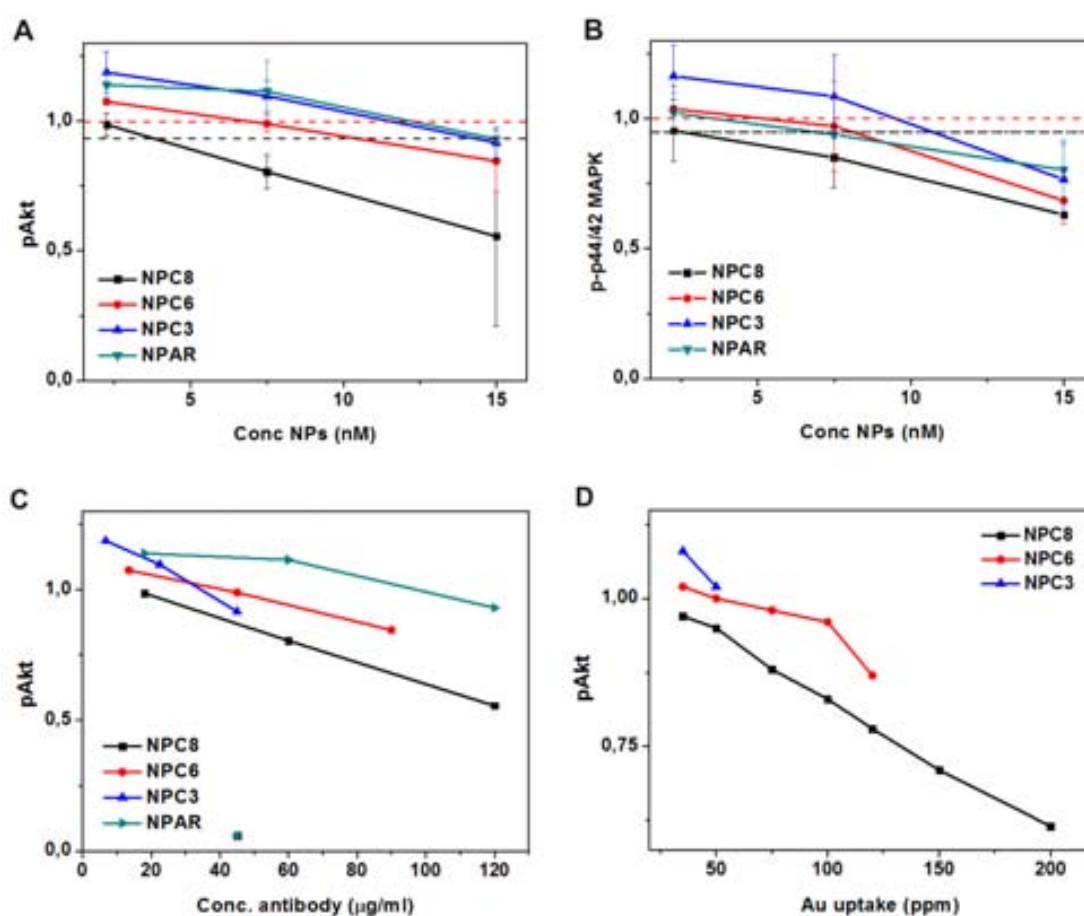


Figure 6.16. A, B) Concentration-dependent effect of Cetuximab-1-Au NP bioconjugates on EGF-induced phosphorylation of AKT and p-p44/42 MAPK, respectively. Red dashed line: EGF stimulated cells; black dashed line: previous incubation with Cetuximab at the maximum Ab concentration on NPC8 (18.2 µg/ml) and EGF stimulation. C) Effect of the concentration of Abs bound to the NPs on EGF-induced phosphorylation of Akt. D) Effect of the uptake of Cetuximab-1-Au NP bioconjugates on pAKT. NPC8 in black (square), NPC6 in red (circle), NPC3 in blue (triangle) and NPAR in green (inverted triangle).

Taken together, it may be construed that a higher inhibition of the signalling pathways by the higher multivalent bioconjugates is a simple effect of i) a higher total amount of Cetuximab MAbs (18.2 µg/ml Cetuximab in NPC8 *versus* 13.7 µg/ml and 6.8 µg/ml Cetuximab in NPC6 and NPC3, respectively, at a concentration of 15 nM Au NPs) and ii) higher uptake rate of the bioconjugates. Interestingly, our results show that the same total amount of Cetuximab MAbs result in an increased signalling inhibition for NPC8 (Figure 6.16-C), probably due to an optimum surface density and presentation/orientation of Abs for interacting with EGF receptors. Additionally,

comparative amounts of Au internalized led to an increased inhibition of signal transduction pathways by higher multivalent bioconjugates (Figure 6.16-D). Such effect suggested that the inhibitory effect of the Cetuximab-1-Au NP bioconjugates was not dependent on their uptake rate but their capacity for multivalent interactions with EGF receptors that propagate the signal across the cell.

6.3.6. EGFR down-regulation.

Recently, it was demonstrated that the treatment with Cetuximab MAbs can enhance receptor down-regulation in A431 cells (~ 20% of total EGF receptors).⁶⁸ The main limitation from this process is the rapid and efficient recycling of most of the internalized MAb (~ 60%) from early endosomal compartments to the cell surface (see Section 6.1.2).⁴⁹ We hypothesized that the enhanced uptake of the NPC6 and NPC8 bioconjugates due to their increased multivalency would also influence the recycling of receptors to the cell surface. Thus, these bioconjugates were selected to study EGFR recycling and compare to Cetuximab alone.

EGFR down-regulation was confirmed by Western Blot (WB) analysis (see Annex I: Materials and Methods). In brief, cells were serum-starved for 24 hours and incubated for 3 hours at 37 °C with serum-free medium containing NPC6, NPC8 and NPAR bioconjugates at concentrations of 4.5, 9 and 13.5 nM Au NPs, and the equivalent maximum concentrations of free Cetuximab (equivalent to MAbs in NPC6 and NPC8 at 13.5 nM NPs). The treated cells were rinsed 3x with PBS and stimulated for 15 minutes with 10 ng/ml of EGF diluted in serum-free DMEM. Cells were again rinsed 3x with cold PBS and processed for WB.

In agreement with recent findings,⁶⁸ Cetuximab alone (18.2 µg/ml) showed a reduction of total EGFR when compared to untreated cells (Figure 6.17). In contrast, the equivalent concentration of Cetuximab MAbs bound to the NPs presented a stronger reduction of total EGFR with respect to Cetuximab alone and untreated cells. For instance, NPC8 were observed to decrease EGFR up to ~ 76%, whereas the same concentration of free Cetuximab reduced ~ 42% EGFR. Likewise, NPC6 induced a

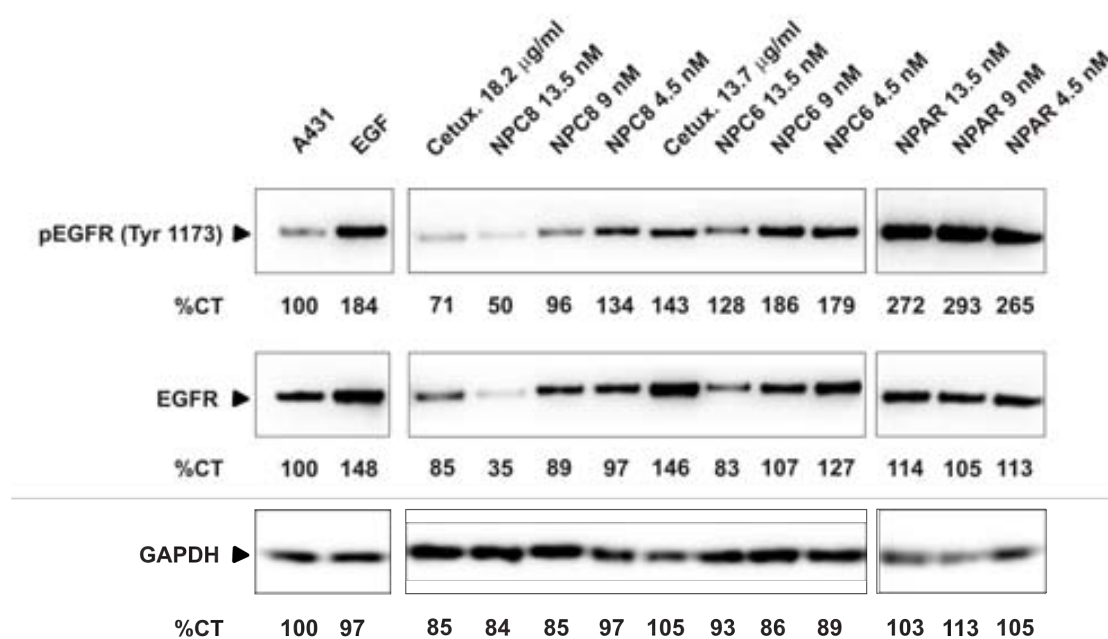


Figure 6.17. Western blot analysis of 431 cells incubated with NPC6, NPC8 and NPAR bioconjugates at 13.5 nM, 9 nM and 4.5 nM Au NPs, and the equivalent maximum concentrations of free Cetuximab for 3 hours, followed by stimulation with 10 ng/ml EGF for 15 minutes at 37°C. Results indicate phosphorylation of the tyrosine residue 1173 of the EGF receptor (pEGFR 1173) after stimulation with EGF ligand, total EGFR concentration (EGFR) after treatment and the well-established load control glyceraldehyde 3-phosphate dehydrogenase (GAPDH).

strong down-regulation (up to ~ 44% decrease in EGFR). However, in this case, the same concentration of free Cetuximab (*i.e.* 13.7 µg/ml) did not show down-regulation of the receptor. The enhanced down-regulation induced by NPC6 and NPC8 were attributed to their possibility of multivalent interactions with EGF receptors, altering receptor recycling. Indeed, an increased down-regulation of the receptor resulted from a higher multivalency of the bioconjugates (NPC8 > NPC6). It can be argued that some of the NP surface-bound receptors (*i.e.* forming a complex with Cetuximab) could be removed during preparation of the samples for WB, such as in the centrifugation step. Nevertheless, receptor down-regulation was also observed with NPC6 by immunofluorescence (see below), where this centrifugation step was not performed.

The reduction of membrane presentation of the receptor in Cetuximab-1-NP treated cells was also accompanied by a decrease in EGFR phosphorylation (*i.e.* in the

tyrosine residue 1173 of the receptor CT domain) after ligand stimulation (Figure 6.17). This indicated that the NP bioconjugates were able to block the receptor tyrosine kinase activity. The greatest inhibition was observed with NPC8, decreasing pEGFR 1173 up to 73%. Interestingly, both, NPC6 and NPC8 were more effective in reducing pEGFR 1173 than unbound Cetuximab, indicating the enhanced activity of these multivalent NP bioconjugates.

To further confirm the potentiality of these bioconjugates in down-regulating EGFR, immunofluorescence analysis was performed on A431 cells (see Annex I: Materials and Methods). NPC6 was chosen as the test case since it provided a multivalent effect, a strongly enhanced down-regulation when compared to the free MAb (Figure 6.17), and it had an enhanced stability/dispersibility at elevated concentrations. In brief, serum-starved cells were treated with NPC6 and NPAR bioconjugates at a concentration of 4.5 nM NPs and the equivalent Cetuximab concentration (4 µg/ml) for 3 hours and 24 hours followed by additional 24 hours incubation with fresh medium. After each treatment, cells were washed with PBS, fixed and incubated with primary and secondary Abs (*i.e.* mouse anti-EGFR Ab and Alexa Fluor 488 goat anti-mouse Ab, respectively). Nuclei were stained with DAPI.

At short incubation times (3 hours), immunofluorescence images show EGF receptors primarily localized on the plasma membrane for all cases, free Cetuximab, NPC6 and NPAR bioconjugates (Figure 6.18). In contrast, at longer incubation times (24 hours of treatment + 24 hours of fresh medium incubation), significant intracellular localization of EGFR was observed with NPC6. This suggested that the receptors do in fact undergo endocytosis when bound to NPC6 (Figure 6.20). Note that co-localization of NPC6 bioconjugates with EGFR could be observed, with a punctuated distribution inside the cell that could be related to the aggregation of receptors inside endosomes. Most importantly, the increased intracellular presence of receptors after 48 hours (24 hours treatment + 24 hours incubation in fresh medium) suggested that due to the multivalent capacity of NPC6, the bioconjugate was able to trap the receptors inside the cells for prolonged time. In cells treated with NPAR, again most of the receptors were localized in the plasma membrane, as expected from its reduced specificity for EGFR.

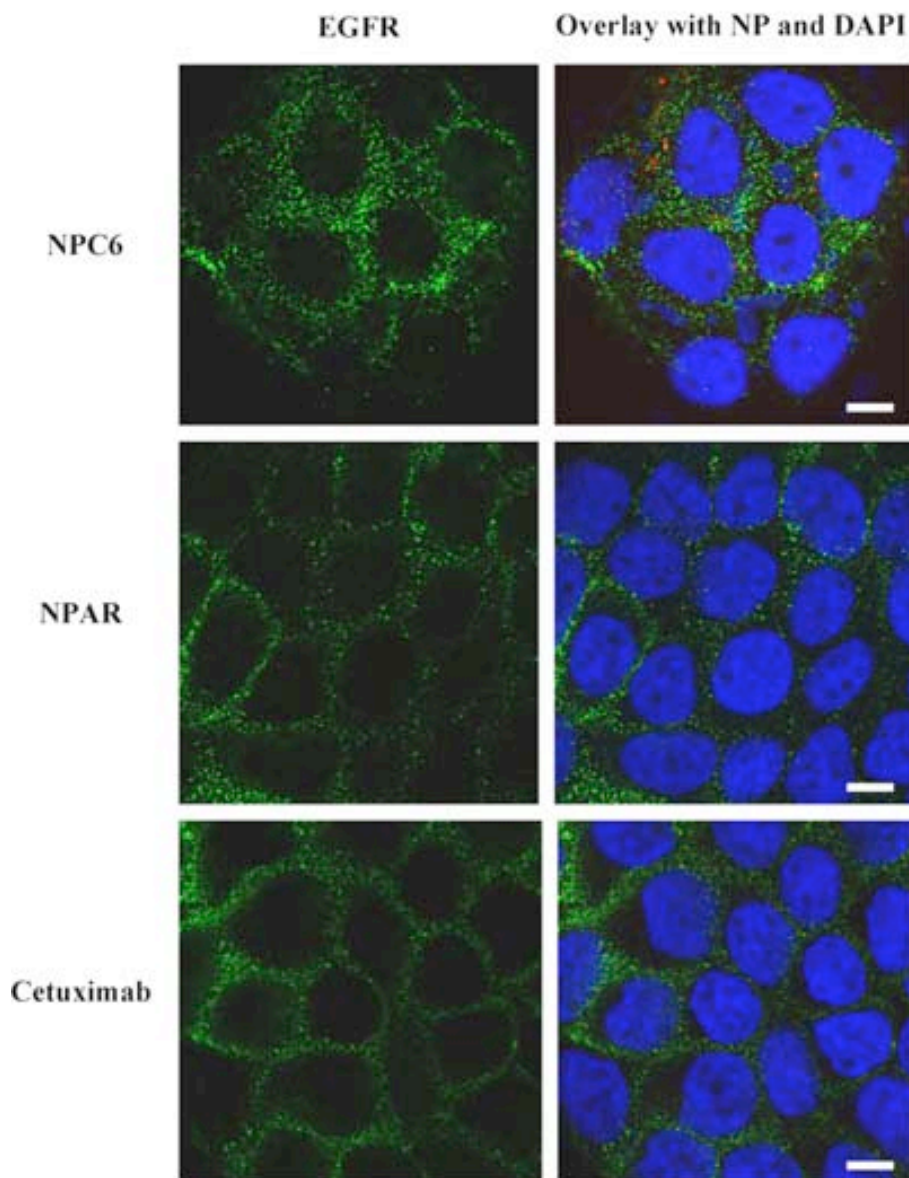


Figure 6.18. Confocal images of 431 cells incubated with NPC6 and NPAR bioconjugates and Cetuximab MAb at 4.5 nM of NPs and 4 $\mu\text{g}/\text{ml}$, respectively, for 3 hours at 37°C. EGFR was counterstained with Alexa Fluor 488 (green) and the nucleus with DAPI (blue). The scattering from Au NPs is false-colored in red. Slides of 0.25 μm of the confocal fluorescence and reflectance images were obtained independently and then overlaid in a maximal projection mode. The scale bars are $\sim 20 \mu\text{m}$.

Interestingly, NPC6 showed a greatly enhanced receptor down-regulation when comparing to its equivalent concentration of free Cetuximab (4 $\mu\text{g}/\text{ml}$) (Figure 6.19). While no significant effects were observed with free Cetuximab, NPC6 bioconjugate showed a marked decrease in membrane presentation of EGFR.

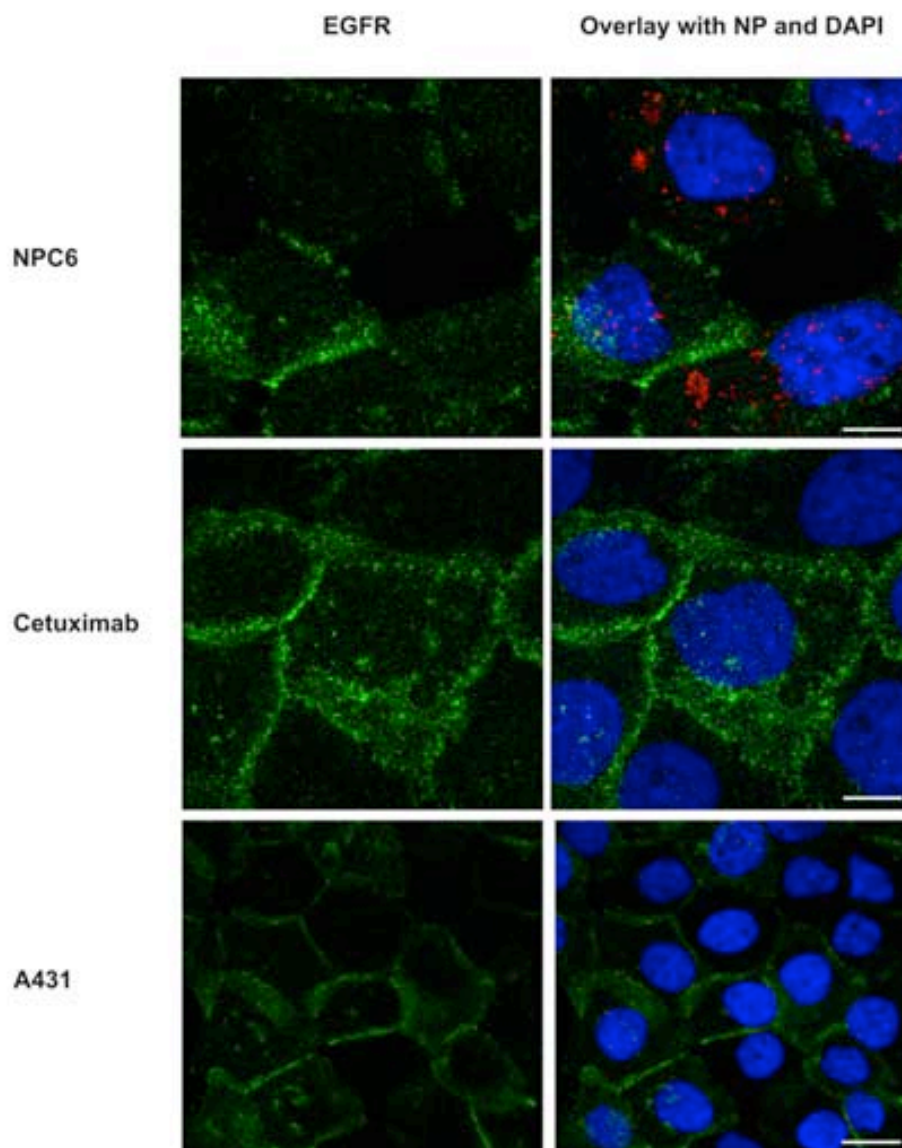


Figure 6.19. Confocal images of 431 cells incubated with NPC6 bioconjugate and Cetuximab MAb at 4.5 nM of NPs and 4 $\mu\text{g/ml}$, respectively, for 24 hours and additional 24 hours with fresh medium at 37°C. EGFR was counterstained with Alexa Fluor 488 (green) and the nucleus with DAPI (blue). The scattering from Au NPs is false-colored in red. Slides of 0.25 μm of the confocal fluorescence and reflectance images were obtained independently and then overlaid in a maximal projection mode. The scale bars are $\sim 20 \mu\text{m}$.

The observed effects in cell signalling (see also Section 6.3.5) could be modulated by varying the concentration of NP bioconjugates or free MAbs. The recycling of receptors, however, is a differential effect that cannot be produced by increasing the concentration of free Abs, and it has clinical/medical relevance.

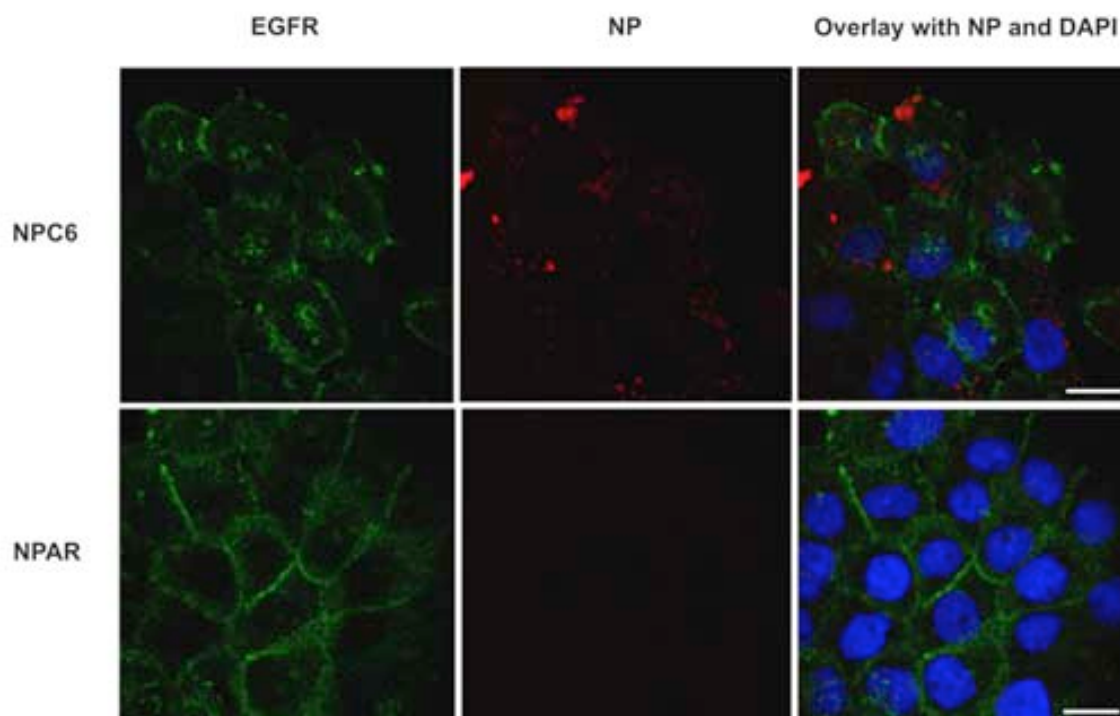


Figure 6.20. Confocal microscopy images of 431 cells incubated with NPC6 and NPAR bioconjugates at 4.5 nM of NPs for 24 hours and additional 24 hours with fresh medium at 37°C. EGFR was counterstained with Alexa Fluor 488 (green) and the nucleus with DAPI (blue). The scattering from Au NPs is false-colored in red. Slides of 0.25 μm of the confocal fluorescence and reflectance images were obtained independently and then overlaid in a maximal projection mode. The scale bars are $\sim 20 \mu\text{m}$.

6.3.7. Cell viability studies.

Because Cetuximab is known to inhibit tumor cell proliferation as a result of its impact on downstream signalling pathways and EGFR down-regulation,⁶⁸ the cell viability was finally studied to ensure that the NP bioconjugates were not cytotoxic but cytostatic. A standard XTT assay was performed in triplicate. XTT is a colorless or slightly yellow tetrazolium dye that when reduced by cellular enzymes becomes brightly orange. This color change is accomplished by breaking apart the positively-charged quaternary tetrazole ring of XTT to obtain a colored formazan derivative. The cell viability assay was performed in 96-well plates according to the manufacturer's instructions. In brief, A431 cells were incubated with Cetuximab MAbs at concentrations of 18 and 100 $\mu\text{g}/\text{ml}$ and the Cetuximab-1-Au NP and NPAR

bioconjugates at a concentration of 10 nM NPs (corresponding to 12.2, 9.1 and 4.6 $\mu\text{g/ml}$ Ab in NPC8, NPC6 and NPC3, respectively) for 72 hours (Figure 6.21). Note that cell medium replacement was performed to avoid interference from Au NPs in the colorimetric analysis. XTT reagent (20 μL) was added to the cell culture and incubated for 2 hours. After incubation, the absorbance was recorded at 450 nm (reference wavelength 620 nm) in a microplate reader. In agreement to previous observations,⁶⁸ a modest decrease in cell proliferation of $\sim 25\%$ was observed after incubating Cetuximab MAb. Similar cell viabilities were obtained after incubating the Cetuximab-1-Au NP bioconjugates, further confirming their cytostatic effect. As expected, no effect on cell viability was found for NPAR bioconjugates.

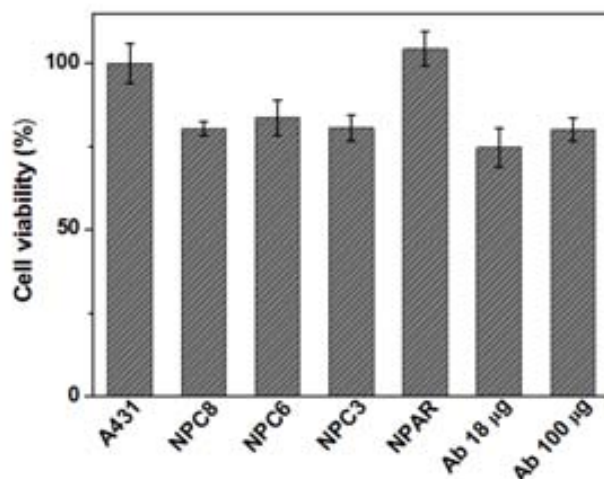


Figure 6.21. XTT cell viability assay of A431 cells after incubation of Cetuximab and the NP bioconjugates for 72 hours at 37 °C.

6.4. Conclusions

Recent observations in biological systems suggest that the safe and controlled use of NP bioconjugates in different areas of biomedicine, such as targeted therapy or imaging, will be predicated on the ability to control their physicochemical parameters, which in turn will dictate their molecular interactions with the target cells. For instance, there is evidence showing that the physical parameters of NP bioconjugates,

such as size and shape, can affect their specific receptor-mediated uptake with potential to modulate cellular responses. This Chapter demonstrates that not only the physical parameters of NP bioconjugates but also their chemical mode of preparation play a role in regulating receptor-mediated effects. By controlling the local concentration of Abs and orientation/presentation of the ligands to the cell surface, NP-EGFR binding affinity, EGFR distribution and internalization, and signal transduction pathways in A431 cells have been precisely tuned. In addition, an important down-regulation of the receptor is observed 48 hours after treatment with the bioconjugates, indicating their capacity to alter the process of receptor recycling. Overall, a direct and quantitative control of the multivalent nature of Ab-Au NP bioconjugates has been demonstrated to be especially critical to their interactions with cell surface receptors, which also determine a specific biological response. Such modulation of the ligand-receptor interaction is unprecedented. Importantly, these findings have significant implications for cancer immunotherapy.

6.5. References

1. Reichert, J. M.; Rosensweig, C. J.; Faden, L. B.; Dewitz, M. C. *Monoclonal Antibody Successes in the Clinic*. *Nat. Biotech.*, **2005**, *23*, 1073-1078.
2. Adams, G. P.; Weiner, L. M. *Monoclonal Antibody Therapy of Cancer*. *Nat. Biotech.*, **2005**, *23*, 1147-1157.
3. Patra, C. R.; Bhattacharya, R.; Wang, E.; Katarya, A.; Lau, J. S.; Dutta, S.; Muders, M.; Wang, S.; Buhrow, S. A.; Safgren, S. L.; Yaszemski, M. J.; Reid, J. M.; Ames, M. M.; Mukherjee, P.; Mukhopadhyay, D. *Targeted Delivery of Gemcitabine to Pancreatic Adenocarcinoma Using Cetuximab as a Targeting Agent*. *Cancer Res.*, **2008**, *68*, 1970-1978.
4. Mamot, C.; Drummond, D. C.; Greiser, U.; Hong, K.; Kirpotin, D. B.; Marks, J. D.; Park, J. W. *Epidermal Growth Factor Receptor (EGFR)-Targeted Immunoliposomes Mediate Specific and Efficient Drug Delivery to EGFR- and EGFRvIII-Overexpressing Tumor Cells*. *Cancer Res.*, **2003**, *63*, 3154-3161.
5. Anhorn, M. G.; Wagner, S.; Kreuter, J. R.; Langer, K.; von Briesen, H. *Specific Targeting of HER2 Overexpressing Breast Cancer Cells with Doxorubicin-Loaded Trastuzumab-Modified Human Serum Albumin Nanoparticles*. *Bioconj. Chem.*, **2008**, *19*, 2321-2331.
6. Arya, G.; Vandana, M.; Acharya, S.; Sahoo, S. K. *Enhanced Antiproliferative Activity of Herceptin (HER2)-Conjugated Gemcitabine-Loaded Chitosan Nanoparticle in Pancreatic Cancer Therapy*. *Nanomedicine: Nanotech. Biol. Med.*, **2011**, *7*, 859-870.

7. Peer, D.; Karp, J. M.; Hong, S.; Farokhzad, O. C.; Margalit, R.; Langer, R. *Nanocarriers as an Emerging Platform for Cancer Therapy*. *Nat. Nano*, **2007**, 2, 751-760.
8. Huang, Y.-F.; Liu, H.; Xiong, X.; Chen, Y.; Tan, W. *Nanoparticle-Mediated IgE-Receptor Aggregation and Signaling in RBL Mast Cells*. *J. Am. Chem. Soc.*, **2009**, 131, 17328-17334.
9. Wang, J.; Tian, S.; Petros, R. A.; Napier, M. E.; DeSimone, J. M. *The Complex Role of Multivalency in Nanoparticles Targeting the Transferrin Receptor for Cancer Therapies*. *J. Am. Chem. Soc.*, **2010**, 132, 11306-11313.
10. Bhattacharyya, S.; Bhattacharya, R.; Curley, S.; McNiven, M. A.; Mukherjee, P. *Nanoconjugation Modulates the Trafficking and Mechanism of Antibody Induced Receptor Endocytosis*. *Proc. Natl. Acad. Sci. U.S.A*, **2010**, 107, 14541-14546.
11. Jiang, W.; KimBetty, Y. S.; Rutka, J. T.; Chan Warren, C. W. *Nanoparticle-Mediated Cellular Response is Size-Dependent*. *Nat. Nano*, **2008**, 3, 145-150.
12. Bartzczak, D.; Sanchez-Elsner, T.; Louafi, F.; Millar, T. M.; Kanaras, A. G. *Receptor-Mediated Interactions between Colloidal Gold Nanoparticles and Human Umbilical Vein Endothelial Cells*. *Small*, **2011**, 7, 388-394.
13. Maus, L.; Dick, O.; Bading, H.; Spatz, J. P.; Fiammengo, R. *Conjugation of Peptides to the Passivation Shell of Gold Nanoparticles for Targeting of Cell-Surface Receptors*. *ACS Nano*, **2010**, 4, 6617-6628.
14. Vácha, R.; Martinez-Veracoechea, F. J.; Frenkel, D. *Receptor-Mediated Endocytosis of Nanoparticles of Various Shapes*. *Nano Lett.*, **2011**, 11, 5391-5395.
15. Mendelsohn, J.; Baselga, J. *The EGF Receptor Family as Targets for Cancer Therapy*. *Oncogene*, **2000**, 19, 6550-6565.
16. Yarden, Y. *The EGFR Family and its Ligands in Human Cancer: Signalling Mechanisms and Therapeutic Opportunities*. *Eur. J. Cancer (Oxford, England: 1990)*, **2001**, 37, 3-8.
17. Arteaga, C. L. *Epidermal Growth Factor Receptor Dependence in Human Tumors: More Than Just Expression?* *The Oncologist*, **2002**, 7, 31-39.
18. Henson, E. S.; Gibson, S. B. *Surviving Cell Death Through Epidermal Growth Factor (EGF) Signal Transduction Pathways: Implications for Cancer Therapy*. *Cellular Signalling*, **2006**, 18, 2089-2097.
19. Nicholson, R. I.; Gee, J. M.; Harper, M. E. *EGFR and Cancer Prognosis*. *Eur. J. Cancer (Oxford, England: 1990)*, **2001**, 37 Suppl 4, S9-15.
20. Mendelsohn, J.; Baselga, J. *Epidermal Growth Factor Receptor Targeting in Cancer*. *Sem. Oncol.*, **2006**, 33, 369-385.
21. Ciardiello, F.; Tortora, G. *EGFR Antagonists in Cancer Treatment*. *N. Engl. J. Med.*, **2008**, 358, 1160-1174.

22. Li, S.; Schmitz, K. R.; Jeffrey, P. D.; Wiltzius, J. J. W.; Kussie, P.; Ferguson, K. M. *Structural Basis for Inhibition of the Epidermal Growth Factor Receptor by Cetuximab*. *Cancer Cell*, **2005**, 7, 301-311.
23. Burgess, A. W.; Garrett, T. P. J. *EGFR Receptor Family Extracellular Domain Structures and Functions*. *EGFR Signaling Networks in Cancer Therapy*; Haley, J. D. and Gullick, W. J., Humana Press, **2008**, 2-13.
24. Harris, R. C.; Chung, E.; Coffey, R. J. *EGF Receptor Ligands*. *Exp. Cell Res.*, **2003**, 284, 2-13.
25. Garrett, T. P. J.; McKern, N. M.; Lou, M.; Elleman, T. C.; Adams, T. E.; Lovrecz, G. O.; Zhu, H.-J.; Walker, F.; Frenkel, M. J.; Hoyne, P. A.; Jorissen, R. N.; Nice, E. C.; Burgess, A. W.; Ward, C. W. *Crystal Structure of a Truncated Epidermal Growth Factor Receptor Extracellular Domain Bound to Transforming Growth Factor α* . *Cell*, **2002**, 110, 763-773.
26. Ogiso, H.; Ishitani, R.; Nureki, O.; Fukai, S.; Yamanaka, M.; Kim, J.-H.; Saito, K.; Sakamoto, A.; Inoue, M.; Shirouzu, M.; Yokoyama, S. *Crystal Structure of the Complex of Human Epidermal Growth Factor and Receptor Extracellular Domains*. *Cell*, **2002**, 110, 775-787.
27. Ushiro, H.; Cohen, S. *Identification of Phosphotyrosine as a Product of Epidermal Growth Factor-Activated Protein Kinase in A-431 Cell Membranes*. *J. Biol. Chem.*, **1980**, 255, 8363-8365.
28. Hunter, T.; Cooper, J. A. *Epidermal Growth Factor Induces Rapid Tyrosine Phosphorylation of Proteins in A431 Human Tumor Cells*. *Cell*, **1981**, 24, 741-752.
29. Alberts, B.; Johnson, A.; Lewis, J.; Raff, M.; Roberts, K.; Walter, P. *Molecular Biology of the Cell*, 5th edition. Garland Science, **2007**, chapter 15.
30. Citri, A.; Yarden, Y. *EGF-ERBB Signalling: Towards the Systems Level*. *Nat. Rev. Mol. Cell Biol.*, **2006**, 7, 505-516.
31. Yarden, Y.; Sliwkowski, M. X. *Untangling the ErbB signalling Network*. *Nat. Rev. Mol. Cell Biol.*, **2001**, 2, 127-137.
32. Jorissen, R. N.; Walker, F.; Pouliot, N.; Garrett, T. P. J.; Ward, C. W.; Burgess, A. W. *Epidermal Growth Factor Receptor: Mechanisms of Activation and Signalling*. *Exp. Cell Res.*, **2003**, 284, 31-53.
33. Gorden, P.; Carpentier, J. L.; Cohen, S.; Orci, L. *Epidermal Growth Factor: Morphological Demonstration of Binding, Internalization, and Lysosomal Association in Human Fibroblasts*. *Proc. Natl. Acad. Sci. U.S.A.*, **1978**, 75, 5025-5029.
34. Johannessen, L. E.; Pedersen, N. M.; Pedersen, K. W.; Madshus, I. H.; Stang, E. *Activation of the Epidermal Growth Factor (EGF) Receptor Induces Formation of EGF Receptor- and Grb2-Containing Clathrin-Coated Pits*. *Mol. Cell Biol.*, **2006**, 26, 389-401.
35. Carpenter, G.; Cohen, S. *Epidermal Growth Factor*. *Annu. Rev. Biochem.*, **1979**, 48, 193-216.
36. Sorkin, A. *Endocytosis and Intracellular Sorting of Receptor Tyrosine Kinases*. *Front. Biosci.*, **1998**, 3, 729-738.

37. Sorkin, A. D.; Teslenko, L. V.; Nikolsky, N. N. *The Endocytosis of Epidermal Growth Factor in A431 Cells: A pH of Microenvironment and the Dynamics of Receptor Complex Dissociation*. Exp. Cell Res., **1988**, 175, 192-205.
38. Sorkin, A.; Carpenter, G. *Dimerization of Internalized Epidermal Growth Factor Receptors*. J. Biol. Chem., **1991**, 266, 23453-23460.
39. Sorkin, A.; Krolenko, S.; Kudrjavtceva, N.; Lazebnik, J.; Teslenko, L.; Soderquist, A. M.; Nikolsky, N. *Recycling of Epidermal Growth Factor-receptor Complexes in A431 Cells: Identification of Dual Pathways*. J. Cell Biol., **1991**, 112, 55-63.
40. Sorkin, A.; von Zastrow, M. *Signal Transduction and Endocytosis: Close Encounters of Many Kinds*. Nat. Rev. Mol. Cell Biol., **2002**, 3, 600-614.
41. Futter, C. E.; Pearse, A.; Hewlett, L. J.; Hopkins, C. R. *Multivesicular Endosomes Containing Internalized EGF-EGF Receptor Complexes Mature and then Fuse Directly with Lysosomes*. J. Cell Biol., **1996**, 132, 1011-1023.
42. Stoscheck, C. M.; Carpenter, G. *Down Regulation of Epidermal Growth Factor Receptors: Direct Demonstration of Receptor Degradation in Human Fibroblasts*. J. Cell Biol., **1984**, 98, 1048-1053
43. Authier, F.; Métioui, M.; Bell, A. W.; Mort, J. S. *Negative Regulation of Epidermal Growth Factor Signalling by Selective Proteolytic Mechanisms in the Endosome Mediated by Cathepsin B*. J. Biol. Chem., **1999**, 274, 33723-33731.
44. Lin, S.-Y.; Makino, W. Xia; A. Martin; Y. Wen; K. Y. Kwong; L. Bourguignon; M.-C. Hung. *Nuclear Localization of EGF Receptor and its Potential New Role as a Transcription Factor*. Nat. Cell Biol., **2001**, 3, 802-808.
45. Oksvold, M.; Huitfeldt, H.; Stang, E.; Madshus, I. *Localizing the EGF Receptor*. Nat. Cell Biol., **2002**, 4, E22-E22.
46. Fan, Z.; Lu, Y.; Wu, X.; Mendelsohn, J. *Antibody-Induced Epidermal Growth Factor Receptor Dimerization Mediates Inhibition of Autocrine Proliferation of A431 Squamous Carcinoma Cells*. J. Biol. Chem., **1994**, 269, 27595-27602.
47. Lammerts van Bueren, J. J.; Bleeker, W. K.; Brännström, A.; von Euler, A.; Jansson, M.; Peipp, M.; Schneider-Merck, T.; Valerius, T.; van de Winkel, J. G. J.; Parren, P. W. H. I. *The Antibody Zalutumumab Inhibits Epidermal Growth Factor Receptor Signaling by Limiting Intra- and Intermolecular Flexibility*. Proc. Natl. Acad. Sci. U.S.A., **2008**, 105, 6109-6114.
48. Liao, H.-J.; Carpenter, G. *Cetuximab/C225-Induced Intracellular Trafficking of Epidermal Growth Factor Receptor*. Cancer Res., **2009**, 69, 6179-6183.
49. Jaramillo, M. L.; Leon, Z.; Grothe, S.; Paul-Roc, B.; Abulrob, A.; O'Connor McCourt, M. *Effect of the Anti-Receptor Ligand-Blocking 225 Monoclonal Antibody on EGF Receptor Endocytosis and Sorting*. Exp. Cell Res., **2006**, 312, 2778-2790.
50. Friedman, L. M.; Rinon, A.; Schechter, B.; Lyass, L.; Lavi, S.; Bacus, S. S.; Sela, M.; Yarden, Y. *Synergistic Down-Regulation of Receptor Tyrosine Kinases by Combinations of mAbs: Implications for Cancer Immunotherapy*. Proc. Natl. Acad. Sci. U.S.A., **2005**, 102, 1915-1920.

51. Kozer, N.; Kelly, M. P.; Orchard, S.; Burgess, A. W.; Scott, A. M.; Clayton, A. H. A. *Differential and Synergistic Effects of Epidermal Growth Factor Receptor Antibodies on Unliganded ErbB Dimers and Oligomers*. *Biochem.*, **2011**, *50*, 3581-3590.
52. Dubois, P. M.; Stepinski, J.; Urbain, J.; Sibley, C. H. *Role of the Transmembrane and Cytoplasmic Domains of Surface IgM in Endocytosis and Signal Transduction*. *Eur. J. Immunol.*, **1992**, *22*, 851-857.
53. Yokoyama, T.; Tam, J.; Kuroda, S.; Scott, A. W.; Aaron, J.; Larson, T.; Shanker, M.; Correa, A. M.; Kondo, S.; Roth, J. A.; Sokolov, K.; Ramesh, R. *EGFR-Targeted Hybrid Plasmonic Magnetic Nanoparticles Synergistically Induce Autophagy and Apoptosis in Non-Small Cell Lung Cancer Cells*. *Plos One*, **2011**, *6*, e25507.
54. Turkevich, J.; Stevenson, P. C.; Hillier, J. *A Study of the Nucleation and Growth Processes in the Synthesis of Colloidal Gold*. *Discuss. Farad. Soc.*, **1951**, *11*, 55-75.
55. Frens, G. *Controlled Nucleation for Regulation of Particle Size in Monodisperse Gold Suspensions*. *Nat. Phys. Sci.*, **1973**, *241*, 20–22.
56. Cho, E. C.; Zhang, Q.; Xia, Y. *The Effect of Sedimentation and Diffusion on Cellular Uptake of Gold Nanoparticles*. *Nat. Nano*, **2011**, *6*, 385-391.
57. Cho, E. C.; Xie, J.; Wurm, P. A.; Xia, Y. *Understanding the Role of Surface Charges in Cellular Adsorption versus Internalization by Selectively Removing Gold Nanoparticles on the Cell Surface with a I2/KI Etchant*. *Nano Lett.*, **2009**, *9*, 1080-1084.
58. Nativo, P.; Prior, I. A.; Brust, M. *Uptake and Intracellular Fate of Surface-Modified Gold Nanoparticles*. *ACS Nano*, **2008**, *2*, 1639-1644.
59. Krpetić, Ž.; Saleemi, S.; Prior, I. A.; Sée, V.; Qureshi, R.; Brust, M. *Negotiation of Intracellular Membrane Barriers by TAT-Modified Gold Nanoparticles*. *ACS Nano*, **2011**, *5*, 5195-5201.
60. Nuzzo, R. G.; B. R. Zegarski; L. H. Dubois. *Fundamental Studies of the Chemisorption of Organosulfur Compounds on Gold(111). Implications for Molecular Self-Assembly on Gold Surfaces*. *J. Am. Chem. Soc.*, **1987**, *109*, 733-740.
61. Tang, Z.; Xu, Bin; Wu, B.; Germann, M. W.; Wang, G. *Synthesis and Structural Determination of Multidentate 2,3-Dithiol-Stabilized Au Clusters*. *J. Am. Chem. Soc.*, **2010**, *132*, 3367–3374.
62. Love, J. C.; Estroff, L. A.; Kriebel, J. K.; Nuzzo, R. G.; Whitesides, G. M. *Self-Assembled Monolayers of Thiolates on Metals as a Form of Nanotechnology*. *Chem. Rev.*, **2005**, *105*, 1103-1170.
63. Kanaras, A. G.; Kamounah, F. S.; Schaumburg, K.; Kiely, C. J.; Brust, M. *Thioalkylated Tetraethylene Glycol: A New Ligand for Water Soluble Monolayer Protected Gold Clusters*. *Chem. Commun.* **2002**, *20*, 2294–2295.
64. Doty, R. C.; Tshikhudo, T. R.; Brust, M.; Fernig, D. G. *Extremely Stable Water-Soluble Ag Nanoparticles*. *Chem. Mater.* **2005**, *17*, 4630–4635.
65. Hermanson, G. T. *Bioconjugate Techniques*, 2nd edition. Elsevier Inc., **2008**, chapter 9.

66. Liz-Marzán, L. M. *Tailoring Surface Plasmons through the Morphology and Assembly of Metal Nanoparticles*. Langmuir, **2005**, 22, 32-41.
67. Gulli, L. F.; Palmer, K. C.; Chen, Y. Q.; Reddy, K. B. *Epidermal Growth Factor-Induced Apoptosis in A431 Cells can be Reversed by Reducing the Tyrosine Kinase Activity*. Cell Growth Diff., **1996**, 7, 173-178.
68. Meira, D. D.; Nóbrega, I.; de Almeida, V. H.; Mororó, J. S.; Cardoso, A. M.; Silva, R. L. A.; Albano, R. M.; Ferreira, C. G. *Different Antiproliferative Effects of Matuzumab and Cetuximab in A431 Cells are Associated with Persistent Activity of the MAPK Pathway*. Eur. J. Cancer, **2009**, 45, 1265-1273.
69. Prior, I. A.; Parton, R. G.; Hancock, J. F. *Observing Cell Surface Signaling Domains Using Electron Microscopy*. Sci. STKE, **2003**, 177, pl9.
70. Hancock, J. F.; Prior, I. A. *Electron Microscopic Imaging of Ras Signaling Domains*. Methods, **2005**, 37, 165-172.
71. Silverstein, S. C.; Steinman, R. M.; Cohn, Z. A. *Endocytosis*, Annu. Rev. Biochem., **1977**, 46, 669-722.
72. Yue, T.; Zhang, X. *Cooperative Effect in Receptor-Mediated Endocytosis of Multiple Nanoparticles*. ACS Nano, **2012**, 6, 3196-3205.
73. Gao, H.; Shi, W.; Freund, L. B. *Mechanics of Receptor-Mediated Endocytosis*. Proc. Natl. Acad. Sci. U.S.A., **2005**, 102, 9469-9474.
74. El-Sayed, I. H.; Huang, X.; El-Sayed, M. A. *Surface Plasmon Resonance Scattering and Absorption of anti-EGFR Antibody Conjugated Gold Nanoparticles in Cancer Diagnostics: Applications in Oral Cancer*. Nano Lett., **2005**, 5, 829-834.
75. Murphy, C. J.; Gole, A. M.; Stone, J. W.; Sisco, P. N.; Alkilany, A. M.; Goldsmith, E. C.; Baxter, S. C. *Gold Nanoparticles in Biology: Beyond Toxicity to Cellular Imaging*. Acc. Chem. Res., **2008**, 41, 1721-1730.

7. General conclusions.

In this work, the two main objectives were satisfactorily accomplished: i) the improved design and formation of the proposed Au NP bioconjugates; and ii) controlling their interaction with human cells by tuning the Au NP bioconjugate design. Thus, the main conclusions of this Doctoral Thesis can be summarized as follows:

1. A rich catalog of highly stable and monodisperse cationic Au NPs, with a range of sizes typically used for drug delivery and cellular uptake, were obtained.
 - i) Monodisperse cationic Au NPs with sizes comprised between 10.3 and 19.7 nm were obtained by using two competitive reducers in aqueous phase. In these syntheses, NaBH₄ acted as a strong reducer and determined the number of seeds, whereas the AUT present in solution reduced slowly the Au⁺³ precursor, resulting in a controlled growth of cationic Au NPs. By taking advantage of these independent roles, larger monodisperse cationic Au NPs (up to ~28 nm in size) were produced upon addition of the slow reducer to the preformed seeds.
 - ii) High-quality Au nanocrystals with narrow dispersions and sizes comprising 4.6, 8.9 and 13.4 nm were functionalized with cationic ligands by using a developed phase transfer methodology. First, these Au NPs were synthesized in the organic phase (toluene) at high concentrations. Then, the NPs were transferred to aqueous dispersions by surface exchange with the desired thiolated ligand, avoiding aggregation typically mediated by the negatively charged surfactants and having potential use for biological applications.
2. High concentrations of monodisperse cationic and anionic peptide-Au NP bioconjugates were efficiently prepared by the studied phase transfer methodology. Both cationic and anionic bioconjugates were shown to be stable under physiological conditions, although having strong and weak interactions, respectively, with proteins in the extracellular media. The surface charge and composition of the cationic bioconjugates allowed them to entry into cells with a high efficiency via endocytosis and being accumulated in endosomes and in the

nucleus, whereas the anionic bioconjugates were barely internalized. Further, no toxicity was observed in both cases.

3. The formation of antibody-Au NP bioconjugates of controlled composition and configuration by a site-directed chemistry was thoroughly studied. The covalent binding of a thiolated linker to the polysaccharide residues of the Abs' Fc region favoured the attachment of Abs to the NPs by strong Au-S bonds with respect to ionic or hydrophobic interactions. This binding, in turn, allowed a maximum exposure of Ab epitopes to their molecular receptors, an advantageous mobility of the Abs in solution, and monitoring the reaction thanks to the surface plasmon resonance of Au NPs and their Brownian motion. As a proof of concept, the preparation of Ab-Au NP bioconjugates of optimum Ab orientation and controlled ratio (Ab/NP) was exploited to rationally design and construct two- and three-dimensional NP superstructures directed by Ab-antigen interactions. The formation of these novel Ab-based superstructures opens the door to employ proteins additional functionality when compared to DNA-based superstructures.
4. The previous "calibration" studies were used to prepare Cetuximab-Au NP bioconjugates of controlled configuration and multivalency. The precise orientation, number and mobility of the Abs on the NP surface were key factors in modulating cellular functions. Bioconjugates with increased multivalency expressed an enhanced affinity for EGFR, and consequently, a high degree of blockade of the stimulating growth factor (EGF) binding site. The enhanced NP-receptor interactions resulted in a greater internalization of receptors and a significant reduction in their membrane presentation, which is of clinical significance. These findings were also associated to an increased inhibition of downstream signaling pathways which regulate tumor cell growth.

Overall, the results presented in this Thesis opened up new avenues to the **formation of high-quality cationic Au NP (bio)conjugates of controlled size and monodispersity as well as the preparation of antibody-Au NP bioconjugates with well-defined configuration and multivalency. In both cases, it has been demonstrated that a careful design of the Au NP bioconjugate can regulate cellular interactions and uptake, amongst other cellular functions.**

8. Future perspectives.

The field of nanotechnology applied to biomedicine has tremendously progressed over the past decade. Although much remains to be understood about the mechanism(s) of cellular interaction and processes of NP bioconjugates, the great promise of these new hybrid materials as tools for drug delivery and scientific discovery make them a worthwhile area for research. Gaining a good understanding of the potential of these bioconjugates will require a multidisciplinary and multidirectional approach. In turn, developing new strategies to ameliorate the NP bioconjugate architecture design and illuminating their biological function will surely lead to the discovery of new and useful applications.

List of abbreviations

Abbreviations for Amino Acids					
A	Ala	Alanine	M	Met	Methionine
B	Asx	Asparagine or aspartate	N	Asn	Asparagine
C	Cys	Cysteine	P	Pro	Proline
D	Asp	Aspartate	Q	Gln	Glutamine
E	Glu	Glutamate	R	Arg	Arginine
F	Phe	Phenylalanine	S	Ser	Serine
G	Gly	Glycine	T	Thr	Threonine
H	His	Histidine	V	Val	Valine
I	Ile	Isoleucine	W	Trp	Tryptophan
K	Lys	Lysine	Y	Tyr	Tyrosine
L	Leu	Leucine	Z	Glx	Glutamine or glutamate

Ab = antibody

AD = aminodextran

Au NP = gold nanoparticle

AUT = 1-aminoundecane-11-thiol

1 = 22-(3,5-bis((6-mercaptohexyl)oxy)phenyl)-3,6,9,12,15,18,21-heptaodocosanic hydrazide (linker)

BSA = bovine serum albumin

CCM = cell culture media

α -CD = α -cyclodextrin

CDR = complementarity determining region

CH = constant domain of H

CI = clathrin independent (endocytosis)

C.I. = confidence interval

CL = constant domain of L

CME = clathrin mediated endocytosis

CoA = coenzyme A

CPPs = cell penetrating peptides

CR = cysteine-rich (domain)

CT = C-terminal (domain)

CTAB = cetyltrimethylammonium bromide

D = dextran

DAPI = 4',6-diamidino-2-phenylindole

DCM = dichloromethane

DDAB = didodecyldimethylammonium bromide
DIC = differential interference contrast
DLS = dynamic light scattering
DMEM = Dulbecco's Modified Eagle Medium
DMSA = dimercaptosuccinic acid
DNP = thiolated dinitrophenyl
DODAB = dimethyldioctadecylammonium bromide
DTT = dithiothreitol
EC = extracellular (domain)
EDC/NHS = 1-ethyl-3-(3-dimethylaminopropyl)carbodiimide/N-Hydroxysuccinimide
EGF = epidermal growth factor
EGFR = epidermal growth factor receptor
EPR = enhanced permeability and retention (effect)
ER = endoplasmic reticulum
Fab = fragment antigen binding
FBS = fetal bovine serum
Fc = fragment crystallizable
FDA = Food and Drug Administration
 β -gal = β -galactosidase
GAPDH = glyceraldehyde 3-phosphate dehydrogenase
H = heavy (chain)
H = heparin
HAuCl₄ = hydrogen tetrachloroaurate
hCG = human chorionic gonadotropin
HEPES = 4-(2-hydroxyethyl)-1-piperazineethanesulfonic acid
Her = herceptin
His₆ = hexahistidine
IC = intracellular (domain)
ICP-MS = inductively coupled plasma mass spectrometry
Ig = immunoglobulin
IgG = Immunoglobulin G
JM = juxtamembrane (domain)
L = light (chain)
LYCH = Lucifer Yellow carbohydrazide
LSPR = localized surface plasmon resonance
MAbs = monoclonal antibodies
Mal = maleimide
MAPK/ERK = mitogen-activated protein kinase/extracellular signal-regulated kinase
2-MEA = 2-mercaptoethylamine
MPCs = monolayer protected clusters

MTS = (3-(4,5-dimethylthiazol-2-yl)-5-(3-carboxymethoxyphenyl)-2-(4-sulfophenyl)-2H-tetrazolium)
 MTT = (3-(4,5-dimethylthiazol-2-yl)-2,5-diphenyltetrazolium bromide)
 MVBs = multivesicular bodies
 NaBH₄ = sodium borohydride
 NLS = nuclear localization sequence
 N_{max} = maximum theoretical number of Abs
 NPAR = goat anti-rabbit Ab-1-Au NP bioconjugate (8 goat anti-rabbit Abs attached onto 17.2 ± 1.8 nm Au NP)
 NPC3 = Cetuximab Ab-1-Au NP bioconjugate (3 Cetuximab Abs attached onto 17.2 ± 1.8 nm Au NP)
 NPC6 = Cetuximab Ab-1-Au NP bioconjugate (6 Cetuximab Abs attached onto 17.2 ± 1.8 nm Au NP)
 NPC8 = Cetuximab Ab-1-Au NP bioconjugate (8 Cetuximab Abs attached onto 17.2 ± 1.8 nm Au NP)
 NTA = nitrilotriacetic acid
 ODT = octadecanethiol
 OLA = oleylamine
 θ = standard deviation
 pA = protein A
 PAA = poly(allyamine hydrochloride)
 PAbs = polyclonal antibodies
 pAKT = phosphorylated AKT
 PBS = phosphate buffered saline
 PBS-T = 0.05 % Tween in PBS
 PEG = polyethylene glycol
 pEGFR 1173 = phosphorylated tyrosine residue 1173 of EGFR
 PEI = poly(ethyleneimine)
 PFA = paraformaldehyde
 pG = protein G
 pI = isoelectric point
 PI3 kinase/Akt = phosphatidylinositol 3 kinase/Akt
 PLC-γ/PKC = phospholipase C gamma /protein kinase C
 PLGA = poly(lactic-co-glycolic acid)
 p-p44/42 MAPK = phosphorylated p44/42 MAPK
 PT-PCT = photothermal optical coherence tomography
 PVA = poly(vinyl alcohol)
 R_{Ab} = radius of the IgG
 R_{AuNP} = radius of the Au NP
 RGD = Arg-Gly-Asp
 RT = room temperature
 SAP = sweet arrow peptide
 scFv = single-chain variable fragments
 SH-PEG = thiolated PEG

siRNA = small interfering RNA

SPDP = N-succinimidyl 3-(2-pyridyldithio) propionate

SPR = surface plasmon resonance

σ = standard deviation

STAT = signal transducer and activator of transcription

TA = thioctic acid

TBAB = tetrabutylammonium borohydride

TCB = thiocholine bromide

TEG = tetraethyleneglycol

TEM = transmission electron microscopy

Tf = transferrin

TGF α = transforming growth factor- α

THF = tetrahydrofuran

TK = tyrosine kinase (domain)

TM = transmembrane (domain)

TOAB = tetraoctylammonium bromide

UA = uranyl acetate

VH = variable domain of H

VL = variable domain of L

WB = western blot

XTT = (2,3-bis-(2-methoxy-4-nitro-5-sulfophenyl)-2H-tetrazolium-5-carboxanilide)

ANNEX I : Materials and Methods.

Experimental from Chapter 2

Materials. Sodium borohydride (NaBH_4 , $\geq 98\%$), hydrogen tetrachloroaurate (III) trihydrate ($\text{HAuCl}_4 \cdot 3\text{H}_2\text{O}$) and 11-amino-1-undecanethiol hydrochloride (AUT, 99%) were purchased from Sigma-Aldrich. Aqueous solutions from the reagents as received were prepared with MilliQ water.

Characterization. UV-vis absorption spectra were acquired with a Shimadzu UV-2401-PC spectrometer. UV-vis time series of the reactions were measured by transferring a small aliquot of the reaction mixture (1 mL) to a plastic cuvette immediately after the addition of NaBH_4 (approx. 15 seconds) and taking a series of absorption spectra at time intervals of 5 minutes. The cuvettes were sealed with a plastic cap to prevent evaporation. The absorption and exact position of the plasmon peak was detected fitting a square function to a small interval (± 5 nm) around the peak. TEM grids were prepared by carefully placing a droplet of the sample onto the grid, which had been placed on parafilm, and wicking off the liquid after about 5 minutes. TEM analysis was carried out on a JEOL 1010 instrument operating at 80 kV. Digital images were analyzed with ImageJ software and a custom macro performing smoothing (3x3 or 5x5 median filter), manual global threshold and automatic particle analysis provided by the ImageJ. The macro can be downloaded from <http://code.google.com/p/psa-macro>. The particle size was calculated as circle-equivalent diameter from the area of each individual particle ($d = 2\sqrt{A/\pi}$) and calculating the number averages from the entire population or individual peaks found in the histograms. Dynamic light scattering (DLS) and zeta potential measurements were carried out with a Malvern Zetasizer ZS-Nano instrument using disposable cuvettes. Data was analyzed with the Malvern DTS software using the general purpose algorithm for DLS and the Smochulowski model for obtaining zeta potential values.

Synthesis of cationic Au NPs (from ~ 10.3 to ~ 28.2 nm) in aqueous solution. A two-step one-pot synthesis was performed by simultaneously injecting two competing reducers (NaBH_4 and AUT) onto the Au^{3+} precursor solution under vigorous stirring, in aqueous phase and at room temperature (RT), obtaining Au NPs stabilized by AUT. A series of identical reactions were performed in which the volume fraction of the stock solution of NaBH_4 was systematically increased under a fixed molar ratio of the other reagents; that is a Au:AUT: NaBH_4 molar ratio of 1:0.66:X, where X was varied from 0.11, 0.053, 0.026, 0.0132, 0.0066, 0.0033, 0.0016, 0.0008, 0.0004 to 0.0002 by keeping a constant reaction volume. Characterization by TEM showed that the resulting Au NPs (monomodal collections) had diameters from 10.3 ± 2.8 to 19.7 ± 2.6 . The as-synthesized Au NPs with a Au:AUT: NaBH_4 ratio of 1:0.66:0.053 were further used as seeds in a two-step seeded growth. Additional amounts of HAuCl_4 and AUT were added to the seed solution (Au NP seeds = 11.1 ± 2.5 nm) in a molar ratio Au:AUT = 1.5. Two different experiments were carried out in which the amount of Au added was 7- and 26-fold the amount of Au^{+3} used to prepare the seeds. These specific amounts of Au^{+3} were chosen with the aim to increase the

original Au NP seeds by 2- and 3-fold respectively ($2^3 = 8$ and $3^3 = 27$), assuming that no additional nucleation occurs. Characterization by TEM showed that the resulting Au NPs had diameters of 25.5 ± 3.0 nm and 28.2 ± 4.1 nm, respectively.

Purification and stability. The as-synthesized Au NPs could be purified by precipitation upon fast centrifugation (20,000 rcf, 10 min, 20 °C) followed by redispersion of the pellet in MilliQ water. The NPs were stable for months at RT on the benchtop. The zeta potential of the AUT-capped particles was strongly positive (approx. + 50 mV at pH = 7 in all the cases), confirming the cationic nature of the NPs. The NPs were stable only in pure (pH = 6.5-7) or acidified water (diluted HCl, pH = 3-4) and in 100 mM glycine-HCl buffer at pH = 2.5, which indicates that the terminal amine has to be protonated to display a positive charge. Other buffers at neutral pH such as citrate, acetate, phosphate, MES, HEPES or borate, yielded aggregation and precipitation due to the presence of ionic species, which screened the electrostatic repulsion between the positive groups. However, due to the dense packing of the AUT monolayer on the surface of the Au NPs, aggregation was reversible and the NPs could be redispersed in diluted 0.1 M HCl.

Experimental from Chapter 3

Materials. Sodium citrate, hydrogen tetrachloroaurate (III) trihydrate ($\text{HAuCl}_4 \cdot 3\text{H}_2\text{O}$), tetraoctylammonium bromide (TOAB, 98%), dodecylamine (98%), oleylamine (OLA, 70%), 11-amino-1-undecanethiol hydrochloride (AUT, 99%), methanol anhydrous (99.9%), toluene (99.8%), chloroform (99%), dichloromethane (DCM, 99.8%), and tetrahydrofuran (THF, 99.9%) were purchased from Sigma-Aldrich and used as received without further purification. Stock solutions (10 mM) of AUT were prepared upon dilution in Milli-Q H_2O .

Characterization. UV-vis absorption spectra were recorded with a Shimadzu UV-2401PC spectrophotometer at room temperature. The samples were left to settle for 30 minutes before measurements. Au NPs were visualized using a transmission electron microscope, TEM (JEOL 1010, Japan), at an accelerating voltage of 80 kV. The sample (10 μL) was drop-casted onto ultrathin Formvar-coated 200-mesh copper grids (Tedpella Inc.) and left to dry in air. For each sample, the size of at least 200 particles was measured to obtain the average and the size distribution. Digital images were analyzed with Image J software and a custom macro performing smoothing (3 x 3 or 5 x 5 median filter), manual global threshold, and automatic particle analysis provided by ImageJ. DLS and ζ -potential measurements were obtained using a Zetasizer Nano ZS (Malvern Instruments). Standard purification by dialysis, unless otherwise stated, was performed using 16 mm membranes (molecular weight cut off (MWCO) = 15 kDa) against distilled H_2O (5000 mL).

Synthesis of Au NPs (4 nm) in Toluene. Au NPs of ~ 4 nm in diameter were prepared in toluene by a modification of the Brust-Schiffrin two-phase approach.¹ Briefly, a solution of 30 mM $\text{HAuCl}_4 \cdot 3 \text{H}_2\text{O}$

was first transferred from an aqueous (30 mL) to a toluene (80 mL) solution containing TOAB (2.2 g, 50 mM), which was followed by reduction with a freshly prepared aqueous solution of NaBH₄ (25 mL, 0.4 M) in the presence of dodecylamine (155.7 mg, 0.84 mmol). Particle size was determined by DLS and TEM.

Synthesis of Au NPs (4 nm) in water and phase transfer to toluene. Au NPs of ~ 4 nm were prepared in aqueous phase by the method reported by Jana *et al.*² Briefly, 0.6 mL of an ice-cold and freshly prepared aqueous solution of 0.1M NaBH₄ was added dropwise to 20 mL of an aqueous solution containing HAuCl₄ · 3H₂O (2.0 mg, 0.25 mM) and trisodium citrate (1.5 mg, 0.25 mM) under vigorous stirring. The as-synthesized Au NPs were then transferred into toluene following reported procedures,³ by using TOAB (0.7 g, 0.13 M) as the phase-transfer reagent at a H₂O/toluene volume ratio of 1:1. Particle size was determined by DLS and TEM.

Synthesis of Au NPs (9 and 13 nm) in toluene. Au NPs of ~ 9 and ~ 13 nm in diameter were prepared in toluene in a one-pot synthesis by a reported method.⁴ Briefly, a solution of HAuCl₄ · 3H₂O (393 mg, 1 mmol) in toluene (50 mL) was mixed with oleylamine (4.6 mL, 10 mmol), which acts as both the reducing agent and surfactant of the resulting Au NPs. The reaction mixture was kept under N₂ protection and heated to either 65 °C for 6 hours or 115 °C for 3 hours to obtain ~ 9 and ~ 13 nm Au NPs, respectively. Particle size was determined by DLS and TEM.

Phase transfer and surface functionalization of Au NPs. Methanol (3 mL) was added to a solution of as-synthesized Au NPs in toluene (5 mL), the cloudy mixture was centrifuged (3000 rcf, 5 minutes) to precipitate the NPs, and the supernatant was discarded. The resulting pellet was resuspended in toluene (5 mL), and the complete cleaning process was repeated. The particles were finally dispersed in chloroform (5 mL). In order to ensure complete coating of the Au NPs, the phase-transfer process was carried out in the presence of an excess of ligand (calculated by the number of Au atoms at the surface of the NP and assuming that each thiolated molecule occupies 21.4 Å² of the Au NP surface).^{5,6} An aqueous solution of AUT in a 50-fold molar excess was added dropwise to a solution of Au NPs in chloroform (1 mL). Immediate transfer was observed after gentle vortexing. The resulting conjugates in the aqueous layer were exhaustively purified by dialysis against Milli-Q water with two cycles of 24 hours each in order to eliminate the excess nonconjugating molecules. NP functionalization and stability of the bioconjugates were determined by UV-vis absorbance spectroscopy, DLS, and TEM. Similarly, experiments with different ligand molar ratios were performed under the same reaction conditions using Au NPs (~ 13 nm) in chloroform and a 0.5-, 1-, 5-, and 10-fold molar excess of AUT. A variety of organic solvents of different polarity (toluene, DCM, and THF) were also employed besides chloroform in the same phase-transfer protocol using Au NPs (~ 13 nm) and a 50-fold molar excess of AUT.

Experimental from Chapter 4

Materials. Sodium citrate, hydrogen tetrachloroaurate (III) trihydrate ($\text{HAuCl}_4 \cdot 3\text{H}_2\text{O}$), tetraoctylammonium bromide (TOAB, 98%), dodecylamine (98%), oleylamine (OLA, 70%), 11-amino-1-undecanethiol hydrochloride (AUT, 99%), methanol anhydrous (99.9%), ethanol (90%), toluene (99.8%), chloroform (99%), were purchased from Sigma-Aldrich and used as received without further purification. Peptidic biomolecules CIPGNVG-PEG-COOH and CIPGNVG-PEG-NH₂ (PEG = polyethyleneglycol of MW = 220) were synthesized following an Fmoc strategy and solid-phase synthesis (bioNova Cientifica S.L., Spain). Stock solutions (10 mM) of peptides were prepared upon dilution in a (85:15) mixture of ethanol/Milli-Q H₂O, and the resulting solutions were filtered using 0.2 μm filters and used immediately under sterile conditions.

Characterization. UV-vis absorption spectra were recorded with a Shimadzu UV-2401PC spectrophotometer at room temperature. The samples were left to settle for 30 minutes before measurements. Au NPs were visualized using a TEM (JEOL 1010, Japan), at an accelerating voltage of 80 kV. The sample (10 μL) was drop-casted onto ultrathin Formvar-coated 200-mesh copper grids (Tedpella Inc.) and left to dry in air. For each sample, the size of at least 200 particles was measured to obtain the average and the size distribution. Digital images were analyzed with Image J software and a custom macro performing smoothing (3 x 3 or 5 x 5 median filter), manual global threshold, and automatic particle analysis provided by Image J. DLS and ζ -potential measurements were obtained using a Zetasizer Nano ZS (Malvern Instruments). Standard purification by dialysis, unless otherwise stated, was performed using 16 mm membranes (MWCO = 15 kDa) against distilled H₂O (5000 mL). FTIR spectra were recorded on a Tensor 27 Bruker spectrometer equipped with ATR (attenuated total reflection) from MKII Golden Gate, Specac. The samples were lyophilized for FTIR measurements. Au content of the cell samples was determined by an Agilent inductively coupled plasma mass spectrometry (ICP-MS) instrument (model: 7500cx) with a detection limit of 0.02386 ppb. Both the supernatant and the pellet samples were digested in aqua regia at 100 °C before ICP-MS analysis. Ga was used as the internal standard, and the integration time/point and time/mass were 0.1 and 0.3 seconds, respectively, with a 3 x times repetition. The confocal images were acquired using a Leica TCS SP5 epifluorescence/reflectance laser scanning confocal microscope with a 63 x oil immersion objective. The excitation was provided by an Ar multiline laser. Consistent laser intensity or camera exposure levels for each fluorescent marker in each experiment were used. Reflectance images were obtained with 488 nm laser excitation. Images were treated using Leica Microsystems LAS AF lite analysis software. Optical microscope images were acquired using an inverted Nikon TS100F optical microscope with an integrated Nikon DS-Fi2/U3 digital camera.

Phase transfer and surface functionalization of ~ 13 nm Au NPs. Methanol (3 mL) was added to a solution of ~ 13 nm Au NPs (Chaper 3) in toluene (5 mL), the cloudy mixture was centrifuged (3000 rcf, 5 minutes) to precipitate the particles, and the supernatant was discarded. The resulting pellet was resuspended in toluene (5 mL), and the complete cleaning process was repeated. The NPs were finally

dispersed in chloroform (5 mL). In order to ensure complete coating of the Au NPs, the phase-transfer process was carried out in the presence of an excess of ligand (calculated by the number of Au atoms at the surface of the NP and assuming that each thiolated molecule occupies 21.4 Å² of the Au NP surface).^{5,6} A solution of either the biomolecule CIPGNVG-PEG-NH₂ or CIPGNVG-PEG-COOH diluted in a mixture of ethanol / Milli-Q H₂O (85:15, 500 µL), was added dropwise to a solution of Au NPs in chloroform (1 mL). A few drops (approximately 300 µL) of 0.1 M of either HCl or NaOH were required to form the respective charged compounds, followed by some additional mixing. The biphasic mixture was left to stand on the bench for about 10-30 minutes, during which it could be observed how the red color of the organic solution was transferred into the aqueous layer. The resulting bioconjugates in the aqueous layer were exhaustively purified by dialysis against Milli-Q water with two cycles of 24 hours each in order to eliminate the excess nonconjugating molecules. NP functionalization and stability of the bioconjugates were determined by UV-vis absorbance spectroscopy, DLS, and TEM.

Cell culture and NP pre-incubation studies. Human fibroblasts (1BR3G, ECACC/Sigma-Aldrich) were cultured in Dulbecco's modified Eagle's medium (DMEM) supplemented with 10% fetal bovine serum (FBS) under a humidified 10% CO₂ atmosphere at 37 °C. Previously to the incubation with cells, both bioconjugates Au NP-CIPGNVG-PEG-NH₂ and Au NP-CIPGNVG-PEG-COOH at a concentration of 50 nM NPs were irradiated with UV light for 1-2 hours, incubated overnight (1:2 dilution) in borate buffer solution (2 mM, pH 8.5) containing 10% FBS, and diluted in DMEM 10% FBS medium up to final concentrations of 0.5 and 5 nM NPs. All samples were centrifuged (8000 rcf, 10 minutes) and resuspended in Milli-Q H₂O before UV-vis, DLS, and ζ-potential measurements were performed to test the stability of the conjugates.

ICP-MS analysis. For Au NP uptake studies, cells were seeded at a density of 10⁵ cells per well in six-well plates. After 48 hours, cells were washed with PBS and fresh culture medium (1 mL) was added containing the Au NP bioconjugates. After a certain incubation time (30 minutes, 1 hour and 3 hours), the medium of the cells was collected for ICP-MS analysis, and the cells were washed three times with PBS (1 mL), trypsinized (Trypsin-EDTA, 1 mL), and centrifuged (400 rcf, 10 minutes). The resulting pellets were also collected for ICP-MS analysis. The percentage of cell-associated NPs was calculated relative to the total number of NPs used in the incubation medium and compared well with the decrease of NPs observed in the incubation medium after cell exposure in all the cases.

Confocal microscopy. For confocal studies cells were seeded at a density of 5 x 10⁴ cells per well on glass coverslips placed in six-well plates and cultured at 37 °C and 10% CO₂ in an incubator. After 48 hours, cells were washed with PBS, and fresh medium was added containing 5 nM of the functionalized Au NP bioconjugates. After 3 hours of incubation, cells were washed 3 x times with PBS (1 mL) and fixed in ice-cold methanol (1 mL) for 15 minutes at 20 °C. Methanol was then allowed to evaporate before cells were washed 3 x times with PBS/0.005% Tween 20 (1 mL), and the nuclei were stained with DAPI for 15 minutes. Glass coverslips were mounted on a slide with Fluoprep mounting medium (Biomérieux).

Cell viability. For toxicity determination, 5×10^3 cells per well were seeded in 96-well plates and incubated overnight to allow for cell attachment. After overnight incubation, cells were washed with PBS and fresh culture medium (100 μ L) was added containing the Au NP bioconjugates at the desired concentration and incubated for 24 hours. Although the duplication time for the 1BR3G cells is approximately 20 hours, the cells did not reach an elevated confluence at the end of the assay. Cell medium replacement was performed to avoid interference from Au NPs in the colorimetric analysis. The concurrent cell viability assay was performed using the XTT assay (Biomedica) in 96-well plates according to the manufacturer's instructions. In brief, XTT reagent (20 μ L) was added to the cell culture and incubated for 2 hours. After incubation the absorbance was recorded at 450 nm (reference wavelength 620 nm) in a microplate reader (Victor 3, PerkinElmer). All conditions were performed in quadruplicate. Cell viability was additionally determined by a Trypan blue dye exclusion assay. After 24 hours exposure to Au NP bioconjugates, the cells were rinsed with fresh medium in order to eliminate excess Au NPs and 0.4% Trypan blue solution was added and left for 3 minutes. The cells were then rinsed thoroughly with PBS buffer and inspected under a phase contrast microscope.

Resin embedding of cells for TEM analysis. For resin inclusion, cells were thoroughly washed with PBS buffer after NP incubation and fixed in a 0.1 M PB solution containing 2.5% glutaraldehyde at 4 °C for 1 hour. The cells were then rinsed 3 x times with PBS and carefully collected in a tube with a cell scraper. The cellular pellet was postfixed in 1% osmium tetroxide solution for 1 hour, rinsed with PBS and distilled H₂O, and dehydrated in a graded series of ethanol (30, 60, 70, 80, and 100%). Finally warm epoxy resin was mixed with ethanol (1:1) for infiltration, and only resin was used for cell embedding (60 °C, 48 hours). Ultrathin sections (50 nm) were cut with a Leica Ultracut UCT Ultramicrotome and stained with 5% uranyl acetate in 50% ethanol and 2% aqueous lead citrate solution. The sections obtained were imaged using a JEOL 1010 TEM operating at an accelerating voltage of 80 kV.

Experimental from Chapter 5

Materials. Sodium citrate, hydrogen tetrachloroaurate (III) trihydrate (HAuCl₄·3H₂O), sodium (meta)periodate (NaIO₄, $\geq 99\%$), Lucifer Yellow CH dipotassium salt (LYCH, 90 %), O-(2-mercaptoethyl)-O'-methyl-hexa(ethylene glycol) (C₁₅H₃₂O₇S, $\geq 95\%$), goat anti-rabbit IgG, rabbit anti-BSA IgG, bovine IgG and PD10 desalting columns were purchased from Sigma-Aldrich. Antibodies were purified by PD10 desalting columns and transferred into a phosphate buffer (PB) solution 0.1 M pH = 7.0 before use. Linker 22-(3,5-bis((6-mercaptohexyl)oxy)phenyl)-3,6,9,12,15,18,21-heptaaxadocosanhydrazide (**1**) was purchased from SensoPath Technologies, Bozeman, MT, USA. Ultrafiltration spin columns (2 mL, MWCO = 50 kDa, polyethersulphone) were from Sartorius Stedim Biotech GmbH, and cellulose membranes (MWCO = 3.5 kDa) from Spectrum Labs (Spectra/Por). Alexa Fluor 488 dye was obtained from Life Technologies.

Characterization. Au NPs were visualized using a transmission electron microscope, TEM (JEOL 1010, Japan), at an accelerating voltage of 80 kV. The sample (10 μ L) was drop-casted onto ultrathin Formvar-coated 200-mesh copper grids (Tedpella Inc.) and left to dry in air. For each sample, the size of at least 200 particles was measured to obtain the average and the size distribution. Digital images were analyzed with Image J software and a custom macro performing smoothing (3 x 3 or 5 x 5 median filter), manual global threshold, and automatic particle analysis provided by ImageJ. Addition of native or 1-modified Abs were calculated to obtain ratios ranging from 1 to 140 Ab/NP (in solution). The mixtures were left to react for 20 minutes at 4°C under slow agitation to reach equilibrium. UV-Vis absorption spectra were recorded with a Shimadzu UV-2401PC spectrophotometer at room temperature. DLS and ζ -potential measurements were obtained using a Zetasizer Nano ZS (Malvern Instruments). UV-Vis and DLS measurements were recorded 20 minutes after every new Abs addition, and after 24 and 72 hours to ensure equilibrium. Note that in the case of native Abs no equilibrium was reached. ζ -potential measurements were performed from goat anti-rabbit IgG, rabbit anti-BSA IgG and bovine IgG in phosphate buffer saline (PBS) solution (10 mM, pH = 7) at a concentration of 1 mg/ml. The Abs solutions were titrated with NaOH/HCl (0.01M and 0.1M) in a range of pH from 2.5 to 10.5 for determination of their isoelectric point. Fluorescence measurements were performed using a SpectraMax M2e microplate reader operating in the fluorescence mode at excitation/emission wavelengths of 494/519 nm.

Synthesis of Au NPs (~ 8 and ~ 17 nm) in citrate aqueous solution. Au NPs of 7.9 ± 1.5 nm and 17.1 ± 2.4 nm were synthesized by the classical method of citrate reduction of HAuCl₄.^{7,8} Briefly, 7.9 ± 1.5 nm Au NPs were synthesized by injecting 5 mL from an aqueous solution of HAuCl₄ (HAuCl₄·3 H₂O, Sigma-Aldrich) 25 mM into a boiling solution of sodium citrate 2.2 mM (150 mL). The reaction mixture turned dark and immediately into red, indicating Au NPs formation. An intense red color was obtained after 5 minutes reaction. An inverse method was used to obtain 17.1 ± 2.4 nm Au NPs, in which an aqueous solution of HAuCl₄ (200 mL , 58.8 μ M) was heated up to boiling and 4.4 mL of SC 38,8 mM were then injected. It was left to react for 5 minutes and similar reaction mechanisms were observed. Larger Au NPs of ~ 24 nm were obtained by seeding growth. Briefly, 30 mL from a colloidal solution of the as-synthesized 7.9 ± 1.5 nm Au NPs were diluted in 120 mL of sodium citrate 2.2 mM and it was heated up to 90 °C, followed by an injection of HAuCl₄ (1 mL, 25 mM). The mixture was let to react for ~ 8 minutes, and NPs of 17.7 ± 1.3 nm were obtained. Following the same protocol, the as-synthesized Au NPs were used as seeds for the next synthesis, in which 24.0 ± 3.8 nm Au NPs were obtained after 15 minutes reaction. All the synthesized Au NPs had reasonably monodisperse size distribution (<16 % standard deviation) as measured by TEM. All the Au NP solutions were centrifuged at 18.000 g (18 and 24 nm NPs) and 40.000 g (8 nm NPs) for 10 minutes, and redispersed in borate buffer 2 mM at pH = 8.5. Working NP concentrations for conjugation were $4.5 \cdot 10^{12}$ NPs/mL, $1.6 \cdot 10^{12}$ NPs/mL and $2.4 \cdot 10^{11}$ NPs/mL corresponding to 8, 17, and 24 nm Au NPs, respectively.

Quantitative analysis of Ab' polysaccharides oxidation. Goat anti-rabbit IgG, rabbit anti-BSA IgG and bovine IgG were diluted to a concentration of 1 mg/ml in PB solution 0.1 M pH = 7.0. Then, 10 μ L of an aqueous solution of NaIO₄ 0.1 M were added to 100 μ L of the Abs solutions. The mixtures were placed in

an aliquot wrapped with aluminium foil and left to react for 30 minutes, at room temperature (RT) under gentle shaking. The oxidation rate was slowed down by dilution in 500 μL of PB 10 mM, pH 7.0. The samples were immediately dialyzed with cellulose membranes (MW 3.5 kDa) at RT for 2 hours against 5 L of PB 10 mM pH = 7. It was followed by two additional dialysis cycles in the same conditions. A 250-fold excess of LYCH (20 μl , 10 mM) was added to the Abs solutions and they were allowed to react for 1 hour in the dark at RT under slow agitation. The reaction mixtures were dialyzed in the same previously described conditions, by performing three additional dialysis cycles for a minimum of 2 hours. Fluorescence measurements from the samples were performed in a 96-well plate with a SpectraMax M2e microplate reader, using a calibration of LYCH diluted in PB 10 mM (pH = 7) at concentrations ranging from 0 to 10 μM . From these measurements, the concentration of LYCH per well was estimated. The concentration of Abs in each well was determined by measuring the absorbance at 280 nm with a Shimadzu UV-2401PC spectrophotometer, on the basis of a molar extinction coefficient (ϵ) of 210.000 $\text{M}^{-1}\text{cm}^{-1}$.⁹ From these values, LYCH labelling per Ab was estimated. To correct for any LyCH that was nonspecifically adsorbed to the Abs, all the results were compared with nonoxidized Abs that had been incubated with a 250-fold excess of LyCH. Under the purification conditions used, the level of nonspecifically bound LyCH was approximately 0.01-0.02 LYCH molecules/Ab.

Preparation of linker-modified Abs (Ab-1 pairs). Abs were diluted to a concentration of 1 mg/ml in PB solution 0.1 M, pH = 7.0. Then, 10 μL of an aqueous solution of NaIO_4 0.1 M were added to 100 μL of the Abs solution. The mixture was placed in an aliquot wrapped with aluminium foil and left to react for 30 minutes, at room temperature (RT) under gentle shaking. The oxidation rate was slowed down by dilution in 500 μL of PB 10 mM, pH 7.0. Then, 2 μL of linker (**1**) in a 90% ethanol solution (50 mg/ml) were immediately added to the Abs solution, and it was let to react for 1 hour at RT under gentle shaking. Unreacted linker molecules were removed using ultrafiltration spin columns, by dilution of the solution in HEPES 40 mM (1 ml, pH 8.5) and centrifugation at 2000 g for 2-3 minutes. The purification was repeated 3 x times, to a final volume of ~ 300 μl . Ab-1 pairs concentration was determined spectrophotometrically at 280 nm on the basis of a molar extinction coefficient, ϵ , of 210.000 $\text{M}^{-1}\text{cm}^{-1}$.⁹ The estimated concentration of Ab-1 pairs after purification was in the range of 200-400 $\mu\text{g}/\text{mL}$ in all cases.

Quantification of Ab/NP ratio with a fluorescent dye. Anti-rabbit Ab-1 pairs were labeled with the fluorescent dye Alexa Fluor 488 (AF) according to the manufacturer's instructions. The Abs were subsequently added to the Au NPs at different ratios, forming AF-Ab-1-Au NP bioconjugates. Centrifugation of the samples was then used to separate the pellet containing the AlexaFluor 488-Ab-1-Au NPs conjugates from the supernatant containing unbound AF-Ab-1. The fluorescence emission intensity of the supernatant was measured to determine the concentration of the AF-Ab-1. The average amount of attached Abs to Au NPs was determined by subtracting the unbound AF-Ab-1 from total. Measurements were done from duplicate experiments and two different sample fractions.

Design and preparation of Ab-NP assemblies. The formation of dimers started with the coupling of rabbit anti-BSA Ab-1 and goat anti-rabbit Ab-1 to 7.9 ± 1.5 nm and 17.1 ± 2.4 nm Au NPs, respectively,

with an Ab-1/NP ratio of 3 in solution, corresponding to an Ab-1/NP ratio of 1.2 (according to quantification with Alexa dye). The mixture was left to react for 20 minutes. Then, a short thiolated PEG (MW 356.48) was added at 3-fold molar excess over the estimated complete NPs coverage (calculated by the number of Au atoms at the surface of the NP and assuming that each thiolated molecule occupies 21.4 \AA^2 of the Au NP surface)⁶ to passivate the remaining NPs surface. After 5 minutes reaction, the bioconjugates were mixed overnight in a stoichiometric amount, at 4°C and under slow agitation. The formed structures were separated from unreacted NPs by gentle centrifugation (5.000 g, 5 minutes) and the pellet was visualized under TEM. For the **satellite-shaped NP superstructures**, goat anti-rabbit Ab-1 were coupled to $17.1 \pm 2.4 \text{ nm}$ Au NPs up to a saturation ratio (~50 Ab-1/NP ratio in solution). In parallel, rabbit anti-BSA Ab-1 were again coupled to $7.9 \pm 1.5 \text{ nm}$ Au NPs with an Ab-1/NP ratio of 3 (in solution). The mixtures were left to react for 20 minutes. Then, a short thiolated PEG (MW 356.48) was added at 3-fold molar excess over the estimated complete NPs coverage, to passivate the remaining NPs surface. After 5 minutes reaction, the two bioconjugates were mixed in an excess (100x) of the smaller rabbit anti-BSA Ab-1-Au NP bioconjugates, and the resulting mixture was gently stirred at 4 °C overnight. Again, a gentle centrifugation step (5.000 g, 5 minutes) was used to purify the NP superstructures from individual bioconjugates, and the pellet was collected for TEM analysis. 3D tomography TEM characterization of one of such satellite-shaped superstructures was performed, obtaining tilt series from -69° to 65° . The formation of **trimers** started with the coupling of anti-BSA Ab-1 to $17.1 \pm 2.4 \text{ nm}$ Au NPs with an Ab-1/NP ratio of 3 (in solution). A short thiolated PEG (MW 356.48) was added as previously described. In parallel, $7.9 \pm 1.5 \text{ nm}$ Au NPs were coupled to BSA using an excess (100 x) of the protein to ensure a complete NP coverage. Then, the anti-BSA Ab-1-Au NP and BSA-Au NP bioconjugates were mixed at 300 rpm and at RT. After 2 h of reaction, the anti-rabbit Ab-1-Au NP bioconjugate (synthesized by coupling anti-rabbit Ab-1 to $17.1 \pm 2.4 \text{ nm}$ Au NPs with an Ab-1/NP ratio of 3, and passivated with a short SH-PEG as previously described) was added to the mixture. The resulting new mixture was stirred overnight at 4°C, and a soft centrifugation step (5000 g, 5 min) was then performed for separating the superstructures. TEM characterization of the resulting pellet was performed.

Experimental from Chapter 6

Materials. Sodium citrate, hydrogen tetrachloroaurate (III) trihydrate ($\text{HAuCl}_4 \cdot 3\text{H}_2\text{O}$), sodium (meta)periodate (NaIO_4 , $\geq 99\%$), Lucifer Yellow CH dipotassium salt (LYCH, 90%), O-(2-mercaptoethyl)-O'-methyl-hexa(ethylene glycol) ($\text{C}_{15}\text{H}_{32}\text{O}_7\text{S}$, $\geq 95\%$) and PD10 desalting columns were purchased from Sigma-Aldrich. Cetuximab IgG1 monoclonal Ab (Erbitux, C225) was purchased from Merck Serono, Spain. Cetuximab MAb was purified by PD10 desalting columns and transferred into a phosphate buffer (PB) solution 0.1 M, pH = 7.0, before use. Linker 22-(3,5-bis((6-mercaptohexyl)oxy)phenyl)-3,6,9,12,15,18,21-heptaaxadocosanic hydrazide (**1**) was purchased from SensoPath Technologies, Bozeman, MT, USA. Ultrafiltration spin columns (2 mL, MWCO = 50 kDa,

polyethersulfone) were from Sartorius Stedim Biotech GmbH, and dialysis cellulose ester membranes (MWCO = 300 kDa, 10 mL) were obtained from Spectrum Labs (Spectra/Por, Float-A-Lyzer). A431 cells (ATCC No. CRL-1555TM) were purchased from LGC Standards, Teddington, UK. Alexa Fluor 555-EGF complex (E-35350) was purchased from Life Technologies Ltd., Paisley, UK. M-PER Mammalian Protein Extraction Reagent, Halt Protease & Phosphatase Inhibitor Cocktail (100X) and 0.5 M EDTA solution (100X) were from Fisher Scientific, Madrid, Spain. Mouse anti-EGFR (sc71032) and rabbit anti-phospho-EGFR (Tyr1173) (sc-101668) Abs were obtained from Santa Cruz Biotechnology, Inc. Rabbit anti-phospho-EGFR (Tyr1045) (#2237), rabbit anti-phospho-AKT (Ser473) (#4060L), mouse anti-phospho-p44/42 ERK 1/2 (Thr202/Tyr204) (#9106L), rabbit anti-AKT (#9272) and rabbit anti-p44/42 ERK 1/2 (#9102) Abs were purchased from Cell Signaling Technology, S.G., Servicios Hospitalarios, S.L, Barcelona, Spain.

Characterization. Au NPs were visualized using a TEM, either JEOL 1010 or Tecnai Spirit, at an accelerating voltage of 80 kV. The sample (10 μ L) was drop-casted onto ultrathin Formvar-coated 200-mesh copper grids (Tedpella Inc.) and left to dry in air. For each sample, the size of at least 200 particles was measured to obtain the average and the size distribution. Digital images were analyzed with Image J software and a custom macro performing smoothing (3 x 3 or 5 x 5 median filter), manual global threshold, and automatic particle analysis provided by ImageJ. UV-Vis absorption spectra were recorded with a Shimadzu UV-2401PC spectrophotometer at room temperature. Purification by dialysis was performed using cellulose ester membranes (MWCO = 300 kDa, 10 mL) against PBS (5000 mL). Fluorescence measurements were performed using a SpectraMax M2e microplate reader operating in the fluorescence mode at excitation/emission wavelengths of 494/519 nm. Au content of the cell samples was determined by an Agilent inductively coupled plasma mass spectrometry (ICP-MS) instrument (model: 7500cx) with a detection limit of 0.02386 ppb. Both the supernatant and the pellet samples were digested in aqua regia at 100 °C before ICP-MS analysis. Ga was used as the internal standard, and the integration time/point and time/mass were 0.1 and 0.3 seconds, respectively, with a 3 x times repetition. The confocal images were acquired using a Leica TCS SP5 epifluorescence/reflectance laser scanning confocal microscope with a 63X oil immersion objective. The excitation was provided by an Ar multiline laser. Reflectance images were obtained with 488 nm laser excitation. Images were treated using Leica Microsystems LAS AF lite analysis software. Fluorescence optical microscope images were acquired using an inverted Nikon Ti-E microscope with a 60X objective, and optical microscope images were acquired using an inverted Nikon Eclipse TE2000-U microscope in dark field configuration with a 100X objective (CFI PL FL 100X OIL IRIS AN 0.5-1.3). Odyssey (LI-COR) and Versadoc (Biorad) imaging systems were used for quantitative IR and chemiluminescent protein detection for western blot, respectively, and bands were quantified using Quantity One software. Absorbance measurements were performed with Victor 3 microplate reader from PerkinElmer at 450 nm and 620 nm (reference wavelength).

Synthesis of Au NPs (~ 17 nm) in aqueous solution. Au NPs of 17.2 ± 1.8 nm were synthesized by the classical method of citrate reduction of H₂AuCl₄.⁷ Briefly, 65.7 mg of H₂AuCl₄·3 H₂O were diluted in 500

ml of milliQ water and the solution was heated up to boiling under vigorous stirring. 15 mL of a sodium citrate 1% (w/v) aqueous solution were added and the solution turned immediately from yellow into dark, and then into red in a few minutes, indicating Au NPs formation. The solution was left to react for 30 minutes and then cooled down under continuous stirring. Before conjugation, Au NPs were centrifuged at 18.000 g for 10 minutes and redispersed in borate buffer 2 mM at pH = 8.5 in a 10 x times concentrated volume. Final Au NPs concentration for conjugation was $\sim 10^{13}$ NPs/mL (~ 18 nM Au NPs).

Quantitative analysis of Cetuximab' polysaccharides oxidation. Cetuximab MAb was diluted to a concentration of 1 mg/ml in PB solution 0.1 M, pH = 7.0. Then, 10 μ L of an aqueous solution of NaIO₄ 0.1 M were added to 100 μ L of the Ab solution. The mixture was placed in an aliquot wrapped with aluminium foil and left to react for 30 minutes, at room temperature (RT) under gentle shaking. The oxidation rate was slowed down by dilution in 500 μ L of PB 10 mM, pH 7.0. The sample was immediately dialyzed with a cellulose membrane (MW 3.5 kDa) at RT for 2 hours against 5 L of PB 10 mM, pH = 7. It was followed by two additional dialysis cycles in the same conditions. A 250-fold excess of LYCH (20 μ l, 10 mM) was added to the Ab solution and it was allowed to react for 1 hour in the dark at RT under slow agitation. The reaction mixture was dialyzed in the same previously described conditions, by performing three dialysis cycles for a minimum of 2 hours. Fluorescence measurements from the samples were performed in a 96-well plate, using a LYCH calibrate in PB 10 mM, pH = 7, at concentrations ranging from 0 to 10 μ M. From these measurements, the concentration of LYCH per well was estimated. The concentration of Cetuximab MAbs in each well was determined by measuring the absorbance at 280 nm with a Shimadzu UV-2401PC spectrophotometer, on the basis of a molar extinction coefficient, ϵ , of $210.000 \text{ M}^{-1}\text{cm}^{-1}$.⁹ To correct for any LyCH that was nonspecifically adsorbed to the Abs, all the results were compared with nonoxidized Abs that had been incubated with a 250-fold excess of LyCH. Under the purification conditions used, the level of nonspecifically bound LyCH was approximately 0.01-0.02 LyCH molecules/MAb.

Preparation of linker-modified Cetuximab MAbs. Cetuximab MAb was diluted to a concentration of 1 mg/ml in PB solution 0.1 M, pH = 7.0. Then, 10 μ L of an aqueous solution of NaIO₄ 0.1 M were added to 100 μ L of the MAb solution. The mixture was placed in an aliquot wrapped with aluminium foil and left to react for 30 minutes, at RT under gentle shaking. The oxidation rate was slowed down by dilution in 500 μ L of PB 10 mM, pH 7.0. Then, 2 μ L of linker (**1**) in a 90% ethanol solution (50 mg/ml) were immediately added to the Abs solution, and it was let to react for 1 hour at RT under gentle shaking. Unreacted linker molecules were removed using ultrafiltration spin columns, by dilution of the solution in HEPES 40 mM (1 mL, pH = 8.5) and centrifugation at 2000 g for 2-3 min. The purification was repeated 3 x times, to a concentrated volume of ~ 300 μ l. Cetuximab-**1** pairs concentration was determined spectrophotometrically at 280 nm on the basis of a molar extinction coefficient, ϵ , of $210.000 \text{ M}^{-1}\text{cm}^{-1}$.⁹ The estimated concentration of Cetuximab-**1** pairs after purification was in the range of 200-400 μ g/mL in all cases.

Surface functionalization of Au NPs. Addition of Cetuximab-1 pairs to Au NPs (10 mL, ~ 18 nM) was calculated to obtain ratios of 6, 20 and 50 MAb/NP (in solution), which corresponded to 3, 6 and 8 MAb/NP (according to quantification with Alexa dye). The mixtures were left to react for 20 minutes at 4°C under slow agitation to reach equilibrium. Then, a short thiolated PEG (MW 356.48) was added at 3-fold molar excess over the estimated complete NPs coverage (calculated by the number of Au atoms at the surface of the NP and assuming that each thiolated molecule occupies 21.4 Å² of the Au NP surface)⁶ to passivate the remaining NPs surface. After 5 minutes reaction, dialysis was performed in 2 cycles of 2 hours and a third cycle overnight at 4°C. A control Ab (goat anti-rabbit IgG) was likewise purified to confirm the successful release of free Abs across the dialysis membrane. After the purification step, the samples were preserved in PBS 0.1% g/ml BSA.

Cell culture and NP preparation. Epidermoid carcinoma cells (A431) were cultured in Dulbecco's modified Eagle's medium (DMEM) supplemented with 10% fetal bovine serum (FBS) under a humidified 10% CO₂ atmosphere at 37 °C. Previously to the incubation with cells, the bioconjugates at a concentration of ~ 18 nM NPs were irradiated with UV light for at least 3 hours.

Au NP bioconjugates binding studies. Plasma membrane sheets from A431 cells were prepared, fixed, and incubated with Cetuximab-1-Au NP bioconjugates by optimizing the method from Prior *et al.*^{9,10} In brief, A431 cells were seeded onto sterile glass coverslips in 6-well plates to be ideally 50-60% confluent and sparse when processing begun. After 48 hours, and previously to the treatment, the medium was changed to serum-free medium for 5 additional hours. Cells were then incubated either with Cetuximab-1-Au NP bioconjugates with a different loading of Abs (3, 6 and 8 Cetuximab Abs attached onto 17.2 ± 1.8 nm Au NPs; named as NPC3, NPC6 and NPC8, respectively) or unspecific anti-rabbit Ab-1-Au NP bioconjugates (8 anti-rabbit Abs attached onto 17.2 ± 1.8 nm Au NPs; named as NPAR) at a concentration of ~ 7.5 nM NPs for 25 minutes and at 4°C to avoid receptor-mediated internalization.¹¹ The incubation was performed in an upright configuration; for instance, a coverslip was placed onto a drop of 100 µl of Ab-1-Au NP bioconjugates. Coverslips were washed 5 x times in PBS after treatment and placed against Formvar and poly-L-lysine coated grids to transfer the cell membranes by exerting a slight pressure on top of them. Grids were immediately placed onto a drop of fixative (PFA 4%), and then quenched in glycine 25 mM, followed by 5 x times PBS and H₂O washes. Finally, the membranes were stained with UA (0.3 %) / methylcellulose (2%) to give them electron contrast and grids were left to air dry in wire loops. Plasma membrane sheets were visualized under a Tecnai Spirit TEM operating at 80 kV.

EGF binding and internalization studies. Cells were seeded on 24-well plates containing sterile coverslips to be 50-60% confluent the day of the experiment and placed in an incubator under a humidified 10% CO₂ atmosphere at 37 °C. Prior to treatment, cells were starved for 5 hours in serum-free medium (DMEM). Cells were then incubated for 2 hours in DMEM containing Cetuximab alone or conjugated to NPs, and NPAR so as to exclude non-specific interactions. The concentrations used were 2 nM of Cetuximab and 2, 4 or 8 nM NPs, respectively. The incubation was followed by 2 x times PBS

washes and stimulation with 20 ng/ml of Alexa Fluor 555-EGF complex. Cells were immediately washed with cold PBS and fixed with PFA 4% at RT during 15 minutes. Coverslips were washed 3 x times with PBS and dried onto filter paper before they were mounted on 40 μ l of moviol with DAPI. Cells were imaged by using an inverted Nikon Ti-E fluorescence optical microscope with a 60X objective, and an inverted Nikon Eclipse TE2000-U microscope in dark field configuration with a 100X objective (CFI PL FL 100X OIL IRIS AN 0.5-1.3).

Quantification of Au NP bioconjugates uptake. For ICP-MS analysis, cells were seeded at a density of 10^6 cells per well in six-well plates. Serum-starved A431 cells were incubated for 3 hours and at 37 °C with three different concentrations of the Cetuximab-1-Au NP bioconjugates (4.5, 9 and 13.5 nM NPs, corresponding to approximately 112, 224 and 335 ppm of Au, respectively) and NPAR bioconjugates as a negative control. After the incubation time, the medium of the cells was collected for ICP-MS analysis, and the cells were washed 3 x times with PBS (1 mL), trypsinized (Trypsin-EDTA, 1 mL) and centrifuged (400 rcf, 10 minutes). The resulting pellets were also collected for ICP-MS analysis. The percentage of cell-associated NPs was calculated relative to the total number of NPs used in the incubation medium and compared well with the decrease of NPs observed in the incubation medium after cell exposure in all the cases.

TEM analysis of Au NP bioconjugates uptake. Cells were seeded at a density of 10^6 cells per well in six-well plates. Serum-starved cells were then incubated either with Cetuximab-1-Au NP bioconjugates (NPC3, NPC6 and NPC8) or a unspecific anti-rabbit Ab-1-Au NP bioconjugate (NPAR) at a concentration of \sim 9 nM of NPs for 3 hours and 24 hours and at 37 °C. After incubation, the cells were immediately processed for TEM analysis. In brief, cells were thoroughly washed (3 x) with PBS buffer and fixed in a 0.1 M PB solution containing 2.5% glutaraldehyde at 4 °C for 1 hour. The cells were then rinsed 3 x times with PBS and carefully collected in a tube with a cell scraper. The cellular pellet was postfixed in 1% osmium tetroxide solution for 1 hour, rinsed with PBS and distilled H₂O, and dehydrated in a graded series of ethanol (30, 60, 70, 80, and 100%). Warm epoxy resin was added for infiltration and embedding, and it was left to polymerize at 60 °C for 48 hours. Ultrathin sections (\sim 50 nm) were cut with a diamond knife in a Leica Ultracut UCT ultramicrotome, and stained with 5 % uranyl acetate and 2% lead citrate for visualization under TEM.

EGFR downregulation studies. For immunofluorescence analysis of EGFR, 10^6 cells were seed onto sterile glass coverslips in 6-well plates and after 48 hours, the medium was changed to serum-free medium for 24 additional hours, previously to the treatment. Treatment with 4.5 nM of NPC6 bioconjugates and the equivalent NPAR and Cetuximab concentrations was applied for 3 hours and 24 hours followed by additional 24 hours incubation with fresh medium. After incubation, cells were washed with PBS and then fixed with cold methanol for 10 minutes at -20 °C. Fixed cells were rehydrated in 0.05 % Tween (Sigma) in PBS (PBS-T) and then permeabilized with cold 0.1 % Triton X-100 (Roche) in PBS for 8 min at 4 °C. Samples were blocked using 5 % non-fat milk in PBS-T for 1 hour and then rinsed once with PBS-T before primary antibody incubation. A 1:200 dilution of mouse anti-EGFR (sc71032) in

2% BSA PBS-T was incubated overnight at 4 °C. Cells were washed 4 x times with PBS-T and incubated for 1 hour in PBS-T containing 2 % non-fat milk, a 1:1000 dilution of the secondary antibody Alexa Fluor 488 goat anti-mouse (Invitrogen) and a 1:500 dilution of 2,4-diamidino-2-phenylindole (DAPI; Sigma). Cells were rinsed twice with PBS-T and twice with PBS. Coverslips were mounted onto slide glasses with ProLong Gold antifade reagent (Invitrogen). Immunofluorescence images were collected on an inverted confocal microscope (Leica SP5) and a 63X objective. Z stacks of 0.5- μ m step section were projected, analysed and images were generated using Leica software LAS AF Lite (Leica) and IMARIS (Bitplane) and composed in Adobe Photoshop CS 8.0.1.

Western blotting (WB) analysis. Cells were seeded to be 60% confluent the day of the experiment, and prior to NP treatment, they were starved for 24 hours in DMEM without serum so as to reduce exogenous growth factors. Cells were incubated for 2-3 hours with DMEM containing Cetuximab alone or conjugated to Au NPs (NPC3, NPC6 and NPC8) and NPAR bioconjugate at the desired concentrations (from 4.5 to 15 nM NPs), followed by 2 x times PBS washes and incubation with 10-20 ng/ml of EGF for 15 minutes. Cells were immediately washed with 1 mL PBS (3 x) at 4 °C, and lysed with a mammalian protein extraction reagent supplemented with a protease and phosphatase inhibitor cocktail. The mixtures were placed into plastic tubes for centrifugation (15 minutes, 13.500 rpm, 4°C) and the supernatants were processed for WB. The resulting membranes were incubated with primary Abs: rabbit anti-phospho-EGFR (Tyr 1173) at dilution 1:1000 overnight; rabbit anti-phospho-EGFR (Tyr 1045) at dilution 1:1000 overnight; rabbit anti-phospho-AKT (Ser473) at dilution 1:2000 overnight; mouse anti-phospho-p44/42 ERK 1/2 (Thr202/Tyr204) at dilution 1:1000 overnight; mouse anti-EGFR at dilution 1:200 overnight; rabbit anti-Akt at dilution 1:1000 overnight; rabbit anti-p44/42 ERK 1/2 at dilution 1:1000 overnight; mouse anti- α -tubulin MAbs at dilution 1:10.000 for 2 hours; mouse anti-glyceraldehyde 3-phosphate dehydrogenase (GAPDH) (ab9484, Abcam) at dilution 1:5.000 for 2 hours. The membranes were washed 3 x times with TBS-T and blocked in 5% BSA TBS-T (Tris-buffered saline with Tween-20) for 1 hour. After 3 x times TBS-T washes, secondary Abs were incubated: goat anti-rabbit IgG-800 IR (Licor), goat anti-mouse IgG-800 IR (Licor) and goat anti-rabbit IgG-700 IR (Licor) at a dilution of 1:15.000; or HRP-labeled donkey anti-rabbit (1:5.000, GE Healthcare) and goat anti-mouse (1:5.000, Biorad). Secondary Abs were washed off by incubating the membranes 2 x times in TBS-T and once in TBS. Odyssey (LICOR) and Versadoc (Biorad) imaging systems were used for quantitative IR and chemiluminescent protein detection for western blot, respectively, and bands were quantified using Quantity One software.

Cell viability. For toxicity determination, 5×10^3 cells per well were seeded in 96-well plates and incubated overnight to allow for cell attachment. After overnight incubation, cells were washed with PBS and fresh DMEM (100 μ L) was added containing the Au NP bioconjugates (NPC3, NPC6, NPC8 and NPAR) and free Cetuximab at the desired concentrations and incubated for 72 hours. DMEM replacement was performed to avoid interference from Au NPs in the colorimetric analysis. The cell viability assay was performed using the XTT assay (Biomedica) in 96-well plates according to the manufacturer's instructions. In brief, XTT reagent (20 μ L) was added to the cell culture and incubated for 2 hours. After

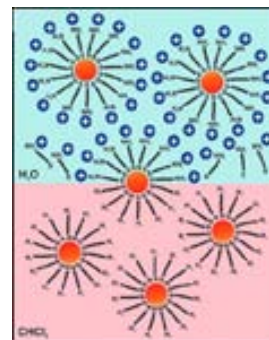
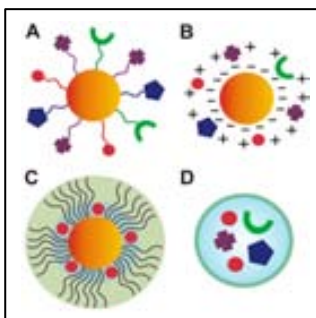
incubation, the absorbance was recorded at 450 nm (reference wavelength 620 nm) in a microplate reader (Victor 3, PerkinElmer). All conditions were performed in triplicate.

References

1. Brust, M.; Walker, M.; Bethell, D.; Schiffrin, D. J.; Whyman, R. *Synthesis of Thiol-Derivatised Gold Nanoparticles in a Two-Phase Liquid-Liquid System*. J. Chem. Soc., Chem. Commun., **1994**, 801-802.
2. Jana, N. R.; Gearheart, L.; Murphy, C. J. *Seeding Growth for Size Control of 5–40 nm Diameter Gold Nanoparticles*. Langmuir, **2001**, 17, 6782-6786.
3. Cheng, W.; Wang, E. *Size-Dependent Phase Transfer of Gold Nanoparticles from Water into Toluene by Tetraoctylammonium Cations: A Wholly Electrostatic Interaction*. The Journal of Physical Chemistry B, 2003, 108, 24-26.
4. Shen, C.; Hui, C.; Yang, T.; Xiao, C.; Tian, J.; Bao, L.; Chen, S.; Ding, H.; Gao, H. *Monodisperse Noble-Metal Nanoparticles and Their Surface Enhanced Raman Scattering Properties*. Chem. Mater., **2008**, 20, 6939-6944.
5. Based on electron diffraction studies of monolayers of alkanethiolates on Au(111) surface, which show a calculated area per molecule of 21.4 \AA^2 (ref. 6), the maximum surface density of 13 nm Au NPs would correspond to approximately 2150 thiolated molecules per NP.
6. Sellers, H.; Ulman, A.; Shnidman, Y.; Eilers, J. E. *Structure and Binding of Alkanethiolates on Gold and Silver Surfaces: Implications for Self-Assembled Monolayers*. J. Am. Chem. Soc., **1993**, 115, 9389–9401.
7. Turkevich, J.; Stevenson, P. C.; Hillier, J. *A Study of the Nucleation and Growth Processes in the Synthesis of Colloidal Gold*. Discuss. Farad. Soc., **1951**, 11, 55-75.
8. Frens, G. *Controlled Nucleation For Regulation of Particle Size in Monodisperse Gold Suspensions*. Nat. Phys. Sci., **1973**, 241, 20–22.
9. Johnstone, A.; Thorpe, R. *Immunochemistry in practice*. 2nd ed. Oxford: Blackwell Scientific Publications, **1987**.

ANNEX II : Manuscripts.

1. García-Fernández, L.; Ojea-Jiménez, I.; Lorenzo, J.; Puentes, V. F. *Facile Preparation of Cationic Gold Nanoparticle-Bioconjugates for Cell Penetration and Nuclear Targeting*. **ACS Nano**, **2012**, *6* (9), 7692-7702.



2. Ojea-Jiménez, I.; Comenge, J.; García-Fernández, L.; Megson, Z. A.; Casals, E.; Puentes, V. F. *Engineered Inorganic Nanoparticles for Drug Delivery Applications*. **Current Drug Metabolism**, **2012**, CDM-EPUB-20120605-5.

3. Imaz, I., Rubio-Martínez, M., García-Fernández, L., García, F., Ruiz-Molina, D., Hernando, J., Puentes, V. and Maspoch, D. *Coordination Polymer Particles as Potential Drug Delivery Systems*. **Chem. Commun.**, **2010**, *46*, 4737-4739.

4. García-Fernández, L.; Sperling, R.; Arbiol, J.; Puentes, V. *Controlling the Loading Number and Orientation of Immunoglobulin G on Gold Nanoparticles and the Induced Formation of Nano-Assemblies*. **European Cells & Materials Journal**, **2010**, *20*, 87.

5. Guix, M.; Carbonell, C.; Comenge, J.; García-Fernández, L.; Alarcón, A.; Casals, E.; Puentes, V. *Nanoparticle for Cosmetics. How safe is safe?* **Contributions to Science**, **2008**, *4*, 213-217.

6. Sperling, R. A.; García-Fernández, L.; Ojea-Jiménez, I.; Puentes, V. F. *One-pot Seeded Growth Synthesis of Cationic Gold Nanoparticles by Differential Reduction*. In preparation.

7. García-Fernández, L.; Sperling, R. A.; Puentes, V. F. *Rational Control of the Design and Programmability of Gold Nanoparticle-Antibody Conjugates and Their Organization in Superstructures*. In preparation.

8. García-Fernández, L., Tort, O., Lorenzo, J., Prior, I., Brust, M., Puentes, V. F. *Trapping Transmembrane Cellular Receptors Inside the Cell, Avoiding Receptor Recycling and Improving Antibody Therapy*. In preparation.

Book Chapter

Paul, R.; Botet, J. R.; Palet, D.; Casals, E.; Bautista, L.; García-Fernández, L.; Garrido-Franco, M.; García-Montaño, J.; De la Fuente, M.; Amantia, D.; Aubouy, L.; De la Varga, M.; Marsal, F.; Puentes, V. *Nano-finishing of cotton yarns and fabrics* – ISBN 978-83-7283-265-8 – in Monograph – Innovative Materials and Technologies in Made-up Textile Articles and Footwear, eds I. Frydrych and M. Pawlowa, Technical University of Lodz, Faculty of Material Technologies and Textile Design, Lodz, pp 91-97, **2008**.